Design and Scaling of Cross-Flow Turbines in Variable Confinement

Aidan Hunt

A dissertation
submitted in partial fulfillment of the
requirements for the degree of

Doctor of Philosophy

University of Washington

2024

Reading Committee:
Brian Polagye, Chair
Michelle DiBenedetto
Owen Williams

Program Authorized to Offer Degree:
Mechanical Engineering

University of Washington

Abstract

Design and Scaling of Cross-Flow Turbines in Variable Confinement

Aidan Hunt

Chair of the Supervisory Committee:
Brian Polagye
Mechanical Engineering

Cross-flow turbines can convert the energy in wind or moving water into renewable power. The efficiency and loading characteristics of a cross-flow turbine depend on both the geometric configuration of the rotor and the properties of the flow the turbine operates in, with the combined effects of these factors influencing the engineering design, control, and management of these systems. However, due to their unsteady fluid dynamics, it can be difficult to predict how the interactions between turbine geometry and flow characteristics affect performance and shape optimal turbine design. Consequently, the aim of this research is to experimentally examine how the interplay between cross-flow turbine geometry and flow characteristics influences the dynamics that govern turbine performance, with the overall goals of identifying pathways for improving their power conversion efficiency and to provide experimental data for the validation of simulations and reduced-order models. This work focuses on two key flow parameters: the Reynolds number (which represents the turbine scale relative to the scale of the flow) and the blockage ratio (which represents how much of a channel is occupied by a turbine in confined flow). Additionally, this work considers three aspects of the rotor geometry: the number of blades, the chord-to-radius ratio, and the preset pitch angle. The first objective of this work is to evaluate the interplay between the Reynolds number, the chord-to-radius ratio, the preset pitch angle, and the blade count on cross-flow turbine performance through parametric variation of these variables in a large-scale experiment. The

results provide a better understanding of the effects of each parameter, as well as how their combined effects influence turbine hydrodynamics across a range of device scales. The second objective of this work is to examine the effects of confinement on the performance and near-wake characteristics of a two-rotor cross-flow turbine array, with an emphasis on the upper end of practically-achievable blockage ratios in river or tidal channels. These blockage ratios are relevant to full-scale turbine deployments, but have received limited experimental investigation. The results improve our understanding of how turbine performance evolves across a wide range of blockage ratios, and allow us to evaluate how well commonly-used analytical models based on linear momentum theory can represent real turbines at high confinement. Third, we combine the methodologies employed to address the first two objectives to examine how the effects of the chord-to-radius ratio, preset pitch angle, and blade count are influenced by confinement. This provides the first experimental examination of the interplay between confinement and rotor geometry on turbine performance, and illuminates key design principles for turbines in confined flows.

Although the effects of the Reynolds number, chord-to-radius ratio, preset pitch angle, and blade count have been investigated in prior work, the combined influences of these parameters on cross-flow turbine performance have not been systematically explored. To examine how turbine scale influences the optimal rotor geometry, we conduct 223 unique experiments across an order of magnitude of diameter-based Reynolds numbers ($\approx 8{\times}10^4 - 8{\times}10^5$), in which the performance implications of the chord-to-radius ratio, preset pitch angle, and number of blades are evaluated. In agreement with prior work, maximum performance is generally observed to increase with Reynolds number and decrease with blade count. The broader experimental space clarifies parametric interdependencies; for example, the optimal preset pitch angle is increasingly negative as the chord-to-radius ratio increases. As these experiments vary both the chord-to-radius ratio and blade count, the performance of different rotor geometries with the same solidity (the ratio of total blade chord to rotor circumference)

can also be evaluated. The results demonstrate that while solidity can be a poor predictor of maximum performance, across all scales and tested geometries it is an excellent predictor of the tip-speed ratio corresponding to maximum performance. Overall, these results present a uniquely holistic view of relevant geometric considerations for cross-flow turbine rotor design and provide a rich dataset for validation of numerical simulations and reduced-order models. Although this work focuses primarily on cross-flow turbines in water channels, the key results are also applicable to wind-driven cross-flow turbines under similar conditions.

The performance and near-wake characteristics of a turbine in a confined flow depend on the blockage ratio, but limited experimental investigation has been performed for turbine performance at the upper range of practically-achievable blockage ratios, which have been hypothesized as a mechanism for reducing cost of energy. Furthermore, while linear momentum actuator disk theory is frequently used to model turbines in confined flows, how well these idealized models can represent the performance and flow fields around real turbines as confinement—and the attendant benefits—increase is largely untested. To address these gaps in understanding, we evaluate the performance and near-wake flow field of a two-rotor cross-flow turbine array at blockage ratios from 30% to 55%. In agreement with prior work, the array-averaged power and thrust coefficients generally increase with blockage, as does the tip-speed ratio at which the array produces the most power. We find that the measured fluid velocity in the bypass region is found to be well-predicted by linear momentum theory, while the measured wake velocity is not. From this, we show that linear momentum theory collapses the measured power and thrust coefficients across this range of blockage ratios when these coefficients are scaled by the bypass velocity in a manner inspired by the bluff-body theory of Maskell [1]. Overall, this demonstrates that simple linear momentum models can be quantitatively descriptive of the dynamics of highly confined turbines. From this, an analytical method for predicting array performance as a function of blockage is developed. This work illuminates turbine performance at relatively high confinement and il-

lustrates the unexpected suitability of analytical models for predicting and interpreting their hydrodynamics.

Although the general effects of confinement on turbine performance are understood, how the optimal cross-flow turbine rotor geometry changes with the blockage ratio has not received significant attention in prior work. Therefore, we combine the methodologies of the preceding components of this research to parametrically examine how the interplay between the number of blades, the chord-to-radius ratio, the preset pitch angle, and the blockage ratio affect the performance of two-rotor cross-flow turbine array. The performance of 45 unique geometric configurations is evaluated at blockage ratios between 35% and 55%, resulting in 135 unique experiments. Array efficiency is found to increase with the blade count—an inversion of trends at lower blockage—whereas trends for the chord-to-radius ratio and preset pitch angle are similar to those at low blockage. When normalized by the corresponding bypass velocities predicted from linear momentum theory, the array-averaged power coefficients at maximum efficiency collapse for each geometry across the tested blockages, demonstrating the broader applicability of these analytical models across the geometric parameter space. While both the efficiency and thrust on the array generally increase with dynamic solidity at high blockage, the individual effects of the blade count and chord-to-radius ratio still influence performance. Overall, these results provide the first experimental investigation of how blockage shapes the optimal cross-flow turbine geometry, illuminating key design principles for turbines in confined flow.

TABLE OF CONTENTS

LIST OF FIGURES

LIST OF TABLES

NOMENCLATURE

Acronyms

ADV	Acoustic Doppler velocimeter
AFT	Axial-flow turbine
BEM	Blade element momentum
CFD	Computational fluid dynamics
CFT	Cross-flow turbine
FoV	Field of view
FST	Free surface transducer
LMADT	Linear momentum actuator disk theory
PIV	Particle image velocimetry
RANS	Reynolds-Averaged Navier-Stokes
UNH	University of New Hampshire
UW	University of Washington

Coordinates

x	Streamwise position [m]
y	Cross-stream position [m]
z	Vertical position [m]

Kinematic Parameters

α	Angle of attack [deg.]
α_n	Nominal angle of attack [deg.]

ω	Angular velocity [rad/s]
θ	Angular position [deg.]
$U_{\text{rel},n}$	Nominal relative velocity on blade [m/s]
U_{rel}	Relative velocity on blade [m/s]

Performance Metrics

λ	Tip-speed ratio
λ_{opt}	Optimal tip-speed ratio
C_L	Lateral force coefficient
C_P	Performance coefficient or power coefficient
C_T	Thrust coefficient
$C_{P,\text{blades}}$	C_P of blades only
$C_{P,\text{supports}}$	C_P of support structures only
L	Lateral force [N]
Q	Hydrodynamic torque [N-m]
T	Thrust force [N]

Flow Parameters

ν	Kinematic viscosity [m^2/s]
Ω_x	Streamwise vorticity [rad/s]
ρ	Density [kg/m^3]
A_{channel}	Channel cross-sectional area [m^2]
g	Gravitational acceleration [m/s^2]
h	Freestream water depth [m]
h_x	Water depth at a particular streamwise location [m]
s	Submergence depth [m]

TI	Turbulence intensity [%]
TKE	Turbulent kinetic energy [m^2/s^2]
U_∞	Freestream velocity [m/s]
U_x	Streamwise velocity [m/s]
U_y	Cross-stream velocity [m/s]
w	Flume width [m]

Geometric Parameters

α_p	Preset pitch angle [deg.]
σ	Solidity
σ_d	Dynamic solidity
A_{turbine}	Projected area of the turbine [m^2]
c	Blade chord length [m]
c/R	Chord-to-radius ratio
D	Turbine diameter (at blade $c/4$) [m]
D'	Outermost diameter swept by the blades [m]
H	Blade span [m]
N	Number of blades
R	Turbine radius (at blade $c/4$) [m]
R'	Outermost radius swept by blades [m]

Non-Dimensional Flow Parameters

β	Blockage ratio [%]
Fr_h	Froude number based on channel depth, h
Fr_s	Froude number based on submergence depth, s
Re_c	Chord-based Reynolds number

Re_D	Diameter-based Reynolds number
$Re_{c,n}$	Nominal chord-based Reynolds number
s/h	Normalized submergence depth

Linear Momentum Theory

a	Axial induction factor
a'	Angular induction factor
a_x	Streamwise induction factor
a_y	Cross-stream induction factor
u_b	Bypass velocity from LMADT [m/s]
u_t	Velocity through the turbine from LMADT [m/s]
u_w	Wake velocity from LMADT [m/s]
λ'	Tip-speed ratio re-scaled by ${U_\infty}'$
λ^b	Tip-speed ratio re-scaled by u_b
${C_P}'$	Power coefficient re-scaled by ${U_\infty}'$
${C_P}^b$	Power coefficient re-scaled by u_b
${C_T}'$	Thrust coefficient re-scaled by ${U_\infty}'$
${C_T}^b$	Thrust coefficient re-scaled by u_b
${U_\infty}'$	Unconfined freestream velocity [m/s]

Array Metrics

$\Delta\theta$	Phase difference [deg.]
$\square_A$	A quantity corresponding to Turbine A in the array
$\square_B$	A quantity corresponding to Turbine B in the array
$C_{L,\text{rotor}}$	Rotor-average lateral force coefficient
$C_{P,\text{array}}$	Array-average performance coefficient

$C_{T,\text{array}}$	Array-average thrust coefficient

Uncertainty Estimation

κ_j	Sensitivity of a performance metric to the j^{th} component measurement.
$\langle X \rangle$	The time-average value of X over all cycles
b_X	Systematic standard uncertainty of X
s_X	Random standard uncertainty of X
u_X	Combined standard uncertainty of X
X	Component measurement of a performance quantity
X_i	The average value of X over the i^{th} rotational cycle

ACKNOWLEDGMENTS

This dissertation would not exist without my family, mentors, and community, who have all supported me throughout my academic pursuits. I would especially like to thank my advisor, Brian Polagye, who has given me so many opportunities to grow as an engineer, teacher, and leader throughout my time as an undergraduate, staff, and graduate student at the University of Washington. Brian, your passion for marine energy, depth of knowledge, eagerness to learn, and willingness to trust your students are all inspirational, and I will always be grateful for having been able to work with you. Thank you for shaping me into the researcher I am today. I would also like to acknowledge my committee members, Michelle DiBenedetto, Owen Williams, and Alex Horner-Device for their insights and guidance.

Several of my other mentors over the past decade have also been instrumental in guiding my professional trajectory. I am especially grateful for the Student Conservation Association (SCA) Massachussets AmeriCorps program for putting me on the path for a sustainability-focused career, and my SCA mentors Melissa Patterson, Leigh Whaley, and Rob Hopkinson for providing early opportunities for me to engage in leadership, teaching, project management, and community building. I would also like to acknowledge Wes Hermann, who gave me the opportunity to conduct meaningful work in research and development at the QuantumScape Corporation long before I had any academic credentials to my name.

The work in this dissertation is built upon the contributions of cross-flow turbine researchers in the Marine Renewable Energy Lab that came before me. Thank you to Hannah Ross, Benjamin Strom, and Isabel Scherl for laying the intellectual and infrastructural foundations that have been crucial for my work, and for modelling excellence and creativity in experimental research. This work would also have been much more difficult without the

dedicated efforts of Gregory Talpey and Gemma Calandra, whose attention to detail and raw endurance during long experimental campaigns significantly elevated the quality of this research. Thank you to Abigale Snortland and Ari Athair for many insightful conversations on hydrodynamics and data visualization, and to Corey Crisp for lending his electronics genius to our work.

While this dissertation reflects my growth as an engineer and scientist over the course of my PhD, a significant portion of my graduate school experience was also dedicated to growing as a teacher. I would like to thank Benjamin Wiggins and the Science Teaching Experience Program for Upcoming PhD's (STEP-UP) for formally training me to be a better instructor, as well as John Kramlich and Kendra Burdett for supporting my teaching within the Mechanical Engineering Department. In this regard I am especially grateful to my advisor, Brian, for always encouraging my teaching ambitions, even when they restricted the time I had available for research.

Being in graduate school during a global pandemic was made much easier by the community woven throughout the Marine Renewable Energy Lab. In addition to the cross-flow turbine group members mentioned above, I would like to acknowledge Brittany Lydon, Curty Rusch, Sarah Edwards, Trevor Harrison, Ariana Mendible, Lindsey Jones, Sarah Palmer, Ama Hartman, Trent Dillon, and Katherine Van Ness. Thank you for all the happy hours, pick-up volleyball games, and spontaneous potlucks. Writing this document was also made much easier by the people in this community who opened up their beautiful spaces to me when I needed a change of scenery. Thank you to Suzanne Strom for allowing me to spend nearly two weeks writing by the warmth of a wood stove in her home on Lopez Island, and to Brian Polagye and Michelle Hickener for letting my wife and I spend a two week writing retreat in their mountain home in Mazama.

I am lucky to have had the opportunity to develop another fluid mechanics related passion—whitewater kayaking—during my time in graduate school. This sport has served

as a crucial connection to people outside of academia, and has shown me that hydrodynamics intuition and expertise take many forms. Thank you to all the patient and experienced boaters who took the time to teach me new paddling techniques, show me a fun splashy line down a rapid, and set safety for me each time I stepped up to a more challenging river. I would especially like to thank Marcus Blair for his early guidance and for teaching me how to roll, Arwyn Hood for her generous mentorship, and Scott Perry, Megan Degelsmith, and Scott McIntosh for bringing so much stoke to the river every day.

Last, I would like to acknowledge my family, both biological and chosen. Thank you to my parents, Lisa and Aaron Hunt, for fostering my intellectual development throughout my entire life, and for your unconditional love and support. Thank you to my best friend, Conor Lanning, for being a steady and reliable companion throughout my engineering education and beyond. Your curiosity and creativity are truly inspirational to me, and your sense of humor is indispensable. I would like to thank my dog, Io, for his unconditional friendship, positive energy, and frequent, unabashed encouragement for me to take step away from my computer and go play fetch outside. Many of my best ideas or breakthroughs occurred on my walks with you; thank you for reminding me to stop and smell the roses (or ferns, or trees, or grass). Finally, thank you to my wife Stacey, without whom none of this would have been possible. Stacey, thank you for always believing in me and advocating for me, for being goofy and adventurous with me, and for being such a kind and thoughtful presence in my life and in our community. Our life together is amazing, and whatever comes next for us after I graduate, I cannot wait to experience it with you.

Funding for the research in this dissertation was provided by the U.S. Navy's Naval Facilities Engineering and Systems Command (NAVFAC) under N0002410D6318 / N0002418F8702 and by the United States Advanced Research Projects Agency – Energy (ARPA-E) under award number DE-AR0001441. Support from the Alice C. Tyler Charitable Trust is gratefully acknowledged for upgrades to the experimental facilities at the University of Washington

that allow us to conduct robust, high-quality research.

DEDICATION

To Stacey, the love of my life.

Chapter 1
INTRODUCTION

The detrimental effects of climate change and increasing global power demands necessitate a transition away from fossil fuels and an increase in the development and uptake of renewable energy technologies [4]. While the expansion of wind and solar power generation is a critical element of this energy transition [5, 6], the energy in natural water flows such as rivers, tidal channels, and ocean currents comprise a largely untapped source of reliable renewable power. Marine renewable energy technologies that harness the power in these flows play a key role in the energy transition by providing sustainable electricity for remote communities, ocean observations, and marine industries situated near these resources [7].

Cross-flow turbines, which can convert the energy in water currents or wind into useful mechanical power, are one such marine renewable energy technology. As opposed to conventional axial-flow turbines, the axis of rotation of a cross-flow turbine is perpendicular to the incoming flow. Cross-flow turbines thus operate omnidirectionally, eliminating the need for active yaw control when the direction of inflow changes. For vertically-oriented cross-flow turbines with short drivelines, the gearbox and generator can be located at the base of the device, facilitating economic installation and maintenance. Additionally, due to their rectangular projected area, cross-flow turbines can achieve high blockage in confined flows—which enhances their power conversion efficiency [8–11]—more easily than axial-flow turbines. These characteristics make cross-flow turbines particularly well-suited for deployment in river and tidal channels.

[1] While cross-flow turbine designs with fixed blade pitch have only a single degree of

[1] This introduction contains content that originally appeared in Ref. [12] (A. Hunt *et al.*, "Effect of

rotational freedom, static geometric parameters have important implications for turbine performance. These parameters include the overall shape and size of the rotor (e.g., aspect ratio [12–14], helix angle [15, 16], and number of blades [17–20]), properties of the blades (e.g., foil profile [21, 22], preset-pitch angle [23–25], and chord-to-radius ratio [26–29]), and the type of support members used to attach the blades to the central shaft (e.g., struts or end-plates [29–31]). The performance of a turbine with a given geometric configuration is also affected by the characteristics of the flow in which it operates. For example, turbine performance is influenced by the scale of the device relative to the scale of the flow (represented by the Reynolds number) [20, 32, 33], and the power conversion efficiency of a turbine operating in a channel depends on how much of the channel the turbine occupies (i.e., its blockage ratio) [8, 10, 11, 34]. While the effects of these geometric and flow parameters have been studied individually, their combined effects ultimately drive the optimal turbine design.

The breadth of this parameter space suggests optimization of cross-flow turbines by reduced-order models, but this is complicated due to their inherently unsteady fluid mechanics. During rotation, the angle of attack on each turbine blade varies significantly, which can induce dynamic stall and subsequent vortex shedding [35–39]. Additionally, the turbine blades pass through disturbed flow during their downstream sweep, potentially interacting with coherent structures. These multi-scale dynamics are difficult to generalize in reduced-order models [40]; unlike the blade element momentum (BEM) models that were influential in the commercialization of axial-flow turbines [41], analytical models for cross-flow turbines [42–44] are often only valid for specific rotor designs. Consequently, cross-flow turbines remain underdeveloped relative to axial-flow turbines, and the design space has not converged on an optimal rotor geometry for any flow condition.

Due to the limitations of reduced-order models, cross-flow turbines are typically studied using computational fluid dynamics (CFD) (e.g., [11, 22, 40, 45–47]) or through laboratory

aspect ratio on cross-flow turbine performance," *Journal of Renewable and Sustainable Energy*, vol. 12, no. 054501, 2020. DOI: 10.1063/5.0016753). AIP allows the inclusion of copyrighted work by the author in a thesis document.

experiments (e.g., [33, 34, 48–50]). However, the challenges of simulating unsteady boundary layer dynamics [51, 52], combined with a lack of exploitable circumferential symmetry and a necessity for high spatial and temporal resolution [53], make accurate two-dimensional simulations of cross-flow turbines computationally expensive. Three-dimensional simulations, which are even more expensive, are required to fully incorporate the effects of span-wise flow, mixing, and parasitic torque from blade supports [54–56]. These challenges create a natural gravity towards experimental exploration of cross-flow turbine dynamics and design, where computational shortcomings are exchanged for limits on turbine size and flow conditions imposed by the test facility (e.g., maximum Reynolds number [33] or ability to maintain dynamic similarity [57]). Furthermore, since experimental data is necessary to validate the results of simulations and reduced-order models, systematic experimental studies of the effects of geometric and flow parameters on turbine performance are warranted.

This work focuses on the experimental investigation of cross-flow turbine fluid dynamics, with the objective of understanding how rotor design and flow parameters come together to influence turbine power conversion and forcing characteristics. Illuminating these interactions is vital to improving the design, implementation, and control of full-scale cross-flow turbines and ultimately reducing their levelized cost of energy. In Chapter 2, metrics for characterizing turbine performance are introduced, the hydrodynamics of cross-flow turbines that govern this performance are discussed, and key geometric and non-dimensional flow parameters that influence performance are reviewed. Chapter 3 presents common experimental methods that are employed throughout Chapters 4 to 6, which address the main objectives of this work. Chapter 4 explores the effects of the Reynolds number and three parameters of cross-flow turbine rotor geometry—the preset-pitch angle, chord-to-radius ratio, and the number of blades— and highlights key interactions between these parameters that inform turbine design. While Chapter 4 focuses on turbines in water channels, the key results are relevant for wind-driven cross-flow turbines as well. Chapter 5 examines the effects of confinement on the performance and near-wake of a cross-flow turbine array at high blockage, and demonstrates the capabilities of analytical linear momentum models for describing the flow

field and governing hydrodynamics of real turbines in confined flows. Chapter 6 combines the methodologies of Chapters 4 and 5 to examine how confinement influences the optimal rotor geometry of a cross-flow turbine, providing the first experimental investigation of the interplay between blockage and rotor design. Chapter 7 summarizes the main contributions of this dissertation and identifies pathways for future work.

Chapter 2
BACKGROUND

2.1 Performance metrics

Before discussing the hydrodynamics of cross-flow turbines in detail, it is useful to establish the metrics upon which turbine performance is typically evaluated. First, for a given rotor geometry and inflow condition, the forces and torques on a cross-flow turbine depend on its kinematics. These kinematics are commonly non-dimensionalized as the ratio of the blade tangential velocity to the freestream velocity, or the tip-speed ratio:

$$\lambda(t) = \frac{R\omega(t)}{U_\infty(t)}, \tag{2.1}$$

where R is the turbine radius, ω is the rotation rate, U_∞ is the undisturbed inflow velocity, and (t) indicates variation in time. These quantities are shown in an overhead view of a cross-flow turbine in Figure 2.1. Since blade kinematics are conventionally evaluated at the quarter-chord point, R is defined here as the distance from the axis of rotation to the quarter-chord position along the chord line. However, the outermost radius swept by the turbine (R' in Figure 2.1) is larger and varies with both blade thickness blade pitch angle.

The forces and torque on the turbine blades during rotation result in net fluid torque (Q), a net thrust force in the streamwise direction (T), and a net lateral force in the cross-stream direction (L) on the turbine as shown in Figure 2.1. The mechanical efficiency of the turbine (formally, the coefficient of performance or power coefficient) is the ratio of the mechanical power produced by the turbine to the flux of kinetic energy that theoretically passes through the rotor projected area,

$$C_P(t) = \frac{Q(t)\omega(t)}{\frac{1}{2}\rho U_\infty^3(t) H D'} \quad , \tag{2.2}$$

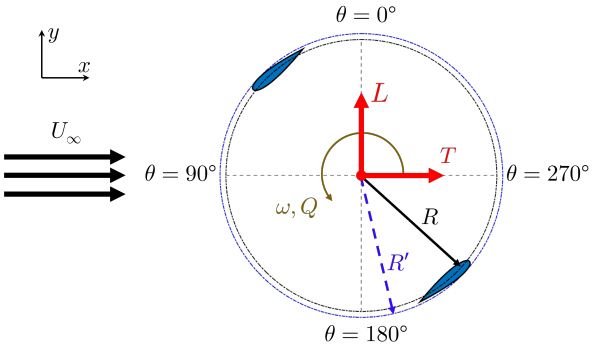

Figure 2.1: An overhead view of a cross-flow turbine with key quantities annotated.

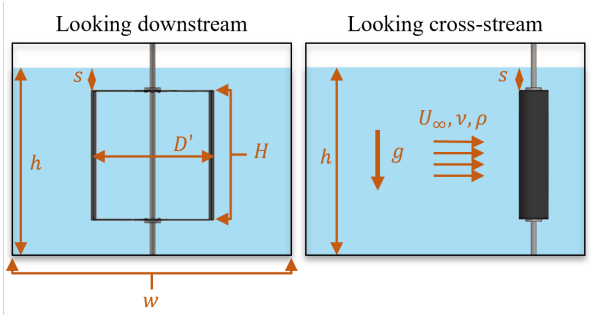

Figure 2.2: Dimensions and fluid properties for a single straight-bladed cross-flow turbine in a water channel, as viewed looking downstream (left) and looking cross-stream (right).

where Q is the hydrodynamic torque on the turbine, ρ is the density of the working fluid, H is the blade span (Figure 2.2), and $D' = 2R'$. It is noted that the conventional definition of C_P considers only the flux of *kinetic* energy through the turbine projected area, and neglects the potential energy in the flow that can be extracted by the turbine under certain conditions. The implications of this conventional kinetic-energy-only definition of C_P for situations in which the potential energy change across the turbine is substantial are discussed further in Chapter 5. Forces in the streamwise and cross-stream directions are similarly non-dimensionalized as the thrust and lateral force coefficients, given respectively as

$$C_T(t) = \frac{T(t)}{\frac{1}{2}\rho U_\infty^2(t) H D'} \quad , \tag{2.3}$$

$$C_L(t) = \frac{L(t)}{\frac{1}{2}\rho U_\infty^2(t) H D'} \quad . \tag{2.4}$$

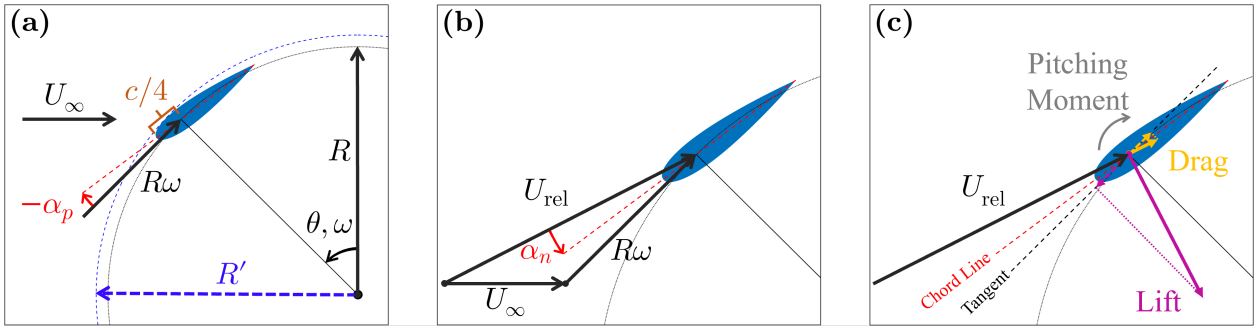

Figure 2.3: (a) The freestream velocity, blade tangential velocity, and preset pitch angle yield (b) a relative velocity on the blade at an angle of attack α_n, which results in (c) lift and drag forces on the foil. The representation in this figure neglects induction effects, which alter the U_∞ and $R\omega$ vectors.

2.2 Cross-Flow Turbine Fluid Dynamics

A simplified model of cross-flow turbine hydrodynamics is shown in Figure 2.3, in which a turbine blade with chord length c rotates with an angular velocity ω around the turbine's axis of rotation at a radius R. The azimuthal position of the blade, θ, is defined as the location where the blade tangential velocity ($R\omega$) vector points directly downstream. At each azimuthal position, the vector sum of the freestream velocity, U_∞, and the blade tangential velocity yields a resultant relative velocity on the blade, U_{rel}, at an angle of attack α_n. (Figure 2.3b). The relative velocity and angle of attack result in lift and drag forces on the foil (Figure 2.3c). The projection of these forces onto the line tangent to rotation gives rise to torque on the turbine, with the projection of lift producing torque in the direction of rotation and the projection of drag opposing rotation. The projection of these forces into a Cartesian coordinate system results in a net streamwise force (T) and net lateral force (L) on the turbine as shown in Figure 2.1. Note that, if the lift and drag forces do not act at the quarter chord of the blade (which can occur for symmetric foils in unsteady or curvilinear

flow), a pitching moment about the quarter chord also contributes to the net torque on the turbine.

As the cross-flow turbine harvests power from a fluid stream, these forces and torques must be balanced by a change in momentum in the freestream. For forces, to satisfy linear momentum conservation, an alteration to the inflow velocity as power is extracted is required. For axial-flow turbines, where the sole significant force is thrust in the streamwise direction, this is described by an "axial induction" factor, a, which represents the fractional decrease of freestream velocity at the rotor plane and is optimally equal to 1/3 [41]. Since cross-flow turbines experience net force in both the streamwise and cross-stream directions, induction from these forces could be described by a pair of "linear induction" factors, a_x and a_y, respectively, such that $U_x = U_\infty(1 - a_x)$ and $U_y = -a_y U_\infty$. Since blade forces vary with azimuthal position, θ, these factors would as well (i.e., $a_x = a_x(\theta)$). Similarly, for both axial-flow and cross-flow turbines, when torque is generated by the turbine, angular momentum conservation gives rise to an "angular induction" factor, a', which optimally approaches zero at sufficiently high rotation rates [41]. Together, these factors alter both the magnitude and direction of U_{rel}.

Using these definitions, the variation in angle of attack, α, throughout the blade's revolution is completely described as

$$\alpha = \arctan\left(\frac{U_x \sin\theta + U_y \cos\theta}{R\omega(1+a') + U_x \cos\theta + U_y \sin\theta}\right) + \alpha_p \quad , \tag{2.5}$$

where the preset pitch angle, α_p, is defined as in Figure 2.3a with $\alpha_p < 0°$ corresponding to a "toe out" (i.e., leading edge out) rotation that reduces the local angle of attack on the upstream sweep ($0° \leq \theta < 180°$). Similarly, the relative velocity, U_{rel}, is defined as the vector sum of the normal and tangential velocities as

$$U_{\text{rel}} = \sqrt{(U_x \sin\theta + U_y \cos\theta)^2 + (R\omega(1+a') + U_x \cos\theta + U_y \sin\theta)^2}. \tag{2.6}$$

Unlike axial-flow turbines, there is not an analytical theory that generally describes a_x, a_y, and a'. The closest analog, Double Multiple Streamtube Theory (DMST) [58, 59], estimates

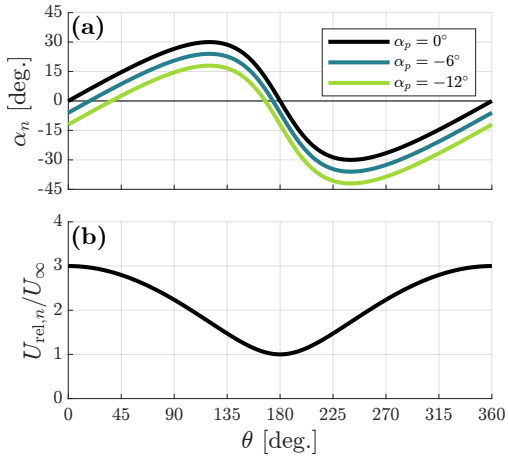

Figure 2.4: (a) Nominal angle of attack, α_n, as a function of azimuthal position during a rotational cycle for $\lambda = 2$ and several α_p. (b) Nominal relative velocity, normalized by U_∞ for the same azimuthal positions.

$a_x(\theta)$, but implicitly assumes $a_y(\theta) = a'(\theta) = 0$. Consequently, in semi-quantitative discussions of cross-flow turbine fluid mechanics, it is often convenient to neglect induction entirely and present nominal versions of α and U_{rel}. If $a_x(\theta) = a_y(\theta) = a'(\theta) = 0$, then Equations 2.5 and 2.6 reduce to

$$\alpha_n = \arctan\left(\frac{\sin\theta}{\lambda + \cos\theta}\right) + \alpha_p \tag{2.7}$$

and

$$U_{\mathrm{rel},n} = U_\infty \sqrt{\lambda^2 + 2\lambda\cos(\theta) + 1}. \tag{2.8}$$

As shown in Figure 2.4, this simplified model provides some insight into cross-flow turbine dynamics throughout a rotation. First, the oscillatory nature of the forces and torque on the rotor are apparent from the variations in α_n and $U_{\mathrm{rel},n}$. Second, the angle of attack variation is relatively large, such that $\alpha_p < 0°$ delays stall during the upstream sweep. Third, the maximum value for $U_{\mathrm{rel},n}$ (Figure 2.4b) is out of phase with that of α_n (Figure 2.4a), such that the phase-maximum for lift-generating torque is unlikely to occur at the phase-maximum for the coefficient of lift. It is important to remember that this model does not

describe the actual relative velocity or angle of attack, especially in the downstream sweep ($180° \leq \theta < 360°$) during which the blade encounters disturbed flow [60]. As such, direct comparisons with the static stall angle are not generally appropriate.

In addition to induction, several other fluid phenomena inherent to cross-flow turbine operation further influence blade-level hydrodynamics. As shown in Figure 2.4a, blade rotation results in significant variation in the angle of attack throughout a rotational cycle. This can cause dynamic stall [35–37, 39, 61], during which the airfoil's static stall angle is exceeded and the blade boundary layer can remain attached at higher angles of attack than it would under the static condition. This yields higher lift coefficients until separation finally occurs, past which lift plummets and drag increases. Consequently, the boundary layer on a cross-flow turbine blade is inherently unsteady, as during dynamic stall the boundary layer rolls up into a vortex that is later shed and, potentially, interacts with other blades.

Cross-flow turbine blades also experience flow curvature during rotation. Although blade kinematics are typically evaluated at a single point for convenience (e.g., the quarter-chord as in Figure 2.3), the true kinematics will vary along the blade chord since the distance from the axis of rotation to each point along the blade varies. Consequently, the actual angle of attack and relative velocity vary along the blade chord, causing a symmetric airfoil in curvilinear flow to perform like a cambered foil in rectilinear flow ("virtual camber") with an altered angle of the relative velocity ("virtual incidence"). The magnitude of virtual camber and virtual incidence experienced by the blade increases with c/R, but also depends on the tip-speed ratio, preset-pitch angle, and blade azimuthal position [26]. The presence of virtual camber and virtual incidence complicate design optimization since reduced order models for blade performance (e.g., blade-element momentum theory) typically utilize airfoil lift and drag coefficients as measured in rectilinear flow [28], although these models can include corrections for flow curvature [62, 63]. Prior research has generally focused on conformal mapping techniques for determining the virtual camber and incidence for blades experiencing flow curvature [26, 28, 64–66]. However, how flow curvature affects turbine performance metrics has received relatively limited attention outside of foundational work by Migliore

et al. [26], who attributed the lower performance of higher c/R turbines to flow curvature effects.

These phenomena further restrict the applicability of simplified models of cross-flow turbine hydrodynamics (Figure 2.4), and, for experiments, complicate direct relation of measured C_P and C_T to forces on the blades. However, these phenomena are important mechanisms for qualitatively interpreting how flow characteristics and rotor geometry influence turbine performance.

2.3 Geometric parameters

While cross-flow turbine designs with fixed blade pitch have only a single degree of rotational freedom, the geometric configuration of the rotor has important implications for turbine performance. Chapters 4 and 6 explore how turbine performance is influenced by three geometric parameters:

1. The "chord-to-radius ratio", c/R, affects the degree of flow curvature over the blade profile. When c is an appreciable fraction of R, the blade tangential speed varies from leading edge to trailing edge, which enhances virtual camber and virtual incidence. [28, 64, 67, 68].

2. The "preset pitch angle" (α_p)—the angle between the blade chord line and rotational tangent, defined at the quarter-chord as in Figure 2.3a—alters the range of angles of attack experienced by the turbine blades during rotation (Figure 2.4a), which in turn influences dynamic stall during the blade's upstream sweep [37, 47]. Prior work has shown that cross-flow turbines benefit from moderate toe-out (i.e. leading-edge out) preset pitch [23–25, 69, 70], shown in Figure 2.3a as a negative α_p.

3. The number of blades, N, influences the forces and torques on the turbine [18–20]. Specifically, in low-blockage flows (e.g., $\beta <= 20\%$) as N is increased, C_P tends to

decrease and C_T tends to increase, and the power produced and loads experienced become more consistent over a given rotational cycle [17, 71].

Other geometric parameters, such as the blade profile (e.g., symmetric or cambered) [27, 72–74], blade shape (e.g., straight or helical) [15, 16], aspect ratio [12, 14, 29] and surface roughness [75, 76] can also influence cross-flow turbine performance, but are not explored in this work.

Interplay between c/R, α_p, and N presents several challenges to exploring the fluid dynamics of cross-flow turbines, as well as to practitioners seeking an optimal turbine design. For example, N and c/R are commonly combined to form another geometric parameter, "solidity", which represents the fraction of the rotor circumference that is occupied by the blades:

$$\sigma = \frac{N}{2\pi}\frac{c}{R} \quad . \tag{2.9}$$

However, because inverse variation of c/R and N holds σ constant, one value of σ can actually correspond to disparate flow regimes. Similarly, when changing c, the blade-local Reynolds number (Section 2.4.1) and flow curvature are simultaneously affected. As a result, careful experimental design is required to isolate the effects of a particular parameter of interest.

2.4 Non-dimensional flow parameters

In addition to its kinematics, the performance of a cross-flow turbine also depends on the characteristics of the flow it is operating in. Important characteristics of the flow are often represented by key non-dimensional flow parameters. Understanding how these parameters influence turbine performance is critical for experimental design, in which it is often desireable to isolate the effects of a particular parameter while holding constant or minimizing the effects of another. Turbine dimensions and fluid properties relevant to these parameters are shown in Figure 2.2.

2.4.1 Reynolds Number

The turbine scale in relation to the flow is typically characterized by the Reynolds number

$$Re = \frac{U^* L^*}{\nu}, \tag{2.10}$$

where U^* is the characteristic velocity scale, L^* is the characteristic length scale, and ν is the kinematic viscosity of the working fluid. The Reynolds number can be interpreted as the balance between viscous and inertial forces in the flow through the turbine. The lift and drag forces on a turbine blade depend on the blade-local Reynolds number, which governs the behavior of the blade boundary layer [41, 77] and is given by

$$Re_c = \frac{U_{\text{rel}} c}{\nu}, \tag{2.11}$$

where ν is the kinematic viscosity of the surrounding fluid. As Re_c increases, the boundary layer on the blade becomes more turbulent, and momentum is injected into the blade boundary layer via turbulent mixing. Ultimately, this reduces profile drag on the blade and allows the boundary layer to stay attached at higher angles of attack [77]. Consequently, as the local Reynolds number increases, cross-flow turbine performance improves until a threshold value of Re_c is achieved, past which the efficiency does not change any further with increases in the Reynolds number [33]. This is called "Reynolds-independence" or "Reynolds-invariance".

Since U_{rel} depends on the velocity induced by the turbine forces and torque, it is not generally a known quantity in experiments. However, because the induced velocities depend on the turbine operating state, specifying λ, U_∞, and ν for a fixed turbine geometry implicitly specifies Re_c regardless of the velocity scale used in the calculation (e.g., $R\omega$, U_∞). Consequently, the Reynolds number is adequately expressed by any readily available length and velocity scale (e.g., Refs. [32, 33]). For convenience, a diameter-based Reynolds number is often employed, which is defined using the freestream velocity, U_∞, and turbine diameter (here referenced at the quarter-chord, $D = 2R$) as

$$Re_D = \frac{U_\infty D}{\nu} \quad . \tag{2.12}$$

Since Re_c is implicitly specified by Re_D and λ, cross-flow turbine performance at a given λ also increases with Re_D until Reynolds-independence is achieved [20, 32, 33]. However, since Re_c is still indeterminate if U_{rel} is unknown, physical interpretation of performance differences between turbines on the basis of Re_c is complicated when geometry and kinematics are simultaneously varied, as in Chapters 4 and 6.

2.4.2 Blockage

The efficiency of a turbine operating in a channel is influenced by how much of the channel the turbine occupies. The size of the turbine relative to the size of the channel is typically represented by the blockage ratio, defined as the ratio between the turbine's projected area and the channel cross-sectional area:

$$\beta = \frac{\mathrm{A}_{\text{turbine}}}{A_{\text{channel}}}. \tag{2.13}$$

As the blockage ratio increases, the turbine presents greater resistance to the oncoming flow. For a constant volumetric flow rate, this resistance, combined with confinement from the channel boundaries, increases flow through the turbine rotor relative to unconfined conditions. As a consequence, as confinement increases, so does turbine efficiency [8, 9, 78, 79]. Arrays of turbines can collectively achieve higher blockage and thus, higher efficiency. While blockage augments the performance of all turbine designs, cross-flow turbines are particularly well-suited for deployment in confined flows. This is because, in river and tidal channels with a fundamentally rectangular form factor, the rectangular projected area of the cross-flow configuration allows dense arrays of these turbines to achieve high blockage more easily than axial-flow turbines.

Garrett and Cummins [8] were the first to establish the theoretical basis for turbine performance in confined flows by applying one-dimensional linear momentum actuator disk theory (LMADT) to a turbine in a tidal channel. For relatively low Froude numbers, they showed that the maximum turbine efficiency in confined flow was augmented by a factor of $(1-\beta)^{-2}$. Subsequent studies further generalized this analytical model. Houlsby *et al.* [3]

and Whelan *et al.* [9] and relaxed the assumption of low Froude number by allowing the free surface to deform in response to momentum extraction. Subsequently, Nishino and Willden [78, 80] introduced a two-scale LMADT model for turbine arrays that considered confinement effects from both the channel boundaries and the presence of neighboring turbines within the array, which Dehtyriov *et al.* [81] later extended to an arbitrary number of scales (i.e., arrays of turbine sub-arrays) using a fractal-like approach. Vogel *et al.* [79] combined the open-channel and two-scale approaches into a single model that incorporates both free surface deformation and inter-turbine proximity effects.

The effects of blockage have also been investigated experimentally [9, 34, 68, 82–90] and numerically [11, 46, 91–101] for various turbine designs. Across these studies, performance results are generally consistent and aligned with theory: for all types of turbines, an increase in blockage results in increased thrust loading on the turbine, increased maximum efficiency, and a higher optimal operating speed (e.g., tip-speed ratio or reduced frequency). Studies that examine the flow field near the turbine [83, 86, 88, 90, 91, 95, 97] find that an increase in blockage accelerates the flow through and around the turbine as predicted by theory, as well as narrows the turbine wake. Many experimental [9, 34, 83–85, 88, 89] and numerical [11, 96, 99, 101] studies investigate the efficacy of analytical blockage corrections, which predict unconfined turbine performance from measured or calculated performance in confined flow. Notably, Whelan *et al.* [9], Kinsey and Dumas [11], and Ross and Polagye [34] applied a bluff-body blockage correction inspired by the theory of Maskell [1], which we further investigate in Chapter 5 in the context of performance scaling for high blockage cross-flow turbine arrays. Additionally, Gauthier *et al.* [96] and Kinsey and Dumas [11] examined how blockage effects change with confinement asymmetry (i.e., different channel widths and heights at constant β), and Goude and Ågren [93], Schluntz and Willden [95], and Abutunis and Menta [100] explored the interplay between rotor geometry and blockage effects, which we investigate further in Chapter 6.

2.4.3 Depth-Based Froude Number

For turbines in open-channel flows, such as river or tidal channels, the Froude number can also influence performance. For a rectangular channel, Froude number based on the channel depth is given as

$$Fr_h = \frac{U_\infty}{\sqrt{gh}} \quad , \tag{2.14}$$

where g is the acceleration due to gravity and h is the depth of the channel in which the turbine is operating (Figure 2.2). The depth-based Froude number represents the balance between inertial forces and gravitational forces in the flow through the channel. When $Fr_h \leq 1$, the flow is "subcritical", and information (e.g., waves) can propogate both usptream and downstream. When $Fr_h \geq 1$, the flow is "supercritical", meaning that inertia dominates and information can only propogate downstream.

In general, an increase in the Fr_h in the subcritical regime has been found to increase turbine C_P [12, 46, 79, 92]. This is typically attributed to an interaction between the turbine and the channel; namely a rise in the free surface upstream of the turbine and subsequent drop in the free surface across the rotor [46, 79], which is hypothesized to yield a localized blockage effect [79]. Overall, Fr_h has a more limited effect on turbine performance than either Re or β [102]. However, relative to Re and β, how Fr_h affects turbine performance has received less attention in the existing literature, especially in experiments. This is likely because it is physically challenging to vary the depth-based Froude number (which is a function of both U_∞ and h) without simultaneously varying the Reynolds number (which depends on U_∞) or the blockage ratio (which depends on h). Although careful experimental design may be employed to independently vary Fr_h while holding other non-dimensional parameters constant—for example, varying ν (via the fluid temperature) and U_∞ simultaneously to change Fr_h at constant Re—the range of flow conditions achievable in a given test facility typically narrows the range of Fr_h that can be explored. Consequently, the Froude number is often intentionally varied in tandem with the Reynolds number [12, 103, 104], maintained

below a threshold value, or neglected entirely [105].

2.4.4 Submergence Effects

Even when Re, β, and Fr_h are specified, the turbines' position in the water column—and thus its proximity to the free surface—is still a free parameter. Since the free surface is a dynamic boundary that responds to the presence of the turbine, these turbine-channel interactions can alter performance. However, there is no agreed-upon non-dimensional parameter for representing free surface proximity, which complicates cross-comparisons between studies. Ross and Polagye [102] define a submergence-based Froude number, Fr_s, as

$$Fr_s = \frac{U_\infty}{\sqrt{gs}} \tag{2.15}$$

where s is the distance between the free surface and the top of the turbine rotor (Figure 2.2). Conversely, Birjandi *et al.* [105] represent free surface proximity with a tip-clearance ratio, as s/H, where H is the turbine blade span. In Chapter 4, we utilize Fr_s to represent free surface proximity. In Chapters 5 and 6, we employ a normalized submergence depth, s/h, which can be combined with Fr_h to yield Fr_s [102] and is related to the tip-clearance ratio through the blockage ratio. Turbine performance is generally observed to increase as the rotor is moved nearer to the surface (i.e., decreasing s/h or increasing Fr_s) [94, 102, 105], although beyond a certain threshold value of s/h, turbine performance begins to decrease [94, 105]. At low s/h or high Fr_s, the turbine blades begin to pierce the free surface, which leads to air entrainment in the rotor (i.e., "ventilation") [106]. While ventilation leads to sharp performance degradation [105, 106], outside of this phenomenon the effects of free surface proximity on turbine performance are small relative to those of Re and β [102].

Chapter 3
METHODS OF INVESTIGATION

This chapter provides detail on elements of the experimental methods that are common throughout Chapters 4 to 6. Additional experimental methods that are specific to certain experiments are provided in the associated chapters.

3.1 Experimental Facility

The experiments in this work are primarily conducted in the Alice C. Tyler recirculating water flume at the University of Washington (UW) in Seattle, Washington (Figure 3.1). The flume has a test section that is 0.76 m wide and 4.88 m long, and can accommodate water depths up to 0.60 m. The flow is driven by two pumps with variable frequency drives, which can generate free stream velocities up to 1.1 m/s. Water temperature in the flume is regulated by in-line heating elements and an external chiller, and can maintain water temperatures between 10°C and 40°C. This allows the Reynolds number to be varied by changing both U_∞ and ν, the latter of which is a function of temperature. Due to a large stilling basin, turbulence intensities are relatively low $(2-4\%)$.

3.2 Cross-Flow Turbine Test Setup

Laboratory-scale cross-flow turbines are tested in the Tyler Flume using the experimental setup shown in Figure 3.2, which is similar to that employed in Refs. [12, 30, 102, 107, 108]. The turbine driveshaft is connected to a servomotor above the water surface (Yaskawa SGMCS-05BC341) via a flexible shaft coupling. The servomotor regulates the turbine's angular velocity and measures the turbine's angular position via an integrated encoder with 2^{16} counts per revolution (angular resolution of 0.0055°). The bottom of the turbine driveshaft

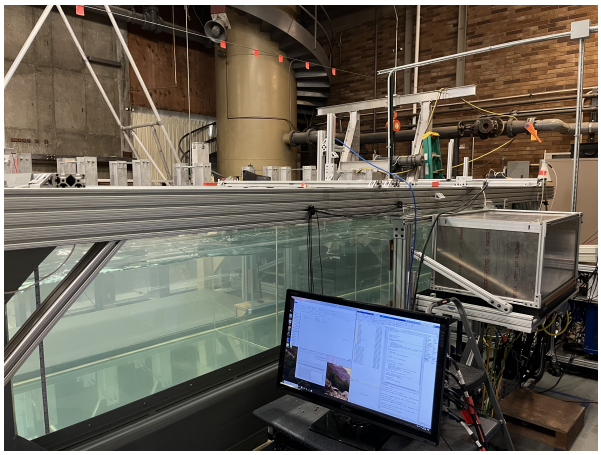

Figure 3.1: Image of the test section of the Alice C. Tyler Flume at the University of Washington.

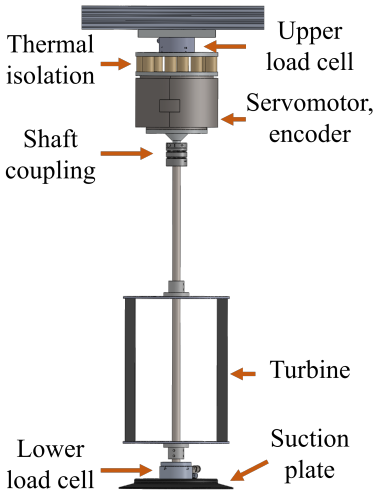

Figure 3.2: Front view of the experimental setup in the Alice C. Tyler flume with a two-bladed turbine installed.

Table 3.1: Instruments used in each chapter to measure turbine performance and flow quantities.

	Upper Load Cell	Lower Load Cell	ADV	FST
Chapter 4	ATI Mini-45 (IP65)	ATI Mini-40 (IP68)	Nortek Vector (64 Hz)	Omega LVU32 (5 Hz)
Chapters 5 and 6	ATI Mini-45 (IP65)	ATI Mini-45 (IP68)	Nortek Vectrino Profiler (16 Hz)	Omega LVU32 (0.5 Hz)

rests in a bearing secured to the bottom of the flume by a suction plate. When the servomotor regulates the turbine rotation rate to a constant value, the fluid torque acting on the turbine is equal to the sum of the resistive torque imposed on the turbine by the servomotor and the frictional torque from the bottom bearing [107]. Forces and torque acting on the turbine

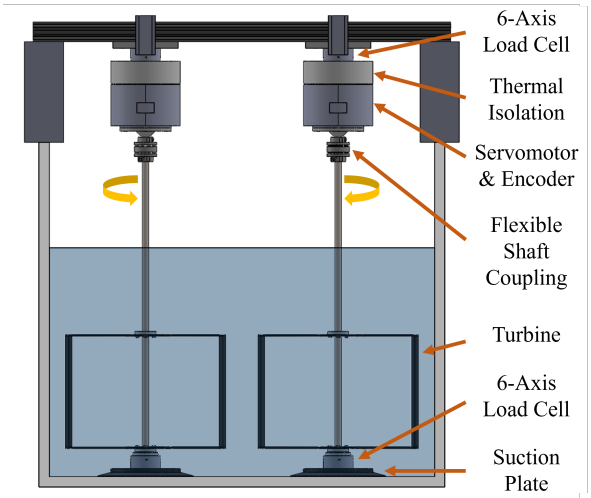

Figure 3.3: A rendering of the dual-turbine experimental test-rig, as viewed from upstream. The configuration shown corresponds to a blockage ratio of 40.1%.

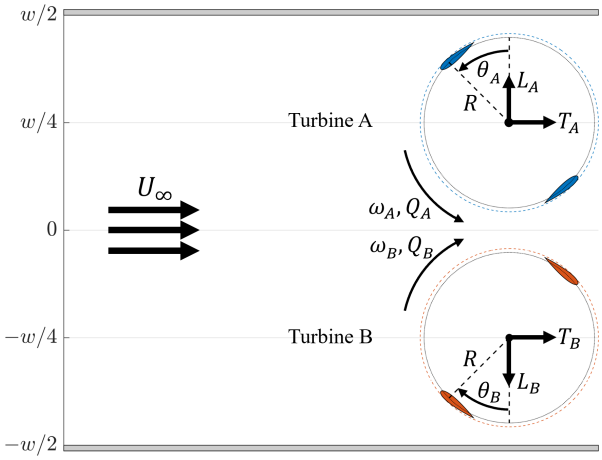

Figure 3.4: Overhead view of the dual-turbine layout in the Tyler flume, with key measured quantities annotated. The outermost circle swept by each turbine (with radius R') is shown as a dashed blue circle.

are measured by a pair of six-axis load cells: one coupled to the servomotor, and another coupled to the bottom bearing. The models of the six-axis load cells used in each chapter are tabulated in Table 3.1. The upper load cell is thermally isolated from the servomotor using ceramic standoffs in Chapter 4 and a Delrin spacer in Chapters 5 and 6. Measurements from the servomotor encoder and load cells are streamed to MATLAB (Simulink Desktop Realtime) at 1000 Hz via a set of National Instrument DAQs (PCIe-635x series). The experimental uncertainty of this system is formally analyzed using the ASME Standard for Test Uncertainty [109] in Appendix A, and quantified throughout this work by either the interquartile range or standard deviation of cycle-average parameters.

3.3 Cross-Flow Turbine Array

Chapters 5 and 6 characterize a two-turbine array by employing a pair of test rigs (Figure 3.3), each of which is identical to that described in Section 3.2. An overhead view of the array layout is shown in Figure 3.4, in which the individual turbines in the array are designated as "Turbine A" and "Turbine B". The center-to-center spacing between the turbines is $\sim 1.2D'$, and the array is positioned laterally such that the blade-to-blade spacing between adjacent turbines ($\sim 0.22D'$; $\sim 0.93c$) is twice the wall-to-blade spacing (i.e., the walls notionally correspond to symmetry planes in a larger array). The turbines are operated under a counter-rotating, phase-locked scheme, wherein both turbines rotate at the same, constant speed, but in opposite directions (i.e., $\omega_A = -\omega_B$), with a constant angular phase offset, $\Delta\theta$, between them. The turbines are counter-rotated such that the blades rotate toward the array centerline, which has been shown to augment performance relative to other rotation schemes [110–112]. For these experiments, $\Delta\theta = 0°$, an operating case in which the lateral forces and reaction torques for a pair of counter-rotating turbines are equal and opposite. A closed-loop controller maintains $\Delta\theta$ to within 1° of the target value across all experiments.

3.4 Flow Measurement

The freestream velocity is sampled at the turbine midplane by an acoustic Doppler velocimeter (ADV) centered laterally in the water column and located $5D'$ upstream of the axis of rotation. ADV measurements are despiked using the method of Goring and Nikora [113]. The freestream water depth is sampled by an ultrasonic free surface transducer (FST) centered laterally in the flume and located two turbine diameters upstream of the ADV. The ADVs, FSTs, and corresponding sample frequencies utilized in each chapter are tabulated in Table 3.1. For Chapters 5 and 6, the ADV sample frequency is reduced for improved signal-to-noise at lower freestream velocities, whereas the FST sample frequency is reduced to allow the upstream sensor to be synchronized with six other FSTs in the vicinity of the turbine array. The water temperature was manually monitored throughout experiments (Omega

Ultra-Precise RTD) and maintained to within +/- 0.1°C of its target value.

3.5 Computation of Performance Metrics

For experiments in the Tyler Flume, measurements of $Q(t)$, $T(t)$, $L(t)$, and $\omega(t)$ are synchronized, but are asynchronous with measurements of $U_\infty(t)$. Therefore, the time-averages of U_∞, $U_\infty^2(t)$, and $U_\infty^3(t)$ at a given set-point are used to calculate $\lambda(t)$ (Equation 2.1), $C_P(t)$ Equation 2.2), $C_T(t)$ (Equation 2.3), and $C_L(t)$ (Equation 2.4) for individual turbines. This approximation is a reasonable approach for experimental conditions with low turbulence intensity. While empirical corrections for advection time between the velocity measurement and turbine can be applied (e.g., [107]), this can artificially increase the variance of calculated $C_P(t)$ relative to measured power for situations when Taylor's frozen field hypothesis is violated.

For the two-turbine array (Figure 3.3), performance is evaluated on an array-average basis. Since the turbines in this array are identical, array-average performance metrics are simply the average of the individual turbine performance metrics. For example, the blade-level array-average efficiency, $C_{P,\text{array}}$ is simply the average C_P between Turbine A and Turbine B. Similarly, the array-average thrust coefficient, $C_{T,\text{array}}$, is the average C_T between Turbine A and Turbine B. Discussion of the array lateral force coefficients is provided in Appendix C.

Chapter 4

AN EXPERIMENTAL EVALUATION OF THE INTERPLAY BETWEEN GEOMETRY AND SCALE ON CROSS-FLOW TURBINE PERFORMANCE

The work in this chapter includes content from Ref. [114], which is under review at *Renewable and Sustainable Energy Reviews*. This work is co-authored by Benjamin Strom, Gregory Talpey, Hannah Ross, Isabel Scherl, Steven Brunton, Martin Wosnik, and Brian Polagye. Data collection was conducted by the author, Benjamin Strom, Gregory Talpey, Hannah Ross, and Isabel Scherl, and the initial set of experiments upon which this work is based can be found in Benjamin Strom's thesis [115]. The author conducted all data analysis and visualization, and led the drafting and editing of the manuscript, to which all authors contributed.

4.1 Motivation

As discussed in Sections 2.3 and 2.4, the general effects of the Reynolds number, c/R, N, and α_p on cross-flow turbine performance have been explored in prior work through both experiments and simulations. However, experimental studies are necessary to validate simulation results, and few experimental studies have parametrically evaluated enough combinations of the Reynolds number, c/R, N, and α_p to identify both individual and combined effects. Furthermore, differences in experimental approaches inhibit detailed cross-comparisons between previous experimental studies. Consequently, a single experimental investigation of cross-flow turbine performance that evaluates numerous combinations of these parameters, clarifies and unifies trends observed in prior work, and provides an expansive dataset for the validation of reduced-order and numerical models is warranted.

In this chapter, the interplay between cross-flow turbine rotor geometry and scale is experimentally investigated through parametric variation of the tip-speed ratio, Reynolds number, c/R, N, and α_p. In Section 4.2, prior experimental research involving narrower investigation of the parameters of interest is reviewed. Section 4.3 presents the methodology for the experiments, Section 4.4 presents the main trends observed across the parameter space and compares these to prior work, and Section 4.5 discusses the fluid dynamics that govern these trends. The study concludes with a summary of the implications of these results for turbine designers and future research in Section 4.6.

4.2 Review of Prior Experimental Work

Prior experimental research varying one or more of c/R, α_p, N, and the Reynolds number is summarized in Table 4.1. While it is acknowledged that there is a broad, complementary body of prior work utilizing numerical simulations to explore similar geometric parameters (e.g., [2, 29, 128, 129]), given the necessity of experimental data for validating simulations, particularly for cases with strong dynamic stall, prior experimental work is focused on here. Additionally, for ease of comparison across studies, the diameter-based Reynolds number(s) (Equation 2.12) associated with each study are provided, as this definition of the Reynolds number is agnostic to blade geometry. Except for five studies which focus on troposkein rotors [23, 116–119], the studies in Table 4.1 utilize turbines with straight blades, although a variety of blade cross-sectional profiles are employed. Prior work has generally varied one or more of c/R, N, α_p, and Re_D, while holding the others constant. All four parameters of interest have been shown to significantly affect cross-flow turbine performance. In general, turbine efficiency is found to increase with Reynolds number until a threshold is reached [20, 32, 33], decrease with increasing blade count [18–20, 103], and benefit from moderate toe-out preset pitch (i.e., $-8° < \alpha_p < -2°$) [18, 23–25, 103, 123, 124]. There are conflicting performance trends for the chord-to-radius ratio [26, 74, 76, 116, 120, 122, 125], though this is difficult to vary independently of other parameters (e.g., Re_c).

While the prior investigations listed in Table 4.1 span a wide range of c/R, α_p, N, and

Re_D, differences in approach complicate in-depth cross-comparisons between these studies. For example, several studies that explore the influences of chord-to-radius ratio or blade count attribute the observed effects to solidity (combining c/R and N as in Equation 2.9) rather than to the individual parameter that was varied [20, 74, 103, 116, 120, 125, 126]. Additionally, α_p depends on the chord-wise location where the angle between the chord line and the tangent line is defined [24, 25, 69, 130]. For example "neutral pitch" ($\alpha_p = 0°$) referenced at the mid-chord corresponds to a toe-out pitch angle ($\alpha_p < 0°$) referenced at the quarter-chord. However, the reference location that was used is seldom reported. Consequently, although Table 4.1 lists the values of α_p reported by the authors of each study, unstated inconsistencies in the reference location for α_p obfuscate direct comparison. Lastly, the studies listed in Table 4.1 employ a variety of blade-strut connection schemes, which can substantially affect turbine-level performance [30]. These factors all likely contribute to apparently conflicting conclusions about geometric trends.

Relative to prior experimental work, this study considers the most commonly tested blade counts (as well as single-bladed performance), moderate to high chord-to-radius ratios, and toe-out preset pitch angles in the general range of those that have been found to benefit performance. The range of Reynolds numbers ($Re_D = 0.75\times10^5 - 8.3\times10^5$) spans roughly an order of magnitude and overlaps with prior experimental work, but is still an order of magnitude lower than the highest Reynolds numbers tested to date [118, 119]. Based on prior work by Bachant *et al.* [32, 48] and Miller *et al.* [20, 33], the Re_D tested in this study are expected to overlap with the transitional regime in which airfoil performance—and thus turbine performance—depends strongly on the Reynolds number. The implications of these lower Reynolds numbers for the broader applicability of the results of this study are discussed in Section 4.5.4. In contrast to most studies in Table 4.1, several combinations of the three geometric parameters and Reynolds number are considered to identify interdependencies. While most prior experimental work characterizes turbine power production, measurements of forces are less common. Of the 31 studies in Table 4.1, only McAdam *et al.* [103, 104], Bachant *et al.* [32, 48], and Li *et al.* [18] characterize thrust force, and no studies charac-

terize lateral force (although this could be derived from normal and tangential blade forces presented by Li *et al.* [18, 71]). Consequently, the experiments in this study—in which turbine power and forces are both reported—provide the most extensive characterization of cross-flow turbine performance to date.

Table 4.1: Prior experimental studies of cross-flow turbines that varied the parameters considered in this work.

Reference	**Year**	N	c/R	α_p [deg.]	Re_D [$\times 10^{-5}$]
Blackwell and Sheldahl [116]	1977	2, 3	0.06 – 0.09	Not specified	$\sim$ 3.6 – 41
Sheldahl *et al.* [117]	1980	2, 3	0.06	Not specified	$\sim$ 10 – 69
Migliore *et al.* [26, 67]	1980	2	0.11 – 0.26	0	$\sim$ 2.5 – 15
Klimas and Worstell [23]	1981	2	0.06	-7 – 3	$\sim$ 11 – 46
Worstell [118]	1981	2, 3	0.07	Not specified	$\sim 100^{\dagger}$
Takamatsu *et al.* [68]	1985	1, 2, 4	0.3	0	$2.0 - 6.0^{\dagger}$
Takamatsu *et al.* [69]	1985	1	0.3	-10 – 10	$3.0^{\dagger}$
Takamatsu *et al.* [27]	1991	1	0.20 – 0.30	-5 – 0	$3.7^{\dagger}$
Ashwill [119]	1992	2	0.07	Not specified	$\sim 423^{\dagger}$
Shiono *et al.* [120]	2000	1 – 3	0.23 – 1.13	0	$1.8 - 4.2^{\dagger}$
Fiedler and Tullis [24]	2009	3	0.32	-8 – 8	$7.8 - 17^{\dagger}$
Howell *et al.* [75]	2010	2, 3	0.33	0	$1.2 - 2.0^{\dagger}$
El-Samanoudy *et al.* [121]	2010	2 – 4	0.2 – 0.75	-60 – 10	$2 - 4^{\dagger}$
Tanino *et al.* [122]	2011	3, 5	0.23 – 0.47	-10 – 20‡	1.3 – 2.4
Armstrong *et al.* [123]	2012	3	0.31	-12 – 12	33
McAdam *et al.* [103, 104]	2013	3 – 6	0.26	-4 – 0	$1.5 - 2.7^{\dagger}$
Zhao *et al.* [124]	2013	3	0.24	-3 – 5‡	9 – 13
Li *et al.* [18]	2015	2 – 5	0.27	-10 – 4	$10^{\dagger}$
Bachant and Wosnik [32]	2016	3	0.28	0	3.0 – 13
Eboibi *et al.* [125]	2016	3	0.09 – 0.11	0	$2.6 - 3.5^{\dagger}$
Li *et al.* [71]	2016	2 – 5	0.27	Optimal from [18]	$10^{\dagger}$
Bachant *et al.* [48]	2016	3	0.10	0	4.3 – 13
Priegue and Stoesser [76]	2017	2 – 4	0.40 – 0.60	-3	$2.9 - 4.6^{\dagger}$
Araya *et al.* [19]	2017	2, 3, 5	0.67	0	0.80
Miller *et al.* [33]	2018	5	0.45	0	5 – 50
Lam *et al.* [126]	2018	2, 3, 5	0.30	Not specified	$2.4^{\dagger}$
Somoano and Huera-Huarte [25]	2018	3	0.32	-16 – 8	3 - 5
Du *et al.* [74]	2019	3	0.22 – 0.33	-4 – 0	2.8 – 4.2
Miller *et al.* [20]	2021	2 – 5	0.45	0	7 – 50
Ross and Polagye [102]	2022	2	0.49	-6	0.61 – 0.79
Szczerba *et al.* [127]	2023	4	0.22	0 – 4‡	$2.7 - 8.2^{\dagger}$
Present Study		1 – 4	0.25 – 0.74	-12 – 0	0.75 – 8.3

† Re_D is not reported by the reference, but estimated here using reported turbine dimensions and flow quantities. If not provided, ν is assumed to be 1.6×10^{-5} for air (30 ^{o}C) and 1.0×10^{-6} for water (20 ^{o}C).

‡ Sign convention for reported α_p is not defined by the study.

4.3 Methods

To characterize cross-flow turbine performance over an order of magnitude of Re_D while holding other dimensionless parameters approximately constant, two different physical turbine sizes were tested, each in a different facility: one at the University of Washington (UW), and the other at the University of New Hampshire (UNH). As such, this section presents the geometric parameter space and Re_D explored, a description of the test facility at UNH, the metrics used to characterize performance, and the methods employed to synthesize the data.

4.3.1 Experimental Turbines

The geometric parameter space explored in this work includes five nominal chord-to-radius ratios (c/R = 0.25, 0.37, 0.49, 0.62, and 0.74), four blade counts (N = 1, 2, 3, and 4), and seven preset pitch angles defined at the quarter-chord (α_p = 0°, −2°, −4°, −6°, −8°, −10°, and −12°). All other relevant turbine geometric parameters, such as the aspect ratio (H/D = 1.42, where H is the blade span) and blade profile (straight-blades with NACA 0018 cross-sections) were held constant. Two turbine sizes were tested at four Re_D (Figure 4.1): the smaller UW rotors configurations (Figure 4.1a) were tested at $Re_D = 0.75\times10^5$, 1.6×10^5, and 2.7×10^5, while the larger UNH rotors (Figure 4.1b) were tested at $Re_D = 8.3\times10^5$. Turbine dimensions and geometric parameters are summarized in Table 4.2, and a subset of geometric configurations are visualized in Figure 4.2. For each combination of c/R, N, and Re_D, only the subset of α_p values required to identify the α_p that yielded maximum performance were tested. Additionally, fewer geometric configurations were tested with UNH rotors than for UW rotors due to the challenges of working with physically larger UNH turbines and the realization, following experiments with the large turbines, that it would be prudent to expand the parameter space. In total, performance was characterized for 223 unique combinations of c/R, α_p, N, and Re_D.

The blades for the UW rotors were machined from 7075-T6 aluminum and painted with an ultra-flat black spray paint. Blades for the UNH rotors were constructed of carbon fiber

Table 4.2: Geometric parameters and Reynolds numbers tested for each turbine size.

Parameter	**UW Turbines**	**UNH Turbines**
H [cm]	23.4	116.6
R [cm]*	8.21	41.02
R' [cm]*	8.23 – 9.13	41.55 – 42.88
c [cm]	2.03, 3.045, 4.06, 5.075, 6.09	10.10, 15.15, 20.20
c/R	0.25, 0.37, 0.49, 0.62, 0.74	0.25, 0.37, 0.49
α_p [deg.]	0, -2, -4, -6, -8, -10, -12	2, 4, 6, 8
N	1, 2, 3, 4	2, 4
Re_D [$\times 10^5$]	0.75, 1.6, 2.7	8.3
Test Facility	Tyler flume (UW)	Chase towing tank (UNH)

* Due to the blade mounting scheme used, R varies slightly with α_p for each geometry, whereas R' varies with both c/R and α_p. The values of R and R' for all tested geometries are provided in Appendix B.

($c = 10.10$ cm) or fiberglass ($c = 15.15$ cm and 20.20 cm). For both materials, blades were constructed using a wet lay-up in halves on open-faced molds and cured under vacuum in an autoclave. Blade halves were bonded together with aluminum inserts in the ends for fastening, a fiberglass dowel along the leading edge to provide additional bonding surface area, and closed-cell expanded foam core to discourage water retention. Due to differences in manufacturing approach, the surface roughness of the UW rotor blades was likely different than that of the UNH rotor blades, but was not characterized for either turbine.

For both turbine sizes, the blades were connected to a drive shaft by circular end plates (Figure 4.2a). While foil-shaped blade-end struts would incur lower parasitic torque losses [30, 48], a unique strut assembly would be needed for each combination of c/R, N, and α_p. To explore the parameter space while minimizing manufacturing costs, sets of end plates for

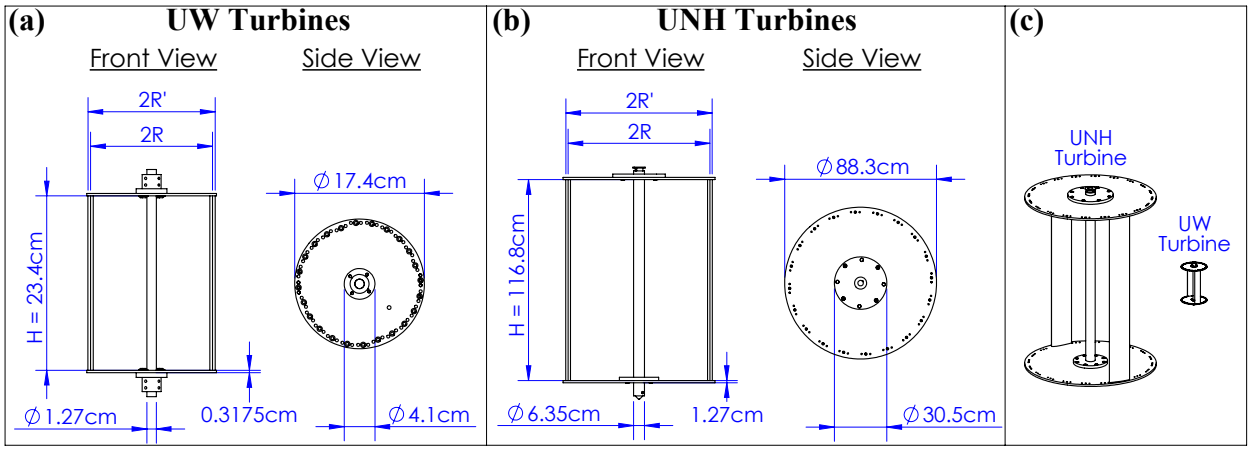

Figure 4.1: Dimensioned schematics of the (a) UW rotors and (b) UNH rotors rotors. (c) Relative size comparison between the two rotors. The configurations shown correspond to $c/R = 0.49$, $N = 2$, and $\alpha_p = -6°$.

each turbine size were machined with hole patterns that accommodated various numbers of equally spaced blades at various preset pitch angles. These common sets of end plates were then used for all chord lengths at each turbine scale.

This modular approach influenced the turbine design in two ways. First, for UW rotor configurations, to allow for the smallest chord lengths ($c/R = 0.25$ and 0.37) to be compatible with the same mounting hardware used for the larger chord lengths, the chord near the blade ends was gradually increased, while the middle 92% of the blade span retained the target chord length. Second, the radius of the outermost circle swept by the blades (R') varied for each combination of c/R and α_p. Specifically, because blades of all chord lengths use the same end plates, the mounting position for each preset pitch angle was selected such that the R' swept by a blade with the mid-range chord length ($c = 4.06$ cm for UW rotor configurations; $c = 15.15$ cm for UNH rotor configurations) was constant for all preset pitch angles. Consequently, for a blade mounted at a given α_p, while the quarter-chord position (R) and chord line orientation are independent of the chord length, R' changes slightly due to the variation in foil thickness and orientation. The difference in R' across chord lengths

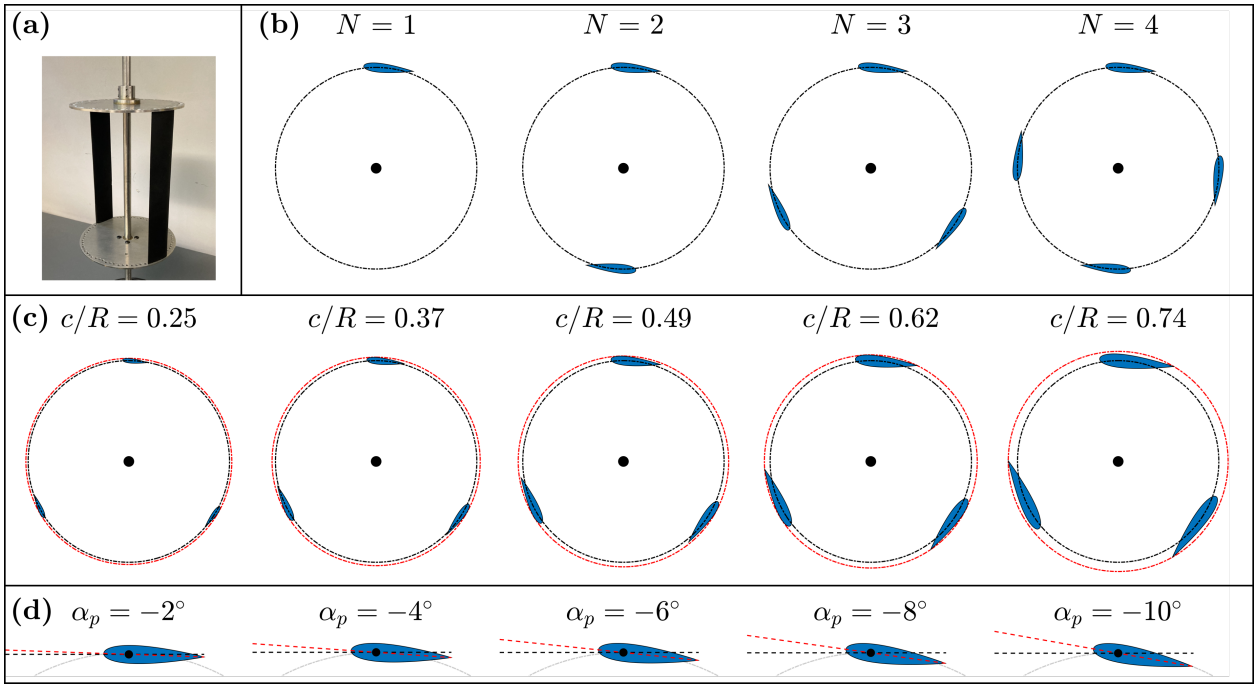

Figure 4.2: Partial visualization of experimental parameter space. (a) Isometric view of an assembled UW rotor with $N = 2$, $c/R = 0.49$, and $\alpha_p = -6°$. (b) Variation in blade count, N, for $c/R = 0.49$ and $\alpha_p = -6°$. (c) Variation in c/R for $\alpha_p = -6°$ and $N = 3$, with corresponding variation in the outermost swept radius R' due to the blade mounting scheme shown in red. (d) Variation in α_p for $c/R = 0.49$ with the chord lines indicated in red and the tangent lines indicated in black.

for $\alpha_p = -6°$ is shown by the red circles in Figure 4.2c. In addition, the quarter-chord radius (R) varies slightly with α_p (maximum deviation from mean value: $\approx 2\%$) and to a lesser degree than R' (maximum deviation from mean value: $\approx 6\%$). To account for this variation, the quarter-chord radius R is used for evaluating all kinematic quantities (e.g., λ, c/R, Re_D), while R' is used to calculate the turbine projected area for normalized performance metrics. The values of R, R', and derived quantities are tabulated in Appendix B for all tested geometries.

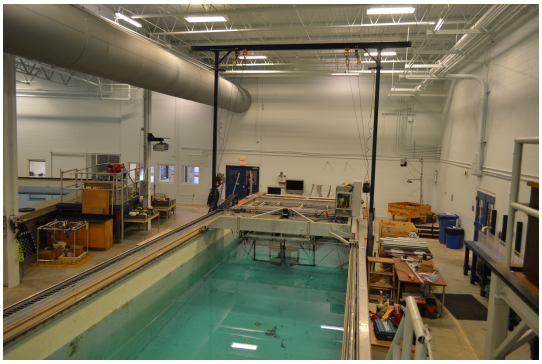

Figure 4.3: Image of the towing tank at the Chase Ocean Engineering Laboratory at UNH

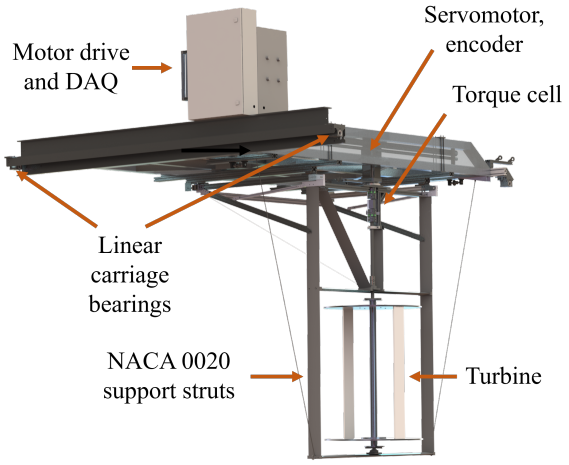

Figure 4.4: Rendering of the experimental setup used in the Chase Ocean Engineering Laboratory towing tank at UNH. The cross-flow turbine test bed attached to the tow carriage travels to the left during towing.

4.3.2 Experimental Facilities

Experiments using the UW rotor configurations were conducted in the Alice C. Tyler flume at the University of Washington in Seattle, Washington (described in Section 3.1) using the test rig described in Section 3.2, while experiments using the UNH rotor configurations were conducted in the towing tank at the Chase Ocean Engineering Laboratory (Figure 4.3) at the University of New Hampshire in Durham, New Hampshire.

The test section of the tow tank at the Chase Ocean Engineering Laboratory measures 3.66 m wide, 2.44 m deep, and 36.6 m long. The experimental setup (Figure 4.4) is similar to the smaller-scale version used at UW in that the turbine driveshaft is connected to the test rig at both ends. Complete details of this system are provided in Peter Bachant's dissertation [131]. The turbine rotation rate is regulated by a servomotor (Kollmorgen AKM62Q) and measured by an integrated encoder with 10^5 counts per revolution (angular resolution of

0.0036°). The toruqe on the turbine is measured by a rotary transducer (Interface T8-200), and losses due to the bottom bearing were characterized by spinning the turbine in air. The turbine test bed is attached to the tow carriage via linear bearings connected to two load cells to measure overall thrust, and the test bed is constructed from extruded aluminum struts (NACA 0020 profile with 0.14 m chord) to minimize drag. The tow carriage speed is measured by a linear encoder (Renishaw LM15). Thrust was measured, but is not reported as subsequent analysis indicated that one of the load cells was malfunctioning. For these experiments, all measured quantities were recorded at 2000 Hz. The temperature of the tow tank was measured manually using a digital thermometer prior to testing. Experimental uncertainty for this system is explored in Appendix A.

At UW, for each c/R, α_p, N, and Re_D combination tested turbine performance was characterized under constant-speed control over a range of λ in steps of 0.05 near the performance peak and in steps of 0.1-0.2 further from the peak. Data were collected at each λ setpoint for 45 seconds, which was sufficient to obtain convergence for time-average quantities. At UNH, each turbine geometry was tested across a range of λ in increments of 0.1, with one tow corresponding to one tip-speed ratio. The turbine was spun up to target rotation rate prior to towing. Since the data acquired during each tow include the linear acceleration and deceleration of the test bed, only the measurements when the test bed was at a quasi-steady state are considered. After towing, the water in the Chase tank was allowed to settle before the next tow began. A saw-toothed geo-textile beach was used to dissipate energy in the tank. The required tank settling times were established by using ADV measurements at mid-tank, mid-height after tows of comparable turbines, from which the time for the measured velocity to drop below the instrument noise floor was determined [132]. This time was then doubled and used as tank settling time; for the data reported here the settling time between tows was four minutes.

Table 4.3: Experimental conditions at each test facility.

Test Facility	$\boldsymbol{Re_D}$	$\boldsymbol{U_\infty}$ **[m/s]**	**Temp. [°C]**	$\boldsymbol{\nu}$ **[m²/s]**	$\boldsymbol{h}$ [m]	$\boldsymbol{s}$ **[m]**	$\boldsymbol{TI}$ **[%]**
Tyler flume	0.75×10^5	0.60	10.0	1.31×10^{-6}	0.48	0.05	2.5
Tyler flume	1.6×10^5	0.90	25.0	8.93×10^{-7}	0.48	0.11	2.7
Tyler flume	2.7×10^5	1.1	38.9	6.72×10^{-7}	0.48	0.17	3.9
Chase tank	8.3×10^5	1.0	20.3	9.96×10^{-7}	2.44	0.62	0

4.3.3 Test Conditions

Turbine performance at $Re_D = 0.75 \times 10^5$, 1.6×10^5, and 2.7×10^5 was evaluated at UW, while performance at $Re_D = 8.3 \times 10^5$ was evaluated at UNH. The velocity-temperature combinations that yield each Re_D (Equation 2.12), along with the dynamic water depth (h), turbine submergence depth (s), and turbulence intensity (TI) at each test condition, are summarized in Table 4.3. It is noted that because multiple c/R were tested at each Re_D, the chord-based Reynolds number, Re_c (Equation 2.11), was simultaneously varied during these experiments. Although this could be counteracted by changing ν accordingly at each c/R, this would restrict the testable range of Re_D. Additionally, as U_{rel} cannot be measured, the actual Re_c for each turbine would still remain indeterminate. The implications of these Re_c variations at constant Re_D across the tested geometric parameter space are further discussed in Section 4.5.1.

For these turbines, the blockage ratio is defined as

$$\beta = \frac{HD'}{hw}, \tag{4.1}$$

where w is the channel width. The size of the turbine used in each facility resulted in a constant nominal blockage ratio of $\approx$11% across all tests, with small variations in blockage due to variations in R' across the parameter space (Section 4.3.1). The range of measured blockages for each geometric configuration are tabulated in Appendix B, and the implications

of blockage effects for these experiments are discussed in Section 4.5.1. At UW, as U_∞ was varied for each Re_D, the submergence depth of the turbine rotor was varied to hold Fr_s (Equation 2.15) approximately constant at 0.85. At UNH, Fr_s was approximately 0.41. Across both facilities, $Fr_h \leq 0.51$, such that all tests were performed in subcritical regimes.

4.3.4 Dimensionless Performance

The mechanical efficiency of the turbine is quantified using the power coefficient, C_P as defined in Equation 2.2. C_P includes losses due to parasitic torque on the disk end plates which are relatively high [30] and can obscure blade-level trends. For example, as the tip-speed ratio increases, gains in blade-level power generation can be more than offset by parasitic losses from the end plates; this complicates the comparison of performance across turbine geometries with different optimal tip-speed ratios. To compensate for this, the efficiency of the turbine blades alone is estimated via a linear superposition principle in which the losses associated with the support structures (dominated by the end plates) are subtracted from measurements of turbine power at the same rotation rate [30, 48]. In other words,

$$C_{P,\text{blades}}(Re_D, \lambda) \approx C_{P,\text{turbine}}(Re_D, \lambda) - C_{P,\text{supports}}(Re_D, \lambda). \tag{4.2}$$

The streamwise forces on the turbine are characterized using the thrust coefficient, C_T, as defined in Equation 2.3. Unlike for C_P, blade-level C_T cannot be estimated by subtracting the C_T of a bladeless turbine. Whereas the parasitic torque associated with rotating the drive shaft is small in comparison to the parasitic torque imposed by the end plates, the thrust force on the drive shaft is appreciable and biased when the induction associated with energy harvesting is absent. Consequently, C_T for the full turbine is presented here. Similarly, the cross-stream loading on the turbine can be characterized via the lateral force coefficient, C_L, as defined in Equation 2.4. As neither the end plates nor the central shaft produce appreciable lateral force, the turbine and blade-only values of C_L are approximately equivalent.

At UNH, measurements of $Q(t)$, $\omega(t)$, and $U_\infty(t)$ (obtained from the tow tank linear

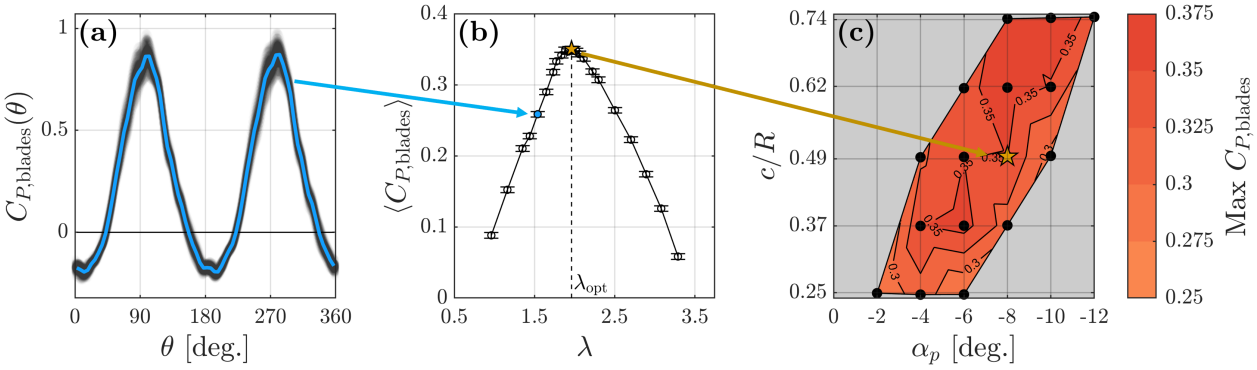

Figure 4.5: Construction of performance contours from instantaneous $C_{P,\text{blades}}$ as a function of c/R and α_p at $Re_D = 1.6 \times 10^5$ and $N = 2$. (a) Instantaneous blade-level performance during a cycle at a given λ. The blue curve indicates the median cycle. (b) Time-average $C_{P,\text{blades}} - \lambda$ curve, with performance peak and corresponding λ annotated. (c) Placement of the maximum performance point for this turbine on a contour map for $Re_D = 1.6 \times 10^5$ and $N = 2$.

encoder) are synchronized. However, as for experiments at UW, the time-averages of $U_\infty(t)$ and $U_\infty^3(t)$ are used to calculate $\lambda(t)$ and $C_P(t)$, respectively, since the variations in tow velocity were even lower than that of the inflow velocity in the Tyler flume. For both facilities, an integer number of turbine rotations are used to calculate turbine performance parameters at each λ.

4.3.5 Synthesis

To visualize trends from experimental data, results are aggregated and presented as contour maps of turbine performance metrics (e.g., maximum $C_{P,\text{blades}}$) as a function of c/R, α_p, N, and Re_D. Figure 4.5 graphically demonstrates the contour map generation process for maximum $C_{P,\text{blades}}$ at one Re_D and N from the collected data. For a given c/R and α_p, turbine performance was characterized under constant speed control over a range of λ. As shown in Figure 4.5a, during each cycle at a given λ, $C_{P,\text{blades}}(\theta)$ oscillates as a consequence of the

periodic fluid dynamics and, for some cases, switches between power production and power consumption within a rotational cycle. In addition to the phase-varying oscillations in C_P, there are cycle-to-cycle variations in the performance at each θ, primarily as a consequence of fluctuations in the inflow conditions [108]. Time-average $C_{P,\text{blades}}$ for this operating condition is represented as a point on a characteristic performance curve (Figure 4.5b). The operating condition associated with the maximum $C_{P,\text{blades}}$ for this geometry is designated as λ_{opt}, and this maximum performance is represented as a single point on a map of c/R versus α_p for one $Re_D - N$ combination (Figure 4.5c). This process is repeated for each $c/R - \alpha_p$ combination tested at that $Re_D - N$ combination, and linear interpolation is used to visualize the $C_{P,\text{blades}}$ contours across all combinations of c/R and α_p within the convex hull spanned by the tested configurations. In Section 4.4, $C_{P,\text{blades}}$ contours at each Re and N are tessellated to visualize the entire parameter space. Similar techniques are used to visualize λ_{opt}, C_T, and C_L associated with maximum $C_{P,\text{blades}}$, as well as the standard deviation of the phase-median performance for these metrics at λ_{opt} (i.e., variation of metrics within a rotational cycle).

4.4 Results

This section includes aggregate results of all experiments. While general trends are highlighted, a more comprehensive discussion of the fluid dynamics that underlie these trends is deferred to Section 4.5.

Figure 4.6 shows maximum blade-level efficiency, $C_{P,\text{blades}}$, across the tested parameter space, from which several trends emerge. First, for a given turbine geometry, as Re_D increases (i.e., moving bottom-to-top along one column of Figure 4.6), maximum $C_{P,\text{blades}}$ increases, which is in agreement with prior work [20, 32, 33, 48, 102]. While the maximum $C_{P,\text{blades}}$ increases with Re_D for all tested geometries, the rate at which maximum $C_{P,\text{blades}}$ increases varies with geometry. Reynolds independence of maximum $C_{P,\text{blades}}$ is not explicitly observed, which is to be expected given the relatively low Reynolds numbers involved. However, based on previous experiments in the Chase towing tank with turbines of similar size and Re_D (e.g., [32, 48]), the experiments reported here were likely approaching Reynolds independence.

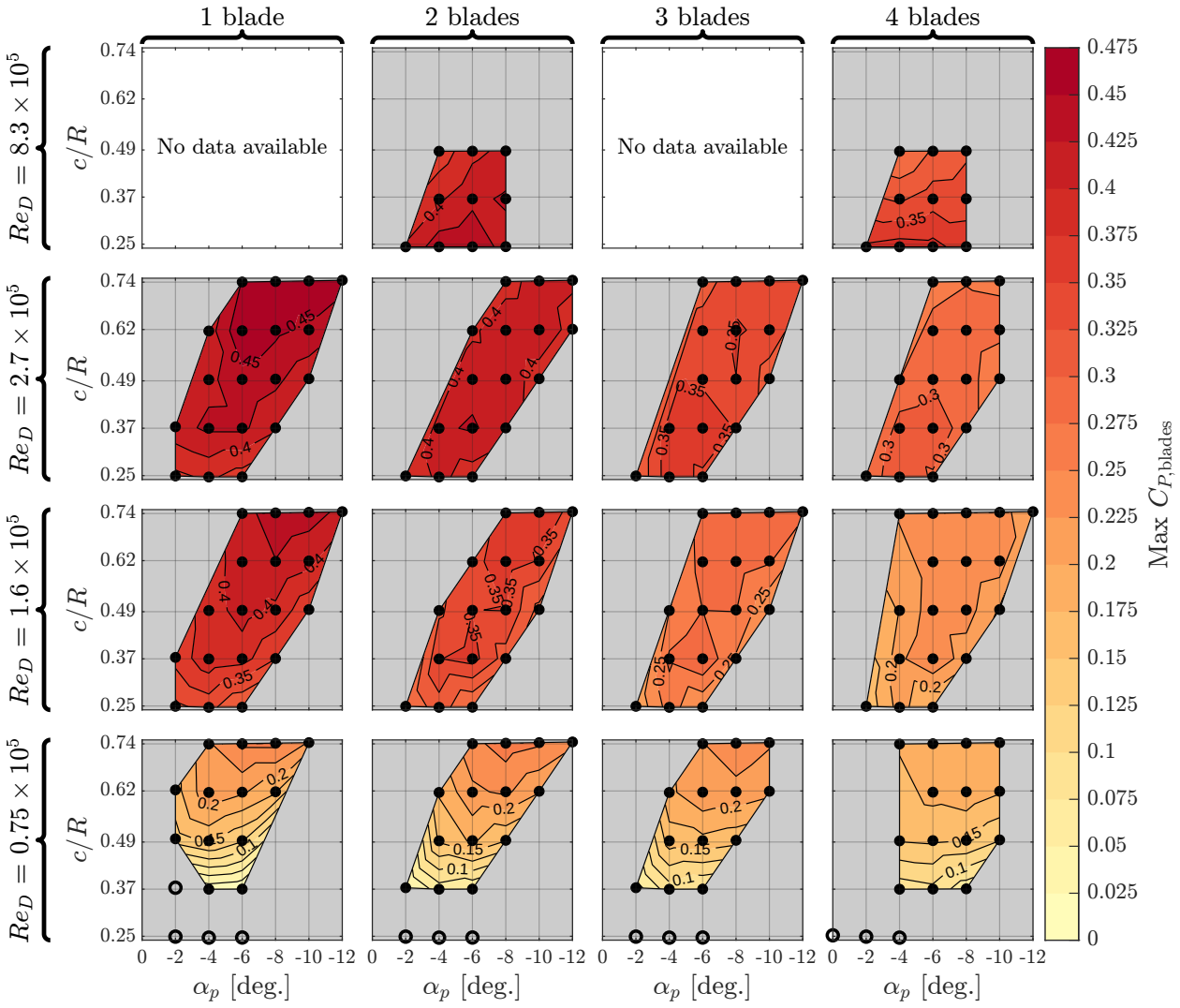

Figure 4.6: Maximum blade-level C_P contours as a function of c/R and α_p at each Re_D and N tested. Points with open circles indicate geometries that did not produce power at any tip-speed ratio and, as such, have no optimal operating condition.

Second, as the number of blades increases (i.e., moving left-to-right along one row of Figure 4.6), the maximum $C_{P,\text{blades}}$ decreases. Decreasing maximum efficiency with increasing blade count is well documented in prior work [18–20, 103], and this relationship holds for nearly all of the tested turbine geometries, with the exception of some of the lowest c/R and

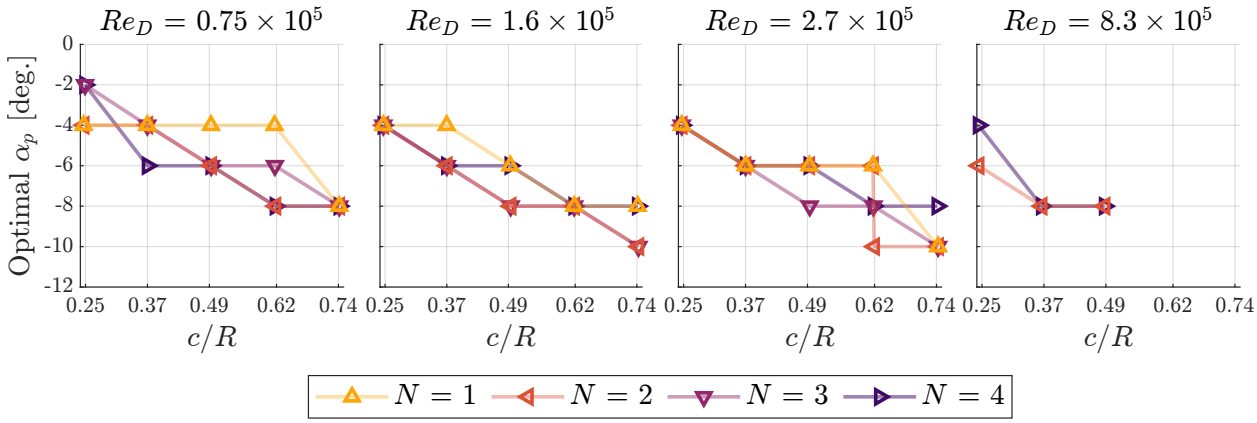

Figure 4.7: Optimal preset pitch angle for each c/R across all N and Re_D tested.

Re_D tested.

Third, at a given Re_D and N (i.e., within a single tile of Figure 4.6), as c/R increases, the α_p for maximum performance becomes more negative. In other words, blades with higher chord-to-radius ratios are more efficient with greater toe-out preset pitch. This relationship is highlighted in Figure 4.7. While first identified in early, narrower work by Takamatsu *et al.* [27], this trend has not previously been systematically demonstrated across a wide operational and geometric range. Additionally, the optimal α_p for each c/R decreases slightly with Re_D. Although this trend is weaker, it is supported by a similar observation by Somoano and Huera-Huarte [25].

Fourth, for a given α_p, optimal c/R decreases with Re_D. This trend is highlighted in Figure 4.8, and is especially clear for the $N = 2$ and $N = 4$ cases, which span the largest range of Re_D. Though this trend is implicitly apparent through comparison of separate prior studies, this is the first time it is shown in a single set of experiments with all other parameters controlled. It is also notable that, for several of the geometries evaluated in this work, the c/R that yields maximum performance at a given Re_D was the minimum or maximum c/R tested. Therefore, for these rotors, it is possible that the true optimal c/R lies outside of the tested domain (i.e., in the gray shaded region in Figure 4.8). Additionally,

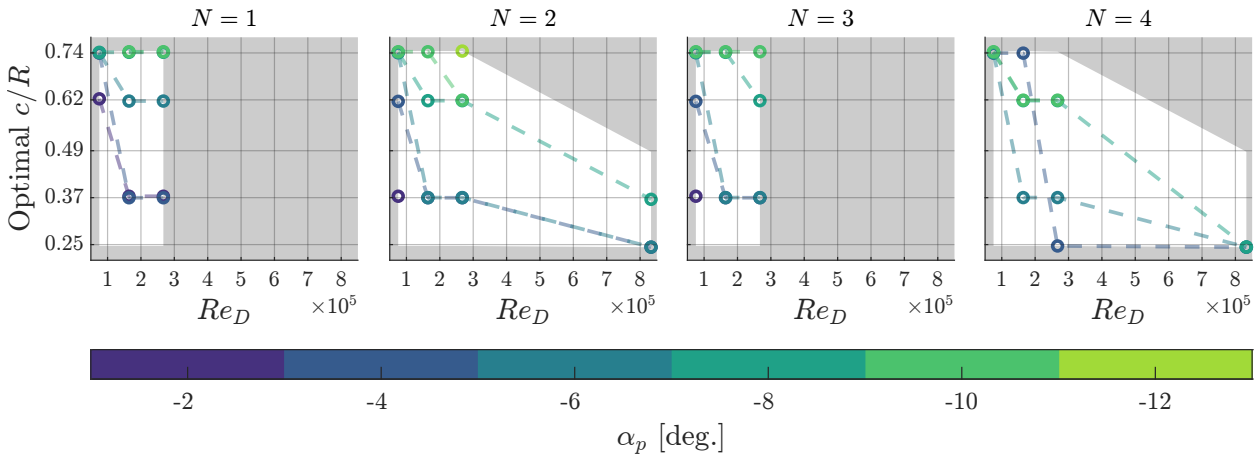

Figure 4.8: Optimal c/R as a function of Re_D for each α_p and N. The grey shaded region denotes the c/R-Re_D domain outside of the parameter space explored.

at all Re_D, as N increases, the performance of low c/R blades approaches —and at some Re_D, surpasses—that of high c/R blades (Figure 4.6). In other words, at high N, blades with low c/R become more efficient, especially at higher Re_D.

Contours of λ_{opt} across the parameter space are shown in Figure 4.9. For all Re_D and N tested, the optimal tip-speed ratio decreases as c/R increases. Additionally, the optimal tip-speed ratio decreases as N increases. Unlike $C_{P,\text{blades}}$, λ_{opt} is relatively independent of Re_D and α_p in the range tested, suggesting that the optimal tip-speed ratio may be invariant with turbine scale, at least above some threshold value for Re_D or within the range of α_p tested at each c/R.

Figure 4.10 shows contours of the time-average thrust force coefficient at λ_{opt} (i.e., $C_T|_{\lambda_{\text{opt}}}$) across the parameter space. As noted in Section 4.3.4, the contours shown are of full turbine C_T, as opposed to blade-level C_T. Consequently, trends in actual blade-level C_T may differ somewhat since the measured full-turbine C_T values include thrust force on the central shaft and end plates. Compared to the differences in maximum $C_{P,\text{blades}}$ across the parameter space in Figure 4.6, differences in $C_T|_{\lambda_{\text{opt}}}$ are less significant. For $N = 1$, $C_T|_{\lambda_{\text{opt}}}$ increases with both c/R and α_p. However, for $N > 1$, trends in $C_T|_{\lambda_{\text{opt}}}$ across the parameter space are more

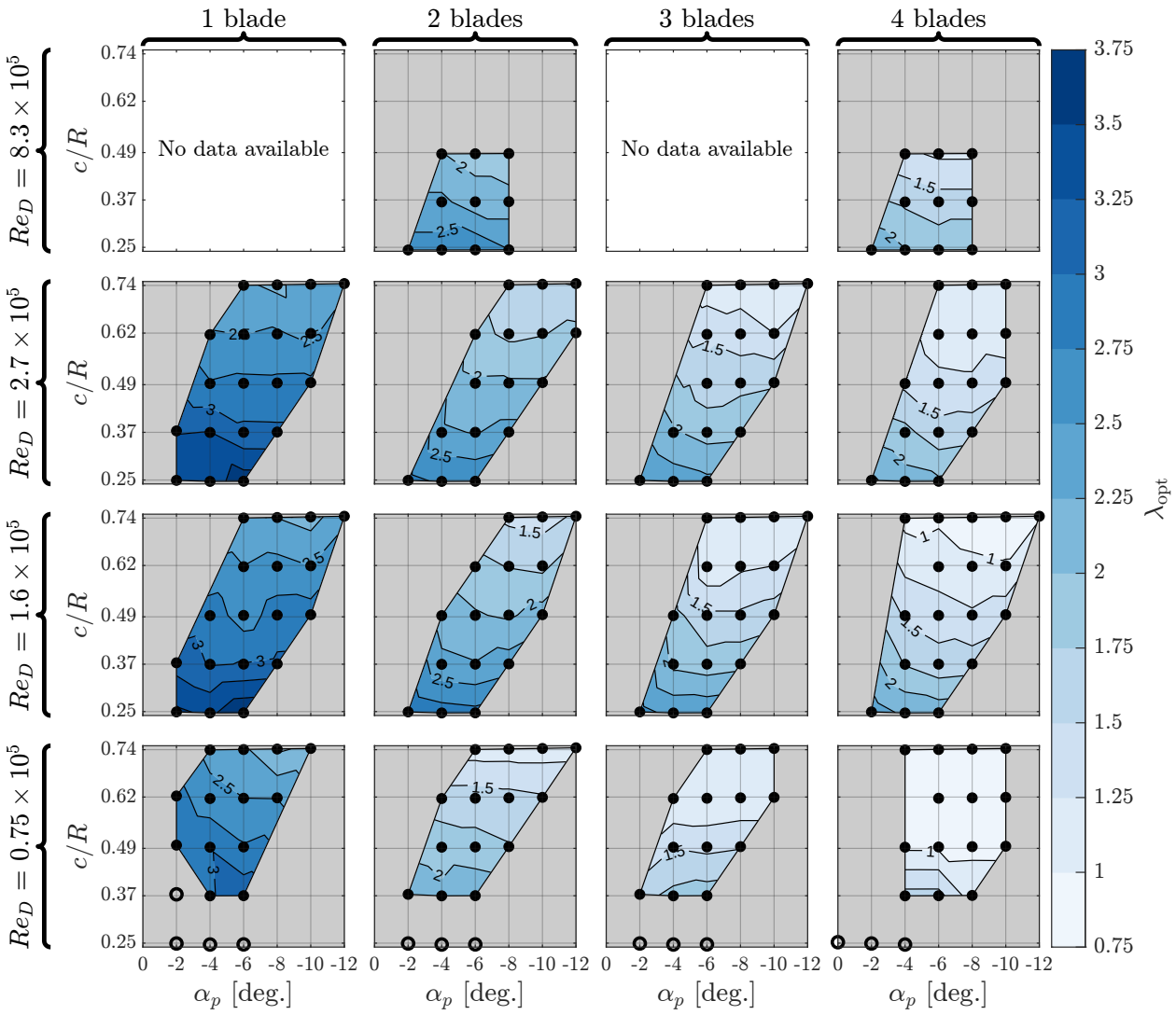

Figure 4.9: Contours of λ_{opt} (based on $C_{P,\text{blades}}$) as a function of c/R and α_p at each Re_D and N tested. Points with open circles indicate geometries that did not produce power at any tip-speed ratio and, as such, have no optimal operating condition.

ambiguous. While prior research has noted slight increases in $C_T|_{\lambda_{\text{opt}}}$ with Re_D [32] and N [18], neither trend is observed in the present data. However, because few studies report C_T measurements, further comparison to prior work is limited. In contrast, periodic variation of the thrust coefficient within a single rotational cycle (e.g., $C_T(\theta)$) is strongly influenced

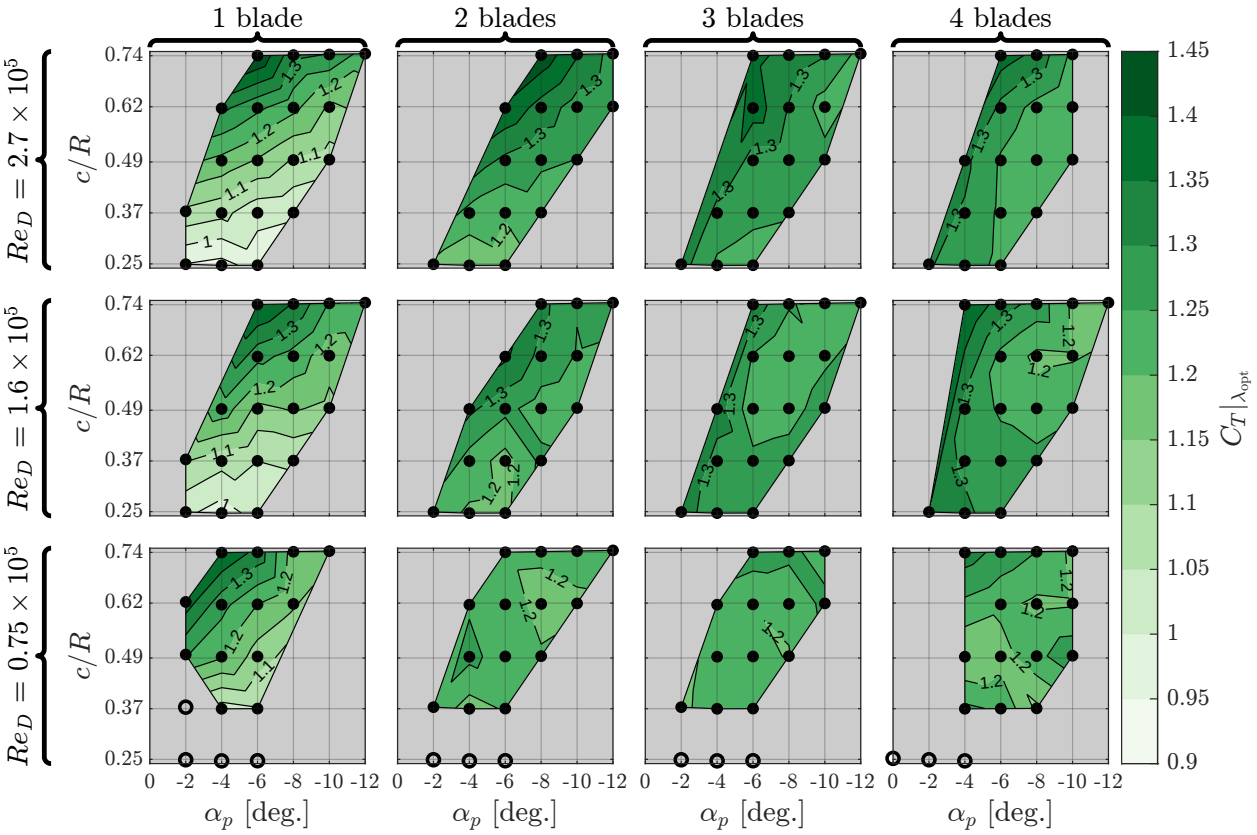

Figure 4.10: Contours of time-average C_T at λ_{opt} for blade performance as a function of c/R and α_p at each Re_D and N tested. Points with open circles indicate geometries that did not produce power at any tip-speed ratio and, as such, have no optimal operating condition.

by turbine geometry. Figure 4.11 shows contours of the standard deviation of $C_T(\theta)|_{\lambda_{\text{opt}}}$ for each rotor geometry. For single-bladed turbines, variability in $C_T(\theta)|_{\lambda_{\text{opt}}}$ is highest, and tends to increase as c/R increases and α_p becomes more positive. The variability in $C_T(\theta)|_{\lambda_{\text{opt}}}$ decreases with each blade added, and, for $N > 1$, neither c/R nor α_p substantially effects the the variation of $C_T(\theta)|_{\lambda_{\text{opt}}}$. Notably, Re_D has little effect on both $C_T|_{\lambda_{\text{opt}}}$ and the standard deviation of $C_T(\theta)|_{\lambda_{\text{opt}}}$ in the range tested. Similar trends are observed for the standard deviations of $C_{P,\text{blades}}(\theta)|_{\lambda_{\text{opt}}}$ and $C_L(\theta)|_{\lambda_{\text{opt}}}$ across the tested parameter space.

Figure 4.12 shows contours of the time-average lateral force coefficient at λ_{opt} (i.e., $C_L|_{\lambda_{\text{opt}}}$)

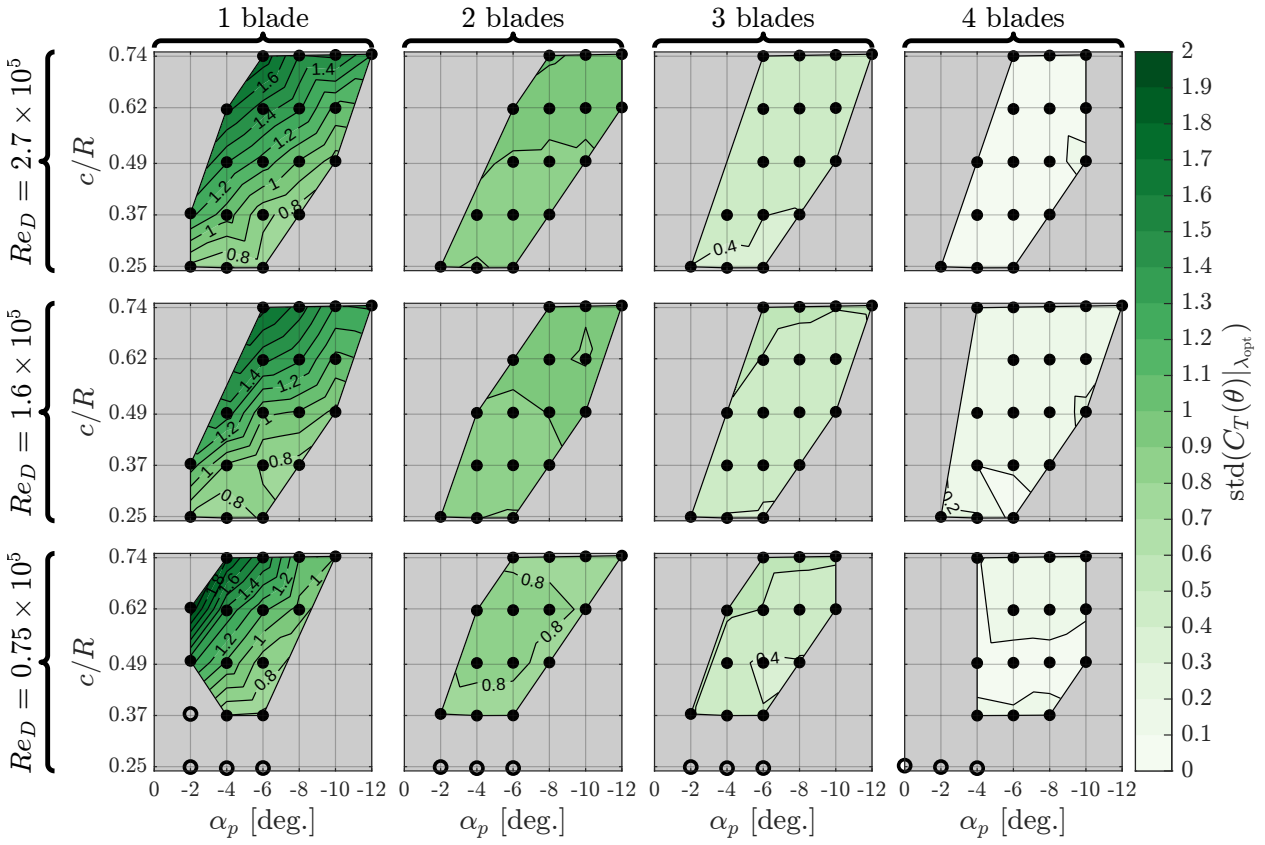

Figure 4.11: Contours of the standard deviation of $C_T(\theta)$ at λ_{opt} as a function of c/R and α_p at each Re_D and N tested. Points with open circles indicate geometries that did not produce power at any tip-speed ratio and, as such, have no optimal operating condition.

across the parameter space. While the magnitude of $C_L|_{\lambda_{\mathrm{opt}}}$ for each geometry is less than that of $C_T|_{\lambda_{\mathrm{opt}}}$, the range of $C_L|_{\lambda_{\mathrm{opt}}}$ across the tested geometries is larger. Across all Re_D and N tested, the magnitude of $C_L|_{\lambda_{\mathrm{opt}}}$ increases most strongly with increasing c/R and more positive α_p. While decreasing α_p at a given c/R can reduce the magnitude of the time-average $C_L|_{\lambda_{\mathrm{opt}}}$, the contours of Figure 4.12 imply that beyond the range tested, further decreases in α_p will reverse the direction of the time-average $C_L|_{\lambda_{\mathrm{opt}}}$ and eventually increase its magnitude. However, because the underlying fluid mechanics of C_L are difficult to interpret without knowledge of the forces acting on individual blades, further discussion of the experimental

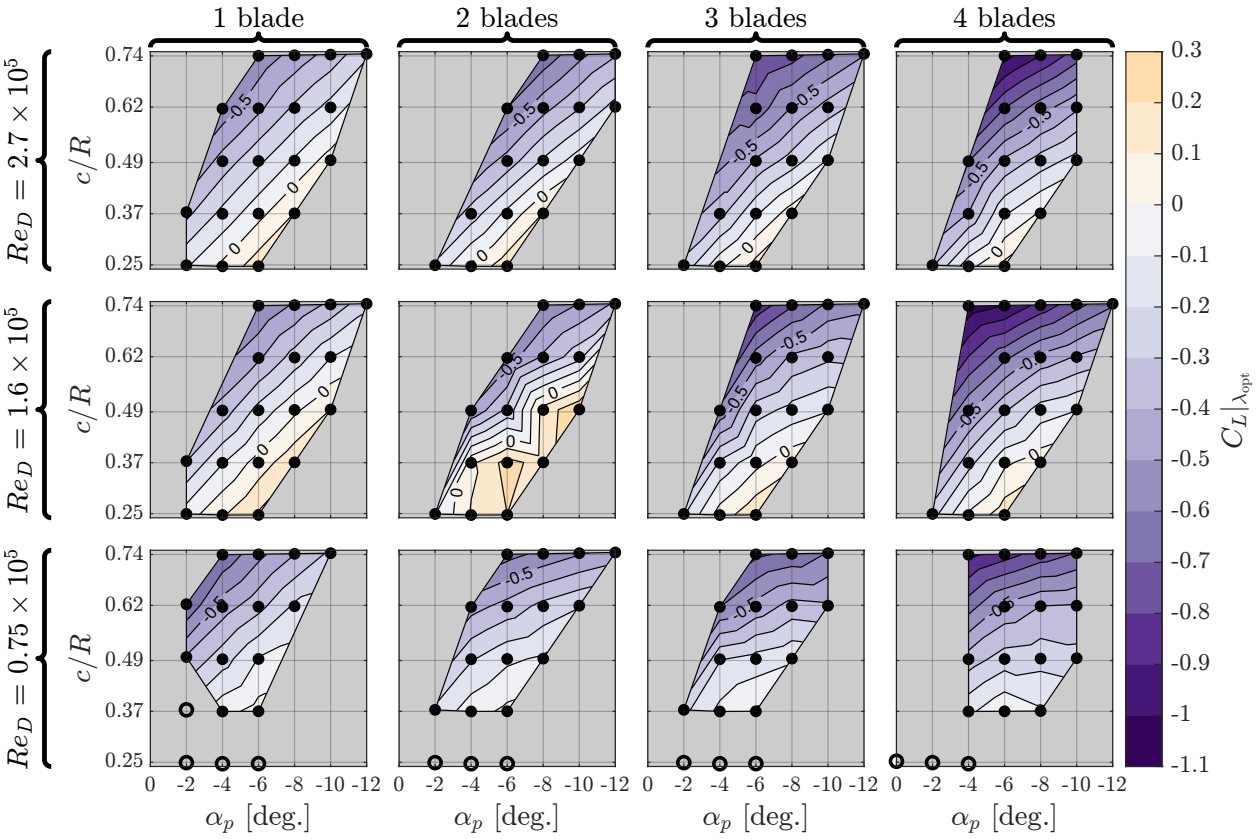

Figure 4.12: Contours of time-average C_L at λ_{opt} for blade performance as a function of c/R and α_p at each Re_D and N tested. Points with open circles indicate geometries that did not produce power at any tip-speed ratio and, as such, have no optimal operating condition.

results is primarily focused on $C_{P,\text{blades}}$ and C_T.

4.5 Discussion

To interpret the experimental results given in Section 4.4, the fluid dynamic context for the observed trends is first established. Then, considering the experimental results and prior research, the effects of each geometric parameter are analyzed. Finally, this section concludes with generalized design considerations for cross-flow turbine rotors.

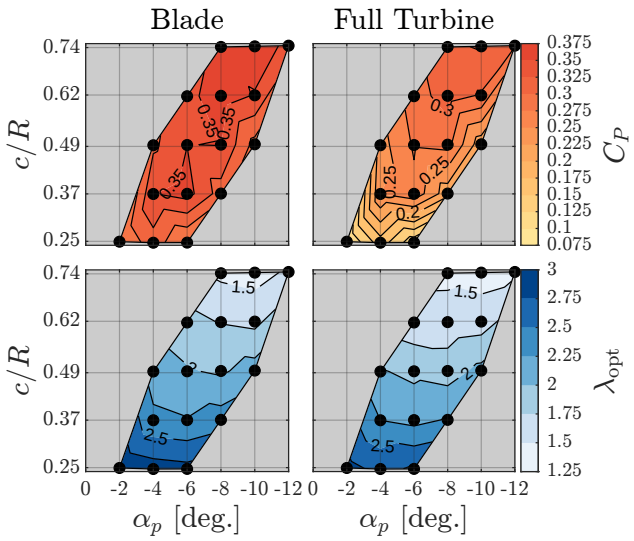

Figure 4.13: Contours of maximum $C_{P,\text{blades}}$ and corresponding λ_{opt} (left column) compared to C_P and corresponding λ_{opt} for the full turbine (right column) at $N = 2$ and $Re_D = 1.6 \times 10^5$.

4.5.1 Contextual Fluid Dynamics

Turbine-Level vs. Blade-Level Performance

In Section 4.4, $C_{P,\text{blades}}$ is presented rather than full turbine C_P, which includes the effects of the support structures for mounting the blades (Equation 4.2). In practice, support structures are obviously required, and for full-scale deployments their design is informed by both structural constraints and turbine operating condition. For relatively low λ, the parasitic torque from the support structures is limited and the choice of support structure can be unimportant. As λ increases, the parasitic losses from the support structures can become considerable and an important part of the design process [29].

Figure 4.13 illustrates how the inclusion of these losses alters the contours of maximum $C_{P,\text{blades}}$ and λ_{opt} for turbines at $Re_D = 1.6 \times 10^5$ and $N = 2$. Relative to $C_{P,\text{blades}}$, the contours of full turbine C_P at this $Re_D - N$ combination show greater dependence on c/R, with the largest tested c/R significantly outperforming the lowest tested c/R. However,

this is, in part, because blades with lower c/R perform best at higher rotation rates, and consequently incur greater support structure losses at peak blade performance. When losses from the support structures are subtracted (Equation 4.2), blades with low c/R are not penalized for operating at higher λ_{opt}, and their performance relative to large c/R blades is improved.

While this demonstrates the importance of considering support structure losses, discussion of the experimental results focuses on $C_{P,\text{blades}}$ rather than full turbine C_P to identify trends that are independent of support structure and facilitate the broader applicability of this data set. As support structure losses depend not only on rotation rate, but also the shape (e.g., rectangular strut, foil strut, end plate, etc.) and mounting location (e.g., mid-span or blade-end) of the support [29–31, 48], trends in full turbine C_P in these experiments would likely change if different supports were used. Additionally, numerical studies of cross-flow turbines often omit support structures to reduce computational expense, such that $C_{P,\text{blades}}$ is most relevant for the validation of these studies.

Blockage Effects

All experiments involved turbines operating in moderately confined flow ($\approx 11\%$ blockage ratio) and the observed $C_{P,\text{blades}}$, C_T, C_L, and λ_{opt} are consequently elevated relative to unconfined conditions [8, 10, 34, 133]. However, the actual blockage effects experienced by each turbine depend on its geometry and operating condition. Setting aside minor differences in blockage associated with projected area (Appendix B), blockage effects are a function of both the channel blockage ratio (Equation 4.1) and the rotor thrust coefficient [8, 10, 34]. Consequently, even if two turbines have the same blockage ratio, the turbine with the higher C_T will experience greater blockage-driven augmentations to $C_{P,\text{blades}}$. Since $C_T|_{\lambda_{\text{opt}}}$ varies by $\approx 45\%$ within the tested parameter space (Figure 4.10), the influence of C_T on blockage effects is non-negligible. However, the largest variation in $C_T|_{\lambda_{\text{opt}}}$ occurs for single-bladed bladed turbines, with variations $< 25\%$ for all turbines with $N > 1$. Therefore, while blockage effects were non-uniform across the parameter space, the distortion of the results by blockage

effects is likely limited for $N > 1$.

To compensate for blockage effects, it is possible to apply analytical corrections to experimental data and estimate performance in unconfined flow [34]. However, a blockage correction has not been applied to these data for several reasons. First, because no thrust data were collected at UNH, corrections could not be applied to performance measurements at all Re_D. Second, it is unclear whether blockage corrections are directly applicable to $C_{P,\text{blades}}$ or if this would require a reliable estimate of the blade-level thrust coefficient. Finally, since blockage corrections are typically applied to time-averaged performance, a focus on blockage-corrected results would preclude discussion of how rotor geometry influences periodic variability in $C_{P,\text{blades}}$ and C_T as a function of azimuthal position.

Reynolds Number Effects

Turbine performance is affected by the local blade Reynolds number, Re_c (Equation 2.11). As Re_c increases, the boundary layer on the blade surface becomes more turbulent and resistant to the adverse pressure gradients that cause flow separation on the suction side of the blade at higher angles of attack [77]. Since this improves the blade's lift-to-drag ratio for a given kinematic condition, efficiency increases with Re_c until an independence threshold is reached [20, 32, 33]. However, the results presented in Section 4.4 are categorized by the diameter-based Reynolds number, Re_D; this definition is used for expediency (D, U_∞, and ν are easily measured) and because it is agnostic to blade geometry and λ, which are both intentionally varied across the parameter space. If induction is neglected, the nominal Re_c can be expressed in terms of other experimental parameters by combining equations Equations 2.8, 2.11 and 2.12, yielding

$$Re_{c,n} = \frac{U_{\text{rel},n} c}{\nu} = Re_D \frac{c}{R} \frac{\sqrt{\lambda^2 + 2\lambda \cos\theta + 1}}{2}. \tag{4.3}$$

From this relation, it is observed that $Re_{c,n}$ increases with Re_D, c/R, and λ. However, these factors often move in competing directions. For example, as c/R increases, λ_{opt} decreases (Figure 4.9), which decreases $Re_{c,n}$ at maximum efficiency.

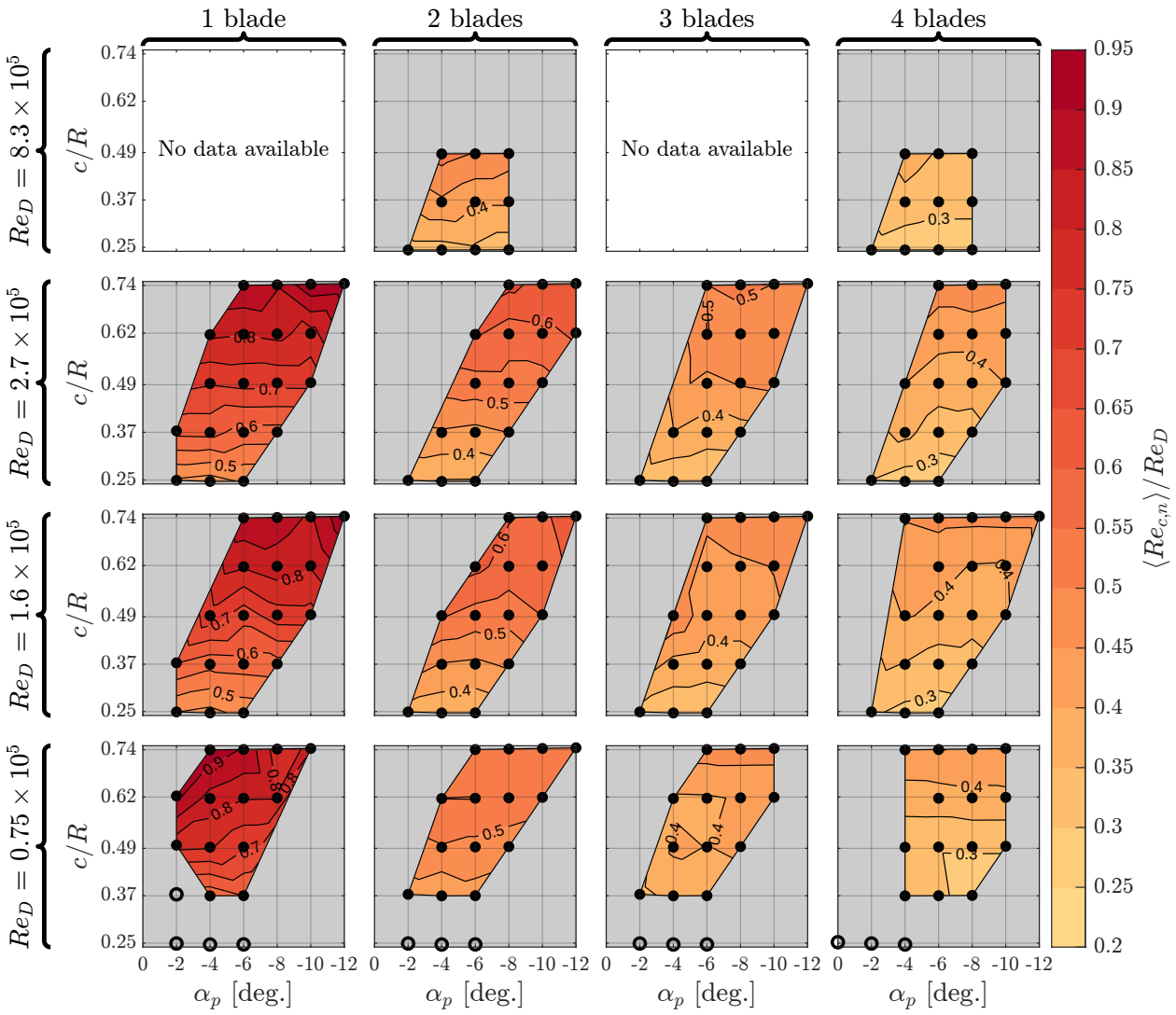

Figure 4.14: Contours of the cycle-average $Re_{c,n}$ at λ_{opt} normalized by the corresponding Re_D. Points with open circles indicate geometries that did not produce power at any tip-speed ratio and, as such, have no optimal operating condition.

To assess how turbine geometry influences $Re_{c,n}$ across the tested parameter space, the average value of Equation 4.3 over a single rotation (i.e., $\langle Re_{c,n} \rangle$) is evaluated at λ_{opt} for each geometry. The resulting contours in Figure 4.14 suggest that, at λ_{opt}, the largest $\langle Re_{c,n} \rangle$ for a given Re_D, α_p, and N is generally achieved by maximizing c/R. In other words, at a given

Re_D, the c/R term in Equation 4.3 has the stronger influence on $\langle Re_{c,n} \rangle$, with increasing c/R more than offsetting the corresponding decrease in λ_{opt}. While this would be explanatory for why blades with the largest c/R perform best at most $Re_D - N$ combinations (Figure 4.6), it is not explanatory for the inversion of this trend at high Re_D, where blades with lower c/R perform best. This contradictory result is indicative of the limitations of interpreting the observed performance trends via nominal Re_c. Equation 4.3 neglects induction, which alters the relative velocity incident on the blade and thus the true local Reynolds number. Additionally, although it is known that increasing c/R increases "flow curvature" experienced by the blade [26, 67, 134], how flow curvature alters Re_c is not understood. Interplay between these factors motivates further study of the influences of induction and flow curvature on blade-level fluid dynamics.

4.5.2 Effects of Geometric Parameters

Chord-to-Radius Ratio

In contrast to the results of Migliore *et al.* [26], for these experiments turbine geometries with the largest c/R—which are expected to experience the greatest flow curvature effect—yielded the highest $C_{P,\text{blades}}$ of the tested geometries at many $Re_D - N$ combinations, particularly for lower Re_D (Figure 4.6). However, large c/R blades were not universally optimal, and were outperformed by low c/R blades at the highest Re_D tested. As previously noted, this study did not determine the true optimal c/R at each $Re_D - N$ combination and, in several cases the best-performing c/R was either the minimum or maximum c/R tested. Specifically, at the two lowest Re_D tested, it appears that c/R greater than 0.74 may benefit performance. This is remarkable, given that, with the exception of the studies by Shiono *et al.* [120] and El-Samanoudy *et al.* [121], $c/R \approx 0.74$ is larger than that tested in any previous experiments (Table 4.1). Similarly, at the highest tested Re_D, further reduction of c/R below 0.25 may continue to improve performance, subject to structural limitations. The improved performance of low c/R blades at higher Re_D agrees with the results of Migliore *et*

al. [26] and is further supported by cross-comparison of previous studies in the Chase towing tank at $Re_D \approx 4\times10^5$ – 13×10^5, which characterized three-bladed turbines (NACA 0020 airfoils) with $c/R = 0.10$ [48] and $c/R = 0.28$ [32, 132]. Bianchini *et al.* [29] also identified a similar change in the optimal c/R with increasing freestream velocity using a BEM-based numerical method, although the turbine diameter (and thus Re_D) was allowed to vary while the projected area (HD) was held constant. It is recommended that future work broaden the range of c/R and Re_D explored to identify the limits of these trends.

Blade Count

Increasing the number of turbine blades for fixed α_p and c/R decreases the maximum blade-level efficiency (Figure 4.6) and the tip-speed ratio at which maximum efficiency occurs (Figure 4.9). While decreases in maximum $C_{P,\text{blades}}$ and λ_{opt} with increasing N are well-documented in prior work [18–20, 103], it is observed that increasing N from 1 to 2 actually increases maximum $C_{P,\text{blades}}$ for a few cases at low Re_D and low c/R (e.g., $Re_D = 0.75\times10^5$ and $c/R = 0.37$). Additionally, away from λ_{opt}, the relationship between N and $C_{P,\text{blades}}$ varies with λ: as shown for a subset of geometries ($c/R = 0.62$, $\alpha_p = -6°$, and $Re_D = 2.7\times10^5$) in Figure 4.15a, the most efficient blade count increases as λ decreases. At lower λ, (e.g., $\lambda \approx 1$ in Figure 4.15a), turbines with more blades have higher time-average efficiencies, whereas at higher λ (e.g., $\lambda \approx 2$ in Figure 4.15a), turbines with fewer blades become most efficient. In contrast, the time-average thrust on the rotor generally increases with N for all λ (Figure 4.15d). Based on these results, it is hypothesized that N primarily influences performance by altering near-blade induction. At a given λ and c/R, as N increases, the rotor appears more solid to the freestream, and thus diverts more flow around the turbine [19]. Consequently, the velocity incident on the blades at a given λ is expected to decrease, which would reduce the power that can be produced by an individual blade at that λ. This hypothesis is supported by the results in Figures 4.15b and 4.15c, where the maxima for individual blade power (periodic peaks) decrease as N increases. Since induction increases with rotation rate [19], the severity of this power-per-blade penalty varies with λ. For example, at

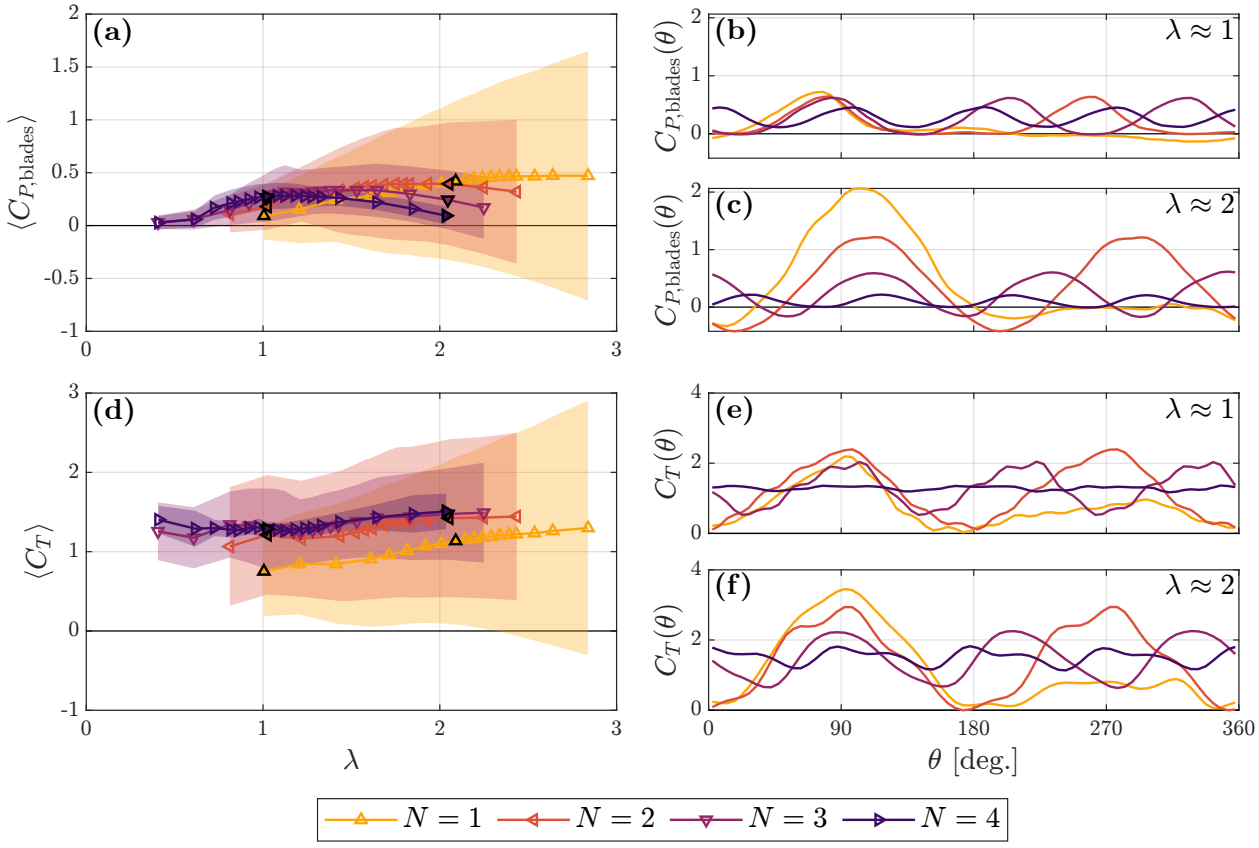

Figure 4.15: Influence of blade count on performance for $c/R = 0.62$, $\alpha_p = -6°$, $Re_D = 2.7 \times 10^5$. (a) Time-average $C_{P,\text{blades}}$ as a function of λ. The shaded region indicates ± 1 standard deviation of the values measured during the median rotational cycle (i.e., $C_{P,\text{blades}}(\theta)$) at each λ set-point. Phase-median $C_{P,\text{blades}}$ is shown for (b) $\lambda \approx 1$ and (c) $\lambda \approx 2$. (d) Time-average C_T as a function of λ with the shaded region indicating ± 1 standard deviation as for (a). Phase-median C_T is shown for (e) $\lambda \approx 1$ and (f) $\lambda \approx 2$.

$\lambda \approx 1$ (Figure 4.15b), the power maxima are only marginally reduced as N increases, whereas at at $\lambda \approx 2$ (Figure 4.15b), the power maxima steeply decline with each blade added. It is noted that, while induction is also expected to increase with c/R for similar reasons as increasing N, the chord-to-radius ratio influences performance through additional mechanisms

(e.g., flow curvature, Re_c length scale) that are absent for N. Additionally, since cross-flow turbines experience both axial and lateral induction, caution is warranted in attempting to correlate induction directly to thrust force, as for axial flow turbines [41]. Future research should quantitatively assess the relationship between turbine geometry, performance, and induction via flow visualization.

Over the course of a rotational cycle, variation in $C_{P,\text{blades}}$ (e.g., Figures 4.15b and 4.15c) and C_T (e.g., Figures 4.11, 4.15e and 4.15f) is significantly reduced as N increases. As indicated by the shaded regions of Figures 4.15a and 4.15d, this effect is especially pronounced as λ increases. Consequently, the choice of blade count constitutes a trade off between 1) maximum efficiency and 2) cyclic variation of power generation and structural loads. A turbine with fewer blades can produce power over a wider range of tip-speed ratios and achieve higher maximum efficiency, but will also be subject to more intense cyclic loading and more susceptible to fatigue. Consequently, while single-bladed turbines are useful for highlighting trends across this parameter space and isolating blade-level dynamics, they are likely impractical in most applications. Conversely, for $N = 4$, the amplitude of cyclic variation is significantly reduced, but at the cost of cycle-average efficiency. Even higher blade counts would likely only offer incremental gains in consistency at the cost of further reductions in efficiency. Therefore, two- and three-bladed turbines may represent a feasible compromise between cycle-average power and cyclic variation.

Preset Pitch Angle

As c/R increases, the α_p that yields maximum time-average $C_{P,\text{blades}}$ generally becomes more negative (i.e., more toe-out) (Figure 4.7). The preset pitch angle influences blade fluid dynamics by changing the angle of attack at each azimuthal position, and thus, the blade's lift and drag coefficients. Considering the nominal angle of attack trajectories shown in Figure 2.4a, a more negative α_p is expected to decrease the maximum nominal angle of attack the blade encounters during the upstream sweep ($0° \leq \theta < 180°$), delaying the onset of dynamic stall and reducing its severity. Therefore, previous studies have hypothesized that

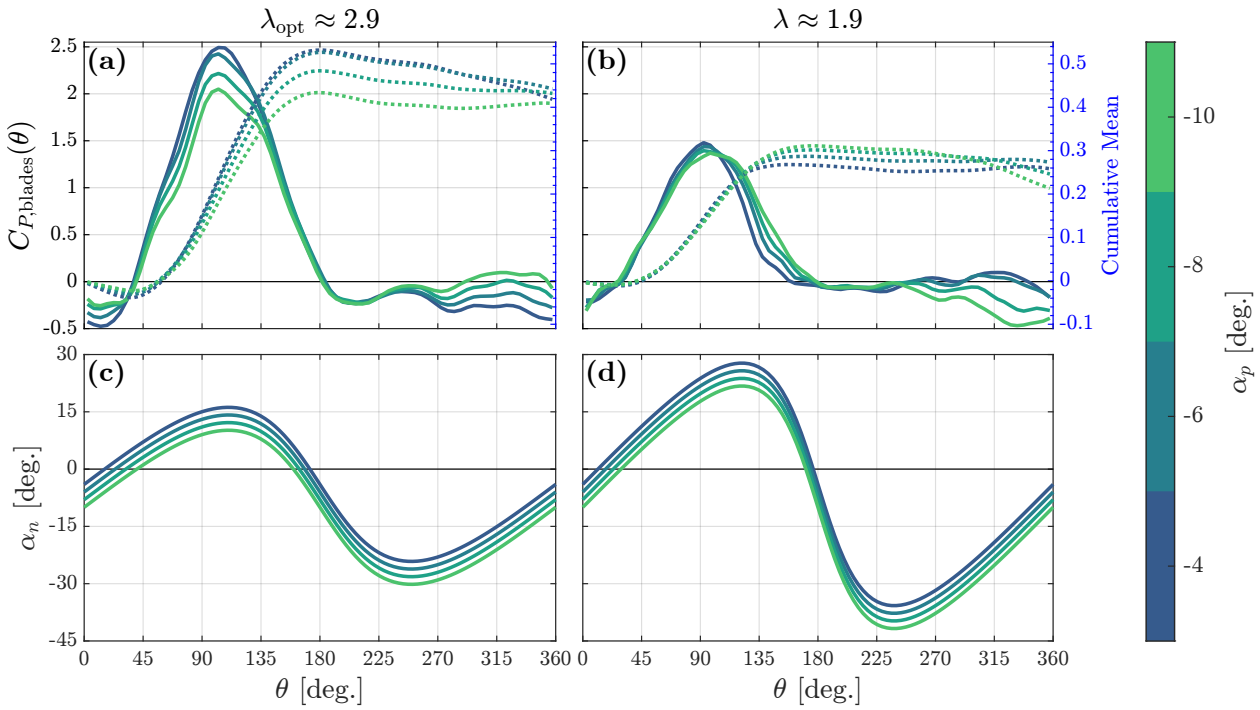

Figure 4.16: (a) Phase-median $C_{P,\text{blades}}$ as a function of azimuthal position for various α_p at $c/R = 0.49$, $N = 1$, $Re_D = 2.7 \times 10^5$, and $\lambda_{\text{opt}} \approx 2.9$. Dashed lines show a cumulative average of $C_{P,\text{blades}}$ over the cycle (i.e., average $C_{P,\text{blades}}$ between 0° and θ). (b) Phase-median and cumulative average $C_{P,\text{blades}}$ for the same turbines operating at $\lambda \approx 1.9$. The nominal angle-of-attack trajectories for various α_p are shown for (c) $\lambda \approx 2.9$ and (d) $\lambda \approx 1.9$.

appropriately decreasing the preset pitch angle increases the net power produced during the upstream sweep by mitigating the abrupt loss of lift and increase in drag caused by boundary layer separation during dynamic stall [70, 74].

To explore the fluid dynamics that drive trends in α_p, a representative set of single-bladed turbines—for which the individual blade power can be isolated within a cycle—are considered at $c/R = 0.49$ and $Re_D = 2.7 \times 10^5$. Phase-median $C_{P,\text{blades}}$ and corresponding nominal angle of attack trajectories for these turbines are visualized at two tip-speed ratios: the optimal tip-speed ratio, at which light dynamic stall is expected ($\lambda_{\text{opt}} \approx 2.9$; Figures 4.16a

and 4.16c), and a lower tip-speed ratio at which deeper dynamic stall is expected ($\lambda \approx 1.9$; Figures 4.16b and 4.16d). At both λ shown, the highest instantaneous $C_{P,\text{blades}}$ is achieved with the least negative (i.e., least toe-out) tested preset pitch of $\alpha_p = -4°$, which corresponds to the highest maximum α_n during the upstream sweep (Figures 4.16c and 4.16d). For the $\lambda_{\text{opt}} \approx 2.9$ case, $\alpha_p = -4°$ also yields the greatest average power over the upstream sweep (Figure 4.16a). While this is contrary to the hypothesized benefits of delaying dynamic stall, the importance of dynamic stall is more limited at this tip-speed ratio [108]. In contrast, for the $\lambda \approx 1.9$ case, a more negative (i.e., more toe-out) pitch angle of $\alpha_p = -10°$ yields the greatest average power over the upstream sweep (Figure 4.16b). Although $\alpha_p = -10°$ results in the lowest peak instantaneous power at this λ, power is produced over a wider range of θ in the upstream sweep, consistent with the hypothesis of a more negative pitch delaying dynamic stall via reduction of the maximum α_n (Figure 4.16b).

Since blades with larger c/R operate at lower tip-speed ratios (Figure 4.9) and thus experience deeper dynamic stall, these blades may benefit from more negative preset pitch relative to blades with smaller c/R. However, for both λ, neither $\alpha_p = -4°$ nor $\alpha_p = -10°$ yields the maximum cycle-average power. Instead, the cumulative phase-median performance profiles (Figures 4.16a and 4.16b) show that the optimal α_p (in this case, $-6°$) maximizes cycle-average power by balancing power production during the upstream sweep with power consumption during the downstream sweep ($180° \leq \theta < 360°$) as the blade moves through the wake. Consequently, an explanation of α_p trends that focuses only on the upstream sweep is incomplete. Unfortunately, trends in the downstream sweep cannot be explained by the nominal angle of attack trajectories (Figures 4.16c and 4.16d), since induction is particularly significant during the downstream sweep. Additionally, both induction and flow curvature vary with λ and θ and cause the actual angle of attack to deviate from the nominal value, complicating a holistic interpretation of the effects of the preset pitch angle. It is recommended that future research focus on identifying the fluid dynamic basis for these performance trends.

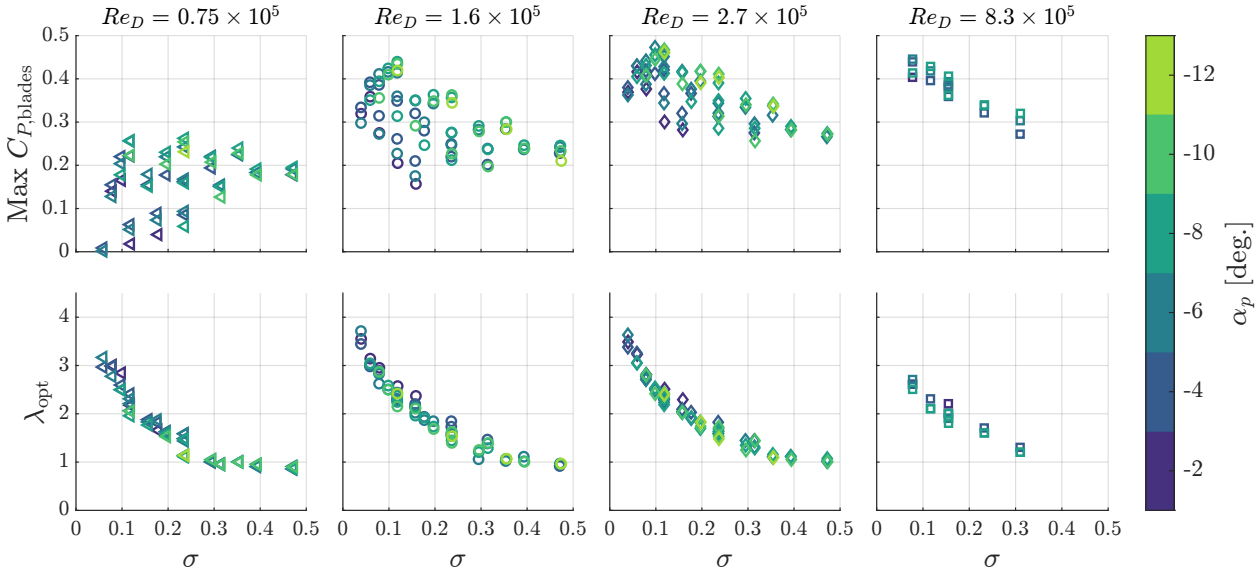

Figure 4.17: Maximum $C_{P,\text{blades}}$ and associated λ_{opt} and as a function of solidity for each α_p and Re_D.

Solidity

As discussed in Section 2.3, it is relatively common to combine c/R and N to form a single dimensionless parameter, solidity, σ (Equation 2.9), that represents the fraction of the rotor circumference containing blades. For a given λ, as σ increases, less flow is able to pass through the turbine since the blades present greater resistance to the flow. At the extreme case of $\sigma = 1$, the entire rotor circumference would be occupied by the blades and the turbine would approximate a cylindrical shell. The c/R – N combinations in this work resulted in an order of magnitude range of solidity ($\sigma \approx 0.04 - 0.47$). Additionally, by simultaneously varying these parameters, the same value of σ was achieved with different combinations of c/R and N (e.g., doubling N and halving c/R). This allows the suitability of solidity as a descriptive dimensionless parameter to be assessed.

As shown in Figure 4.17, holding solidity constant does not guarantee constant characteristic performance. At low-to-moderate σ, turbine geometries with similar solidity exhibit

a wide range of maximum $C_{P,\text{blades}}$, even when both Re_D and α_p are held constant. This is not unexpected, given that c/R and N affect $C_{P,\text{blades}}$ through distinct mechanisms. For example, if σ is increased by increasing N only, the local Reynolds number can change due to variations in induction. However, if σ is increased by increasing c/R only, then in addition to changes in the local Reynolds number due to changes in induction and length scale (c), flow curvature also increases. Consequently, for two turbines with the same σ, but different c/R and N, the underlying fluid dynamics for the two turbines are unlikely to be equivalent, nor are the associated fluid dynamics likely to scale in the same way with Reynolds number. While not shown, a similarly wide range is observed for C_T and C_L at λ_{opt} for a given σ.

Due to the unique hydrodynamic influences of c/R and N, cross-comparisons made solely on the basis of solidity can be misleading, and likely contribute to contradictory trends across both experimental and numerical prior studies regarding the effect of solidity on maximum C_P. Multiple studies report that maximum C_P decreases as σ increases [19, 20, 40, 71, 75, 103], which is expected for an increase in N (Figure 4.6). In contrast, several other studies find that maximum C_P increases with increasing solidity [2, 93, 116, 125, 126, 133], an effect that is observed in this work for increasing c/R at lower Re (Figure 4.6). Across prior studies, σ is not consistently varied: some studies changed σ only by varying N [19, 20, 71, 75, 103, 126, 133], others varied c/R [2, 29, 40, 74, 93, 120, 125], and still others varied both N and c/R [76, 116, 135]. While a few studies hold solidity constant through simultaneous variation of c/R and N [116, 120], no prior studies have systematically demonstrated that identical performance is obtained for a given σ, regardless of the values of c/R and N. However, when σ is used as a dimensionless parameter for performance characterization, this assumption is seldom questioned. For example, with the exception of the study by Miller *et al.* [20] there appears to be no acknowledgement that changing σ via c/R rather than N could introduce flow curvature effects, even though these effects have been documented since 1980 [26].

This is not, however, to say that solidity is a universally poor parameter for describing cross-flow turbine performance. At the highest solidities tested (corresponding to geometries with both high c/R and high N), turbines with similar σ have similar maximum $C_{P,\text{blades}}$ (i.e.,

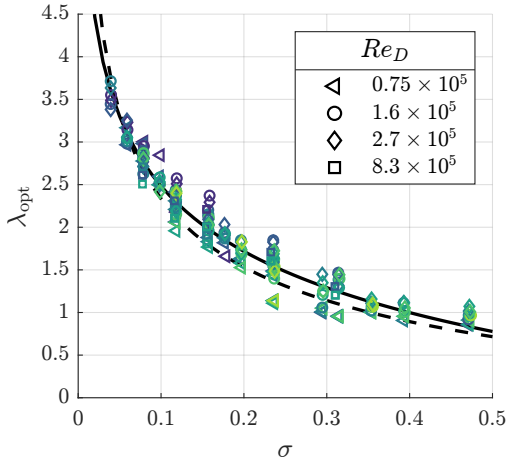

Figure 4.18: λ_{opt} versus solidity for all turbines tested. Marker color indicates α_p as in Figure 4.17. The curve fit in Equation 4.4 is shown as a solid black line, whereas the curve fit from Rezaeiha *et al.* [2] is shown as the dashed black line.

performance is relatively insensitive to α_p). Similar results are observed at $Re_D = 8.3 \times 10^5$, which is consistent with a hypothesis that at high Reynolds numbers and low c/R, the flow curvature and Reynolds number effects linked to c/R are negligible, and solidity is thus a good predictor of C_P. This hypothesis is supported by foundational research by Blackwell and Sheldahl [116], who held σ constant by varying c/R and N simultaneously and observed similar—but not identical—characteristic performance at high Re_D ($\approx 3.6 - 41 \times 10^5$) and low c/R (< 0.1). They were unable to identify the root cause for the small disagreement in performance, which is unsurprising, given that these studies took place several years prior to the first documentation of flow curvature effects.

Notably, λ_{opt} varies closely with solidity since increases in c/R and N both decrease λ_{opt}, regardless of α_p or Re_D (Figure 4.17). This inverse relationship between σ and λ_{opt} has been well documented in prior experimental studies [18–20, 75, 103, 120, 125] and simulation studies [2, 40, 93, 133, 135], but this work expands the geometric and operational space over which this is observed. Furthermore, the relationship between λ_{opt} and σ suggests that turbines with the same "static" solidity (σ) have similar optimal dynamic solidities

as defined by Araya *et al.* [19]. Overlaying λ_{opt} versus σ for all tested geometries as in Figure 4.18 illustrates that, across the parameter space tested, λ_{opt} is determined primarily by σ, with α_p and Re_D having only secondary effects, particularly at the extrema of the tested Re_D. This is consistent with the relative insensitivity of λ_{opt} to Re_D and α_p observed in Figure 4.9, as well as the Re_D-independence of λ_{opt} observed in prior work [32, 33, 128]. Additionally, some spread in λ_{opt} at a given σ is likely attributable to differences in how finely λ_{opt} was resolved across tests. Following Rezaeiha *et al.* [2], who observed a similar trend between σ and λ_{opt} for $\sigma \approx 0.03 - 0.36$, the data in Figure 4.18 are fit to a two-term power law of the form

$$\lambda_{\text{opt}} = 9.882\sigma^{-0.093} - 9.764. \tag{4.4}$$

The result (solid line in Figure 4.18) is similar to that obtained by Rezaeiha *et al.* (dashed line), although Rezaeiha *et al.*'s equation yields slightly lower values of λ_{opt} for the range of solidities tested here.

Considering these results as a whole, while solidity may capture trends in λ_{opt} and, in some cases, $C_{P,\text{blades}}$, it is clear from Figure 4.17 that solidity is an incomplete descriptor of turbine dynamics. Consequently, the use of solidity as a representative dimensionless quantity is discouraged and future research is recommended to differentiate the overlapping and unique influences of c/R and N on performance.

4.5.3 Design Considerations

While the trends in Re_D, c/R, N, and α_p are discussed from a fluid dynamics perspective in Section 4.5.2, in a field-scale application the ultimate choice of turbine geometry will be informed by design objectives. For example, while operating at the highest Re_D possible will maximize $C_{P,\text{blades}}$ for any geometry, Re_D is typically set by site conditions (e.g., expected inflow velocities) as well as physical and economic constraints on rotor dimensions. Similarly, in addition to material costs, structural limitations will dictate the choice of c/R (e.g., minimum allowable chord length at high Re_D) and number of blades (e.g., maximum

allowable amplitude of cyclic loading). In contrast, from a design perspective, α_p is a free parameter and may be chosen simply to maximize efficiency based on the selected Re_D, c/R and N.

λ_{opt} for each turbine provides a convenient point of reference for visualizing trends across the broad parameter space spanned by these experiments (e.g., as in Figure 4.6). This does, however, obscure a considerable amount of information about each turbine's performance over the full range of operating conditions (i.e., characteristic performance away from the optimal point, such as that briefly explored in Figure 4.15), as well as the variations that occur within a cycle at a given λ set point (e.g., Figures 4.5a, 4.15 and 4.16). This information plays an important role in co-design. First, for economic reasons driven by capacity utilization, wind and water turbines do not operate at λ_{opt} for all inflow conditions. Instead, beyond a "rated" inflow condition, generation systems often enter a mode of approximately constant power [41]. For fixed-pitch turbines, this can be achieved via the intentional reduction of C_P by operating at a higher- or lower-than-optimal λ. As such, characteristic performance at other operating points is relevant to design. Second, turbine structural and driveline components (e.g., generator) are sized based on the maximum, not cycle-average, expected loads. The magnitudes of these cyclic loads will affect cost and may affect component efficiency within a cycle, as well as fatigue life. To support design efforts, as well as numerical model validation, the full data archive—including both time-average and phase-median performance for each geometry—is openly available through UW ResearchWorks [136].

4.5.4 Limitations and Knowledge Gaps

While the 223 experiments conducted in this study provide insights into the interplay between c/R, α_p, N, and Re_D, some trends are not fully resolved. Foremost, as described in Section 4.5.2, despite the wide range of c/R tested (0.25-0.74), the true optimal c/R was not resolved for every $Re_D - N$ combination. Furthermore, interpretation of c/R trends is also complicated by the influence of flow curvature effects (virtual camber and virtual incidence),

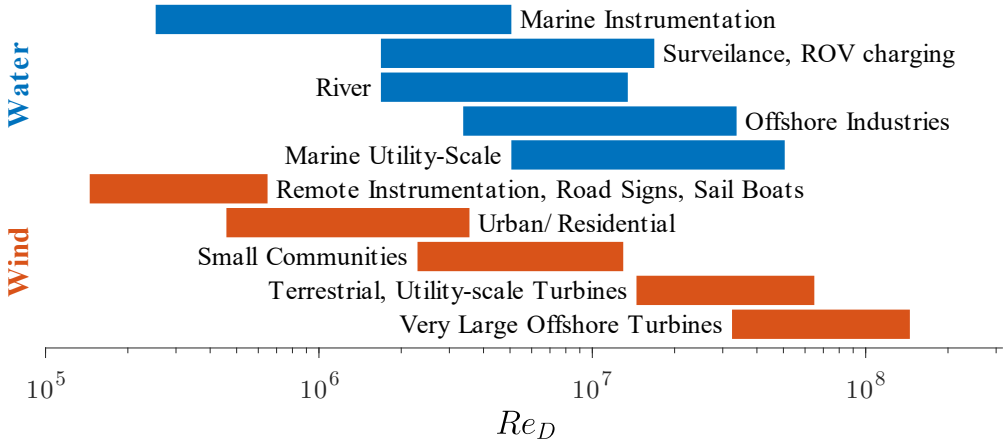

Figure 4.19: Ranges of expected diameter-based Reynolds numbers for cross-flow turbines by application.

which would benefit from further experimental investigation. Additionally, while the optimal preset pitch angle was captured at each c/R for all $Re_D - N$ combinations, the α_p that were tested at each c/R were limited for expediency to those around the optimal value. Additional tests farther from the optimal value of preset pitch could illuminate how α_p influences power production and flow recovery across c/R and λ.

Although the Re_D considered in this study span an order of magnitude, experiments at UW were conducted at transitional Reynolds numbers ($Re_D = 0.75 \times 10^5 - 2.7 \times 10^5$), and it is unknown whether Reynolds independence was achieved at UNH ($Re_D = 8.3 \times 10^5$). Consequently, trends in performance with geometry may differ outside of the range of Re_D tested in this study, although certain trends appear insensitive to Re_D (e.g., Figures 4.11 and 4.18). Since, in general, the absolute power output from a cross-flow turbine scales with physical dimension, it is natural to question the value of exploring these parameters for cross-flow turbines at relatively low Reynolds numbers. However, as shown in Figure 4.19, the range of relevant values of Re_D for the full application space in wind and water spans several orders of magnitude, and distributed power generation across these scales is critical for meeting international energy and climate goals [4, 7]. The Re_D tested in this study overlap

with that of smaller vertical-axis wind turbines in the field [137] that still exhibit Reynolds-dependence [33], and cross-flow turbines can still perform well at small physical scales (i.e., low Re_D in Figure 4.6). Further, from an experimental perspective, unless compressed-air wind tunnels are employed [20, 33], turbines that are small enough to test in laboratories will necessarily have low Reynolds numbers. Similarly, direct numerical simulations of cross-flow turbines, which can provide additional insight into blade-level fluid dynamics, are often limited to relatively low Reynolds numbers by computational cost. Here, experimental data at low Reynolds numbers can be helpful for validation.

Finally, several geometric parameters that impact performance were not considered here. These include the blade profile (e.g., other symmetric foils, cambered foils), blade cant angle, spanwise profile (e.g., helical blades), and surface roughness. While the trends observed in this work may change if, for example, all experiments were repeated with cambered blades, the portion of the parameter space explored here lays a foundation for interpreting the results of future studies.

4.6 Conclusions

The geometric configuration of a cross-flow turbine influences blade fluid dynamics, and thus the power produced and loading experienced. Here, the interplay between three geometric parameters—the chord-to-radius ratio, the preset pitch angle, and number of blades—is considered across diameter-based Reynolds numbers spanning an order of magnitude ($\approx 8 \times 10^4 - 8 \times 10^5$). Expanding upon prior research, 223 unique experiments were conducted, from which the following key trends emerge:

1. The Reynolds number has the greatest overall effect on turbine efficiency across all geometries. Until Reynolds independence is reached, increasing Re_D will increase $C_{P,\text{blades}}$ for a given geometry.

2. The optimal c/R is primarily determined by the Reynolds number. At low Re_D, blades with large c/R generate the most power. As Re_D increases, blades with low c/R are

more efficient. The number of blades has a secondary effect on optimal c/R, but this effect also depends on the Reynolds number.

3. Across all geometries, moderate toe-out preset pitch substantially improves efficiency (e.g., $-4°$ to $-10°$ in this study). In general, as a turbine's chord-to-radius ratio increases, the α_p that yields maximum efficiency becomes more negative.

4. As N increases, maximum efficiency decreases, and net loading of the turbine rotor increases; however the amplitude of cyclic loading decreases with each additional blade. As such, the choice of N constitutes a trade-off between maximum power and consistency of power and loading within a cycle.

5. Solidity (Equation 2.9) does not capture trends in $C_{P,\text{blades}}$ for the range of c/R and Re_D investigated. Turbines with the same solidity, but different c/R and N, can have different efficiencies. However, λ_{opt} is strongly correlated with solidity—turbines with greater chord-to-radius ratios and/or more blades tend to operate at slower tip-speeds. Therefore, outside of λ_{opt}, the use of solidity as a non-dimensional parameter for characterizing turbine performance is discouraged.

Importantly, these results provide a uniquely holistic view of how the effects of these geometric parameters combine to influence turbine performance across a broad parameter space. Given these performance trends and the inter-dependencies observed, the following design strategies are suggested. First, for small turbine sizes or low freestream velocities, where the chord-based Reynolds number is in the transitional regime, an optimal turbine geometry will consist of few blades with relatively large chord-to-radius ratios. This type of rotor, which has a high solidity, will operate at lower tip-speed ratios to maintain optimal induction. As dynamic stall is more significant at lower tip-speeds, these turbines perform best with larger toe-out preset pitch angles (e.g., $-6°$ to $-10°$ in this study). Second, optimal turbine geometries at large scales, well above the transitional chord-based Reynolds

number, will benefit from a higher blade count with a smaller chord-to-radius ratio. Since these rotors have lower solidity, they will tend to operate at higher tip-speed ratios, where dynamic stall is less severe and smaller toe-out preset pitch angles provide the greatest cycle-average efficiency.

This work focuses primarily on trends at maximum-performance across the parameter space, but turbine design is informed by performance at off-optimal conditions, as well. Additionally, certain mechanisms, such as the specific effects that flow curvature has on turbine performance or how the preset pitch angle influences near-blade hydrodynamics during the blade's downstream sweep, require further investigation. Nonetheless, this study provides a rich data set for interpreting turbine fluid dynamics, validating reduced-order models and numerical simulations, informing turbine design, and unifying apparently contradictory trends in prior studies.

Chapter 5

PERFORMANCE AND FLOW FIELD CHARACTERISTICS OF A HIGH-CONFINEMENT CROSS-FLOW TURBINE ARRAY

The work in this chapter is co-authored by Ari Athair, Owen Williams, and Brian Polagye. The author led the performance experiments and conducted the associated data analysis and visualization. Ari Athair led flow field characterization via particle image velocimetry and conducted the associated data analysis and visualization. The author led the drafting and editing of the manuscript, which all co-authors contributed to.

5.1 Motivation

As discussed in Section 2.4.2, the effects of confinement on turbine performance have been explored analytically, numerically, and experimentally for various turbine designs. A summary of prior experimental and numerical work that has evaluated turbine performance at multiple blockage ratios is provided in Table 5.1. While this may appear to provide a comprehensive understanding of confinement effects, turbine performance at the upper end of blockage ratios that are achievable in a realistic channel ($\beta = 30\% - 60\%$) has been characterized primarily through numerical simulation [e.g., 11, 92, 100]. This is likely a consequence of the difficulty in physically achieving a wide range of blockages while maintaining dynamic similarity [57], but this means that trends in the turbine performance and wake characteristics observed in simulation at these higher blockages have not been experimentally validated. In addition, only a handful of the experimental studies in Table 5.1 consider blockage ratios greater than 30%, and of this subset, only Ross and Polagye [90] characterize the turbine wake. Furthermore, studies that do explore this upper-end of blockage ratios consider only a sparse set

Table 5.1: Summary of experimental and numerical studies that consider the effects of varying the blockage ratio for different types of turbines. Studies that consider $\beta \geq 30\%$ are bolded.

Experimental			**Numerical**		
Author	Turbine Type	β tested [%]	Author	Turbine Type	β tested [%]
Takamatsu *et al.* [68]	**CFT**	**75, 95**†	**Nishino and Willden [91]**	**Actuator disk**	3.1 - **50.3**
Whelan *et al.* [9]	**AFT**	5, **64**	**Consul *et al.* [92]**	**CFT**	12.5, 25, **50**
McAdam *et al.* [103, 104]	**CFT**	**47, 59**	**Goude and Ågren [93]**	**CFT**	0, 12.5, 25, **50**
Battisti *et al.* [83]	CFT	2.8†, 10	**Kolekar and Banerjee [94]**	**AFT**	4.2, 8.2, 11, 17, 20, **33, 42**
Chen and Liou [84]	AFT	10.2, 20.2, 28.3	**Schluntz and Willden [95]**	**AFT**	0, 7.9, 19.6, **31.4**
Ross and Altman [85]	CFT (Savonius)	2, 3.5, 8	**Gauthier *et al.* [96]**	**Oscillating foil**	0.2 - **60.5**
Birjandi *et al.* [105]	**CFT**	24.5 - **49.2**†	Sarlak *et al.* [97]	AFT	2, 5, 9, 20
McTavish *et al.* [86]	AFT	6.3, 9.9, 14.3, 19.4, 25.4	**Kinsey and Dumas [11]**	**AFT**	0, 10, 20, **50, 60**
Gaurier *et al.* [138]	AFT	1.2, 3.3, 4.8		**CFT**	0, 13, 26, **51**
Ryi *et al.* [87]	**AFT**	8.1, 18.0, **48.1**	Badshah *et al.* [98]	AFT	2 - 19
Dossena *et al.* [88]	CFT	2.8†, 10	**Gauvin-Tremblay and Dumas [46]**	**CFT**	5, 20, **40**
Jeong *et al.* [89]	CFT	3.5, 13.4, 24.7	**Zilic de Arcos *et al.* [99]**	**AFT**	1, 5, 10, 20, **40**
Ross and Polagye [34]	**AFT**	2, **35**	**Abutunis and Menta [100]**	**AFT**	4.2, 20.8, **41.6, 62.5**
	CFT	3, **36**	Zhang *et al.* [101]	AFT	2, 2.8, 4.4, 7.9, 17.7
Ross and Polagye [90]	**CFT**	14, **36**		CFT (Savonius)	2.5, 3.6, 5.6, 10, 22.5

† Value(s) estimated from provided turbine and channel dimensions.

of blockages, limiting the ability to draw conclusions about performance trends. Although the experimental studies in Table 5.1 collectively span a wide range of blockages, meaningful cross-comparisons are limited due to differences in rotor geometry, which can strongly influence performance [95, 114], and several studies convolve the effects of blockage with those of the Reynolds and Froude numbers [e.g., 103–105]. Given the lack of high-resolution experimental data at high blockage, the computational methods used in numerical studies are often validated only at lower blockage [11, 92, 94, 96]—or not at all—before being used to simulate high blockage cases. Consequently, although the general effects of blockage on turbine performance are well-known, there is underlying uncertainty as to how these effects evolve at higher confinement and the benefits that can be realized in practice. For these reasons, a high-resolution experimental examination of turbine performance and the associ-

ated near-wake flow field across this upper end of blockage ratios is warranted. In doing so, the efficacy of theoretical models for turbine operation under these conditions may also be evaluated.

The objective of this chapter is to develop a more comprehensive understanding of performance and flow fields around a cross-flow turbine array at higher confinement. Such information can be used to understand the relevance of theory to non-ideal arrays that arguably violate multiple underpinning assumptions of these analytical models (e.g., treating the turbines as porous, non-rotating disks). Similarly, these experimental results provide a high-resolution data set for future validation of simulations at high confinement. To this end, a symmetric two-turbine array is tested in a recirculating water channel at blockage ratios ranging from 30% to 55%, and particle image velocimetry (PIV) is used to measure the flow field in the near-wake. The use of a pair of turbines, rather than an individual turbine, is motivated by the application of the research to understand the potential for confinement to reduce energy costs for turbine arrays. The Reynolds and Froude numbers are controlled to avoid convolving changes in blockage with other relevant non-dimensional flow parameters [102]. Section 5.2 describes the experimental methods used for performance and flow field measurements, and trends in the performance and near-wake velocities are discussed in Section 5.3. In Section 5.4, the open-channel LMADT model developed by Houlsby *et al.* [3] is applied to the experimental performance data to predict the wake and bypass velocities in the vicinity of the array. The analytically-predicted velocities are compared to those measured using PIV and are used to interpret high-blockage turbine hydrodynamics. Based on the characteristic dynamics observed, a method for forecasting confined turbine performance based on linear momentum theory and the bluff body theory of Maskell [1] is proposed in Section 5.5.

5.2 Experimental Methods

5.2.1 Cross-Flow Turbine Test Setup

Experiments are conducted in the Alice C. Tyler recirculating water flume at UW (Section 3.1) using the two-turbine array test setup described in Section 3.3. The laboratory-scale array consists of two identical straight-bladed cross-flow turbines. The rotors each have two blades, with each blade consisting of a NACA 0018 profile with a 0.0742 m chord length and mounted at a -6° preset pitch angle as referenced from the quarter chord. The blade span is 0.215 m. The blades are at a radius of $R = 0.151$ m from the axis of rotation with respect to the quarter-chord, resulting in an outermost swept diameter of $D' = 0.315$ m due to the foil thickness. For completeness, as in Chapter 4, the radial distance to the quarter chord is used to calculate kinematic quantities (e.g., the tip-speed ratio and Reynolds number), whereas the outermost swept diameter is used to calculate the turbine projected area for blockage and normalized performance quantities (e.g., efficiency). The blades are attached to the central driveshaft of each rotor using thin, hydrodynamic blade-end struts (NACA 0008 profile, 0.0742 m chord length). This arrangement results in $H/D = 0.68$, $c/R = 0.49$, and $\sigma = 0.16$.

The freestream velocity, freestream water depth, and water temperature are sampled upstream of the array as described in Section 3.4. However, the water depth was also sampled in the vicinity of the array ($0.5D'$, $1.0D'$, and $2.0D'$ directly upstream and downstream of Turbine B) using six additional FSTs synchronized with the upstream sensor and all sampling at 0.5Hz. As the array is symmetric about the channel centerline (Figure 3.4) the streamwise free surface profile in the vicinity of Turbine B is assumed to be representative of that in the vicinity of Turbine A.

5.2.2 Non-Dimensional Parameters and Test Conditions

For the two-turbine array, the blockage ratio is defined as:

$$\beta = \frac{A_{\text{turbines}}}{A_{\text{channel}}} = \frac{2HD'}{hw}. \tag{5.1}$$

The blockage ratio is varied by holding the array geometry constant and changing the water depth in the flume. However, to experimentally isolate the effects of blockage on array performance while changing the water depth, other non-dimensional flow parameters must be controlled. For example, to increase the blockage ratio, the water depth, h, is decreased. This decrease in depth increases the Froude number based on channel depth, as well as the proximity of the array to the free surface represented here by the normalized submergence, s/h. Therefore, as h decreases, U_∞ and s must also decrease to hold Fr_h and s/h, respectively, constant. However, a decrease in U_∞ also decreases the Reynolds number, which is defined here with respect to the turbine diameter (Re_D; Equation 2.12). To compensate for the decrease in U_∞ necessitated by holding Fr_h constant, the kinematic viscosity is increased by changing water temperature. In this way, β can be varied while holding Fr_h, s/h, and Re_D constant.

Array performance is measured at blockage ratios ranging from 30.0% to 55.0%, which is the widest range of blockages possible given the size of these turbines and flume capabilities. The flume conditions used to achieve each blockage while holding Fr_h and Re_D constant are summarized in Table 5.2. Across all experiments, the measured β are within 1.5% of the target values in Table 5.2, and the measured Fr_h and Re_D do not deviate more than 5% from the nominal values in Table 5.2. The measured turbulence intensity is ∼2% for all test conditions.

The value of Re_D in this study is constrained by the maximum U_∞ for the highest blockage ratio. This maximum velocity, in turn, is constrained by the entrainment of air from the free surface into the rotor (i.e., ventilation), which decreases the lift on the blades and degrades performance [105, 106]. Consequently, the maximum U_∞ for the highest tested blockage ratio is set such that any ventilation occurred beyond the optimal performance point. Since

Table 5.2: Experimental parameters for each blockage condition tested.

Target Blockage Condition	Flume Parameters				Non-Dimensional Flow Parameters		
β [%]	h [m]	U_∞ [m/s]	s [m]	Temp [°C]	s/h	Fr_h	Re_D
30.0	0.593	0.528	0.326	21.0	0.55		
33.4	0.534	0.501	0.267	23.3	0.50		
36.7	0.485	0.477	0.218	25.4	0.45		
40.1	0.445	0.457	0.178	27.3	0.40	0.22	1.62×10^5
45.0	0.396	0.431	0.129	30.1	0.33		
50.0	0.356	0.409	0.090	32.6	0.25		
55.0	0.324	0.390	0.057	35.0	0.18		

ventilation becomes more likely as s/h decreases, to further limit the risk of ventilation, s/h is maximized at each blockage rather than held constant across all blockages. Array performance at various s/h and β is separately evaluated (Appendix D), and confirms that varying s/h has minor effects on performance before the onset of ventilation.

Array performance is characterized over a range of tip-speed ratios at each β in Table 5.2. Data are collected at each tip-speed ratio for 60 seconds, and the time series is cropped to an integer number of turbine rotations before array-average performance metrics are calculated as described in Section 3.5. The performance results in Section 5.3 focus on $C_{P,\text{array}}$ and $C_{T,\text{array}}$, whereas the measured array lateral forces are provided in Appendix C.

5.2.3 Flow Visualization

Two-camera, three-component particle image velocimetry is used to unobtrusively record the near-wake flow field in a plane perpendicular to the flow $0.6D'$ downstream of the array. Two cameras (50fps frame rate, Imager sCMOS 5.5 MPx) with a 35mm and 60mm lens, are positioned horizontally on either side of the flume perpendicular to water-filled acrylic prisms shown in Figure 5.1. The prisms were used to reduce refractive distortion from the angled

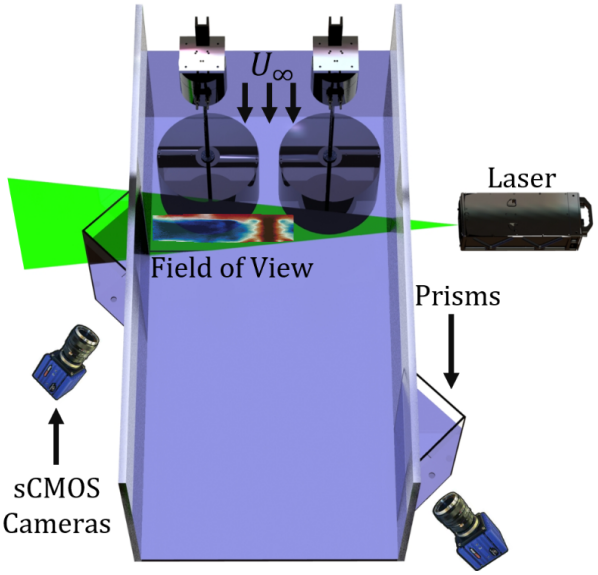

Figure 5.1: Schematic of PIV test setup with the array and sample flow field data shown.

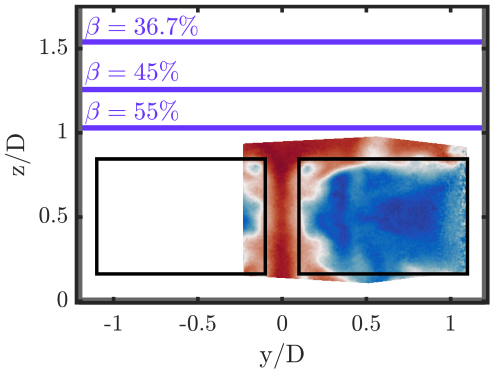

Figure 5.2: Location of PIV field of view within the flume. The black rectangles indicate the projected areas of the turbines. The blue lines indicate the nominal location of the free surface at each blockage ratio.

camera positioning relative to the flume. The cameras are positioned at $\sim 45°$ incidence to the image plane. Scheimpflug camera lens adaptors correct any leftover focal length distortions from angled fields of view (FoV). The FoV of each camera is focused on a domain centered behind one of the turbines and results in an overlapping 42.3×27.7 cm^2 data collection region. The FoV is positioned 5.2 cm above the bottom of the flume and 6 cm from the side wall to maximize capture of the flow through and around the array while reducing overexposure from laser scattering from the test section walls. The resulting FoV (Figure 5.2) encompasses the full projected area of Turbine B, the bypass region above Turbine B, and the bypass region between the turbines. Although the FoV does not capture the full array, given the symmetry (Figure 3.4) the flow measured around Turbine B is expected to be descriptive of that near Turbine A. The entire flume is seeded with neutrally buoyant hollow glass spheres with a

diameter of $\sim 10\mu$m (Potters Industries Sphericel 110P8), and illumination is provided by a 532nm, 200 mJ per pulse laser (EverGreen 200 - Big Sky Series), which produced a light sheet $\sim$2 mm thick.

Flow field data are collected at $\beta = 36.7\%$, 45.0%, and 55.0% at tip-speed ratios of $\lambda = 1.5$, 2.5, 2.8, and 3.5 (all β) and $\lambda = 4.0$ ($\beta = 55.0\%$) only. These tip-speed ratios include the "optimal" λ corresponding to maximum $C_{P,\text{array}}$ for $\beta = 36.7\%$, 45.0%, and 55.0%, as well as λ lower ("underspeed") and higher ("overspeed") than the optimal λ at these blockage ratios, which are relevant for shedding power above a certain flow speed for economic reasons [139]. Data acquisition is synchronized with turbine phase (θ), with images collected in 12° increments. A total of 40 images are collected at each phase, and the replicates are used to phase-average the flow fields and reduce measurement noise from reflections. All phases are then averaged together to produce representative time-averaged fields.

LaVision Davis 10.2.1 software is used to acquire and process the PIV data. A dual-plane calibration target paired with planar self-calibration is used to correct for slight misalignment in the system and convert the image scale to physical positions. The resulting scale factor between the cameras is 7.97 pix/mm with fitting errors of 0.81 and 0.92 pixels for each camera, respectively. Raw image pre-processing involved a minimum filter to subtract background noise and an average polynomial filter using an interrogation window of 11×11 pixels to eliminate unsteady reflections. Vector calculation employed an initial 128×128 interrogation window with a 50% overlap followed by four sequentially reducing passes to 32×32 pixels at a 75% overlap. After vector calculation, vector post-processing comprised three passes of a universal outlier detection median filter [140] that removed vectors with a median normalized residual greater than 1.5 and reinstated them if less than 2.5 for a filter domain of 7×7. Groups with fewer than five vectors were removed. No smoothing or interpolation was applied.

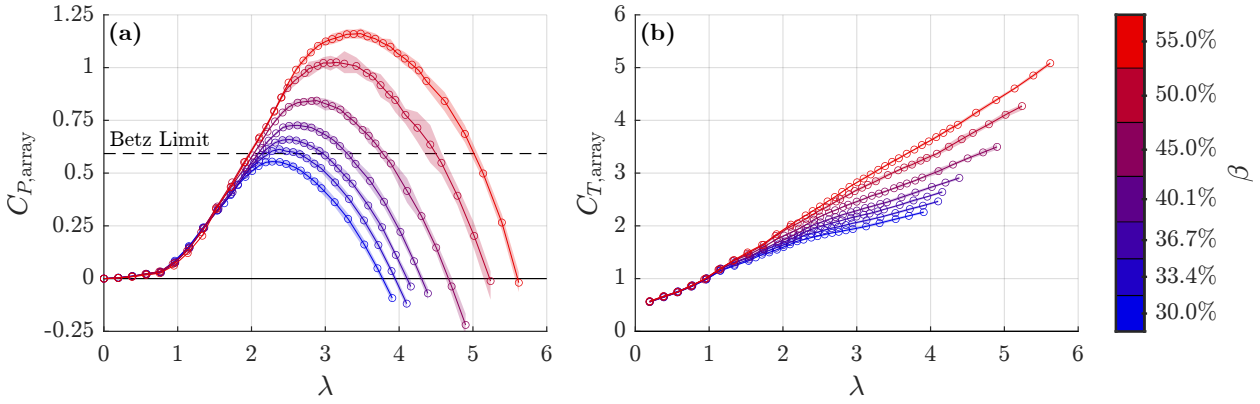

Figure 5.3: Time-averaged (a) $C_{P,\text{array}}$ and (b) $C_{T,\text{array}}$ as a function of β and λ. The shaded regions indicate the interquartile range of the array- and cycle-averaged performance at each β and λ (the vertical span of the shaded region at each point is similar to the size of the markers for most operating conditions).

5.3 Experimental Results

5.3.1 Array Performance

The time-average $C_{P,\text{array}}$ as a function of β and λ is shown in Figure 5.3a. In agreement with prior work in Table 5.1, as β increases, the maximum $C_{P,\text{array}}$ increases, the array produces power over a broader range of tip-speed ratios, and the tip-speed ratio corresponding to maximum efficiency increases. Similarly, the time-averaged $C_{T,\text{array}}$ (Figure 5.3b) generally increases with β, and $C_{T,\text{array}}$ increases more strongly with λ at higher blockage ratios. Above $\beta = 33.4\%$, maximum $C_{P,\text{array}}$ exceeds the Betz limit, and above $\beta = 50.0\%$, maximum $C_{P,\text{array}}$ exceeds unity. Such efficiencies are not violations of energy conservation since the definition of C_P given in Equation 2.2 considers only the kinetic power that passes through the array projected area. This conventional definition neglects the power associated with the fluid's potential energy, which is appreciably drawn down as β and thrust increase. Given the relevance of the static and dynamic head for turbines in confined flows, as β increases

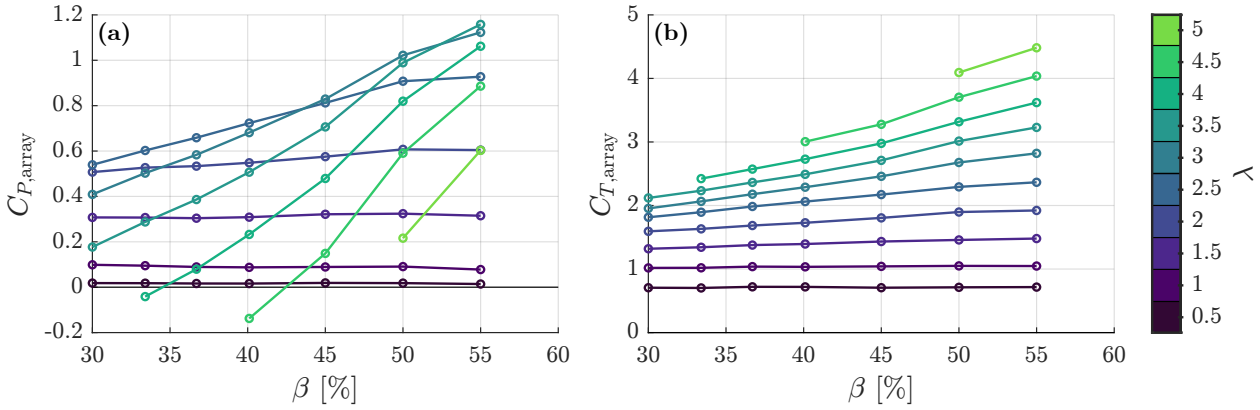

Figure 5.4: Time-averaged (a) $C_{P,\text{array}}$ and (b) $C_{T,\text{array}}$ versus β at constant λ. The data for each β are interpolated at each λ from the points in Figure 5.3.

a better-bounded efficiency metric may resemble the hydraulic efficiency of a hydropower turbine (such as that employed by Takamatsu *et al.* [68] or McAdam *et al.* [103]) in which the available power is a function of volumetric flow rate through and the head drop across the rotor. However, the conventional, velocity-based definitions of C_P and C_T are used here for ease of comparison with prior studies, as well as to allow the application of analytical LMADT models—which are formulated using the definition of C_T in Equation 2.3—in Section 5.4.

When the array power and thrust coefficients are regressed against β at constant λ (Figure 5.4), approximately linear relationships are revealed. For $\lambda < 1.5$, both $C_{P,\text{array}}$ and $C_{T,\text{array}}$ depend only on the tip-speed ratio and are independent of the blockage ratio, which corresponds to the collapsed regions of the $C_{P,\text{array}} - \lambda$ and $C_{T,\text{array}} - \lambda$ curves in Figure 5.3. This is similar to observations in prior work [92, 94, 98]. As λ increases further, both $C_{P,\text{array}}$ and $C_{T,\text{array}}$ become more sensitive to the blockage ratio. $C_{P,\text{array}}$ and $C_{T,\text{array}}$ are most linear with the blockage ratio for $\beta \leq 45.0\%$ and moderate λ, but as β and λ increase further, performance is more greatly affected by incremental changes in the blockage and tip-speed ratios. While similar linear relationships between the blockage ratio, power, and thrust have

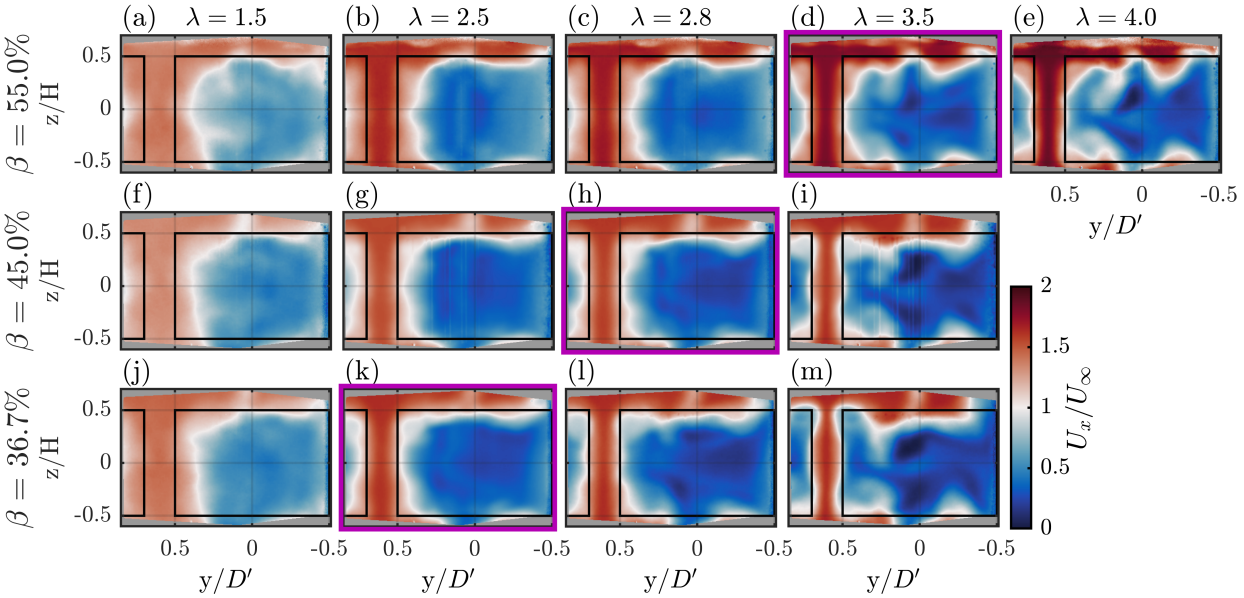

Figure 5.5: Time-averaged streamwise velocity $0.6D'$ downstream of the array as function of β and λ. Velocity measurements are normalized by the freestream velocity measured by the ADV. The black rectangles in each tile indicate the projected area of the turbines in the field of view. Tiles corresponding to the optimal λ for each blockage are outlined in purple.

been previously identified for oscillating foils [96], axial-flow turbines [11, 100] and cross-flow turbines [11], these relationships have not been demonstrated over such a continuous range of β and λ.

5.3.2 Flow Fields

Figure 5.5 shows the normalized time-average streamwise velocity field $0.6D'$ downstream of the array (i.e., within the near-wake) as a function of β and λ. For each β and λ, the velocity field at this location is characterized by a wake region behind the turbines slower than the freestream ($U_x/U_\infty < 1$, indicated by blue hues) and a bypass region above, below, and between the turbines where the flow is accelerated ($U_x/U_\infty > 1$, indicated by red hues).

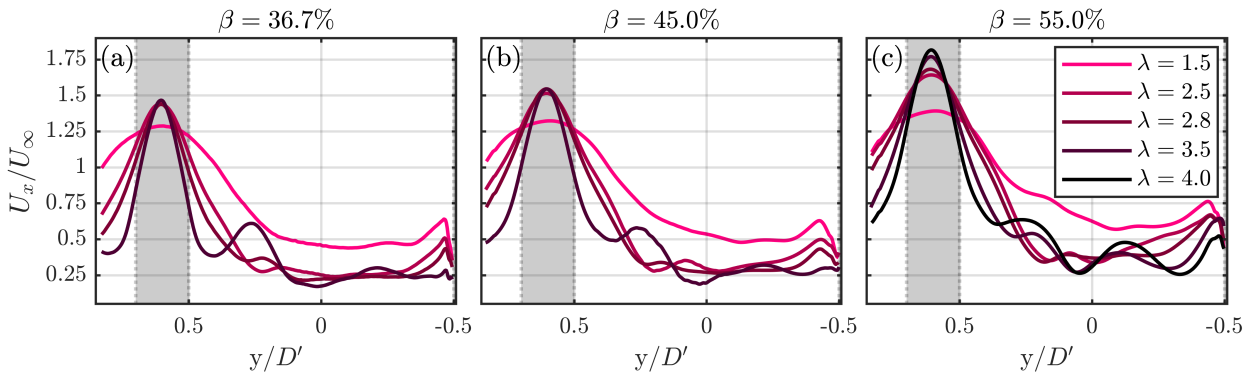

Figure 5.6: Time-averaged normalized streamwise velocity profiles measured $0.6D'$ downstream of the array for various λ at (a) $\beta = 36.7\%$, (b) $\beta = 45.0\%$, and (c) $\beta = 55.0\%$. The profiles shown correspond to the average velocity along the middle 70% of the turbine blade span. Vertical grey rectangles correspond to the bypass region and delineate the relative turbine position and wake flow region (white). Curves in (b) and (c) are smoothed with moving average to remove blade reflection noise.

The accelerated flow region between the turbine and the flume side wall lies outside of the field of view (Figure 5.2).

Trends across β and λ are more apparent when visualized as two-dimensional velocity profiles of the average velocity field over the middle 70% of the blade span at each y/D' position (Figure 5.6). Ripples in the velocity profiles in the wake region are attributed to the passage of vortices shed from the blades during their downstream sweep. At $\lambda = 1.5$ (Figures 5.5a, 5.5f and 5.5j), where array performance is independent of β (Figure 5.4), U_x/U_∞ still slightly increases with β throughout the entire profile, although the general shape of the velocity profile is unaffected. This is likely because, at lower β, fluid more readily bypasses the top of the rotor, outside of the field of view (Figure 5.2). As λ increases and the turbines impart greater resistance on the flow, more fluid is diverted around the turbines at all β, which causes U_x/U_∞ to increase in the bypass. Similarly, as the blockage

ratio increases, the bypass velocity at the array centerline increases, and the magnitude of this increase becomes more sensitive to the tip-speed ratio. Additionally, as β increases at a given λ, U_x/U_∞ generally increases in the wake region since confinement accelerates the flow through the turbines. However, this acceleration of the wake is less pronounced that the corresponding acceleration of the bypass flow since momentum is extracted from the flow through the turbines. Although the maximum bypass velocity at the array centerline increases with both λ and β, U_x/U_∞ decreases more rapidly away from the centerline as λ increases. Conversely, an increase in β at constant λ reduces the rate at which U_x/U_∞ decreases away from the centerline. Although this latter effect is slight and most pronounced at higher λ, it may imply increased turbulent mixing between the core and bypass flows as β increases, which Nishino and Willden [91] suggest provides a secondary enhancement of power with blockage by accelerating the core flow through the turbine.

The shapes of the bypass and wake regions are also influenced by λ and β. Most notably, as λ increases at a given β, the bypass flow above Turbine B extends further down into the area directly behind the turbine. This is attributed to the drop in the free surface behind the rotors, which is shown for Turbine B at the same β and λ in Figure 5.7. The free surface drop corresponds to the pressure drop across the array due to energy extraction by the turbines from an open channel flow [79], and this free surface deformation further constrains the bypass and can result in downward deflection of the wake [94]. Since $C_{T,\text{array}}$ increases as the blockage ratio increases (Figure 5.3b), the pressure drop across the array increases. Thus the free surface drop across Turbine B increases with β (Figure 5.7), as does the downward extent of the upper bypass region. This effect is most clearly observed through comparison of Figures 5.5d, 5.5i and 5.5m. The persistent region of decelerated flow below the turbine projected area at all λ may due to downward deflection of the wake by the upper bypass flow, as well as obstruction of the flow by the lower load cell and suction plate (Figure 3.3).

Although $C_{T,\text{array}}$, and thus the pressure drop across the array, also increases continuously with λ at a given β, the measured free surface drops across Turbine B at $\beta = 36.7\%$ (Figure 5.7a) and 45.0% (Figure 5.7b) do not continuously increase with λ, but instead appear

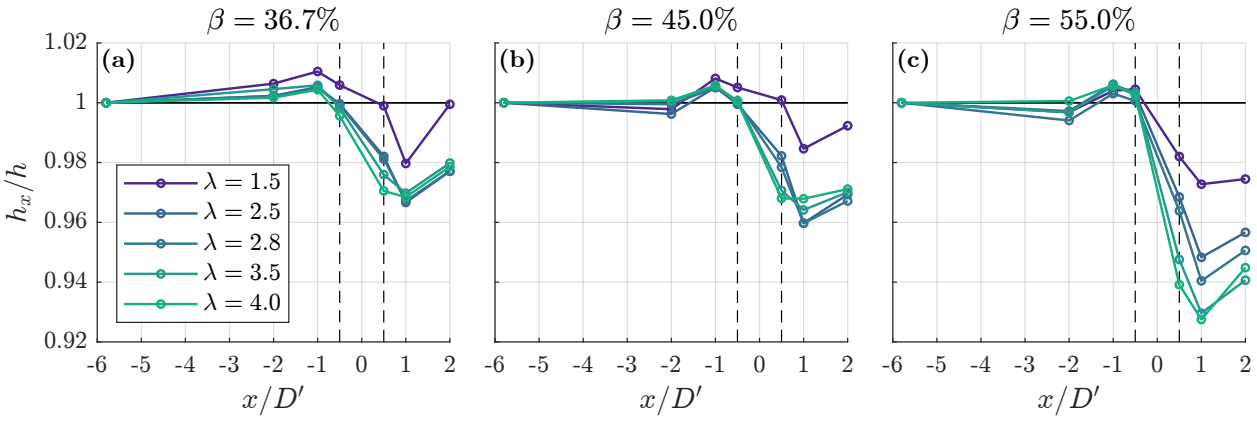

Figure 5.7: Time-averaged streamwise water depth profiles for various λ at (a) $\beta = 36.7\%$, (b) $\beta = 45.0\%$, and (c) $\beta = 55.0\%$. The farthest upstream measurement is taken at the center of the channel, whereas depth measurements in the vicinity of the array are directly upstream and downstream of Turbine B (Figure 3.4). Depth measurements at each streamwise location (h_x) are normalized by the far-upstream water depth (h) measured at the same β and λ. The dashed lines indicate the swept area of Turbine B.

to roughly stabilize above a threshold value of λ. As this result would appear to contradict theory, it suggests that the free surface profiles measured across Turbine B are not fully representative of the interaction between the array and the channel. Therefore, additional samples of the dynamic water depth at other cross-stream locations are required to further assess the influence of β and λ on the free surface. Furthermore, as shown in Appendix D, the free surface drop behind the array is also a function of the normalized submergence depth (s/h) which decreases with β in these experiments as described in Section 5.2.2. Consequently, the downward extension of the upper bypass may be augmented somewhat at higher β by the closer proximity of the array to the free surface.

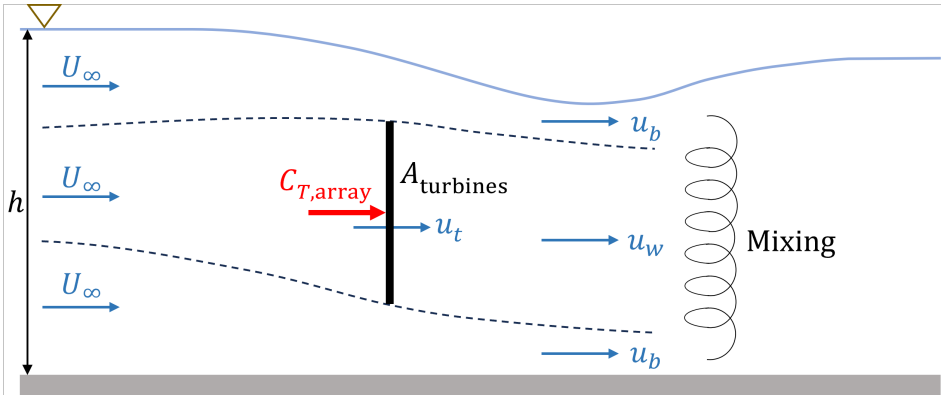

Figure 5.8: Linear momentum model for an actuator disk in open-channel flow defined by Houlsby *et al.* [3] and adapted to the cross-flow turbine array.

5.4 Evaluation of Analytical Model

5.4.1 Model Overview

Given the performance and flow field measurements described in Section 5.3, the efficacy of one-dimensional linear momentum actuator disk theory for modelling this high confinement cross-flow turbine array can be evaluated. Based on the free surface deformation observed during experiments (Figure 5.7), the open-channel LMADT model introduced by Houlsby *et al.* [3] is considered here. In the limiting case of negligible free surface drop across the turbine array ($Fr^2 \to 0$), this model reduces to the well-known model of Garrett and Cummins [8] for a turbine in a channel with constant cross-sectional area. The reader is referred to Houlsby *et al.* [3] and Houlsby and Vogel [10] for a detailed derivation.

A schematic of the open-channel model as applied to the present cross-flow turbine array is shown in Figure 5.8. The cross-flow turbine array is modeled as a single actuator disk with the same blockage ratio and thrust coefficient as the array. Although some LMADT models can represent individual turbines in the array as separate actuator disks [e.g., 78, 79, 81], these reduce to models of a single actuator disk when the turbines are spaced equally throughout the channel as they are here (Section 3.3). The flow upstream of the turbine

is unidirectional, uniform, and subcritical with velocity U_∞ and depth h. In response to the momentum extraction by the turbine, the flow in the streamtube that passes through the rotor slows from U_∞ to u_t just upstream of the turbine, and further decelerates to u_w downstream of the turbine in the near-wake. To satisfy continuity, the fluid outside of this streamtube is accelerated from U_∞ to u_b. The core wake velocity (u_w) and bypass velocity (u_b) are defined at a location downstream of the turbine where the pressure in the core and bypass flows is equal and hydrostatic. The flow is assumed to be axisymmetric and inviscid up to this location, downstream of which u_w and u_b mix. Far downstream, the flow is once again uniform, with reduced depth due to the energy extracted by the disk, but higher velocity to maintain constant mass flux through the channel.

This model clearly reflects qualitative aspects of the experimentally observed wake and bypass velocities. Although LMADT models are widely used to model turbine hydrodynamics in confined flows—most often as the basis for analytical blockage corrections [e.g., 9, 141, 142]—several of the underlying assumptions are violated in practice. For example, the wake is assumed to be axisymmetric and no mixing is assumed to occur until the pressure has equilibrated between the core and bypass flows. Here, we have the opportunity to evaluate the quantitative efficacy of such a model for a situation that departs from these idealizations.

The implementation of the open-channel model used here follows that of Ross and Polagye [34], who reorganized Houlsby *et al.*'s original formulation into two equations from which u_w and u_b can be obtained numerically if U_∞, $C_{T,\text{array}}$, Fr_h, and β are known:

$$u_w = \frac{Fr_h^2 u_b^4 - (4 + 2Fr_h^2)U_\infty^2 u_b^2 + 8U_\infty^3 u_b - 4U_\infty^4 + 4\beta C_{T,\text{array}} U_\infty^4 + Fr_h^2 U_\infty^4}{-4Fr_h^2 u_b^3 + (4Fr_h^2 + 8)U_\infty^2 u_b - 8U_\infty^3} \,, \tag{5.2}$$

$$u_w = \sqrt{u_b^2 - C_{T,\text{array}} U_\infty^2} \,. \tag{5.3}$$

The velocity through the turbine, u_t, is then given as

$$u_t = \frac{u_w(u_b - U_\infty)(2gh - u_b^2 - u_b U_\infty)}{2\beta g h(u_b - u_w)} \,. \tag{5.4}$$

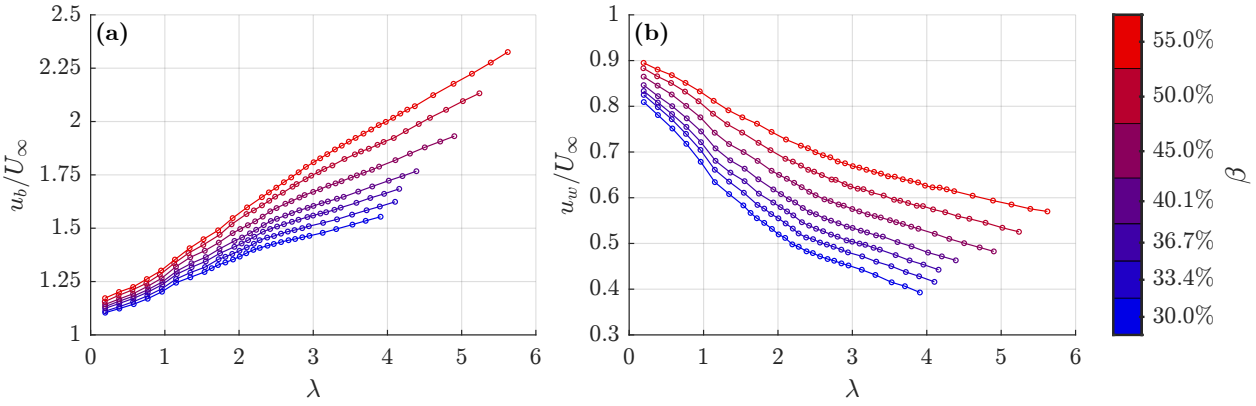

Figure 5.9: The (a) bypass velocities, and (b) wake velocities (all normalized by the freestream velocity) predicted by the open-channel LMADT model of Houlsby *et al.* [3] from measurements of array thrust and flow conditions.

For the solutions to Equations 5.2 to 5.4 to be physically valid, the core and bypass flows must be subcritical and satisfy $u_b > u_t > u_w$ and $u_b > U_\infty > u_t$.

It is noted that expressions for the water depth at various locations along the channel are provided in Houlsby *et al.*'s open-channel LMADT model, such that analytical predictions of free surface deformation in the near-wake could also be calculated. However, the ultrasonic transducers employed in this study sampled the free surface at much lower spatial and temporal resolution than was used to measure the near-wake velocities using PIV, such that only qualitative trends in free surface deformation with β and λ can be identified. Consequently, the water depth along the channel is not compared to that predicted by LMADT in this work.

5.4.2 Comparison between Experimental and Analytically-Predicted Near-Wake Velocities

Using the measured values of $C_{T,\text{array}}$, U_∞, and Fr_h and β, u_b and u_w are calculated at each λ using Equations 5.2 and 5.3. The resulting analytically-predicted velocities are normalized

by the corresponding freestream velocity in Figure 5.9. Qualitatively, trends in near-wake velocities predicted by LMADT agree with trends in the experimental near-wake velocities (Figure 5.5). At a given tip-speed ratio, both u_b (Figure 5.9a) and u_w (Figure 5.9b) increase with β because confinement accelerates the flow through and around the turbine. As λ increases, u_b increases at all β since thrust increases with λ and more flow is diverted around the array, whereas u_w decreases at all β due to momentum extraction by the array. In agreement with trends in the velocity profiles in Figure 5.6, u_b increases more strongly with tip-speed ratio at higher blockage, and u_w becomes less sensitive to the tip-speed ratio at higher λ. It is noted that the calculated u_w is always positive, indicating that the upper limit of the thrust coefficient for physically-valid solutions to open-channel LMADT (analogous to $C_T \leq 1$ for LMADT in unconfined flow) is not reached for any of the β in these experiments.

For a quantitative comparison, the time-averaged streamwise near-wake velocities at $\beta = 36.7\%$, 45.0%, and 55.0% are normalized by u_b and u_w in Figure 5.10. Here, blue hues correspond to experimental velocities lower than the LMADT-predicted value, red hues correspond to experimental velocities higher than the LMADT-predicted value, and white indicates good agreement between the experimental and analytical velocities. The measured bypass velocity is well-predicted by LMADT. As shown in the bypass-normalized velocity profiles in Figures 5.11a to 5.11c, the predicted u_b tend to be slightly higher than the experimental bypass velocity at the array centerline, but are within $3\% - 8\%$ of the measured value for all β and λ at which flow fields were measured. In contrast, the experimental wake velocities are lower than u_w at all λ, and there is no substantive region of the flow that is well represented by u_w (Figures 5.10d to 5.10f).

Although the time-averaged flow fields in Figure 5.5 show distinct wake and bypass regions downstream of the array, the quantitative agreement between the calculated u_b and the measured velocities in the bypass region is remarkable given that the instantaneous flow field is non-ideal. Qualities of the near-wake flow field that deviate from the assumptions of the analytical model are highlighted at peak performance for $\beta = 36.7\%$, 45.0% and 55.0% in Figure 5.12. For example, unlike the uniform and one-dimensional flow assumed by the

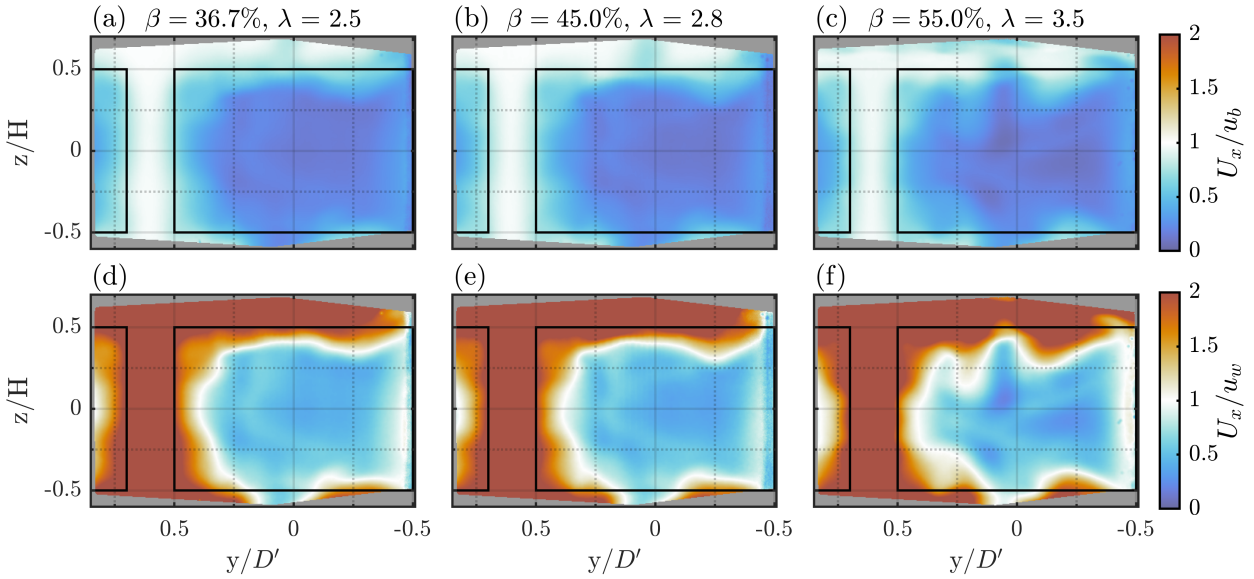

Figure 5.10: Time-averaged streamwise velocities measured $0.6D'$ downstream of the array at $\beta = 36.7\%$, 45.0%, and 55.0% and optimal λ, normalized by the corresponding analytically-predicted (a)-(c) bypass velocity, u_b, and (d)-(f) wake velocity, u_w. The black rectangles indicate the projected area of the turbines in the field of view.

LMADT model, the flow in the near-wake varies in space and time, even within the bypass and wake regions (Figures 5.12a to 5.12c). The flow is also highly rotational (Figures 5.12d to 5.12f): the periodic hydrodynamics of cross-flow turbines give rise to dynamic stall vortices that are shed into the region between the two turbines, and edge effects at the blade-strut interface yield vortices along the top and bottom of the turbine projected area. Finally, u_b is specified at a location downstream of the turbines where the static head is equal in both the wake and bypass flows. Although it is unknown whether this condition is satisfied $0.6D'$ downstream of the array, u_b describes the measured flow in the bypass at this location.

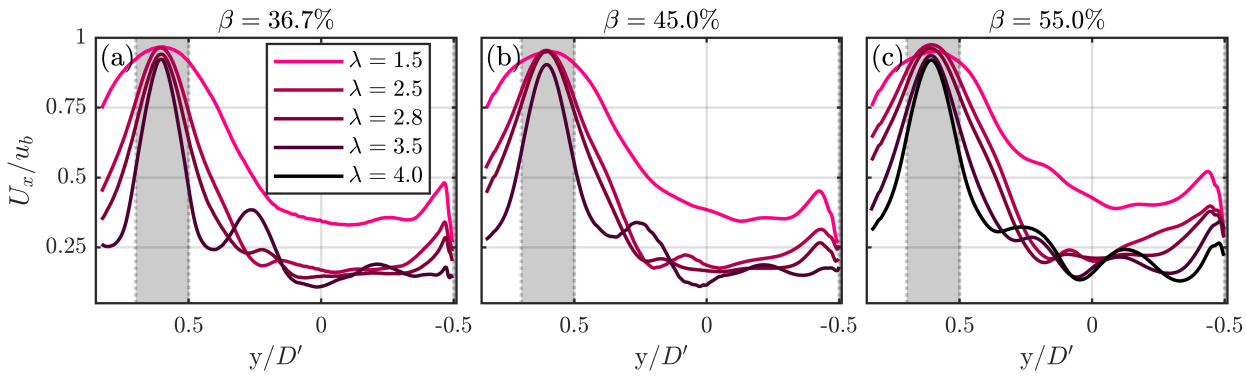

Figure 5.11: Time-averaged streamwise velocity profiles measured $0.6D'$ downstream of the array normalized by the analytically predicted bypass velocity at peak performance at (a) $\beta = 36.7\%$, (b) 45.0%, and (c) 55.0%. The profiles shown correspond to the average velocity along the middle 70% of the turbine blade span. Vertical dashed lines correspond to the relative turbine position and delineate the bypass from the wake flow region.

5.4.3 Bluff-Body Scaling of Performance Data

Given that the analytically-predicted bypass velocity is descriptive of the experimental bypass flow across a range of array operating conditions, this raises the question of whether u_b can describe array performance. To explore this relationship, we apply the method of Whelan *et al.* [9] based on the bluff-body theory of Maskell [1] to scale the experimental array performance by the corresponding bypass velocities predicted from linear momentum:

$$C_P{}^b = C_{P,\text{array}} \left(\frac{U_\infty}{u_b} \right)^3, \tag{5.5}$$

$$C_T{}^b = C_{T,\text{array}} \left(\frac{U_\infty}{u_b} \right)^2, \tag{5.6}$$

$$\lambda^b = \lambda \left(\frac{U_\infty}{u_b} \right), \tag{5.7}$$

where $C_P{}^b$, $C_T{}^b$, and λ^b are respectively the array power, thrust, and tip-speed normalized by u_b rather than U_∞. As shown in Figure 5.13a, the resulting $C_P{}^b - \lambda^b$ and $C_T{}^b - \lambda^b$ curves

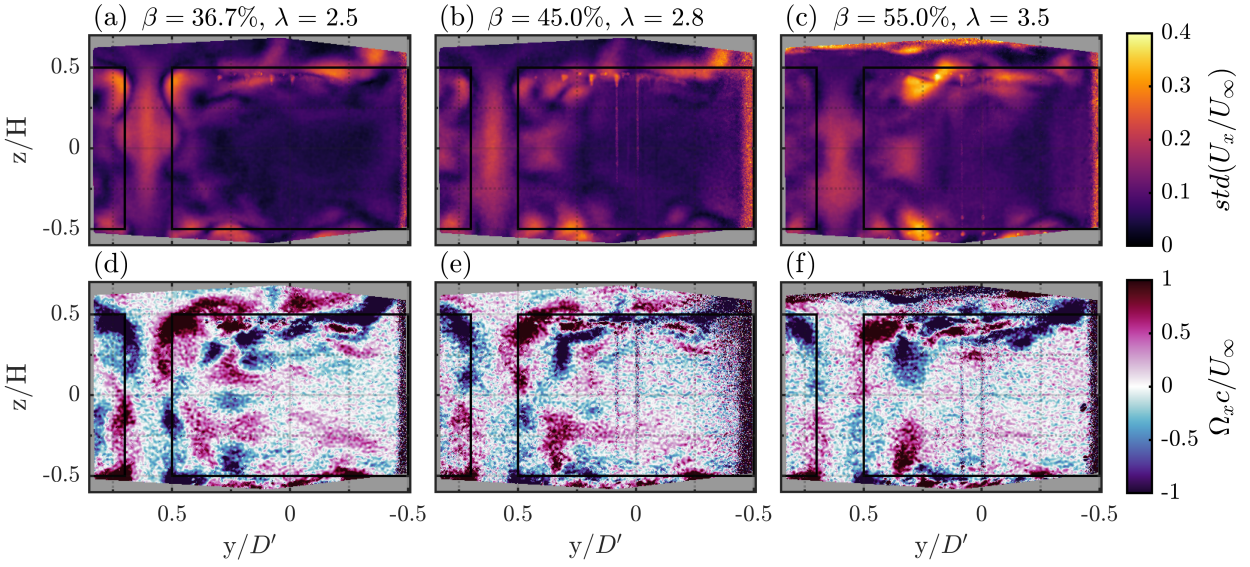

Figure 5.12: Examples of non-idealities in the measured flow fields relative to the flow fields assumed by linear momentum theory. (a)–(c) Standard deviation of the measured streamwise velocity from the time-average streamwise velocity field in a plane measured $0.6D'$ downstream of the array at $\beta = 36.7\%$, 45.0%, and 55.0% and peak performance. (d)–(f) Time-averaged streamwise vorticity at the same location and conditions.

collapse across the tested blockage and tip-speed ratios, indicating that array power and thrust scale with the bypass velocity under these conditions. Some spread in the bypass-scaled thrust curves is observed (maximum $\Delta {C_T}^b \approx 0.06$), particularly at lower λ^b, but the bypass-scaled power curves exhibit excellent collapse at all λ^b (maximum $\Delta {C_P}^b \approx 0.016$). As u_b is calculated using the measured $C_{T,\text{array}}$ in Equations 5.2 and 5.3, it is not surprising that $C_{T,\text{array}}$ appears to scale with u_b. However, given that measurements of $C_{P,\text{array}}$ are not involved in the calculation of u_b, the collapse in the ${C_P}^b - \lambda^b$ curves in Figure 5.13a is notable, especially since the rotation, torque, and lateral forces experienced by the physical cross-flow turbines are all neglected in an actuator disk model.

The hydrodynamics that underlie the connection between the bypass velocity and array

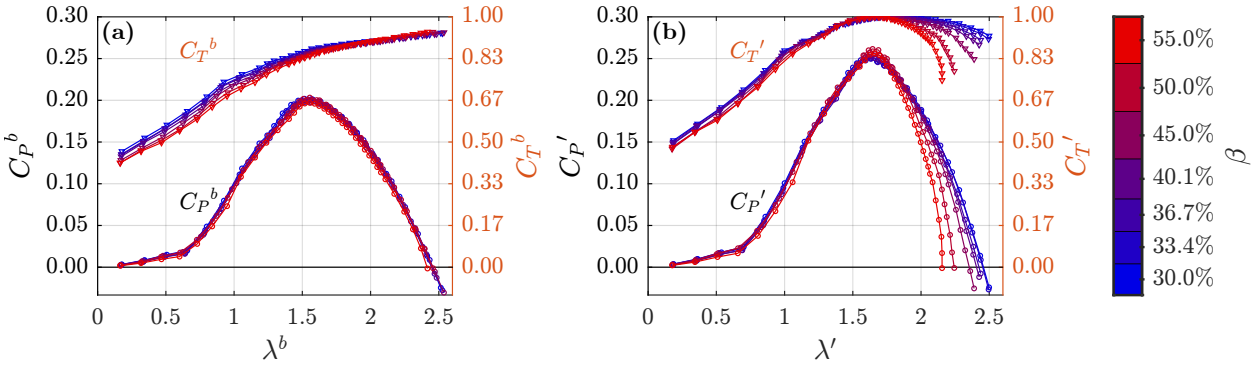

Figure 5.13: Time-averaged array performance from Figure 5.3 scaled by (a) the corresponding analytical bypass velocities (Figure 5.9a) and (b) the unconfined freestream velocity calculated using Equation 5.8.

performance are well-described by Nishino and Willden [91]. As β increases, the velocity of the fluid bypassing the array increases (Figures 5.5 and 5.13a). Since energy is conserved in the bypass flow, this acceleration corresponds to an increased pressure drop in the bypass. To satisfy pressure equilibrium between the core and bypass flows both far upstream and far downstream, the pressure drop in the core flow through the turbines must also increase. In an open-channel flow, these pressure drops manifest as a free surface drop along the channel. The increased pressure drop across the array as β increases accelerates the flow through the turbines, which increases power and thrust at higher blockage.

The connection between the bypass velocity and array performance parallels the theory of Maskell [1], who proposed that the drag force on a bluff body in confined flow is related to the accelerated flow around the body. Assuming a uniform and unidirectional inflow and axisymmetric wake, Maskell developed a model for this behavior by combining conservation of momentum in the flow outside the wake with an empirical relationship for wake contraction due to confinement, and demonstrated through experiments that this model was descriptive of the drag on square flat plates at a variety of low blockage ratios ($\beta \leq 10\%$). Maskell

leveraged this relationship to propose a blockage correction that could be used to predict the drag on a bluff body in unconfined flow given measurements of the same body in a wind tunnel. As the wake characteristics of wind and water turbines can resemble those of a bluff body under certain conditions [19, 143, 144], several subsequent studies have extended Maskell's theory. While some have directly applied Maskell's flat plate blockage correction to turbine performance data, [99, 101], others have adapted this theory to specific turbine designs through analogous empirical relationships [85, 89, 101, 145].

Whelan *et al.* [9] was the first to combine the core idea of Maskell's theory—that the thrust on a bluff body in confined flow scales with the accelerated flow past it—with linear momentum actuator disk theory to develop a blockage correction for highly loaded turbines. Rather than directly implementing Maskell's blockage correction, Whelan *et al.* utilized an open-channel LMADT model to calculate the expected u_b from axial-flow turbine thrust measurements at high blockage ($\beta = 64\%$), and utilized Equations 5.6 and 5.7 to scale the measured thrust coefficients and tip-speed ratios by this bypass velocity. The resulting ${C_T}^b - \lambda^b$ data agreed closely with the unconfined thrust coefficients predicted for the same turbine using BEM theory. Kinsey and Dumas [11] applied the same correction to simulated thrust data for a cross-flow turbine at $\beta = 13\%$, 25%, and 51% with u_b calculated via closed-channel LMADT. The resulting ${C_T}^b - \lambda^b$ curves yielded better agreement with the simulated unconfined thrust coefficients than was obtained with the popular Barnsley and Wellicome [146] blockage correction. Ross and Polagye [102] extended this correction to the power coefficient as in Equation 5.5, and utilized the LMADT model of Houlsby *et al.* [3] (as in the present study) to calculate u_b and scale the corresponding performance data of both an axial-flow turbine ($\beta = 2\%$ and 35%) and cross-flow turbine ($\beta = 3\%$ and 36%). However, in contrast to Whelan *et al.* and Kinsey and Dumas, at tip-speed ratios beyond the performance peak ($\lambda > 5$ for axial-flow, $\lambda > 1.75$ for cross-flow) Ross and Polagye observed moderately poor agreement between the measured low-blockage turbine performance and the ${C_P}^b$ and ${C_T}^b$ calculated from high-blockage turbine performance. Relative to prior work, the bypass-scaled power and thrust coefficients in Figure 5.13a exhibit the strongest collapse across

blockages observed to date, and highlight the similarities between array hydrodynamics and bluff-body dynamics for a wide range of high-blockage operating conditions.

Since the normalizations in Equations 5.5 to 5.7 have traditionally been interpreted as a Maskell-inspired bluff-body blockage correction, it is of interest to compare the bypass-scaled performance (Figure 5.13a) to that obtained via a "standard" LMADT blockage correction based on the theory of Glauert [141], in which it is assumed that the thrust on the turbine responds to the velocity through the turbine (u_t). Using the values of u_t calculated using Houlsby *et al.*'s LMADT model (Equation 5.4), the unconfined freestream velocity, ${U_\infty}'$, that yields the same u_t and dimensional thrust in unconfined flow as in the confined system is obtained at each operating point as

$$ {U_\infty}' = \frac{U_\infty \left((u_t/U_\infty)^2 + C_{T,\text{array}}/4 \right)}{u_t/U_\infty} \ . \tag{5.8} $$

The unconfined power coefficient (${C_P}'$), thrust coefficient (${C_T}'$), and tip-speed ratio (λ') are then calculated using Equations 5.5 to 5.7 with ${U_\infty}'$ in place of u_b, and are shown in Figure 5.13b. Up to ${C_T}' \approx 1$, the ${C_P}' - \lambda'$ and ${C_T}' - \lambda'$ curves exhibit similar collapse across blockages to that obtained using bluff-body scaling (maximum $\Delta {C_P}' \approx 0.018$; maximum $\Delta {C_T}' \approx 0.04$), with the values of ${C_P}'$ and ${C_T}'$ generally exceeding those of ${C_P}^b$ and ${C_T}^b$ at comparable normalized tip-speed. However, for LMADT in unconfined flow, the thrust coefficient cannot exceed unity as this implies reversed flow in the turbine wake. Thus, above the λ' corresponding to ${C_T}' \approx 1$, only non-physical solutions exist, and the unconfined efficiency and thrust coefficient curves no longer collapse. Given this constraint on ${C_T}'$, a key advantage of Maskell-inspired bluff-body scaling over a conventional LMADT blockage correction is the ability to describe the performance of high-blockage turbines over a wider range of confined $C_{T,\text{array}}$, and thus a wider range of β and λ. However, since measurements of array performance at $\beta \approx 0\%$ are not available, the accuracy of either scaling method for predicting unconfined performance cannot be cannot be assessed.

5.5 *Prediction of Confined Performance*

Since Maskell-inspired bluff-body performance scaling connects array behavior at different blockages through common characteristic dynamics (Figure 5.13a), it provides a pathway for using performance data collected at one blockage to forecast array performance at a different blockage. For example, such information is useful for understanding how performance changes in time in a tidal channel with varying surface elevation. Although "correcting" performance to non-zero blockages using LMADT is briefly mentioned in prior work [e.g., 147, 148], there have been limited demonstrations of such methods and no details describing the implementation. Whelan *et al.* [9] applied their Maskell-inspired bluff-body blockage correction in reverse to predict the thrust coefficients of a turbine at $\beta = 64\%$ from unconfined thrust calculated from BEM, but provide no details and do not quantify prediction accuracy. Kinsey and Dumas [11] proposed an empirical forecasting method based on their observation that both the power and thrust coefficients exhibit approximately linear relationships with β at constant λ (similar to that in Figure 5.4). Specifically, at several λ, Kinsey and Dumas fit lines between the confined performance from simulations at $\beta = 20\%$ and the corresponding performance at $\beta = 0\%$ estimated using the LMADT blockage correction of Barnsley and Wellicome [146]. Performance at other β was then obtained by linear interpolation or extrapolation. Although this method was able to accurately predict the power and thrust coefficients at $\beta = 10\%$, predictions were less accurate for $\beta \geq 50\%$ where the $C_T - \beta$ and $C_P - \beta$ relationships are expected to become less linear (Figure 5.4).

Here, a method for forecasting confined performance based on Houlsby *et al.*'s LMADT model and the Maskell-inspired bluff-body relationship between turbine performance and the bypass velocity is proposed. We expect that this approach is likely similar to that employed by Whelan *et al.* [9]. For the following discussion, the "array" subscript in $C_{P,\text{array}}$ and $C_{T,\text{array}}$ is dropped for brevity.

Consider a turbine in a channel (or an array of equally-spaced turbines spanning the channel width) with known performance at blockage ratio β_1 and Froude number Fr_h. At a

given operating condition (e.g., λ_1) the turbine's thrust coefficient is $C_{T,1}$ and bypass velocity is $u_{b,1}$. For the same turbine or array operating at a different blockage ratio, β_2, assume that there is a freestream velocity, $U_{\infty,2}$, which yields the same dimensional thrust on the turbine as at β_1 and $U_{\infty,1}$:

$$T_1 = T_2 \ . \tag{5.9}$$

Therefore,

$$C_{T,2} = C_{T,1}\left(\frac{U_{\infty,1}}{U_{\infty,2}}\right)^2 . \tag{5.10}$$

Since the thrust on the turbine scales with the bypass velocity in a Maskell-inspired approach, equal thrust at β_1 and β_2 requires equal bypass velocity:

$$u_{b,1} = u_{b,2} = u_b \ . \tag{5.11}$$

Therefore, $C_{T,2}$ can be calculated from Equation 5.10 if the value of $U_{\infty,2}$ that yields u_b at β_2 can be determined. In other words, $C_{T,1}$ and $C_{T,2}$ are connected through a shared value of ${C_T}^b$ when Maskell-inspired bluff-body scaling is applied:

$${C_T}^b = C_{T,1}\left(\frac{U_{\infty,1}}{u_b}\right)^2 = C_{T,2}\left(\frac{U_{\infty,2}}{u_b}\right)^2 . \tag{5.12}$$

Since rotor power also scales with the bypass velocity, $C_{P,2}$ is given as

$$C_{P,2} = C_{P,1}\left(\frac{U_{\infty,1}}{U_{\infty,2}}\right)^3 . \tag{5.13}$$

Finally, assuming constant rotation rate (i.e., $\omega_1 = \omega_2$):

$$\lambda_2 = \lambda_1\left(\frac{U_{\infty,1}}{U_{\infty,2}}\right) . \tag{5.14}$$

In Equations 5.10 and 5.13, it is implicitly assumed that $\rho_1 = \rho_2$ (and thus, $\nu_1 = \nu_2$), which implies a difference in the freestream Re_D (Equation 2.12) between β_1 and β_2. However, the Reynolds number based on the bypass velocity ($u_b D/\nu$) remains constant.

Using u_b as a bridge between β_1 and β_2, LMADT can be used to calculate $U_{\infty,2}$ from known quantities at β_1. The procedure for calculating $U_{\infty,2}$ using the LMADT model of Houlsby

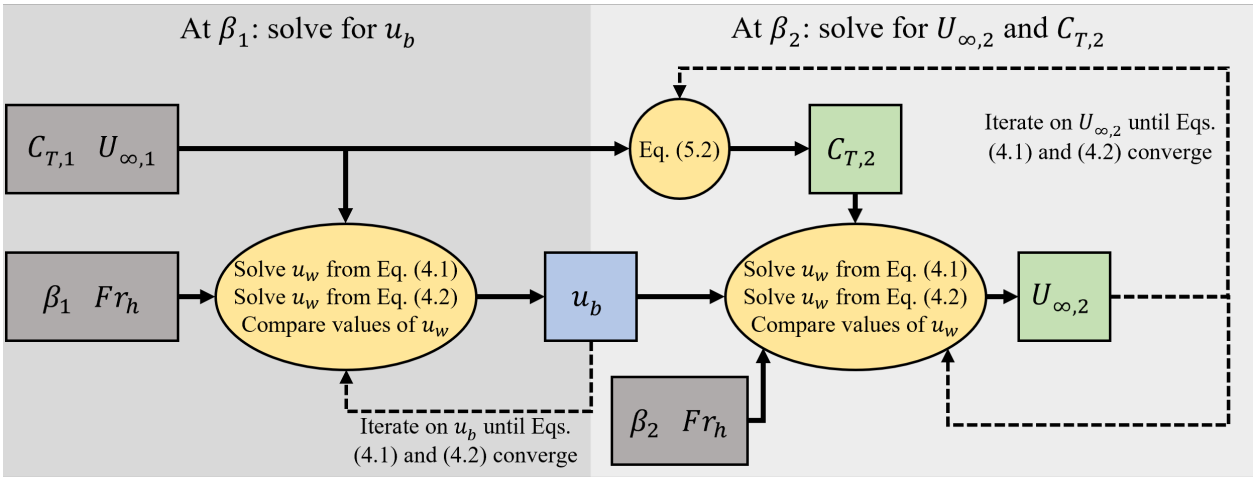

Figure 5.14: Flowchart describing the procedure for forecasting performance at β_2 based on performance at β_1. Gray boxes indicate known or specified inputs, yellow circles/ovals indicate equation solving, blue boxes indicate quantities associated with bluff-body scaling, and green boxes indicate the outputs at β_2. The dashed arrows indicate steps where iteration is required.

et al. [3] is outlined in Figure 5.14. First, u_b is determined at β_1 by solving Equations 5.2 and 5.3 iteratively as described in Section 5.4.1, using $C_{T,1}$, $U_{\infty,1}$, and Fr_h as inputs. Next, a reasonable value of $U_{\infty,2}$ is guessed, from which a corresponding guess for $C_{T,2}$ is calculated via Equation 5.10. Assuming constant Froude number between β_1 and β_2, Equations 5.2 and 5.3 are then solved separately for u_w at β_2 using u_b, Fr_h, and the guesses for $U_{\infty,2}$ and $C_{T,2}$. The resulting values of u_w are compared, and this process is repeated until the value of $U_{\infty,2}$ that minimizes the error between Equation 5.2 and Equation 5.3 is determined. With $U_{\infty,2}$ known, $C_{T,2}$, $C_{P,2}$ and λ_2 may be calculated from $C_{T,1}$, $C_{P,1}$, and λ_1 via Equations 5.10, 5.13 and 5.14. Note, however, that $C_{T,1}$ is the only performance metric at β_1 that influences the value of $U_{\infty,2}$.

In the limiting case of unconfined flow ($\beta_2 \to 0\%$), the flow bypassing the turbine is not accelerated and $U_{\infty,2} \to u_b$. Consequently, Equations 5.10, 5.13 and 5.14 revert to Equa-

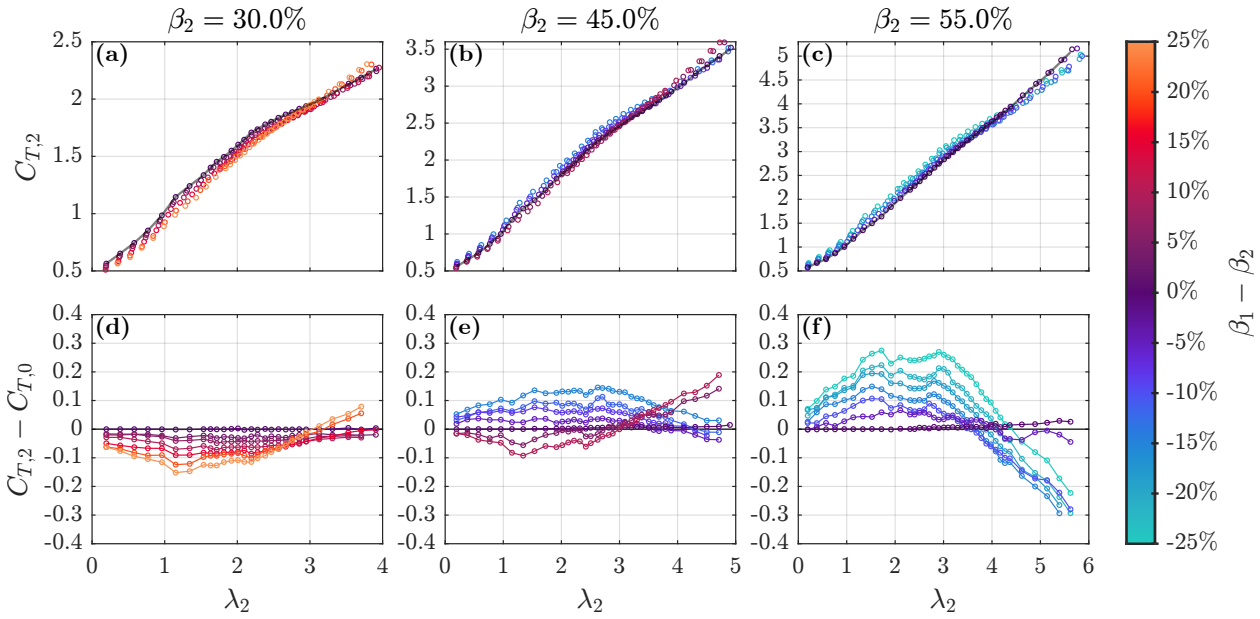

Figure 5.15: (a)-(c) Predicted thrust coefficient and (d)-(f) error between the predicted thrust coefficient and measured thrust coefficient ($C_{T,0}$, shown as the gray lines in (a)-(c)) for $\beta_2 = 30.0\%$, 45.0%, and 55.0%. Color indicates the difference between the nominal blockage ratio of the performance data that was used to make each prediction (β_1) and the target blockage ratio (β_2). Note the different axes limits for each β_2 in (a)-(c).

tions 5.5 to 5.7 corresponding to a Maskell-inspired bluff-body blockage correction (Figure 5.13a). Conversely, as $\beta_2 \to 100\%$, the solution space is constrained by the assumptions of equal bypass velocity and Fr_h between β_1 and β_2, such that physically meaningful subcritical solutions do not exist at all β_1 and $C_{T,1}$. The maximum value of β_2 at which a physical solution can be obtained depends on $C_{T,1}$, β_1, and Fr_h. However, for the performance data in this study, physically meaningful solutions exist for all practically-achievable blockages (i.e., $\beta_2 \leq 65\%$).

To quantify the effectiveness of this forecasting method, the experimental array performance at $\beta_1 = 30.0\% - 55.0\%$ (Figure 5.3) is used to predict array performance at various β_2

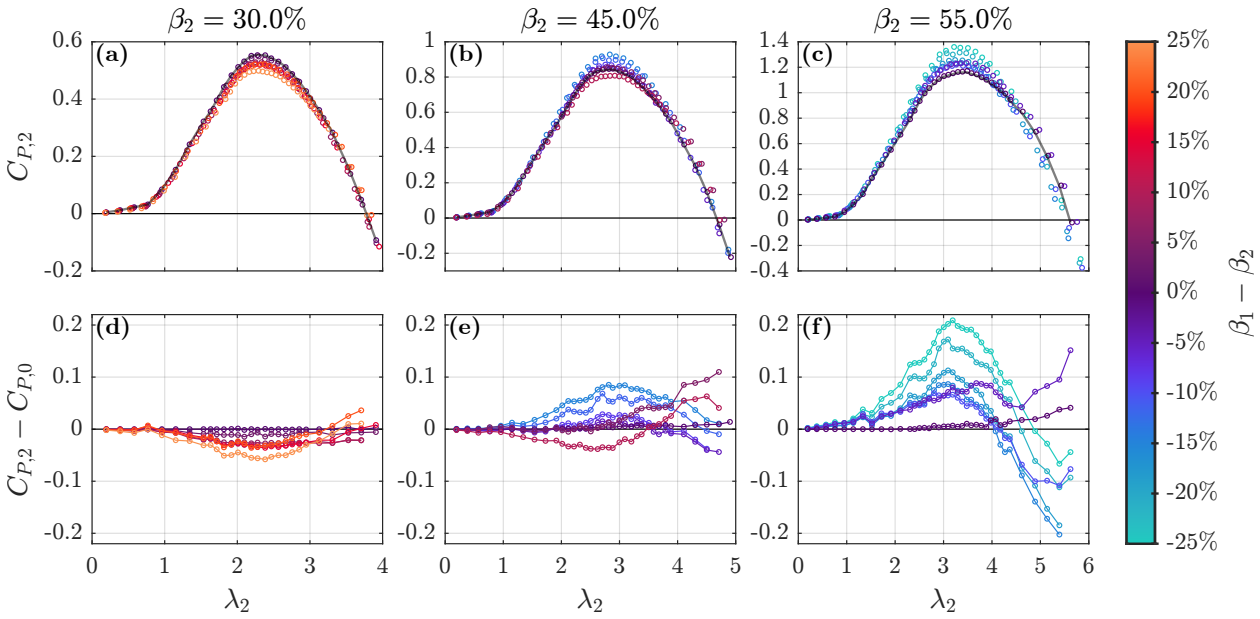

Figure 5.16: (a)-(c) Predicted efficiency and (d)-(f) error between the predicted efficiency and measured efficiency ($C_{P,0}$, shown as the gray lines in (a)-(c)) for $\beta_2 = 30.0\%$, 45.0%, and 55.0%. Color indicates the difference between the nominal blockage ratio of the performance data that was used to make each prediction (β_1) and the target blockage ratio (β_2). Note the different axes limits for each β_2 in (a)-(c).

within this range. The resulting $C_{T,2}$ and $C_{P,2}$ at each operating point are then compared to experimental data (denoted as $C_{T,0}$ and $C_{P,0}$) at each β_2. The predicted thrust coefficients at $\beta_2 = 30.0\%$, 45.0% and 55.0% and the corresponding difference between the predicted and measured thrust coefficients are given in Figure 5.15. The measured thrust coefficients are predicted within ~ 0.2 at $\beta_2 = 30.0\%$ and 45.0% (Figures 5.15d and 5.15e) and within ~ 0.3 at $\beta_2 = 55.0\%$ (Figure 5.15f). In general, the magnitude of the thrust prediction error increases with the difference between β_1 and β_2 (i.e., predictions further from the starting blockage are less accurate), and the absolute prediction error tends to grow as β_2 increases for the same difference between β_1 and β_2. In relative terms, these errors are appreciable

at lower λ_2 where C_T is relatively low, but decline for higher λ_2. Since the foundation of this forecasting method is Maskell-inspired bluff-body scaling (Equations 5.5 to 5.7), the differences in the predicted $C_{T,2}$ across β_1 are driven by differences in ${C_T}^b$ across β_1. Thus, the shapes and relative positions of the ${C_T}^b - \lambda^b$ curves across β_1 (Figure 5.13a) dictate the shapes and relative positions of the resulting $C_{T,2} - \lambda_2$ curves when scaled to β_2 (Figures 5.15a to 5.15c). For the current data set, at low to moderate tip-speed ratios this corresponds to underpredicted $C_{T,2}$ if $\beta_1 > \beta_2$ and overpredicted $C_{P,2}$ if $\beta_1 < \beta_2$, with these trends inverting at higher tip-speed ratios.

The corresponding predicted power coefficients and prediction error are shown in Figure 5.16. The measured power coefficients are predicted within ~ 0.05 at $\beta_2 = 30.0\%$ (Figure 5.16d), ~ 0.1 at 45.0% (Figure 5.16e), and ~ 0.2 at $\beta_2 = 55.0\%$ (Figure 5.16f). The greatest prediction error tends to occur near the performance peak and at tip-speed ratios well beyond the optimal operating point. However, the tip-speed ratio corresponding to maximum performance is well-predicted (Figures 5.16a to 5.16c). Since only the thrust influences the outcome of the bluff-body forecasting procedure, trends in the $C_{P,2} - \lambda_2$ curves with β_1 resemble those for the ${C_T}^b - \lambda^b$ curves.

The proposed forecasting method combines linear momentum theory and the bluff-body theory of Maskell to analytically predict confined turbine performance from experimental or simulation data. However, since this method utilizes u_b as a link between β_1 and β_2, the prediction accuracy depends on whether the bypass velocity is descriptive of array performance at both β_1 and β_2. Consequently, the effectiveness of this forecasting scheme outside of the tested range of β is unknown, and the method may be less accurate under conditions where array performance is not adequately described by a bluff-body model. A bluff-body model may be less representative of turbine performance at lower blockage, which may be why Ross and Polagye [90] found a Maskell-inspired blockage correction to be less accurate than the correction proposed by Barnsley and Wellicome [146]. It is recommended that future work explore the broader applicability of this forecasting method to other turbine geometries and flow conditions.

5.6 Conclusions

The objective of this work is to identify the potential of theoretical frameworks to describe the effects of confined flows on turbine performance at the upper end of what is practically achievable (i.e., blockage ratios ≤ 55 %). To this end, the performance and near-wake flow field of a two-turbine array were experimentally characterized over a wide range of operating conditions at array blockage ratios from 30.0% to 55.0%, and other non-dimensional flow parameters were maintained to isolate blockage effects. The observed array performance supports the general trends broadly observed in prior work while providing a uniquely high-resolution view of how performance changes with the blockage ratio within the high-confinement regime. This highlights relatively subtle trends, such as the linear behavior of both the power and thrust coefficients with blockage at constant λ for low-to-moderate β and λ. Similarly, the measured near-wake velocity fields quantitatively illustrate how the wake and bypass flows respond to changes in both blockage and tip-speed ratios. Critically, this work provides a set of experimental performance and flow field data for cross-flow turbines at high blockage, which will aid in the validation of numerical simulations and reduced-order models that seek to examine confinement effects and inform the design of full scale systems that can exploit these physics.

A key outcome of this work is that analytical linear momentum actuator disk models can be quantitatively descriptive of real turbine arrays in highly confined flows. It is shown that, at a location 0.6 turbine diameters downstream of the array, the velocity of the flow bypassing the array measured using PIV is well represented by the bypass velocity calculated using the measured array thrust coefficients as an input to the open-channel LMADT model of Houlsby *et al.* [3]. This result was observed for a wide range of blockages and tip-speed ratios, and the bypass velocity calculated from LMADT falls within $3\% - 8\%$ of the measured velocity between the turbines at the array centerline. Following Whelan *et al.* [9] and inspired by the bluff-body theory of Maskell [1], scaling the array power and thrust coefficients by this analytical bypass velocity collapses these coefficients across the tested blockage and tip-

speed ratios. These results highlight similar dynamics between high-blockage turbine arrays and bluff bodies, and demonstrate that, despite their inherent simplicity, LMADT models can effectively model aspects of the flow around non-ideal turbines and provide insights into the salient hydrodynamics that govern their performance in confined flows. Leveraging the connection between array performance and the bypass velocity, an analytical forecasting method based on LMADT is proposed by which known turbine performance at one confinement (β_1) can be used to predict turbine performance at a different confinement (β_2) with moderate accuracy. Although blockage corrections are frequently used to estimate unconfined performance (i.e., $\beta = 0\%$), the proposed forecasting method provides a pathway for estimating turbine performance under confined conditions based on the dominant dynamics of high-blockage arrays.

Although this work focuses on cross-flow turbines, the characteristic hydrodynamics of confinement highlighted here are not exclusive to this archetype, and the analytical models employed are agnostic to turbine geometry. However, the design of the rotor is expected to influence how these characteristic dynamics change with blockage and the tip-speed ratio [95]. Consequently, the effectiveness of Maskell-inspired bluff-body scaling and forecasting may depend on turbine geometry and operating condition. It is recommended that future work explore the broader application of these analytical methods to turbines at lower confinement, as well as to different turbine designs. Additionally, although this work focuses on the time-averaged array performance and near-wake flow fields, the unsteady fluid dynamics of cross-flow turbines also inform their performance and the properties of the near-wake. Future research should examine how the phase-resolved performance of cross-flow turbines scales with confinement, and how these dynamics influence the temporal and spatial evolution of the flow field in the near- and far-wake regions.

Chapter 6

INFLUENCE OF ROTOR GEOMETRY ON THE PERFORMANCE OF HIGH-BLOCKAGE CROSS-FLOW TURBINE ARRAYS

The work in this chapter is co-authored by Gregory Talpey, Gemma Calandra, and Brian Polagye. The author directed the turbine performance experiments and conducted all data analysis and visualization. Gregory Talpey and Gemma Calandra conducted all turbine performance experiments. The author led the drafting and editing of the manuscript, to which all co-authors contributed.

6.1 Motivation

Although the effects of confinement influence the performance of all turbine designs, CFD simulations of axial-flow turbines have shown that optimal rotor design depends on the blockage ratio. Schluntz and Willden [95] utilized a BEM model embedded in a Reynolds-averaged Navier-Stokes (RANS) CFD solver to optimize the blade geometry of an axial-flow turbine for $\beta = 0\%$ (i.e., unconfined flow) to 31.4%. The authors allowed the blade chord length and pitch to vary along the blade span, and primarily interpreted their results in the context of rotor solidity, a geometric parameter that represents the fraction of the turbine swept area that is occupied by the blades. Schluntz and Willden found that, as β increased, the optimal rotor solidity increased and the optimal blade pitch decreased. While the efficiency of all rotor geometries was shown to improve with increasing blockage ratio, at a given β the best performing rotor geometry was that which was optimized for that particular blockage ratio. Schluntz and Willden attributed these trends to the increased thrust on higher solidity rotors, which causes greater acceleration of the bypass flow and

a correspondingly larger pressure drop across the rotor. A similar trend was observed by Abutunis and Menta [100] in three-dimensional RANS simulations of three-bladed axial-flow turbines with various chord lengths and pitch angles at $\beta = 4.2\%$ to 62.5%. Abutunis and Menta observed that the efficiency of higher-solidity rotors (in this case, rotors with larger chord lengths) increased with β at a faster rate than for rotors with lower solidity, and that this trend became more pronounced as the tip-speed ratio increased.

How the optimal rotor geometry of a cross-flow turbine changes with blockage has seen limited investigation, but numerical simulations suggest that, as for axial-flow turbines, confinement increases the optimal rotor solidity. Goude and Ågren [93] simulated a cross-flow turbine at $\beta = 0 - 50\%$ using a two-dimensional vortex method, and varied the turbine solidity via the chord length. The authors found that, at constant β, efficiency increased as solidity increased, and incremental changes in solidity yielded larger increases in efficiency at higher β. Kinsey and Dumas [11] simulated both one-bladed and three-bladed cross-flow turbines at $\beta = 0\%$, 26%, and $\approx 50\%$ using three-dimensional unsteady RANS, and found that the power and thrust coefficients of the three-bladed rotor increased more rapidly with blockage than those of the single-bladed rotor. However, the scope of these results is narrow for several reasons. First, the simulations by Goude and Ågren [93] and Kinsey and Dumas [11] were not compared to experimental data at similar blockage ratios, such that the numerical results are only partially validated. This is a consequence of scarce experimental performance data for cross-flow turbines at higher blockage ratios (e.g., $\beta = 30\% - 60\%$) as discussed in Section 5.1. Second, the combined effects of c/R, N, α_p, and blockage on cross-flow turbine performance have not been systematically explored, and no prior studies have examined how blockage affects the optimal preset pitch angle. Some studies have varied individual geometric parameters at a constant, relatively high value of blockage. For example, prior experimental work has explored independent variation of N and α_p for cross-flow turbines at $\beta = 49\%$ [103, 104] and $\beta = 75\%$ [68, 69]. However, because these studies were performed at a single blockage, they cannot provide insight into how the optimal rotor geometry changes as blockage varies. In addition, differences in experimental approaches

preclude a comprehensive synthesis across prior work. Finally, prior work has often framed geometric trends in terms of rotor solidity, which is a function of two parameters (c/R and N) which have distinct hydrodynamic effects [114]. Consequently, an experimental study that examines how the individual and combined effects of c/R, N, and α_p evolve across a range of blockages—and provides an extensive dataset for the validation of simulations and reduced-order models—is warranted.

In this chapter, how the optimal cross-flow turbine rotor geometry is influenced by confinement is explored through parametric variation of c/R, N, α_p, and β for a two-rotor cross-flow turbine array. Array performance is characterized for various geometric configurations at $\beta = 35 - 55\%$, which represent the upper end of blockage ratios that are practically achievable in a tidal or river channel. Section 6.2 describes the experimental methods employed, which are similar to those in Chapters 4 and 5. Section 6.3 presents the performance trends measured across the tested parameter space and compares them to those observed in prior work at lower blockage. In Section 6.4, the hydrodynamic implications of these results are discussed, and the concept of dynamic solidity originally introduced by Araya *et al.* [19] is used to interpret geometric trends at high blockage. Additionally, the effectiveness of a Maskell-inspired bluff-body model for describing how the performance of each geometry scales with blockage is evaluated. The study concludes with a summary of key results and their implications for high-blockage turbine design in Section 6.5.

6.2 Methods

6.2.1 Geometric Parameters

The geometric parameter space explored in this work is similar to that in Chapter 4 and comprises three nominal chord-to-radius ratios (c/R = 0.37, 0.49, and 0.62), three blade counts (N = 1, 2, 3) and seven preset pitch angles ($\alpha_p = 0°$, $-2°$, $-4°$, $-6°$, $-8°$, $-10°$, and $-12°$). Turbine dimensions and the corresponding geometric parameters are summarized in Table 6.1, and a subset of geometric configurations are shown in Figure 6.1. At each c/R, five

Table 6.1: Geometric parameters of the tested turbines.

Geometric Parameter	**Value**
R^*[cm]	15.01 (14.73 - 15.08)
R'^*[cm]	15.75 (15.31 - 16.16)
c [cm]	5.57, 7.42, 9.28
c/R	0.37, 0.49, 0.62
α_p [°]	0, -2, -4, -6, -8, -10, -12
N	1, 2, 3

* Due to the blade mounting scheme used, R varies slightly with α_p for each geometry, whereas R' varies with both c/R and α_p. The average values of R and R' over all tested geometric configurations are listed here, and the ranges of R and R' across the tested parameter space are given in parentheses. actual values of R, R', and derived quantities for each combination of c and α_p are provided in Appendix B.

values of α_p are tested so as to both resolve the optimal preset pitch angle and characterize turbine performance at non-optimal pitch. Relative to Chapter 4, a narrower range of c/R are explored, but more α_p are considered at each c/R. In total, 45 unique combinations of c/R, N, and α_p are considered, with both turbines in the array sharing the same geometry in a given experiment. The blade span ($H = 21.5$ cm) and foil profile (NACA 0018) are the same for all geometric configurations.

All turbine blades are machined from 7075-T6 aluminum, anodized, and painted with an ultra-flat black spray paint. The final treatment is to prevent reflections during particle image velocimetry measurements in related work. As in Chapter 4, the turbine blades are connected to the central driveshaft via circular end plates, which allows for different numbers

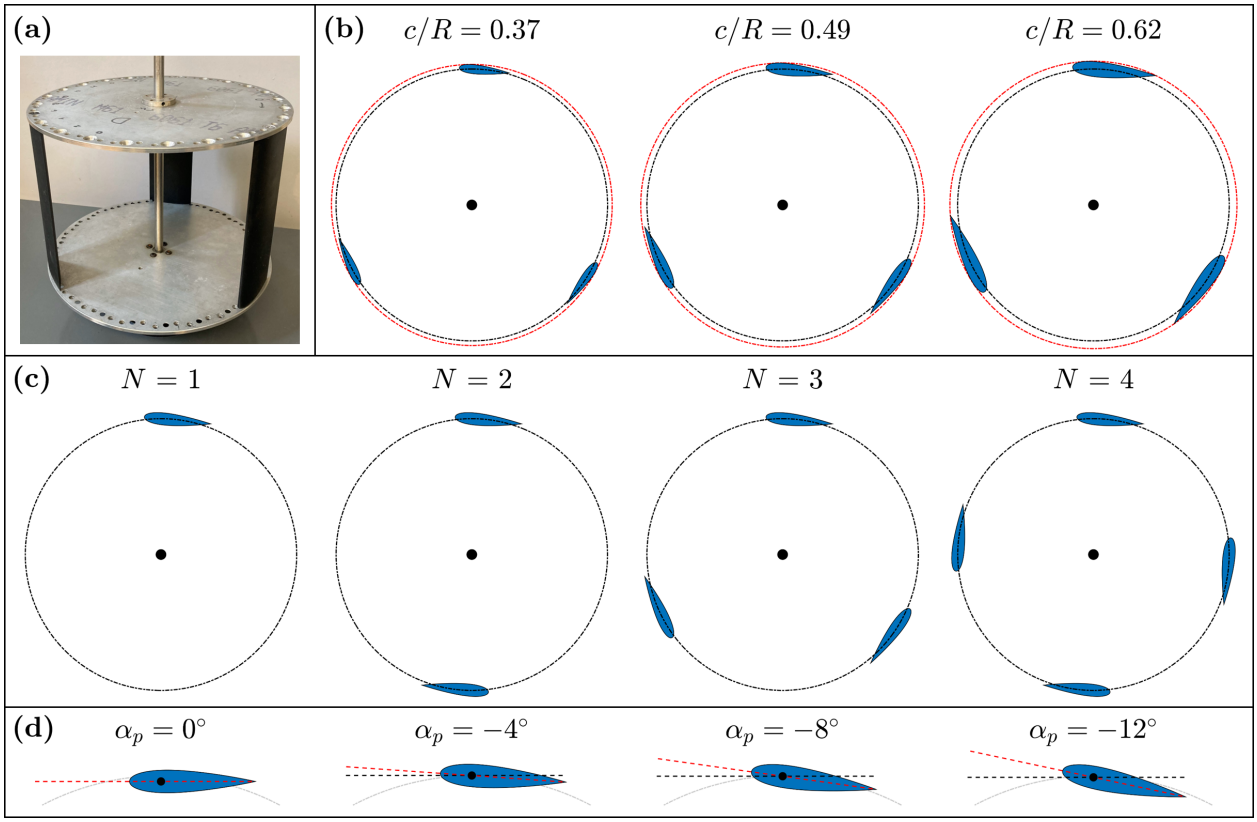

Figure 6.1: Partial visualization of experimental parameter space. (a) Image of an assembled rotor with $N = 3$, $c/R = 0.49$, and $\alpha_p = -6°$. (b) Variation in c/R for $N = 3$ and $\alpha_p = -6°$, with the quarter-chord radius R shown in black and the resulting outermost swept radius R' shown in red. (c) Variation in N for $c/R = 0.49$ and $\alpha_p = -6°$. (d) Variation in α_p for $c/R = 0.49$ with the chord lines indicated in red and tangent lines indicated in black.

of equally-spaced blades to be mounted at various preset pitch angles. To economically explore the parameter space, the same sets of end plates are used for all blades. However, for the smallest chord length ($c = 5.57$ cm) to be compatible with the same mounting hardware used for the larger chord lengths, the chord near the blade ends is gradually increased to accommodate the mounting hardware, while the middle 91% of the blade span retained the

Table 6.2: Measured experimental parameters (median value ± one standard deviation) across all experiments at each target blockage ratio.

Blockage Ratio	Non-Dimensional Flow Parameters			Flume Conditions			
β [%]	Re_D [$\times 10^5$]	Fr_h	s/h	h [m]	U_∞ [m/s]	s [m]	T [°C]
35.0 ± 0.5	1.59 ± 0.02	0.215 ± 0.001	0.472 ± 0.001	0.508 ± 0.001	0.482 ± 0.003	0.240 ± 0.001	24.3 ± 0.1
44.9 ± 0.6	1.57 ± 0.02	0.212 ± 0.003	0.324 ± 0.002	0.397 ± 0.001	0.419 ± 0.005	0.129 ± 0.001	30.1 ± 0.1
55.0 ± 0.8	1.59 ± 0.01	0.214 ± 0.002	0.172 ± 0.004	0.324 ± 0.002	0.383 ± 0.003	0.056 ± 0.002	35.0 ± 0.1

target chord length. Additionally, as in Chapter 4, the radius of the outermost circle swept by the blades (R', given by the red circles in Figure 6.1b) varies for each combination of c/R and α_p. Over the tested range of c/R and α_p, the R' of an individual configuration deviates by $< 3\%$ from the average R' given in Table 6.1. Similarly, the quarter-chord radius (R) varies slightly with α_p (e.g., $< 2\%$ deviation from average value in Table 6.1) to maintain constant R' at $c/R = 0.49$. The values of R, R', and derived quantities for all tested geometries are tabulated in Appendix B. As in Chapters 4 and 5, R is used for evaluating all kinematic quantities (e.g., λ, c/R) and R' is used to calculate the turbine projected area for the blockage and non-dimensional performance metrics.

6.2.2 Experimental Set-Up and Test Conditions

The test facility, laboratory array test setup, and experimental approach for varying the blockage ratio are identical to that used in Chapter 5. Each geometric configuration is tested at blockage ratios of $\beta = 35\%$, 45%, and 55%, resulting in 135 unique experiments. The measured values of β, Re_D, Fr_h, s/h, and corresponding flume conditions at each target β are given in Table 6.2. The value of Re_D in this study ($\approx 1.6 \times 10^5$) facilitates comparison to the work in Chapter 4 at $\beta \approx 11\%$ with a single turbine at the same Re_D. Although the Fr_h in this study (≈ 0.21) is roughly half of the Fr_h at the same Re_D in Chapter 4 (0.41), this does not preclude comparison of general trends between these studies. The effects of

β on performance are expected to outweigh those of Fr_h [102], and although the influence of Fr_h on turbine performance is expected to increase with the blockage ratio [79], the lower Fr_h used here relative to the work in Chapter 4 may serve to limit this effect. As in Chapter 5, s/h is allowed to vary with the blockage ratio to minimize the risk of ventilation. Small differences in D and D' across geometries (Section 6.2.1) contribute to variations in β and Re_D across the parameter space. Across all experiments, the turbulence intensity was $< 2.2\%$.

6.2.3 Turbine performance metrics

Array performance for each geometric configuraition is characterized over a range of tip-speed ratios at each β. Data are collected at each tip-speed ratio for 45 seconds, and the time series is cropped to an integer number of turbine rotations before performance metrics are calculated.

Array-average performance metrics are calculated by averaging the performance metrics of the individual turbines as described in Section 3.5. However, as in Chapter 4, the parasitic torques on the disk end plates are significant and complicate direct comparisons between turbine geometries on the basis of C_P. Specifically, geometric configurations that perform best at high λ are penalized more steeply by parasitic torque on the end plates, and this choice of support structure could influence the trends observed. Therefore, as in Chapter 4, to account for this a blade-level efficiency for each turbine is estimated via superposition following Bachant *et al.* [48] and Strom *et al.* [30] as

$$C_{P,\text{blades}}(\beta,\lambda) \approx C_{P,\text{turbine}}(\beta,\lambda) - C_{P,\text{supports}}(\beta,\lambda)\ . \tag{6.1}$$

$C_{P,\text{array}}$ is then calculated as the average of $C_{P,\text{blades}}$ between Turbine A and Turbine B. The limitations of this approach—which assumes that secondary interactions between the blades and supports are negligible—for rotors at high blockage are discussed in Appendix E. To summarize, the presence of appreciable secondary interactions in these experiments means that the reported maximum efficiency at the lowest blockage ratio is likely somewhat under-

estimated, thereby inflating the apparent change in performance between $\beta = 35\%$ and 45%. Since the thrust on the support structures is small relative to that on the blades at high blockage (Appendix E), turbine-level C_T is approximately equal to the blade-level C_T. Since C_L is not as strongly influenced by blockage as C_P and C_T, discussion of the lateral force coefficients is deferred to Appendix C.

6.2.4 Array Performance and Data Synthesis

Results are aggregated and presented as contour maps of turbine performance metrics (e.g., maximum $C_{P,\text{array}}$) as a function of c/R, α_p, N, and β in a manner similar to that employed in Chapter 4. Figure 6.2 graphically outlines the contour map generation process for maximum $C_{P,\text{array}}$ at one β and N from the collected data. For a given combination of c/R and α_p, array performance is characterized under coordinated constant speed control (Section 3.3) at a specified λ, at which the instantaneous performance of each turbine is measured (Figures 6.2a and 6.2b). The time-average blade-level efficiency for each turbine at this λ is represented as a point on the respective characteristic performance curve (Figures 6.2c and 6.2d), and this process is repeated at other λ to obtain representative performance curves for both turbines. The average of these performance curves is the array-average performance curve (Figure 6.2e). The operating condition associated with the maximum $C_{P,\text{array}}$ for this geometry is designated as λ_{opt}, and this maximum performance is represented as a single point on a map of c/R versus α_p for one $\beta{-}N$ combination (Figure 6.2f). This process is repeated for each $c/R{-}\alpha_p$ combination tested at that $\beta{-}N$ combination, and linear interpolation is used to visualize the $C_{P,\text{array}}$ contours across all combinations of c/R and α_p within the convex hull spanned by the tested configurations. In Section 6.3, $C_{P,\text{array}}$ contours at each $\beta - N$ combination are tessellated to visualize the entire parameter space. Similar techniques are used to visualize λ_{opt} and $C_{T,\text{array}}$ associated with maximum $C_{P,\text{array}}$.

As shown by the uncertainty analysis in Appendix A, cycle-to-cycle variations in turbine performance (i.e., the shaded regions in Figures 6.2c to 6.2e) are driven primarily by periodic fluctuations in the measured inflow velocity rather than uncertainty in load cell measure-

ments. Across all experiments, the median standard deviation of the cycle-average values of $C_{P,\text{array}}$ at λ_{opt} is 0.023 ($\approx$ 3.2% of the corresponding average value of $C_{P,\text{array}}$ over all cycles), and the median standard deviation in the cycle-average values of $C_{T,\text{array}}$ at λ_{opt} is 0.035 ($\approx$ 1.3% of the corresponding average value of $C_{T,\text{array}}$ over all cycles). While cycle-to-cycle variation increases with λ in all experiments, it is not significantly correlated with β or rotor geometry.

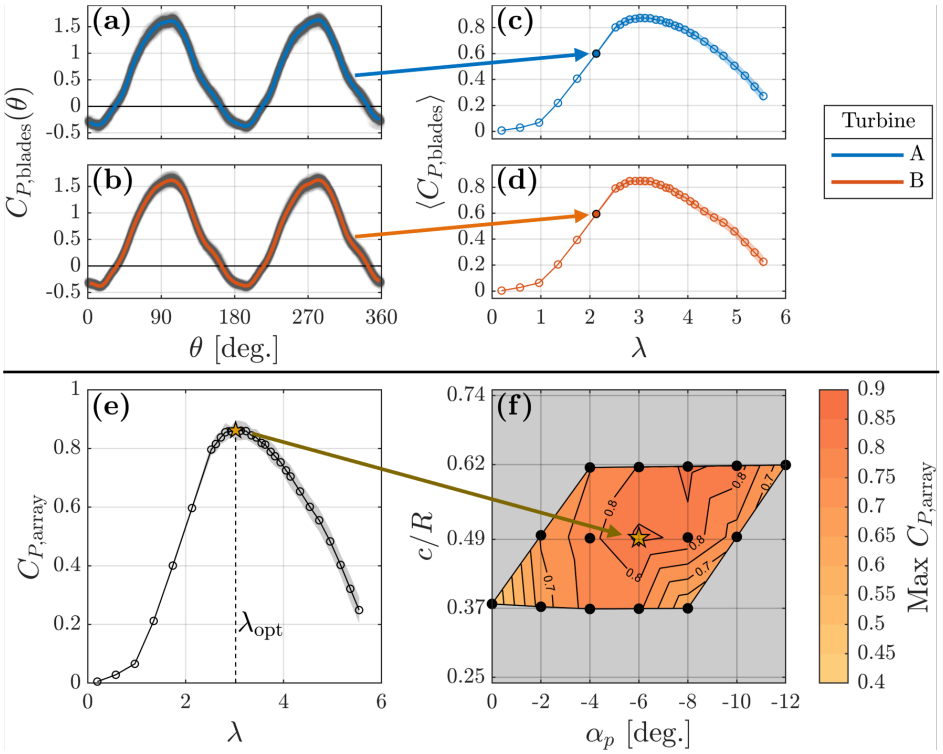

Figure 6.2: Construction of performance contours from the instantaneous blade-level efficiency for each geometric configuration as a function of c/R and α_p at $\beta = 45\%$ and $N = 2$. (a)–(b) Instantaneous blade-level performance for each turbine during a rotational cycle at a given λ. The blue and orange curves indicate the median cycles for each turbine, whereas the gray region indicates the spread in the instantaneous values. (c)–(d) The resulting time-average blade-level efficiency as a function of λ each turbine. The shaded regions (which are approximately the same width as the marker size) indicate ± 1 standard deviation in the cycle-averaged values measured at each λ. (e) The array-average blade-level efficiency (obtained as the average of the performance curves in (c)–(d)), with the maximum performance and corresponding λ annotated, and ± 1 standard deviation in the array-averaged cycle-averages at each λ indicated by the shaded region. (f) Placement of the maximum performance point for this $c/R - \alpha_p$ combination on a contour map for all geometric configurations at $\beta = 45\%$ and $N = 2$.

6.3 Results

This section presents the key trends observed across the tested parameter space, with an emphasis on the performance and thrust coefficients at the maximum efficiency point for each geometric configuration and blockage. Hydrodynamic interpretation of these trends is provided in Section 6.4.

Prior to presenting aggregate results, it is instructive to highlight the general effects of blockage on the characteristic array power and thrust curves, which are shown for two representative cases in Figure 6.3. As the blockage ratio increases, the maximum array efficiency increases, λ_{opt} increases, and the array produces power over a wider range of tip-speed ratios (Figure 6.3a). Consistent with greater power extraction, the array also experiences higher thrust as β increases (Figure 6.3b). Additionally, $C_{P,\text{array}}$ and $C_{T,\text{array}}$ are nearly invariant with β up to a threshold value of λ, which is consistent with observations in Chapter 5 and in prior studies [92, 94, 98].

Although the same general effects of blockage are observed for all rotor geometries, the geometric configuration of the rotor influences the exact manner in how these trends manifest. As shown in Figure 6.3, the rotor geometry can change the rates at which $C_{P,\text{array}}$, $C_{T,\text{array}}$, and λ_{opt} increase with the blockage ratio, as well as the threshold value of λ below which power and thrust are invariant with β. To contextualize the effects of c/R, N, and α_p on array efficiency across the tested β, contours of maximum $C_{P,\text{array}}$ across the entire parameter space are visualized in Figure 6.4. Although β (i.e, moving between rows Figure 6.4) has the strongest overall effect, each geometric parameter influences $C_{P,\text{array}}$ (i.e., there are no vertical or horizontal contours). Trends between c/R, α_p, and $C_{P,\text{array}}$ largely follow those observed in Chapter 4. For example, the optimal preset pitch angle tends to become more negative (i.e., more toe-out) as the chord-to-radius ratio increases. This relationship between c/R and the optimal α_p is highlighted at each β and N in Figure 6.5. Remarkably, this trend is largely invariant with β, and is consistent with similar trends by observed at a single blockage ratio in Chapter 4 ($c/R = 0.25 - 0.74$; $\beta \approx 11\%$) and by Takamatsu *et al.* [27] ($c/R = 0.20 - 0.30$;

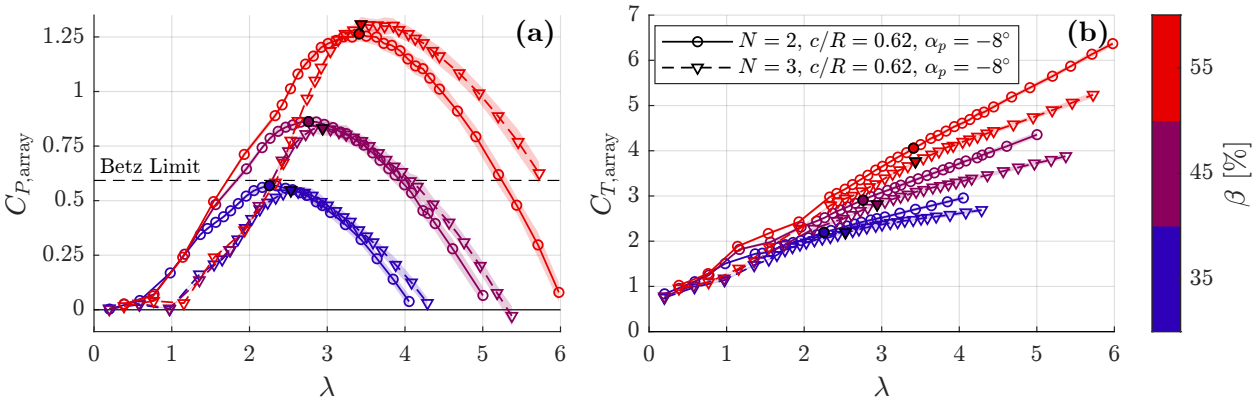

Figure 6.3: Time-average (a) $C_{P,\text{array}}$ and (b) $C_{T,\text{array}}$ as a function of λ for a few representative geometries. Data corresponding to maximum efficiency point are indicated by the filled markers. The shaded regions (which are approximately the same width as the plotted lines at lower λ) indicate ± 1 standard deviation in the cycle-average values.

$\beta = 75\%$). Additionally, as c/R increases, maximum efficiency at optimal preset pitch generally increases at all tested β, which is similar to the trend observed in Chapter 4 at $\beta \approx 11\%$ and the same Re_D. Although there are several cases where $c/R = 0.49$ yields comparable or slightly higher maximum $C_{P,\text{array}}$ than $c/R = 0.62$, this could be a byproduct of the 2° resolution in α_p employed and not an indication of a global maximum for optimal c/R.

Of the geometric parameters considered, the blade count has the strongest effect on maximum array efficiency. For a given $c/R - \alpha_p$ combination at $\beta = 35\%$, maximum $C_{P,\text{array}}$ tends to increase slightly from $N = 1$ to $N = 2$, but does not change significantly from $N = 2$ to $N = 3$. However, at $\beta = 45\%$, $C_{P,\text{array}}$ clearly increases with each blade added, and this effect is even more pronounced at $\beta = 55\%$. These results are in agreement with the numerical results of Kinsey and Dumas [11] ($N = 1$ and $N = 3$; $\beta = 0 - 50\%$), and represent a notable reversal of the inverse relationship between blade count and maximum efficiency consistently observed at lower blockage ratios [18–20, 114]. Figures 6.6a to 6.6c highlight the

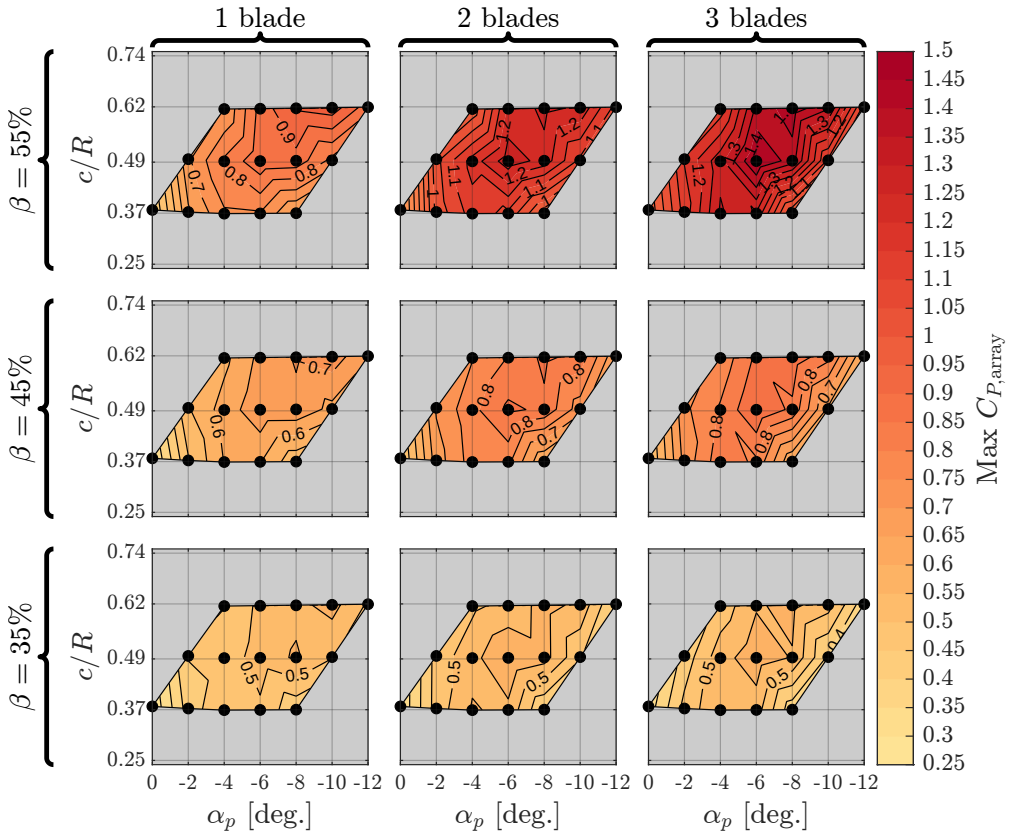

Figure 6.4: Contours of the maximum time-average array efficiency as a function of c/R and α_p for each combination of β and N tested.

increasing influence of N on $C_{P,\text{array}}$ as β increases for three representative geometries with different c/R at optimal α_p. At all β, the largest change in maximum efficiency occurs when N increases from 1 to 2, with the subsequent addition of blades yielding smaller incremental changes in maximum efficiency. Additionally, the optimal preset pitch is slightly influenced by the blade count, in that single-bladed turbines consistently have more negative optimal α_p relative to that of two- and three-bladed turbines (Figure 6.5).

A similar interaction between N and β is observed for the array thrust coefficient at the optimal tip-speed ratio (i.e,. $C_{T,\text{array}}|_{\lambda_{\text{opt}}}$), the contours of which are shown in Figure 6.7. For a given c/R and α_p, the array thrust coefficient at λ_{opt} increases as the number of

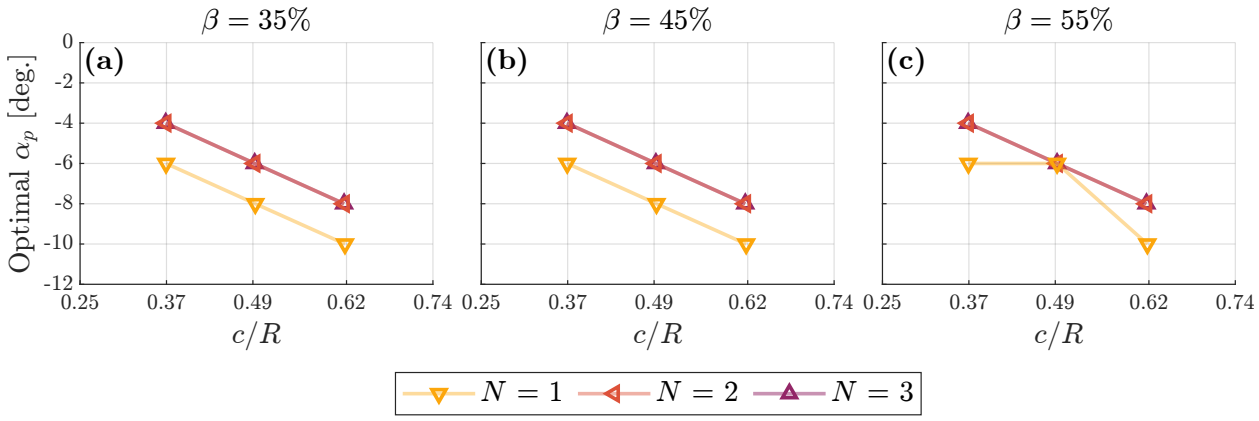

Figure 6.5: Optimal preset pitch angle as a function of c/R and N at each β.

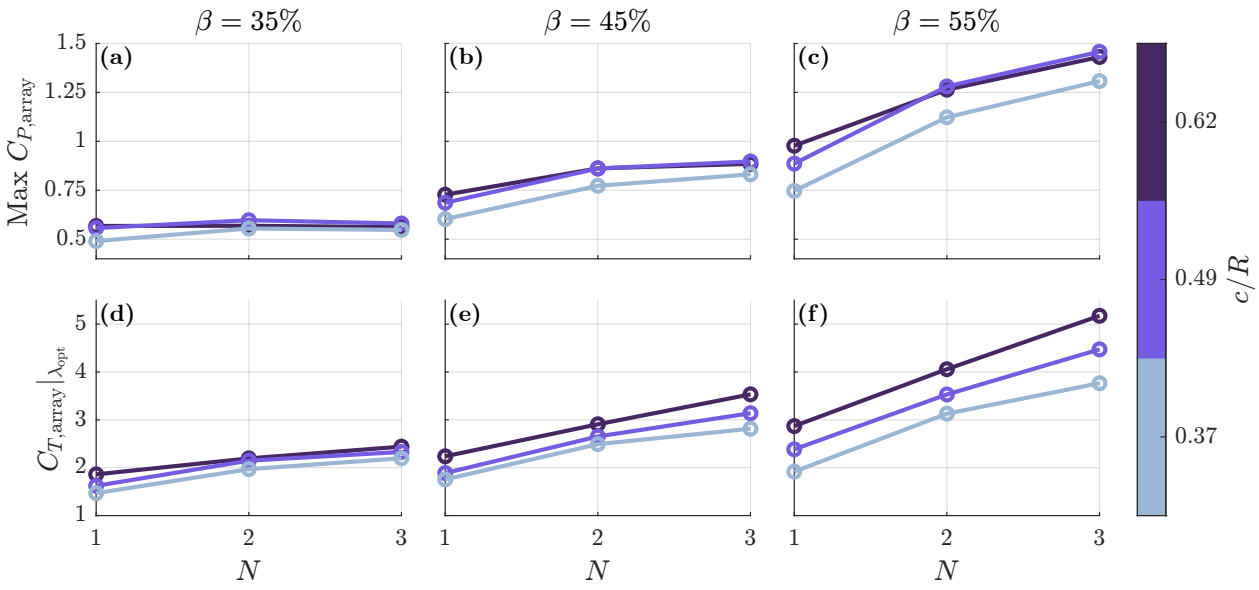

Figure 6.6: (a)–(c) maximum $C_{P,\text{array}}$ and (d)–(f) $C_{T,\text{array}}$ at maximum efficiency various c/R and optimal α_p. Note that the y-axis limits are substantially wider for thrust than efficiency.

blades increases, and this effect is amplified as the blockage ratio increases. The influence of N on $C_{T,\text{array}}|_{\lambda_{\text{opt}}}$ at each blockage ratio is shown for three representative geometries in Figures 6.6d to 6.6f. Relative to maximum $C_{P,\text{array}}$, array thrust is more dependent on the

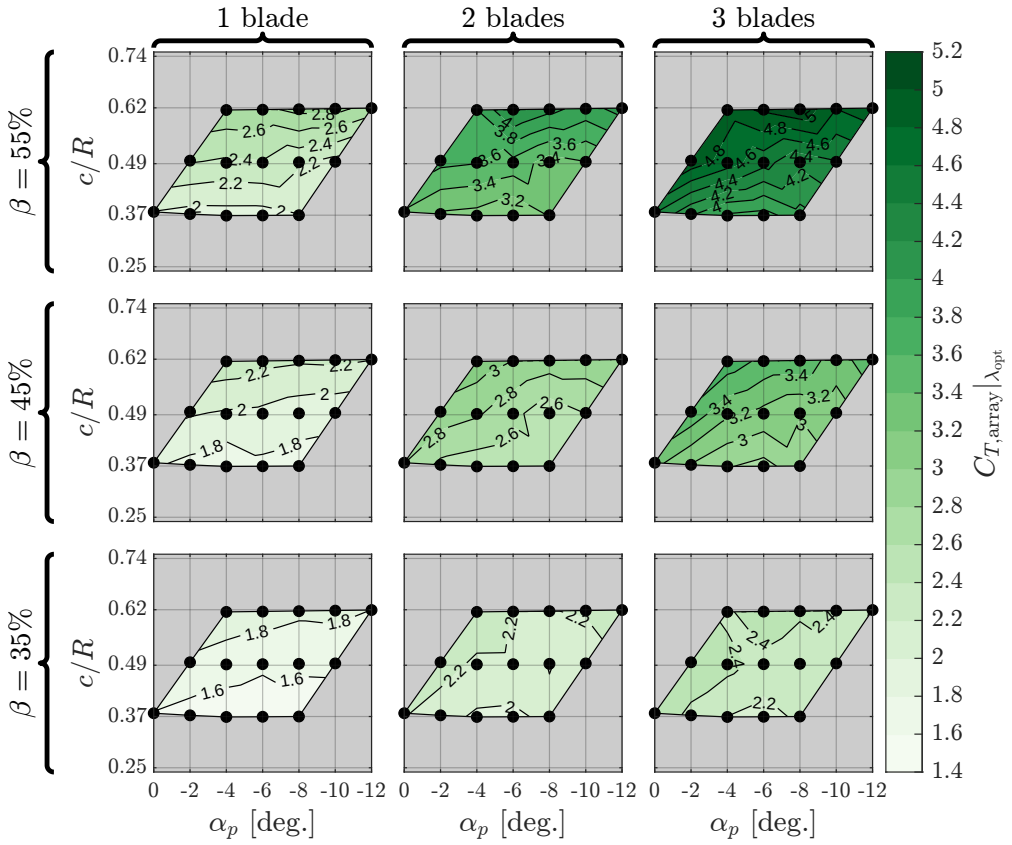

Figure 6.7: Contours of the time-average array thrust coefficient at maximum array performance as a function of c/R and α_p at each β and N tested.

blade count. In a similar manner, larger c/R tends to yield larger $C_{T,\text{array}}|_{\lambda_{\text{opt}}}$, and this effect is also augmented as β increases. Of the tested parameters, α_p has the least influence on $C_{T,\text{array}}|_{\lambda_{\text{opt}}}$, with array thrust slightly increasing for α_p less negative than optimal and decreasing for α_p more negative than optimal.

Since increases in both the number of blades and the chord-to-radius ratio yield increases in array power and thrust at λ_{opt}, their net effects might be well-represented by solidity, which combines these two geometric parameters (Equation 2.9). To evaluate the descriptiveness of solidity for these results, $C_{T,\text{array}}|_{\lambda_{\text{opt}}}$, $C_{P,\text{array}}$, and the λ_{opt} are regressed against solidity for each geometric configuration at each β in Figure 6.8. A strong correlation between σ

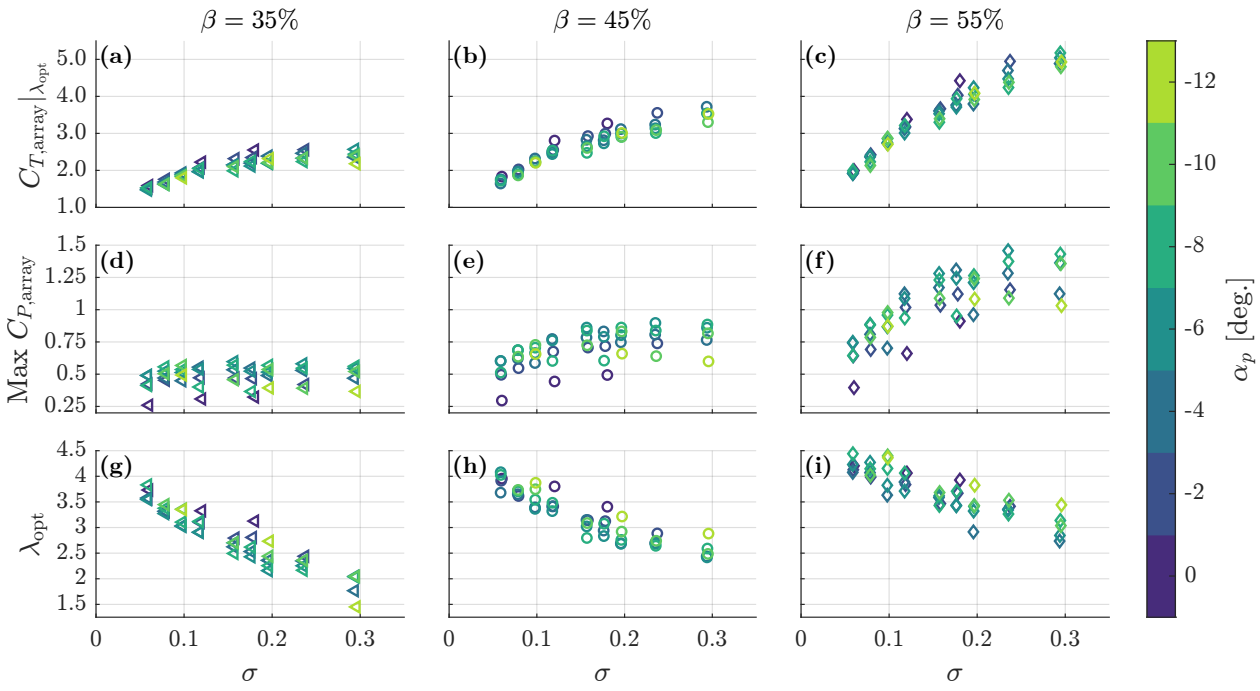

Figure 6.8: (a)–(c) $C_{T,\text{array}}$ at max efficiency, (d)–(f) maximum $C_{P,\text{array}}$, and (g)–(i) optimal tip-speed ratio as a function of solidity at each blockage.

and the thrust coefficient at λ_{opt} is observed at each blockage ratio (Figures 6.8a to 6.8c), indicating that arrays with similar solidity have similar thrust coefficients at λ_{opt}, regardless of the particular N and c/R. Since the way that confinement affects the flow through and around the turbine is a function of both the channel blockage ratio and the thrust coefficient [8, 10], this implies that the flow fields in the vicinity of rotors with similar solidities are similarly affected by blockage at λ_{opt}. Relative to solidity and the blockage ratio, α_p has only a limited influence on $C_{T,\text{array}}|_{\lambda_{\text{opt}}}$ at a given σ.

In contrast, solidity is less descriptive of trends in maximum efficiency. At $\beta = 35\%$ (Figure 6.8d), maximum $C_{P,\text{array}}$ is relatively insensitive to solidity. However, as β increases (Figures 6.8e and 6.8f), maximum $C_{P,\text{array}}$ is more greatly affected by solidity, with preset pitch continuing to exert a significant influence. In agreement with prior numerical studies

of cross-flow and axial-flow turbines [93, 95, 100] as β increases, the highest efficiencies are generally obtained with higher solidity. However, higher maximum efficiency from higher σ is not guaranteed due to the effects of preset pitch angle, especially since the optimal α_p is primarily influenced by one component of solidity (c/R) while the other (N) has only a minor effect (Figure 6.5). In other words, even at high blockage, a high solidity turbine with off-optimal preset pitch can still be outperformed by a lower solidity turbine at optimal α_p. Consequently, relative to $C_{T,\text{array}}|_{\lambda_{\text{opt}}}$, maximum $C_{P,\text{array}}$ is more sensitive to the particular configuration of c/R, N, and α_p. Nonetheless, at a high level, solidity is qualitatively descriptive of the relationship between rotor geometry and array performance in high-blockage flows.

Additionally, solidity is quantitatively descriptive of the optimal tip-speed ratio (Figures 6.8g to 6.8i). In a manner similar to that observed in prior low-blockage work by Rezaeiha *et al.* [2] and in Chapter 4, λ_{opt} decreases with σ across the tested blockages. Compared to the results in Chapter 4 (Figure 4.17), there is somewhat greater spread in λ_{opt} at each σ, likely due to the broader range of α_p tested at each c/R and a corresponding shift in λ_{opt} at off-optimal preset pitch. While Figure 6.8 focuses solely on the relationship between array performance and solidity at λ_{opt}, extension of the observed trends to other operating conditions is explored in Section 6.4.5.

6.4 Discussion

6.4.1 Connection Between the Reynolds Number and Blockage

Before discussing the hydrodynamic implications of the results presented in Section 6.3, it is important to acknowledge the interplay between blockage effects and the Reynolds number. Although the Reynolds number with respect to the rotor diameter and freestream velocity (Re_D; Equation 2.12) is held constant, the lift and drag forces on the turbine blades depend on Reynolds number local to the blade (Re_c; Equation 2.11). In confined flow, the presence of channel boundaries, combined with thrust on the rotors, accelerates flow through the

array relative to unconfined conditions [8, 10]. For a given geometry and tip-speed ratio, this confinement-driven acceleration of the near-blade inflow velocity increases U_{rel}, and thus Re_c. Consequently, as noted by Ross and Polagye [102], for a given rotor geometry and rotation rate, an increase in blockage effects—whether via the blockage ratio, the thrust coefficient, or both—is inextricably linked to an increase in Re_c. This is not to say that an increase in blockage is equivalent to an increase in Re_c at constant blockage. Rather, blockage-driven flow acceleration influences the blade boundary layer, particularly for experiments such as these that are conducted in a transitional Reynolds number regime. Therefore, blockage would have less effect on performance in a Reynolds-independent regime.

The geometric parameters considered in this study are also expected to influence Re_c through various—and often competing—mechanisms. For example, increasing c/R increases Re_c via the length scale c. Through solidity, c/R and N are expected to increase induction [2, 114] (which reduces U_{rel}), but increase thrust (Figure 6.8) and thus acceleration of flow through the rotors (which increases U_{rel}). Since a measurement of U_{rel} is not available, Re_c is indeterminate and non-constant across the tested parameter space.

6.4.2 Effects of Blade Count

The number of blades changes the resistance the turbines apply to the flow, and thus the confinement effects experienced for a given β and λ. As N increases, the rotor solidity increases and the rotors experience greater thrust (Figure 6.7 and Figures 6.8a to 6.8c), corresponding to a larger pressure drop across the turbines in the array. In response to this thrust and constriction from the channel boundaries, linear momentum theory suggests that the flow must accelerate through and around the array to maintain a constant mass flow rate through the channel [8, 10]. Consequently, following Schluntz and Willden [95], we hypothesize that the interplay between this pressure drop and the accelerated flow through the rotor allows rotors with more blades to generate more power (Figure 4.6). This benefit is not present in unconfined and low-blockage flows [2, 18–20, 114], where the increased resistance to the flow by additional blades acts primarily to divert flow around the rotor,

thus decreasing the maximum efficiency. Both linear momentum theory and Figures 6.8a to 6.8c) imply a direct connection between the pressure drop and $C_{T,\text{array}}$. However, the manner in which the pressure drop influences $C_{P,\text{array}}$ is expected to depend on geometry of the blades and the associated near-blade hydrodynamics (e.g., Figures 6.8d to 6.8f), which are not accounted for in linear momentum theory.

For the range of N considered in these experiments, the maximum array efficiency is observed to continually increase with blade count. However, as $N \to \infty$, more flow will be diverted around the array rather than accelerated through the rotors, causing $C_{P,\text{array}}$ to reduce and $C_{T,\text{array}}$ to tend toward a steady-state value at a given λ. Prior experimental studies provide evidence of the limits to increasing efficiency with N at high blockage. For example, experiments by McAdam *et al.* [103] at $\beta = 47\%$ showed a continual decrease in maximum efficiency with blade count for $N = 3 - 6$, and Takamatsu *et al.* [68] found that two-bladed turbines outperformed four-bladed turbines at $\beta = 75\%$. Therefore, there is likely an optimal blade count at each blockage that balances the benefits of a larger pressure drop across the array (greater for larger N) and the penalty of decreased mass flow rate through the rotors (lower for larger N). This is consistent with observations by Schluntz and Willden [95] in a numerical study of confined axial-flow turbines with different solidities. Since, in these experiments, $C_{P,\text{array}}$ does not vary significantly for $N = 1 - 3$ at $\beta = 35\%$, this particular blockage ratio may represent conditions for this experimental system in which the effects of N and β are balanced.

The number of blades also influences the steadiness of turbine loading over the course of a rotational cycle. These trends are explored in Figure 6.9 at λ_{opt} for representative geometries with $c/R = 0.49$, optimal α_p, and various N across the tested β. Although the cycle-average power and thrust coefficients increase with both β and N, at a given β the amplitude of cyclic power and thrust fluctuations is reduced with each blade added. In other words, although increasing the blade count increases the average force on the turbines, it reduces the maximum instantaneous forces experienced by the turbines. This characteristic is also present for turbines in unconfined and low-blockage flows [71, 114]. Since the peak

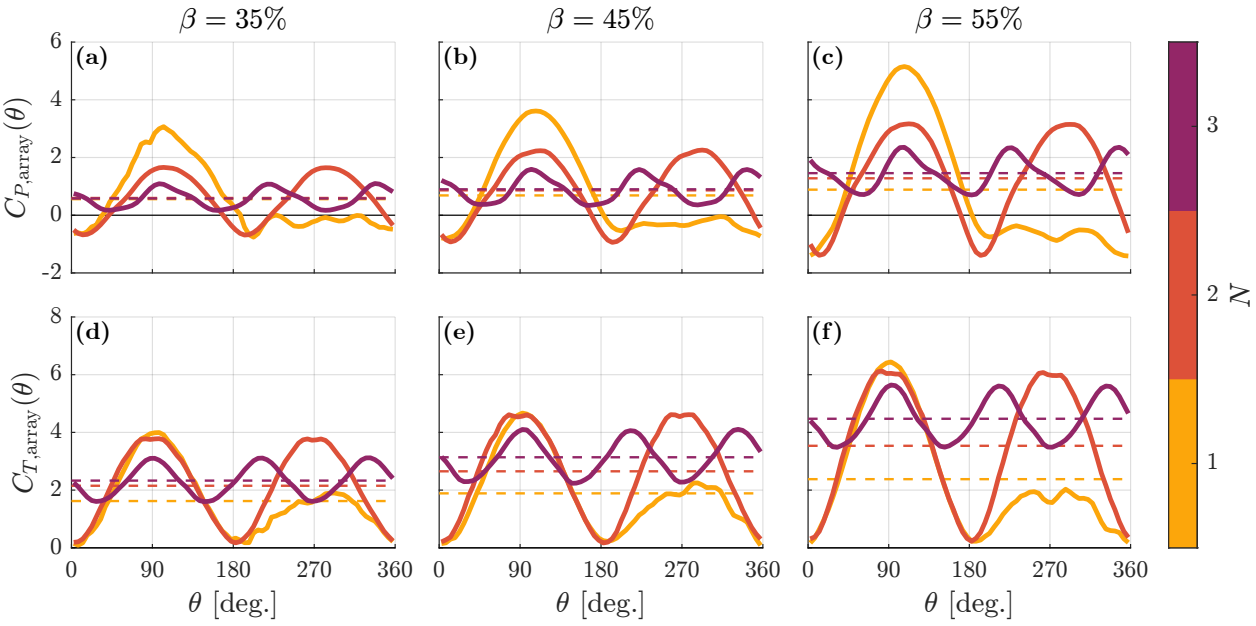

Figure 6.9: Phase-median (a)–(c) $C_{P,\text{array}}$ and (d)–(f) $C_{T,\text{array}}$ over a rotational cycle at λ_{opt} as a function of blade count and blockage for $c/R = 0.49$ and optimal α_p. The dashed lines represent the average $C_{P,\text{array}}$ and $C_{T,\text{array}}$ over the median cycle.

forces and torques on the rotor often drive structural and electrical design more so than the average loads, these factors suggest that turbines with more blades may have a clear economic advantage in confined flows.

6.4.3 Effects of Chord-to-Radius Ratio

Like the blade count, the chord-to-radius ratio changes the rotor solidity, and thus the resistance the turbines apply to the flow and the blockage effects experienced. Therefore, an increase in c/R increases the thrust on the array (Figure 6.7) and the power generated (Figure 6.4), with the optimal c/R likely influenced by a tradeoff between a higher pressure drop across the rotors and reduced mass flow rate through the rotors. However, while the relationship between c/R and $C_{T,\text{array}}|_{\lambda_{\text{opt}}}$ is well described by this interaction between solidity

and blockage (Figures 6.8a to 6.8c), the influence of c/R on $C_{P,\text{array}}$ cannot be completely attributed to σ and β since c/R simultaneously exerts several unique hydrodynamic influences that N does not. First, while N and c/R both influence the local Reynolds number at the blade (Re_c) through changes to the relative velocity from induction (Section 6.4.1), c/R also changes Re_c through the length scale c, which affects performance in a Reynolds-dependent regime [33, 48]. Second, the optimal preset pitch angle depends primarily on c/R (Figure 6.5), such that a change in c/R at constant α_p inherently convolves the effects of these two parameters. Third, an increase in c/R increases the flow curvature effects experienced by the blades, which causes a symmetric blade to appear to the flow as a cambered blade ("virtual camber") with an altered angle of attack ("virtual incidence") [26, 28, 68].

While the interplay between c/R and α_p on $C_{P,\text{array}}$ is explored in this study, more clearly identifying the contributions of Re_c and flow curvature effects requires further investigation. Furthermore, trends in $C_{P,\text{array}}$ with c/R may evolve as Re_D increases, since, at lower blockage ratios, the optimal c/R has been shown to decrease with the Reynolds number [29, 114]. Therefore, the optimal c/R for arrays operating at both high Re_D and high β may be that which balances the confinement effects (facilitated by higher solidity) with the favorable hydrodynamics achieved by lower c/R at higher Reynolds numbers.

6.4.4 Effects of Preset Pitch Angle

The preset pitch angle influences array performance by altering the range of angles of attack experienced by the blades throughout a rotational cycle. Although the actual angle of attack on the blades is unknown, a simplified model that neglects the influence of the rotor on the near-blade inflow velocities indicates that a negative preset pitch angle reduces the maximum magnitude of the angle of attack on the blade during the upstream sweep ($0° \leq \theta < 180°$) and increases the magnitude during the downstream sweep ($180° \leq \theta < 360°$) [114]. Consequently, the preset pitch angle is expected to alter the characteristics of dynamic stall and flow separation during the upstream sweep and those of flow reattachment during the downstream sweep. Work in Chapter 4 at $\beta = 11\%$ showed that the optimal preset

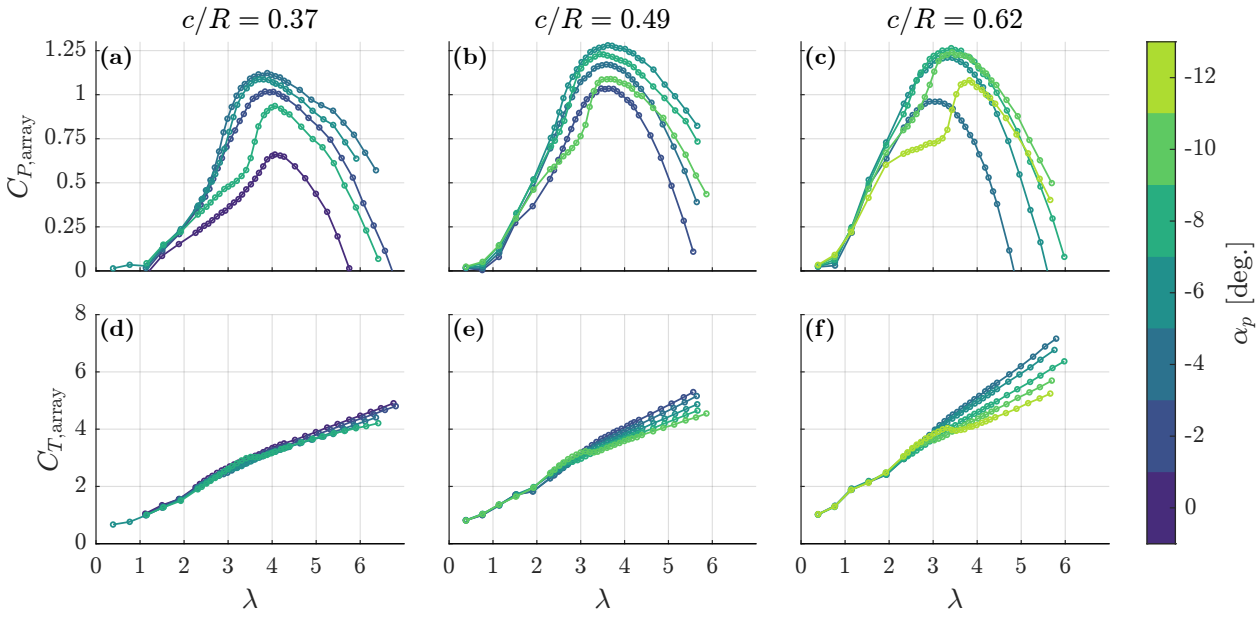

Figure 6.10: Time-average (a)–(c) $C_{P,\text{array}}$ and (d)–(f) $C_{T,\text{array}}$ as a function of λ at $\beta = 55\%$ for turbines with $N = 2$ and various c/R and α_p.

pitch angle is that which balances power production during the upstream sweep with power consumption during the downstream sweep. Given that the trends in α_p observed here parallel those in Chapter 4, similar hydrodynamic mechanisms are expected to be at play. However, since blockage-driven flow acceleration alters the velocity incident on the blades, the exact hydrodynamic influences of the preset pitch angle—and the corresponding interactions with the chord-to-radius ratio—are difficult to ascertain under these conditions without measurements of the near-blade flow field.

The contours of maximum $C_{P,\text{array}}$ across the parameter space indicate that the optimal value of α_p depends primarily on c/R, has a secondary dependence on N for single-bladed turbines (Figure 6.5), and is independent of β. Therefore, in terms of cross-flow turbine design in confined flow, α_p is effectively a free parameter that should be chosen based on the chord-to-radius ratio and Re_D to maximize efficiency. However, performance at off-

optimal α_p is also of interest to understand the implications of incremental deviations from the optimum, especially since α_p is often set arbitrarily to 0° (i.e., "neutral pitch") in prior work. To examine this, the time-average array efficiency and thrust for a representative set of geometries at $\beta = 55\%$, $N = 2$, and various c/R and α_p are shown in Figure 6.10. While excursions away from the optimal pitch angle always reduce maximum efficiency, the characteristic power and thrust curves are influenced by the direction of these excursions, as well as c/R. For example, for preset pitch that is less toe-out than optimal (i.e., $\alpha_p \to 0°$ in these experiments), maximum efficiency is shifted to higher λ for $c/R = 0.37$ (e.g., $\alpha_p = 0°$ in Figure 6.10a) and to lower λ for $c/R = 0.62$ (e.g., $\alpha_p = -4°$ in Figure 6.10c), and array thrust coefficients are generally higher for all c/R, particularly as λ increases (Figures 6.10d to 6.10f). In contrast, for preset pitch that is more toe-out than optimal (e.g., $\alpha_p \to -12°$ in these experiments), maximum efficiency is delayed to higher λ for all tested c/R, and $C_{T,\text{array}}$ is generally lower for all c/R except for a slight increase at moderate λ (e.g., $\lambda \approx 2.5 - 3.5$ in Figure 6.10f). Although not shown, it is noted that the sharp, delayed increase in $C_{P,\text{array}}$ for more negative preset pitch (e.g. $\alpha_p = -10°$ in Figure 6.10b) is most strong for single-bladed turbines, which shifts the optimal α_p to slightly more negative values (Figure 6.5). However, this sharp enhancement of $C_{P,\text{array}}$ weakens as more blades are added, likely due to alterations of the in-rotor flow field caused by the presence of these blades.

6.4.5 Dynamic Solidity

As discussed in Sections 6.4.2 and 6.4.3, both the blade count and the chord-to-radius ratio—through solidity—influence the confinement effects at a particular blockage ratio and operating condition. However, for a given β and rotor geometry, confinement effects are also a function of the tip-speed ratio due to the monotonic increase in C_T with tip-speed ratio. Therefore, it is also important to consider how blockage effects evolve with λ across β and the geometric parameter space.

Examples of the interplay between λ, β, and rotor geometry can be observed in the $C_{P,\text{array}} - \lambda$ and $C_{T,\text{array}} - \lambda$ curves for representative geometries at $\beta = 35\%$ and 55%

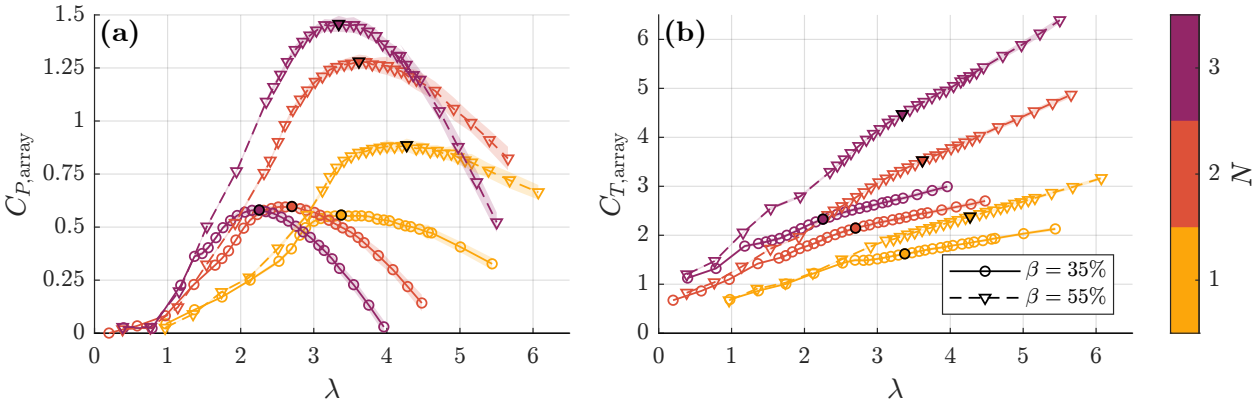

Figure 6.11: Time-average (a) $C_{P,\text{array}}$ and (b) $C_{T,\text{array}}$ as a function of N and λ for $c/R = 0.49$, optimal α_p, and $\beta = 35\%$ and 55%. Data corresponding to maximum efficiency point are indicated by the filled markers. The shaded regions (which are approximately the same width as the plotted lines at lower λ) indicate ± 1 standard deviation in the cycle-average values.

with different N (Figure 6.11) and different c/R (Figure 6.12). $C_{T,\text{array}}$ increases at all λ if solidity is increased via N (Figure 6.11b) or c/R (Figure 6.12b). Furthermore, for larger N or c/R, $C_{T,\text{array}}$ increases with λ at a faster rate, and confinement begins to affect array performance at lower tip-speed ratios. For example, in Figure 6.11a, $C_{P,\text{array}}$ is identical at 35% blockage and 55% blockage up to $\lambda \approx 2.7$ for the single-bladed turbine, but only up to $\lambda \approx 1.4$ for three-bladed turbines. The range of λ for which the array thrust coefficient is invariant with β is similarly affected, which suggests that confinement effects may only begin to influence performance above a threshold value of $C_{T,\text{array}}$, which is achieved at lower λ by higher solidity rotors. However, despite benefiting from blockage effects due to their increased thrust, geometries with larger c/R and N still have lower λ_{opt} and produce power over a narrower range of tip-speed ratios at a given β due to their higher solidity.

To model the effective flow resistance of each geometric configuration over all operating conditions, we apply the concept of dynamic solidity originally introduced by Araya *et al.*

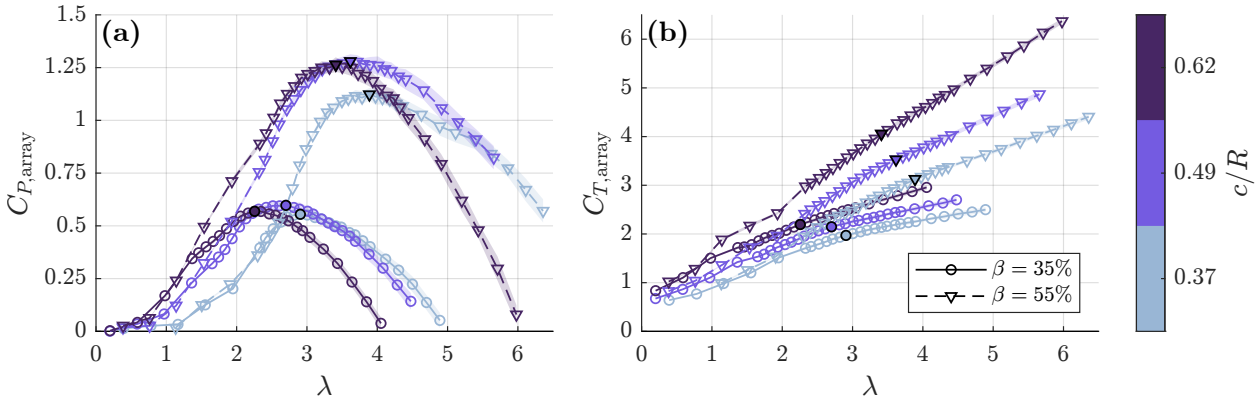

Figure 6.12: Time-average (a) $C_{P,\text{array}}$ and (b) $C_{T,\text{array}}$ as a function of c/R and λ for $N = 2$, optimal α_p at each c/R (Figure 6.5), and $\beta = 35\%$ and 55%. Data corresponding to maximum efficiency point are indicated by the filled markers. The shaded regions (which are approximately the same width as the plotted lines at lower λ) indicate ± 1 standard deviation in the cycle-average values.

[19]. Araya *et al.* related the advective timescale of the fluid to the timescale of blade passage by combining the "static solidity" of the rotor geometry (σ) and λ as

$$\sigma_d = 1 - \frac{1}{2\pi\sigma\lambda} \ , \tag{6.2}$$

For low σ_d (i.e., low σ or λ), the gaps between the blades are wide or transit slowly around the rotor circumference, such that the rotor appears relatively porous to the flow and fluid easily passes through the turbine. As σ_d increases, the temporal gaps between the blades narrow, such that it is more difficult for the fluid to pass through, increasing flow resistance by the turbine. In the limiting case of $\sigma_d \to 1$, the rotor begins to resemble a solid cylindrical shell. It is noted that this definition of dynamic solidity implicitly chooses the freestream velocity, U_∞, as the advective time scale, rather than the actual velocity through the rotors. While the latter is indeterminate, it is itself influenced by rotor geometry, rotation rate, and blockage. Furthermore, as noted by Araya *et al.* [19], σ_d loses physical meaning when

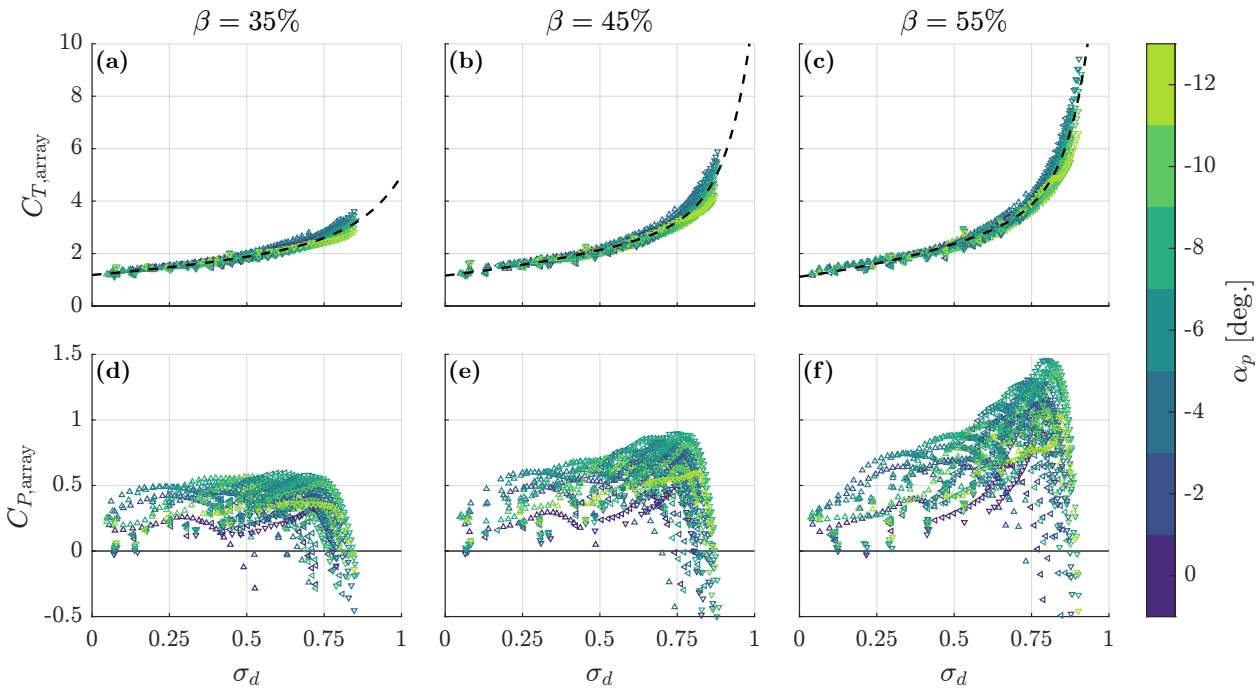

Figure 6.13: (a)–(c) $C_{T,\text{array}}$ and (d)–(f) $C_{P,\text{array}}$ as a function of dynamic solidity for all geometries and β. Only points with $\sigma_d \geq 0$ are shown. The dashed lines in (a)–(c) correspond the exponential fit of $C_{T,\text{array}}$ versus σ_d at each β (Equation 6.3; Table 6.3).

$\lambda < 1/2\pi\sigma$, which results in $\sigma_d < 0$. Consequently, for the subsequent analysis, operating points with $\sigma_d < 0$ ($\approx 8\%$ of all data points, corresponding to the lowest λ tested in each experiment) are omitted.

When the array thrust coefficient is regressed against dynamic solidity, a clear relationship between σ_d and $C_{T,\text{array}}$ is observed for all blockage ratios and geometries (Figures 6.13a to 6.13c). At each β, $C_{T,\text{array}}$ increases linearly with dynamic solidity up to $\sigma_d \approx 0.5$ before increasing exponentially as σ_d increases further. Since arrays at higher blockage ratios produce power over a broader range of λ, rotors at higher β can achieve higher σ_d, and consequently higher $C_{T,\text{array}}$. However, even at constant σ_d, $C_{T,\text{array}}$ increases with β, indicating that σ_d alone does not fully capture how the effects of confinement scale across

blockage ratios. Nonetheless, the general trend between $C_{T,\text{array}}$ and σ_d is well-described at each blockage ratio by a two-term exponential function of the form

$$C_{T,\text{array}} = c_1 e^{c_2 \sigma_d} + c_3 e^{c_4 \sigma_d} \ , \tag{6.3}$$

where $c_1 - c_4$ are coefficients selected for best fit at each β (Table 6.3). The resulting fits are shown as the dashed black lines in Figures 6.13a to 6.13c. In contrast, there is no clear relationship between the array efficiency and the dynamic solidity (Figures 6.13d to 6.13f). Although, the highest efficiencies are obtained at higher dynamic solidities as β increases, there is considerable spread in $C_{P,\text{array}}$ at each σ_d. This may be exacerbated by the variations in Re_c with σ_d (Section 6.4.1), as well as amplification of blade-level $C_{P,\text{array}}$ at high λ as a result of the disk loss subtraction method (Appendix E). Consequently, as for static solidity (Figures 6.8d to 6.8f), dynamic solidity is an incomplete descriptor of the hydrodynamics that govern array efficiency across operating conditions.

As emphasized in Figure 6.14, the thrust on the array at a particular dynamic solidity depends on the blockage ratio, especially as σ_d increases. However, by combining the individual exponential fits of $C_{T,\text{array}}$ versus σ_d at each β, a single empirical equation that describes $C_{T,\text{array}}$ as a function of both σ_d and β can be obtained. This is accomplished by fitting c_2 and c_4 to polynomials as a function of β and, for simplicity, taking the average values of c_1 and c_3 since these coefficients do not change significantly with β. The resulting coefficients

Table 6.3: Coefficient values for Equation 6.3 at each β, as well as for the unified fit at all β.

β	c_1	c_2	c_3	c_4
35%	1.181	0.877	1.035×10^{-3}	7.629
45%	1.160	1.206	3.156×10^{-5}	12.396
55%	1.114	1.498	1.230×10^{-5}	13.971
Unified Fit	1.151	$3.107\beta - 0.2041$	3.596×10^{-4}	$-159.6\beta^2 + 175.3\beta - 34.19$

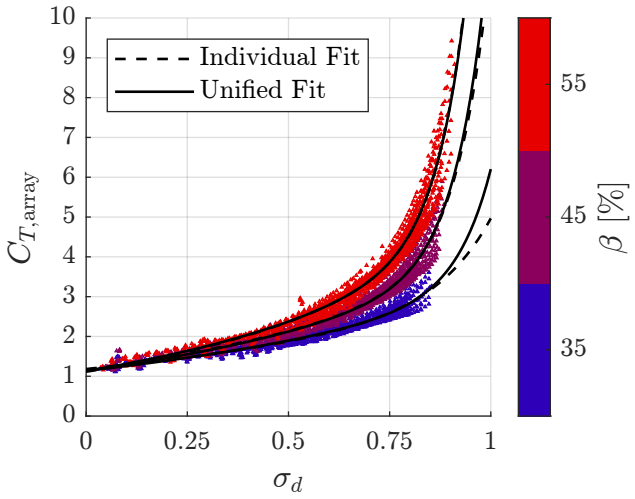

Figure 6.14: $C_{T,\text{array}}$ as a function of dynamic solidity and blockage. The dashed lines correspond to the exponential fits of $C_{T,\text{array}}$ versus σ_d obtained individually at each β, whereas the the solid black lines correspond to the unified fit of $C_{T,\text{array}}$ as a function of both σ_d and β. Only points corresponding to $\sigma_d \geq 0$ are shown.

of the unified fit are given in the last row of Table 6.3, and when evaluated over a range of σ_d at each tested β, the unified fit closely matches the individual exponential fits obtained from the data at each β.

6.4.6 Bluff-Body Scaling

Given the wide variety of geometric configurations tested in this study, we can evaluate how effective Maskell-inspired bluff-body performance scaling is for representing the performance of arrays with different rotor geometries across the tested blockage ratios. Using the open-channel LMADT model of Houlsby *et al.* [3] and the methodology described in Section 5.4.1, u_b is calculated for each rotor configuration from the measured $C_{T,\text{array}}$, U_∞, and Fr_h at each β and λ. u_b is then used to calculate ${C_P}^b$, ${C_T}^b$, and λ^b via Equations 5.5 to 5.7 for that rotor geometry and β. Contours of the maximum bluff-body scaled efficiency across the tested parameter space are shown in Figure 6.15, and contours of the corresponding ${C_T}^b$ and λ^b are

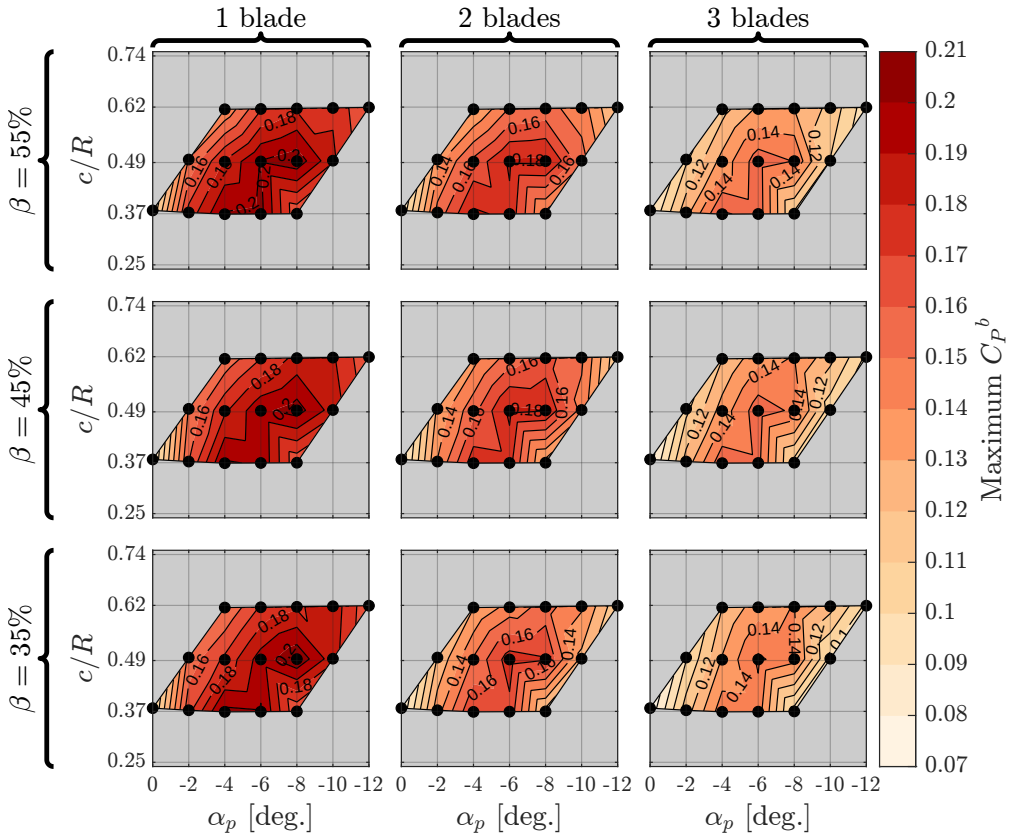

Figure 6.15: Contours of the maximum bluff-body scaled $C_{P,\text{array}}$ as a function of c/R and α_p for each combination of β and N.

provided in Appendix F. Although the contours of maximum ${C_P}^b$ vary with rotor geometry, they do not vary significantly with the blockage ratio. In other words, Maskell-inspired bluff-body scaling collapses $C_{P,\text{array}}$ across the tested β for each of the tested geometries. As this scaling approach does not account for differences in Re_c that arise from blockage, the collapse in $C_{P,\text{array}}$ may indicate that variations in Re_c with β are limited for a given geometry.

Since the array was not tested in unconfined flow (i.e., $\beta = 0\%$), the accuracy of Equations 5.5 to 5.7 as a bluff-body blockage correction cannot be assessed. Nonetheless, the trends in maximum ${C_P}^b$ with rotor geometry in Figure 6.15 can be compared to those observed by Chapter 4 for single turbines with similar geometries at lower blockage ($\beta = 11\%$)

and the same Re_D. Relative to the values of maximum efficiency measured in Chapter 4, the maximum ${C_P}^b$ in Figure 6.15 are lower and show less dependence on the blade count, although maximum ${C_P}^b$ does decrease with N as is expected in low blockage flow. Furthermore, the relationship between c/R and optimal α_p (Figure 6.5) appears to be preserved when bluff-body scaling is applied, and remains similar to that observed in Chapter 4. However, the contours in Figure 6.15 suggest that ${C_P}^b$ increases at lower c/R, whereas in Chapter 4 the reverse is observed at lower blockage at this Re_D. Since the analytically-predicted bypass velocity is proportional to the array thrust coefficient, LMADT predicts higher u_b for geometries with greater c/R, and thus lower ${C_P}^b$ via Equation 5.5. However, in a Reynolds-dependent regime, efficiency is expected to increase with c/R [29, 114] due to the increase in chord length and thus Re_c. As this effect is not accounted for in Maskell-inspired bluff-body scaling, ${C_P}^b$ decreases with c/R instead of increasing as expected.

6.5 Conclusions

The objective of this work is to experimentally investigate how the optimal rotor geometry for a cross-flow turbine depends on confinement, with a focus on the upper end of practically achievable blockage ratios. Using an array of two matching cross-flow turbines, the power and force characteristics of 45 unique rotor geometries are tested at $\beta = 35\% - 55\%$ in a recirculating water tunnel. Three geometric parameters are considered in this study: the number of blades ($N = 1 - 3$), the chord-to-radius ratio ($c/R = 0.37 - 0.62$), and the preset pitch angle ($\alpha_p = -12° - 0°$). While the maximum efficiency and corresponding thrust coefficient and tip-speed ratio all increase with the β regardless of rotor geometry, the effects of blockage can manifest differently depending on the values of N and c/R. As the number of blades and the chord-to-radius ratio increase, the power and thrust coefficients increase with β at a faster rate, and higher maximum efficiencies are achieved. Notably, increased maximum efficiency at higher blade counts is an inversion of what has been previously observed at lower β [18–20, 114]. In contrast, the optimal preset pitch angle does not depend on β in the range tested, and, in agreement with prior work at lower blockage (Chapter 4), primar-

ily depends on the chord-to-radius ratio. For each of the tested geometries, the power and thrust coefficients collapse across the tested β when scaled by the bypass velocity predicted via linear momentum theory, demonstrating that a Maskell-inspired bluff-body model can represent high-blockage dynamics for a variety of rotor designs.

Since both the number of blades and the chord-to-radius ratio are parametrically varied in this study, how well static solidity—a geometric parameter which combines N and c/R—describes array power and force at high blockage is evaluated. The array thrust coefficient at peak performance is shown to be proportional to the static solidity and increases exponentially with the dynamic solidity when the influence of the tip-speed ratio is incorporated. Furthermore, as β increases, the highest efficiencies are obtained with increasingly larger dynamic solidity, although this parameter alone does not completely describe array performance due to the unique influences of N, c/R, and α_p. Since blockage effects are a function of both the channel blockage ratio and the thrust coefficient, the design process for high-blockage turbines is expected to be driven by the optimal solidity that most effectively exploits confinement at a given β. Increasing the number of blades is the simplest and most favorable pathway for achieving the optimal solidity, as it increases the power generated while providing the key advantage of reducing the amplitude of cyclic loading. The optimal solidity may also be achieved by changing the chord-to-radius ratio, although the chosen c/R will likely be influenced structural limitations on the rotor and blade size, as well as the target Reynolds number. In contrast, the preset pitch angle is a free parameter in the design process, and should be chosen based on the chord-to-radius ratio to maximize efficiency. To aid in turbine design, as well as the validation of numerical and reduced-order models, the underlying performance data from this study will be made openly available upon publication of this work.

Although this work illuminates how the effects of N, c/R, and α_p evolve at high confinement, certain trends are not fully resolved, and it is recommended that future work expand upon the geometric and operational range explored here. Specifically, the highest tested chord-to-radius ratios and blade counts often performed best across the tested β, such that

the optimal values of these parameters were not clearly determined. Additionally, several other geometric parameters, such as the blade profile, shape, and surface roughness can also influence performance, but their interactions with blockage were not explored here. Finally, due to the effects of blockage on the local Reynolds number, as well as the influence of the Reynolds number on the optimal c/R [29, 114], the trends observed in this study may change as Reynolds independence is approached. Overall, this study provides the first experimental examination of the influence of blockage on optimal rotor geometry, and informs design principles for cross-flow turbines in high-blockage flows.

Chapter 7

CONCLUSIONS AND FUTURE WORK

7.1 Conclusions

Cross-flow turbine performance depends on the geometric configuration of the rotor and the characteristics of the flow it operates in. However, due to their inherently unsteady fluid mechanics, both the individual and combined effects of geometric parameters and flow parameters on turbine performance are not well understood. Therefore, the main aim of this research was to experimentally explore how the fluid dynamics of cross-flow turbine performance are affected by two non-dimensional flow parameters (the Reynolds number and the blockage ratio) and three geometric parameters (the number of blades, the preset pitch angle, and the chord-to-radius ratio), with the primary goal of identifying design strategies for improving turbine efficiency and secondary goal of providing experimental results for simulation validation and reduced-order model development. The first objective of this work was to understand how the optimal cross-flow turbine geometry changes with turbines scale, represented by the Reynolds number. The second objective of this work was to understand how the performance of a cross-flow turbine array evolves with confinement at the upper end of practically achievable blockage ratios, and to evaluate how well their governing dynamics are captured by analytical models. The third objective of this work was to understand how confinement influences the optimal turbine geometry over the same range of blockage ratios, and compare these trends to those observed at low blockage.

In Chapters 1 and 2, the motivation for this work was provided, the fundamental fluid mechanics of cross-flow turbines were reviewed, and key geometric and flow parameters were introduced. In Chapter 3 common elements of the experimental methodology used throughout this work were described. In Chapter 4, we addressed the first objective by

experimentally evaluating the interplay between rotor geometry and turbine scale (i.e., the Reynolds number) on cross-flow turbine performance. Using two experimental facilities (a recirculating water channel at UW and a towing tank at UNH) and two physical turbine sizes, we evaluated turbine performance over an order of magnitude difference in diameter-based Reynolds number ($Re_D \approx 8 \times 10^4 - 8 \times 10^5$). In total, 223 unique combinations of the Reynolds number, the chord-to-radius ratio, the preset-pitch angle, and the blade count were considered, and turbine power and force were characterized for each configuration. The results highlighted the individual effects of these parameters: for example, maximum efficiency generally increased with Re_D and decreased with blade count. Important interactions between parameters were also illuminated: for example, the optimal preset pitch angle became more negative (i.e., more toe-out) as the chord-to-radius ratio increased, whereas the optimal chord-to-radius ratio decreased with Reynolds number. Importantly, we evaluated the relationship between turbine performance and solidity, a commonly-used geometric parameter that combines c/R and N. We found that while solidity is an excellent descriptor of the tip-speed ratio at which maximum efficiency occurs, it is not descriptive of the maximum efficiency itself, owing to the distinct effects of c/R and N. The key contributions of this work are the identification of key design principles for cross-flow turbines across a range of scales, as well as the unification and clarification of narrower prior work that explored subsets of these parameters.

In Chapter 5, we addressed the second objective by characterizing the performance and near-wake of a high-confinement cross-flow turbine array. The blockage ratio was varied between 30% and 55% (which represent the upper end of practically achievable blockage ratios in river or tidal channels) for a two-rotor array in a recirculating water flume, while the rotor geometry was held constant. At each blockage, the power and force on the array where characterized and the near-wake flow field was visualized using PIV at several operating conditions for $\beta = 36.7\%$, 45.0% and 55.0%. In agreement with theory and prior work, as the blockage ratio increased, the maximum efficiency of the array increased, eventually surpassing both the Betz limit for unconfined flow and unity. Additionally, both the thrust

coefficient and the tip-speed ratio corresponding to maximum efficiency increased with the blockage ratio, as did the measured velocities in the wake and bypass regions. Utilizing the analytical open-channel linear momentum model of Houlsby *et al.* [3], we used the measured turbine performance to predict the bypass and wake velocities, and compared these analytical values to the velocities measured using PIV. We found that the analytically predicted bypass velocity showed good agreement with the measured velocities in the bypass region, whereas the analytical wake velocity showed poor agreement with the measured wake velocity. Following Whelan *et al.* [9] and inspired by the bluff body theory of Maskell [1], we showed that the array power and force coefficients respectively collapsed across the tested blockages when scaled by the analytical bypass velocity. We attributed these trends to the pressure drop across the array, which increases with the bypass velocity and corresponds to acceleration of the core flow passing through the array. Building upon this, we proposed an analytical method that leverages these dynamics to predict turbine performance as a function of blockage. In addition to providing a high-resolution experimental illustration of how the array performance and near-wake evolve over a range of blockage ratios and operating conditions, the key contribution of this work is the demonstration that analytical linear momentum models can be quantitatively descriptive of the hydrodynamics of real turbines in confined flows.

In Chapter 6, we addressed the third objective by combining the methodologies used in Chapters 4 and 5 to examine the influence of confinement on the optimal cross-flow turbine rotor geometry. The power and loading characteristics of a two-rotor cross-flow turbine array were evaluated at blockage ratios between 35% and 55% in a recirculating water flume for various combinations of the blade count, chord-to-radius ratio, and preset pitch angle, with both rotors in the array sharing a given geometric configuration. In total, 135 unique experiments were conducted. While the array power and thrust coefficients increased with blockage regardless of geometric configuration, the rotor geometry was shown to influence the manifestation of these effects. Most notably, the maximum efficiencies of turbines with higher blade counts increased more rapidly with the blockage ratio, and, in an inversion of

trends observed at lower blockage in Chapter 4 and prior work, surpassed that of turbines with fewer blades. Since confinement effects are a function of both the blockage ratio and the flow resistance imparted by the array, we hypothesize that the greater thrust on arrays with higher N corresponds to greater blockage-driven augmentation of performance. In contrast, trends in c/R and α_p were similar to those observed at lower blockage. By combining the rotor geometry and tip-speed ratio through the concept of dynamic solidity (originally introduced by Araya *et al.* [19]), we observed an exponential relationship between the array-average thrust coefficient and the dynamic solidity, whereas the array-average efficiency cannot be completely described by dynamic solidity. Additionally, we applied the Maskell-inspired bluff body scaling technique from Chapter 5 to all tested geometries. When scaled in this way, the power coefficients for each geometry collapsed across the tested blockages, indicating the applicability of this method across the broader geometric parameter space. The key contribution of this work is the identification of important design principles for cross-flow turbines in confined flow, some of which are notably different than those in unconfined flow. Importantly, to the authors' knowledge, this work comprised the first experimental investigation of the relationship between blockage and optimal turbine geometry for cross-flow turbines, and provided validation of the general trends observed in prior simulations of both axial-flow and cross-flow turbines.

7.2 Future Work

Although the experiments in this work explored a broad geometric parameter space spanned by c/R, α_p, and N, the results highlight numerous pathways for future work within this parameter space. For example, the optimal c/R was not identified in all cases in Chapters 4 and 6, and the numerous effects of c/R (e.g., Re_c effects, flow curvature, solidity) remain difficult to parse independently of each other. Similarly, in Chapter 6, the limits of increasing efficiency with increasing N at high blockage were not identified. Therefore, we recommend that future work expand upon the results in this study to improve our understanding of the relationships between c/R and Re_D and between N and β. We also recommend that future

work leverage the results of this study to interpret how other geometric parameters, such as blade camber and blade shape, affect turbine hydrodynamics and performance.

Another area for future research is continued exploration of the applicability and limitations of Maskell-inspired bluff body performance scaling method discussed in Chapter 5. While this research demonstrated that this method is descriptive of cross-flow turbine performance at $\beta = 30\% - 55\%$ and across a wide range of rotor geometries, it is unknown whether this technique continues to be effective for $\beta < 30\%$, which are also relevant conditions for full-scale turbine deployments in river or tidal channels. Consequently, it is recommended that future work study the effectiveness of bluff body performance scaling across a wide range of blockage ratios between 0% and 30%. This would inform the broader applicability of the bluff body forecasting method described in Section 5.5, as well as the accuracy of bluff body scaling as a blockage correction to unconfined conditions.

Finally, further research is necessary to understand how the confinement effects highlighted in this work will translate to a wide range of real-world channels. Unlike the recirculating water flume used in this study, river and tidal channels can have considerable shear gradients, higher turbulence, and irregular boundaries or obstructions to flow. Therefore, we recommend that future work examine how confinement effects are altered when these non-idealities are present, and assess whether linear momentum models can still quantitatively describe turbine performance under these conditions. Additionally, future work should examine the interplay between confinement and both the effects of lateral boundary proximity (i.e., turbine proximity to a wall) and the effects of Fr_h, as both of these parameters may vary considerably in real-world channels. Although the effects of free surface proximity were explored briefly in Appendix D, a better understanding of the fluid mechanics that drive the onset of ventilation for cross-flow turbines and performance changes with s/h requires further investigation.

Appendix A

EXPERIMENTAL UNCERTAINTY

Using the data collected in Chapter 4, the experimental uncertainty of the measured time-average efficiency, $\langle C_P \rangle$, is evaluated for both the UW and UNH test rigs via the American Society of Mechanical Engineers standard on test uncertainty, ASME PTC 19.1-2005 [109]. Through this procedure, the uncertainty of each component measurement of $\langle C_P \rangle$ (e.g., $\langle Q \rangle$, $\langle \omega \rangle$, $\langle U_\infty^3 \rangle$) is estimated, from which the total uncertainty of $\langle C_P \rangle$ is obtained. Uncertainty is evaluated on a cycle-average basis; in other words, the uncertainty of the average value of a given component measurement, X, that is obtained for a single rotational cycle is estimated. The cycle-averages are related to the time-average as

$$\langle X \rangle = \frac{\sum_{i=1}^{n} X_i}{n} \quad , \tag{A.1}$$

where n is the number of turbine rotational cycles, X_i is the measured average value of X over the i^{th} cycle, and $\langle X \rangle$ is the average value of X over all cycles, which is equal to the time-average measurement. Uncertainty is evaluated at the turbine-level rather than at the blade-level since $C_{P,\text{supports}}$ is measured independently from C_P. A similar analysis could be conducted to quantify the uncertainty of $\langle C_{P,\text{supports}} \rangle$. However, since common support-structure loss relations were used to compute blade-level efficiency for all tested turbine geometries, this analysis would not inform variability in the trends observed across the parameter space.

A.1 Method for Estimating Uncertainty

The following implementation of the standard on test uncertainty is similar to that of Cavagnaro and Polagye [149] and Snortland *et al.* [108] who have previously applied this method

Table A.1: Specifications and systematic standard uncertainty for the instruments used to measure turbine efficiency.

Facility	**Instrument**	C_P **component**	**Measured Quantity**	**Systematic Standard Uncertainty** $b_{\langle X \rangle}$
UW	ATI Mini45-IP65	Q	Q_{top} [N-m]	Accuracy: ±1.25% of full scale load
	ATI Mini40-IP68	Q	Q_{bottom} [N-m]	Accuracy: ±1.50% of full scale load
	Motor Encoder	ω	θ [deg.]	Accuracy: ±0.0055 degrees
	Nortek Vector ADV	U_∞^3	U_∞ [m/s]	Accuracy: ±0.5% of measured value ±1 mm/s[†]
UNH	Interface T8-200	Q	Q [N-m]	Accuracy: ±0.25% of full scale load Nonrepeatability: ±0.05% of full scale load[‡]
	Kollmoregen AKM62Q	ω	θ [deg.]	Accuracy: ±0.0036 degrees
	Renishaw LM15	U_∞^3	Tow carriage position [m]	Accuracy: ±100μm per meter[†]

[†] $b_{\langle U_\infty \rangle}$ converted to $b_{\langle U_\infty^3 \rangle}$ by converting the listed value to percentage error of U_∞, multiplying by 3 to obtain percentage error of U_∞^3, and then multiplying by U_∞^3 to convert back to absolute error.

[‡] Accuracy and nonrepeatability combined via root sum of squares.

to cross-flow turbine systems. The uncertainty of each component measurement of $\langle C_P \rangle$ is composed of systematic standard uncertainty and random standard uncertainty. Systematic standard uncertainty, $b_{\langle X \rangle}$, represents the constant error associated with the instruments used to measure X. The values of systematic standard uncertainty are estimated for each instrument using the sensor specifications provided by the manufacturers, which are given in Table A.1 for each instrument employed in the UW and UNH experimental set-ups.

The random standard uncertainty, $s_{\langle X \rangle}$, represents the variable error associated with repeated measurements of X and is calculated as

$$s_{\langle X \rangle} = \sqrt{\frac{1}{n(n-1)} \sum_{i=1}^{n} (X_i - \langle X \rangle)^2} \quad . \tag{A.2}$$

For the UW and UNH experimental set-ups, sources of random standard uncertainty include white electrical noise, Doppler noise, and normally distributed variations in torque,

servomotor rotation rate, and inflow or tow carriage velocity.

The combined standard uncertainty of component measurement X, $u_{\langle X\rangle}$, is calculated by as

$$u_{\langle X\rangle} = \sqrt{b_{\langle X\rangle}^2 + s_{\langle X\rangle}^2} \quad , \tag{A.3}$$

and the interval $\langle X\rangle \pm 2u_{\langle X\rangle}$ is expected to contain the true cycle-average value of X with 95% confidence.

The standard uncertainty for $\langle C_P\rangle$ is obtained by weighting the $b_{\langle X\rangle}$ and $s_{\langle X\rangle}$ of each component measurement by the sensitivity of $\langle C_P\rangle$ to that component. The sensitivity of $\langle C_P\rangle$ to the j^{th} component measurement is defined as

$$\kappa_j = \frac{\partial\langle C_P\rangle}{\partial\langle X_j\rangle} \quad . \tag{A.4}$$

The systematic standard uncertainty and random standard uncertainty are then obtained, respectively, as

$$b_{\langle C_P\rangle} = \sum_{j=1}^{J} \sqrt{(\kappa_j b_{\langle X_j\rangle})^2} \quad , \tag{A.5}$$

$$s_{\langle C_P\rangle} = \sum_{j=1}^{J} \sqrt{(\kappa_j s_{\langle X_j\rangle})^2} \quad . \tag{A.6}$$

where J is the total number of measurement components. Finally, the combined standard error for $\langle C_P\rangle$ is calculated as

$$u_{\langle C_P\rangle} = \sqrt{b_{\langle C_P\rangle}^2 + s_{\langle C_P\rangle}^2} \quad , \tag{A.7}$$

with the interval $\langle C_P\rangle \pm 2u_{\langle C_P\rangle}$ corresponding to 95% confidence.

A.2 Predicted and Measured Uncertainty

For the experimental test set-up at UW (Section 3.2), the time-average of C_P (Equation 2.2) can be expressed in terms of its component measurements as

$$\langle C_P\rangle = \frac{(\langle Q_{\text{top}}\rangle + \langle Q_{\text{bottom}}\rangle)\langle\omega\rangle}{\frac{1}{2}\rho A\langle U_\infty^3\rangle} \quad , \tag{A.8}$$

where Q_{top} and Q_{bottom} are the torques measured by the top and bottom load cells, respectively, ρ and A are assumed to be constant, and $\omega(t) \approx \langle\omega\rangle$. Since under constant speed control the instantaneous angular velocity varies from the time-average angular velocity by at most $\sim$1% at both facilities, the assumption $\omega(t) \approx \langle\omega\rangle$ is valid and allows the uncertainty contribution of the mechanical power $\langle Q\omega\rangle$ to be decomposed into the individual contributions of $\langle Q_{\text{top}}\rangle$, $\langle Q_{\text{bottom}}\rangle$ and $\langle\omega\rangle$. However, for other control strategies where both the hydrodynamic torque and angular velocity vary appreciably over the course of a cycle (e.g., intracycle control [49]), the uncertainty of $\langle Q\omega\rangle$ cannot be decomposed in this way. The sensitivities corresponding to these component measurements are obtained via Equation A.4 and given as

$$\kappa_{\langle Q_{\text{top}}\rangle} = \kappa_{\langle Q_{\text{bottom}}\rangle} = \frac{\langle C_P\rangle}{\langle Q\rangle} \quad , \tag{A.9}$$

$$\kappa_{\langle\omega\rangle} = \frac{\langle C_P\rangle}{\langle\omega\rangle} \quad , \tag{A.10}$$

$$\kappa_{\langle U_\infty^3\rangle} = \frac{-\langle C_P\rangle}{\langle U_\infty^3\rangle} \quad , \tag{A.11}$$

where $\langle Q\rangle = \langle Q_{\text{top}}\rangle + \langle Q_{\text{bottom}}\rangle$. As described in Section 3.5, at UW measurements of Q_{top}, Q_{bottom}, ω, and turbine position within a rotational cycle are synchronized with each other, whereas measurements of U_∞ are acquired separately. Consequently, while average values of Q and ω can be obtained for each rotational cycle, cycle-average values of U_∞^3 cannot be directly calculated. Instead, for n rotational cycles, "quasi-cycle-average" values of U_∞^3 are calculated by breaking the U_∞^3 time-series into n equal-length segments and computing the average of each segment. This provides an estimate of how much average of U_∞^3 varied throughout a given test.

For the experimental test set-up at UNH (Section 4.3.2), $\langle C_P\rangle$ can be expressed in terms of its component measurements as

$$\langle C_P\rangle = \frac{\langle Q\rangle\langle\omega\rangle}{\frac{1}{2}\rho A\langle U_\infty^3\rangle} \quad , \tag{A.12}$$

where once again $\omega(t) \approx \langle\omega\rangle$ under constant speed control. The sensitivities corresponding to Q, ω, and U_∞^3 are the same as those given in Equations A.9 to A.11. As described in

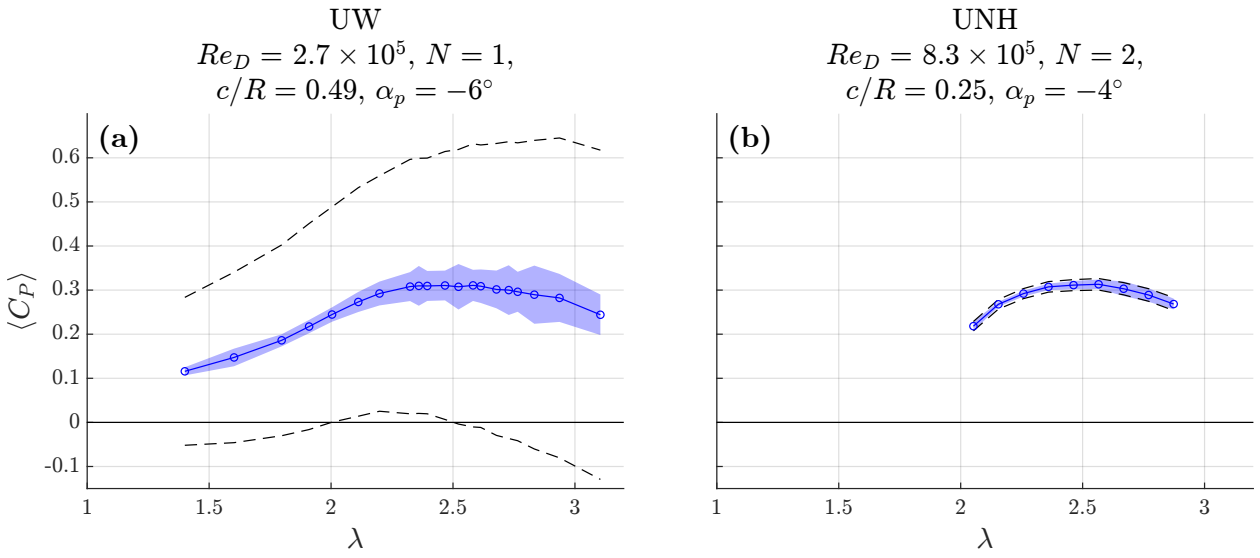

Figure A.1: Uncertainty of $\langle C_P \rangle$ for representative experiments at (a) UW and (b) UNH. The dashed lines indicate the 95% confidence intervals obtained via the standard for test uncertainty, whereas the shaded blue region indicates ± 2 standard deviations of the measured cycle-average values.

Section 3.5, at UNH measurements of Q, ω, U_∞, and turbine position within a rotational cycle are synchronized with each other. Therefore, average values of each of these component measurements can be obtained for each rotational cycle.

Figure A.1 shows the predicted uncertainty and the observed variability at each point on the $\langle C_P \rangle - \lambda$ for representative experiments at UW and UNH in Chapter 4. Across all experiments at UW, the average standard deviation of the cycle-average values of C_P is ≈ 0.015 at λ_{opt}. As shown in Figure A.1a, the 95% confidence interval for $\langle C_P \rangle$ calculated at each λ is much larger than the actual range of cycle-average C_P measured at each λ during the experiment.

The disparity between predicted uncertainty and observed variability appears to be driven by the relatively large systematic uncertainties for the torques measured by the top and

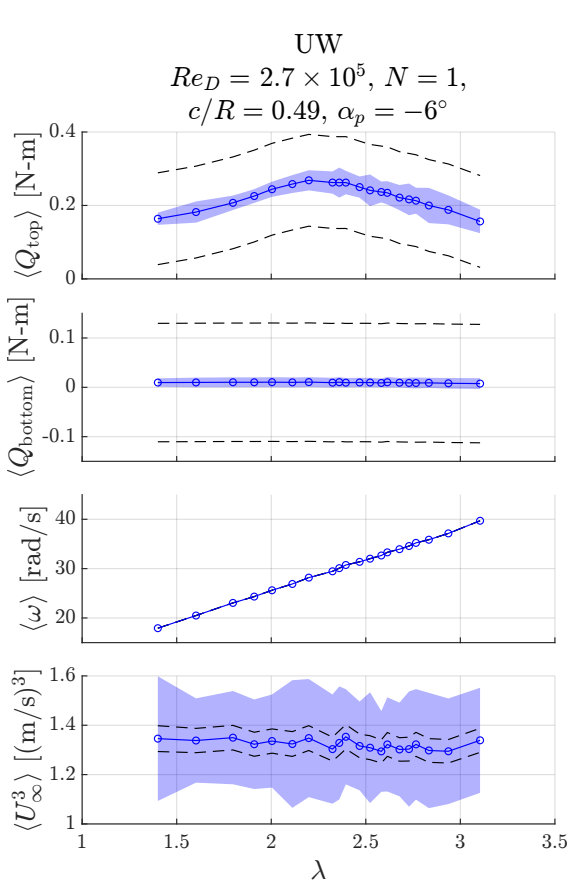

(a) Uncertainties of $\langle Q_{\text{top}} \rangle$, $\langle Q_{\text{bottom}} \rangle$, $\langle \omega \rangle$, and $\langle U_\infty^3 \rangle$ for a representative experiment at UW (same as in Figure A.1a).

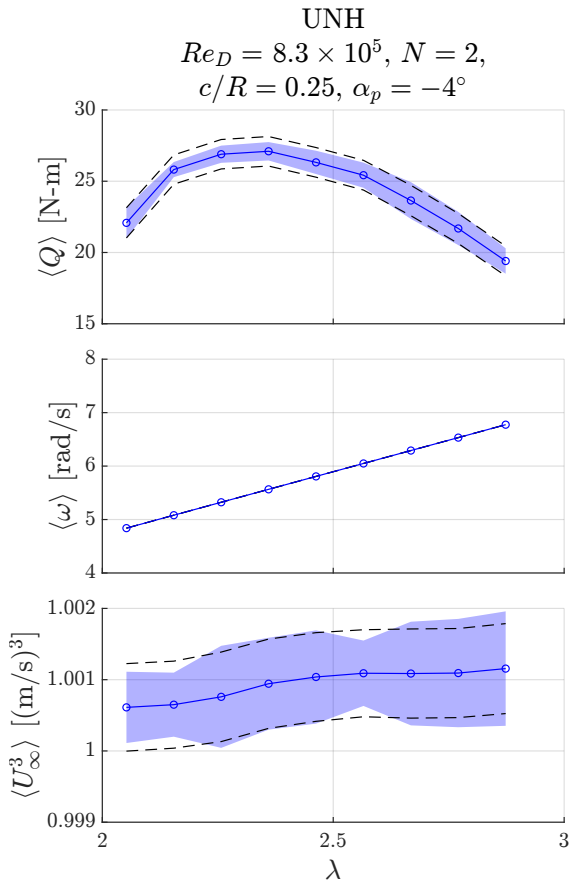

(b) Uncertainties of $\langle Q \rangle$, $\langle \omega \rangle$, and $\langle U_\infty^3 \rangle$ for a representative experiment at UNH (same as in Figure A.1b).

Figure A.2: Uncertainties of the component measurements of $\langle C_P \rangle$ for representative experiments at (a) UW and (b) UNH. The dashed lines indicate the 95% confidence intervals obtained via the standard for test uncertainty, whereas the shaded blue region indicates ± 2 standard deviations of the measured cycle-average values. For $\langle \omega \rangle$ at both facilities, both intervals are on the order of the line width shown.

bottom load cells (Figure A.2a), which show much higher repeatability in practice than what is implied by the manufacturer specifications. Conversely, larger fluctuations in the

quasi-cycle-averaged U_∞^3 are observed (Figure A.2a), which are the result of oscillations in the inflow velocity about the mean as the pumps recirculate water through the flume. These inflow variations likely drive cycle-to-cycle variations in average fluid torque [108] and thus increases cycle-to-cycle variation in C_P. However, the influence of these cycle-to-cycle variations on $\langle C_P \rangle$ is reduced by testing each turbine over many cycles ($\sim 50 - 200$ at λ_{opt} across the parameter space) such that convergence to a "steady-state" $\langle C_P \rangle$ is achieved.

Across all experiments at UNH, the average standard deviation of the cycle-average values of C_P is ≈ 0.005 at λ_{opt}. Compared to the UW results in Figure A.1a, at UNH there is good agreement between the 95% confidence interval for $\langle C_P \rangle$ and ± 2 standard deviations of the measured cycle-average values (Figure A.1b). Similar agreement is observed for the component measurements of $\langle C_P \rangle$ (Figure A.2b). In general, there is less cycle-to-cycle variability than that observed at UW. This is attributable to the steady freestream velocity provided by the tow carriage controller relative to the UW flume pumps. Consequently, cycle-to-cycle variations in the average fluid torque on the rotor are low, even though the UNH turbines were tested for fewer rotational cycles ($\sim 10 - 20$ cycles at λ_{opt}) due to the finite tow tank length.

Appendix B

VARIATION IN PARAMETERS WITH GEOMETRIC CONFIGURATION

Table B.1: Variation in quarter-chord radius, swept radius, and derived quantities due to the blade mounting scheme for each combination of c/R and α_p tested at UNH in Chapter 4.

c [cm]	α_p [deg.]	R [cm]	R' [cm]	R'/R	c/R	A [cm^2]	β [%]
10.10	-2	41.52	42.42	1.02	0.243	9911.6	11.1
	-4	41.51	42.41	1.02	0.243	9910.7	11.1
	-6	41.47	42.40	1.02	0.244	9907.7	11.1
	-8	41.43	42.38	1.02	0.244	9903.5	11.1
15.15	-4	41.51	42.87	1.03	0.365	10016.7	11.2
	-6	41.47	42.87	1.03	0.365	10016.7	11.2
	-8	41.43	42.87	1.03	0.366	10016.7	11.2
20.20	-4	41.51	43.32	1.04	0.487	10123.1	11.3
	-6	41.47	43.34	1.04	0.487	10126.8	11.3
	-8	41.43	43.36	1.05	0.488	10131.7	11.3

Table B.2: Variation in quarter-chord radius, swept radius, and derived quantities due to the blade mounting scheme for each combination of c/R and α_p tested at UW in Chapter 4.

c [cm]	α_p [deg.]	R [cm]	R' [cm]	R'/R	c/R	A [cm^2]	β [%]
2.03	0	8.04	8.23	1.02	0.252	385.0	10.7
	-2	8.15	8.33	1.02	0.249	389.9	10.7 – 10.8
	-4	8.24	8.42	1.02	0.246	393.9	10.8 – 10.9
	-6	8.23	8.41	1.02	0.247	393.7	10.8 – 10.9
3.045	-2	8.15	8.42	1.03	0.374	394.1	10.9
	-4	8.24	8.51	1.03	0.370	398.2	10.9 – 11.1
	-6	8.23	8.51	1.03	0.370	398.0	10.9 – 11.0
	-8	8.21	8.50	1.04	0.371	397.8	11
4.06	-2	8.15	8.60	1.06	0.498	402.5	11.1
	-4	8.24	8.60	1.04	0.493	402.5	11.0 – 11.2
	-6	8.23	8.60	1.05	0.494	402.5	11.0 – 11.2
	-8	8.21	8.60	1.05	0.494	402.5	11.1 – 11.2
	-10	8.20	8.60	1.05	0.495	402.5	11.1 – 11.2
5.075	-2	8.15	8.87	1.09	0.623	415.3	11.5
	-4	8.24	8.83	1.07	0.616	413.2	11.4 - 11.5
	-6	8.23	8.70	1.06	0.617	407.0	11.2 – 11.3
	-8	8.21	8.70	1.06	0.618	407.2	11.2 – 11.3
	-10	8.20	8.71	1.06	0.619	407.4	11.2 – 11.3
	-12	8.18	8.71	1.07	0.621	407.7	11.3
6.09	-4	8.24	9.13	1.11	0.739	427.5	11.7 – 11.9
	-6	8.23	8.98	1.09	0.740	420.3	11.5 – 11.7
	-8	8.21	8.82	1.07	0.742	413.0	11.3 – 11.5
	-10	8.20	8.82	1.08	0.743	412.5	11.3 – 11.4
	-12	8.18	8.83	1.08	0.745	413.1	11.3 – 11.5

Table B.3: Quarter-chord radius R, outermost radius R', and derived quantities for each combination of chord length and preset pitch tested in Chapter 6. The listed β correspond to variations in the *nominal* blockage ratio across geometric configurations, whereas the measured values in Table 6.2 take into account small variations in the water depth across experiments.

c [cm]	α_p [deg.]	R [cm]	R' [cm]	R'/R	c/R	A_{turbines} [cm^2]	β [%]
	0	14.73	15.31	1.04	0.378	1317.0	34.0, 43.8, 53.5
	-2	14.93	15.43	1.03	0.373	1326.6	34.3, 44.1, 53.9
5.57	-4	15.08	15.58	1.03	0.369	1340.1	34.6, 44.5, 54.4
	-6	15.07	15.58	1.03	0.369	1339.6	34.6, 44.5, 54.4
	-8	15.04	15.57	1.04	0.370	1338.9	34.6, 44.5, 54.4
	-2	14.93		1.05	0.497		
	-4	15.08		1.04	0.492		
7.42	-6	15.07	15.75	1.05	0.492	1354.5	35.0, 45.0, 55.0
	-8	15.04		1.05	0.493		
	-10	15.01		1.05	0.494		
	-4	15.08	16.16	1.07	0.615	1390.1	35.9, 46.2, 56.4
	-6	15.07	15.93	1.06	0.616	1369.6	35.4, 45.5, 55.6
9.28	-8	15.04	15.93	1.06	0.617	1370.3	35.4, 45.5, 55.6
	-10	15.01	15.94	1.06	0.618	1371.2	35.4, 45.6, 55.7
	-12	14.98	15.95	1.07	0.619	1372.1	35.5, 45.6, 55.7

Appendix C

LATERAL FORCE COEFFICIENTS FOR THE HIGH-CONFINEMENT CROSS-FLOW TURBINE ARRAY

As noted in Section 3.3, the net lateral force on the array of two identical counter-rotating turbines is approximately zero when $\Delta\theta = 0°$ since the array is symmetric about its centerline. However, by defining the directions of L_A and L_B with this counter-rotation in mind as in Figure 3.4, the array-average lateral force coefficient is nonzero and represents the average lateral force coefficient experienced by an individual rotor in the array, $C_{L,\text{rotor}}$.

C.1 Effect of blockage

Figure C.1 shows the effect of blockage on $C_{L,\text{rotor}} - \lambda$ curves for the same β, flow conditions, and geometry tested in Chapter 5. As for $C_{P,\text{array}}$ and $C_{T,\text{array}}$, the magnitude of $C_{L,\text{rotor}}$ at a particular λ tends to increase with the blockage ratio. Additionally in a similar manner to the array power and thrust coefficients, $C_{L,\text{rotor}}$ also exhibits invariance to β at lower tip-speed ratios ($\lambda \leq 1$ in Figure C.1).

C.2 Effect of geometry

Figure C.2 shows the contours of the time-averaged rotor-average lateral force coefficient at maximum efficiency (i.e., $C_{L,\text{rotor}}|_{\lambda_{\text{opt}}}$) across the parameter space explored in Chapter 6. Trends in $C_{L,\text{rotor}}|_{\lambda_{\text{opt}}}$ with blockage are similar to those of $C_{P,\text{array}}$ and $C_{T,\text{array}}|_{\lambda_{\text{opt}}}$, in that $C_{L,\text{rotor}}|_{\lambda_{\text{opt}}}$ increases with blockage for all geometries, and increases more rapidly for geometries with larger solidity. Other trends in $C_{L,\text{rotor}}|_{\lambda_{\text{opt}}}$ match those observed at for a single turbine at $\approx 11\%$ blockage in Chapter 4 (Figure 4.12). $C_{L,\text{rotor}}|_{\lambda_{\text{opt}}}$ exhibits a strong dependence on the preset pitch angle, and for all tested $\beta{-}N$ combinations, $C_{L,\text{rotor}}|_{\lambda_{\text{opt}}}$ increasing

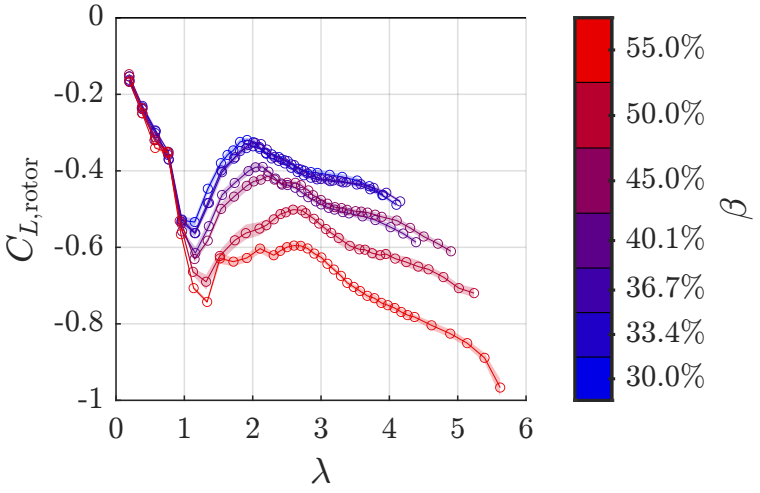

Figure C.1: Time-averaged rotor-average lateral force coefficient as a function of β and λ for the turbine geometry from Chapter 5. The shaded regions indicate the interquartile range of the array- and cycle-averaged performance at each β and λ (the vertical span of the shaded region at each point is similar to the size of the markers for most operating conditions).

with increasing c/R and α_p (i.e., more toe-in preset pitch). Lower lateral force with more negative preset pitch is consistent with trends in the array-average thrust coefficients with α_p (Figures 6.10d to 6.10f), where more toe-out preset pitch reduced the forcing on the array.

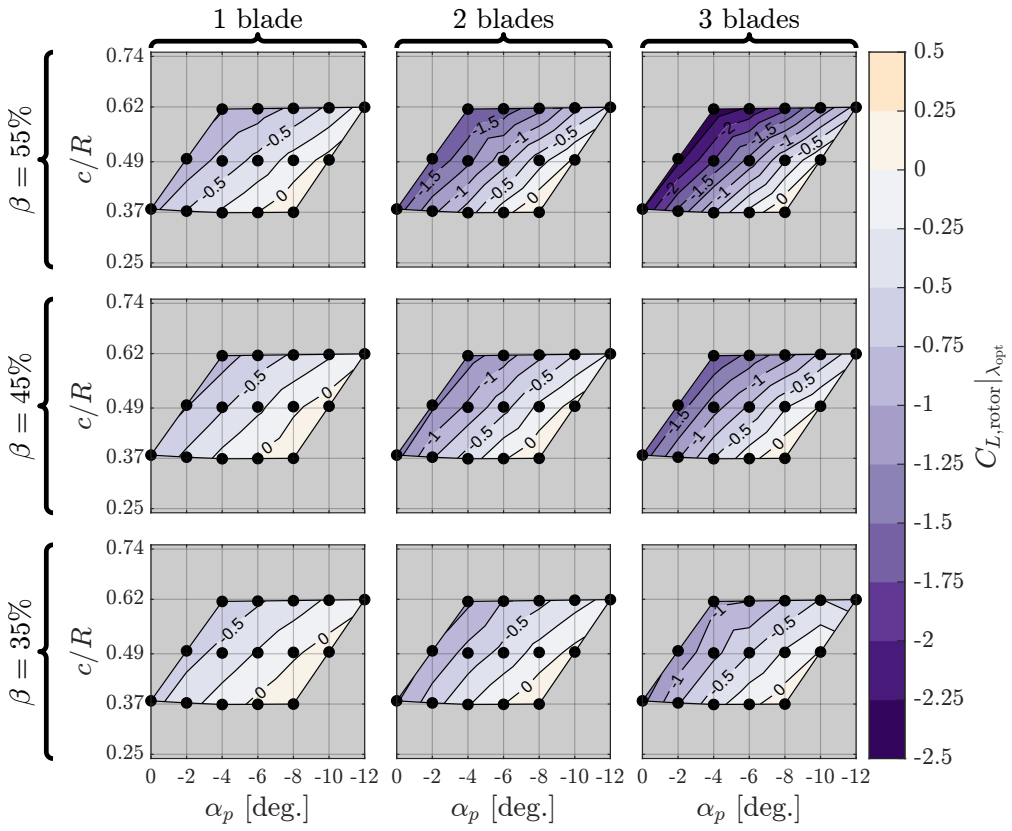

Figure C.2: Contours of the time-average rotor-average lateral coefficient at maximum array performance as a function of c/R and α_p at each β and N tested in Chapter 6.

Appendix D

INFLUENCE OF SUBMERGENCE DEPTH ON ARRAY PERFORMANCE

As mentioned in Section 5.2.2, s/h was maximized at each blockage to limit the influence of ventilation on array performance, particularly at the highest blockage ratios. However, this resulted in variation of s/h across the tested β (Table 5.1). To assess the sensitivity of array performance to submergence depth, the array was also tested at a range of s/h at $\beta = 36.7\%$, 45.0%, and 55.0% through variation of the rotors' vertical position in the water

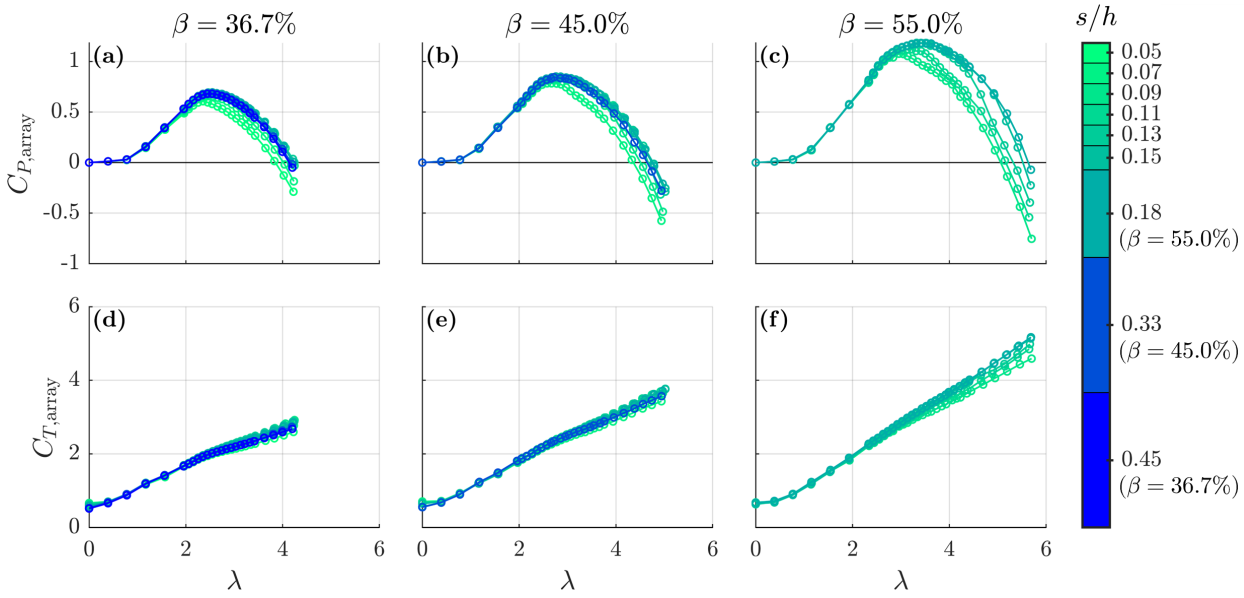

Figure D.1: Time-averaged (a)-(c) $C_{P,\text{array}}$ and (d)-(f) $C_{T,\text{array}}$ as a function of s/h and λ at $\beta = 36.7\%$, 45.0%, and 55.0%. The value of s/h for each β that corresponds to core experimental results (Figure 5.3) is indicated in the colorbar.

column. The ADV position was likewise adjusted such that U_∞ was sampled at the turbine midplane.

The resulting $C_{P,\text{array}}$–λ and $C_{T,\text{array}}$–λ curves are shown in Figure D.1. At $\beta = 36.7\%$ and $\beta = 45.0\%$, both $C_{P,\text{array}}$ and $C_{T,\text{array}}$ increase slightly as s/h decreases (i.e., the turbines are moved closer to the free surface), particularly for λ beyond the performance peak. However, at all β, once s/h drops below a critical value, ventilation begins, resulting in decreased $C_{P,\text{array}}$ and $C_{T,\text{array}}$ relative to deeper submergence depths. As β increases, the onset of ventilation occurs at larger s/h (i.e., deeper submergence), and at a given β, as s/h decreases, ventilation begins at lower λ. However, other than ventilation, the effects of submergence depth on both $C_{P,\text{array}}$ and $C_{T,\text{array}}$ are minor relative to the influence of β, and the associated effects are mainly limited to λ beyond the performance peak. Consequently, variation in s/h across the tested β is unlikely to have significantly affected the trends observed in Figure 5.3.

The normalized submergence depth also affects free surface deformation in the vicinity of the array, as shown in the water depth profiles across Turbine B in Figure D.2 for $\lambda = 1.5$, 2.5, and 3.5 at $\beta = 36.7\%$, 45.0%, and 55.0%. Decreasing s/h tends to elevate the free surface upstream of Turbine B and lower the free surface directly downstream of Turbine B at $x/D' = 0.5$. In other words, the magnitude of the free surface drop across Turbine B generally increases with greater proximity of the rotor to the free surface, and this drop becomes more pronounced as λ and β increase. Trends in the free surface with s/h further downstream ($x/D' = 1 - 2$) are less clear and require further investigation. Since s/h was not held constant in the core set of experiments (Table 6.2), the results in Figure D.2 suggest that the measured flow fields at $x/D' = 0.6$ (Figure 5.5) may be influenced by the decrease in s/h with increasing β. Specifically, the increased free surface deformation at lower s/h would further constrain the flow passing above the turbines, which is expected to increase the bypass velocity in this region and may deflect the wake downward [94].

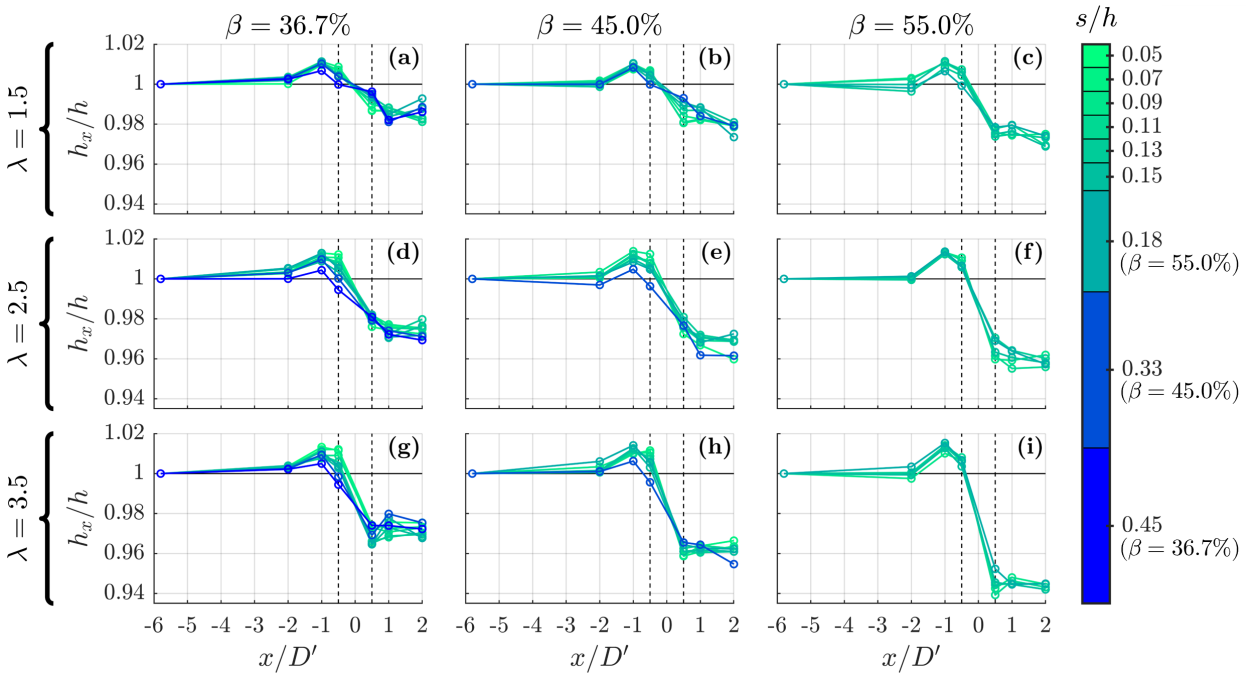

Figure D.2: Time-averaged streamwise water depth profiles at (a) $\beta = 36.7\%$, $\beta = 45.0\%$, and (c) $\beta = 55.0\%$ for (a)–(c) $\lambda = 1.5$, (d)–(f) $\lambda = 2.5$, and (g)–(i) $\lambda = 3.5$. The farthest upstream measurement is taken at the center of the channel, whereas depth measurements in the vicinity of the array are directly upstream and downstream of Turbine B (Figure 3.4). Depth measurements at each streamwise location (h_x) are normalized by the far-upstream water depth (h) measured at the same β and λ. The dashed lines indicate the swept area of Turbine B. The value of s/h for each β that corresponds to core experimental results (Figure 5.3) is indicated in the colorbar.

Appendix E

LIMITATIONS OF BLADE-LEVEL PERFORMANCE ESTIMATION AT HIGH BLOCKAGE

As described in Section 6.2.1, disk end plates are used to connect blades to the central driveshaft of each rotor, which allows for economically testing numerous rotor geometries at high confinement with a common set of blade support structures. However, these end plates generate considerable parasitic torque, which significantly reduces the measured array-average efficiency relative to the same rotor geometry with blades supported by thin, hydrodynamic struts (Figure E.1a). The latter choice of support structure more closely approximates the performance of the blades alone, but would necessitate a unique strut assembly to be fabricated for each geometric configuration. To generalize results, the efficiency of the blades only is estimated using a linear superposition method, in which the measured C_P for the support structures only (i.e., an array of bladeless turbines) is subtracted from the full turbine C_P (Equation 6.1) at the same rotation rate. This technique, which has been shown to yield similar blade-only C_P for turbines with different types of support structures at low blockage ($\beta = 11\%$) [30], assumes that secondary interactions between the blades and the support structures are negligible.

While estimating blade-level efficiency in this way yields moderate agreement in blade-only $C_{P,\text{array}}$ between arrays with strut or disk end plates (Figure E.1b), the blade-only performance curves have greater dependency on the type of support structure used than in prior work [30]. For example, at most λ, blade-only $C_{P,\text{array}}$ is lower for arrays with disk supports than for strut supports, except for at higher λ beyond the performance peak where blade-only $C_{P,\text{array}}$ is artificially elevated for turbines with disks. We hypothesize that this is because, at high blockage, as λ increases, the blade thrust significantly alters the flow field

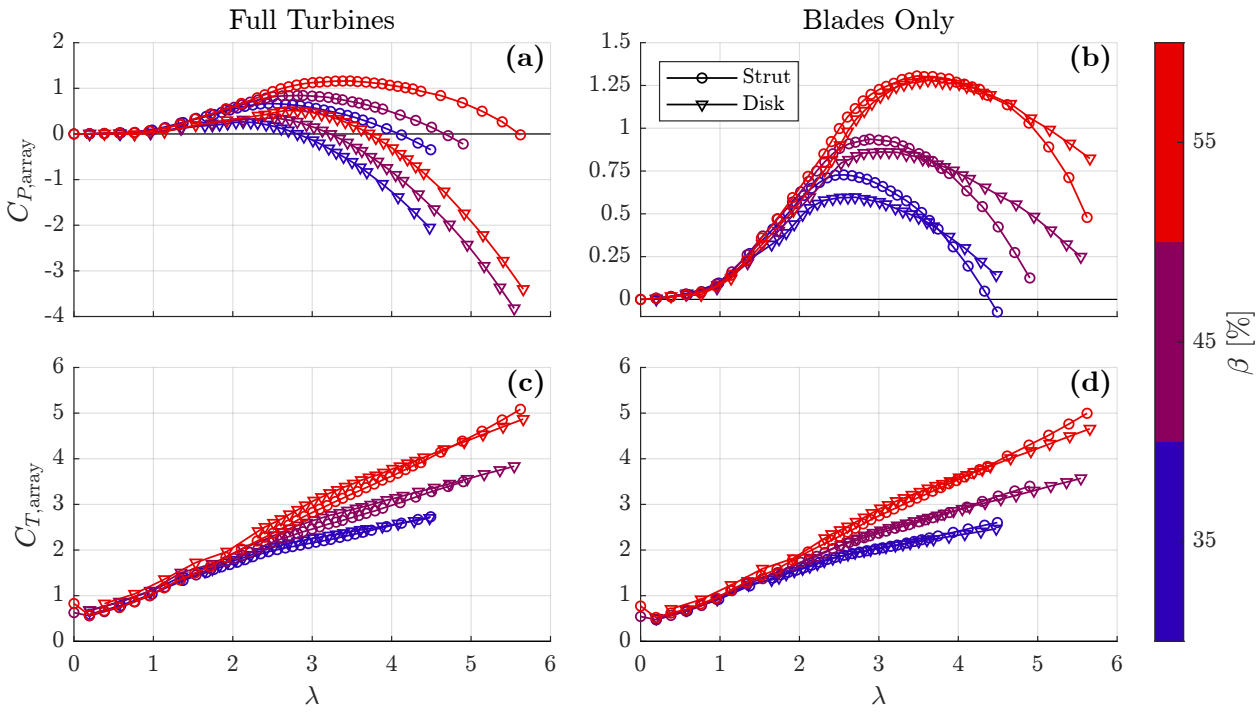

Figure E.1: (a) $C_{P,\text{array}}$ calculated using the full turbine efficiencies (i.e., including support structure losses) compared to (b) $C_{P,\text{array}}$ calculated when those support structure losses are subtracted using Equation 6.1 for a single turbine geometry ($N = 2$, $c/R = 0.49$, $\alpha_p = -6°$) across the tested β. Performance curves shown compare turbines with blade-end strut supports (as in Chapter 5) and for turbines with disk end plates (as in Chapter 6). (c) $C_{T,\text{array}}$ for the full turbines compared to (d) $C_{T,\text{array}}$ if the thrust on the support structures is subtracted using an analogous equation to Equation 6.1.

around the turbine and changes the parasitic torque on the support structures. Consequently, the C_P measured for the support structures alone is not fully representative of that when the blades are present for tip-speed ratios greater than 2. This means that the maximum blade-level efficiency reported for the lowest blockage is likely somewhat under estimated, thereby artificially inflating the difference between $\beta = 35\%$ and 45%. However, the support

structure dependency at higher tip-speed ratios is not material to these results, as this divergence occurs well past the point of maximum efficiency. The uncertainty introduced into the results is, on the balance, reasonable in comparison to the cost of constructing two sets of struts for each geometric configuration ($\approx$ \$2k USD per strut set).

In contrast, the measured array thrust coefficient does not depend significantly on whether struts or disk end plates are used to support the blades (Figure E.1c), implying that the thrust measured for the full turbines is dominated by the force on the blades and driveline. However, given the size of the rotors and their thrust coefficients, the driveline contribution is likely limited. Consequently, support structure subtraction is not employed for $C_{T,\text{array}}$, although the results of an analogous method to Equation 6.1 for thrust are shown in Figure E.1d.

Since similar blade support structures were used for all turbines in this study, the choice of support structure is not expected to significantly affect the trends observed in blade-only $C_{P,\text{array}}$. However, if using these results to validate numerical and reduced-order models, it would be important to be mindful of how the choice of support structure affects the estimated values for blade-only $C_{P,\text{array}}$, particularly a higher tip-speed ratios.

Appendix F

ADDITIONAL BLUFF BODY SCALING RESULTS

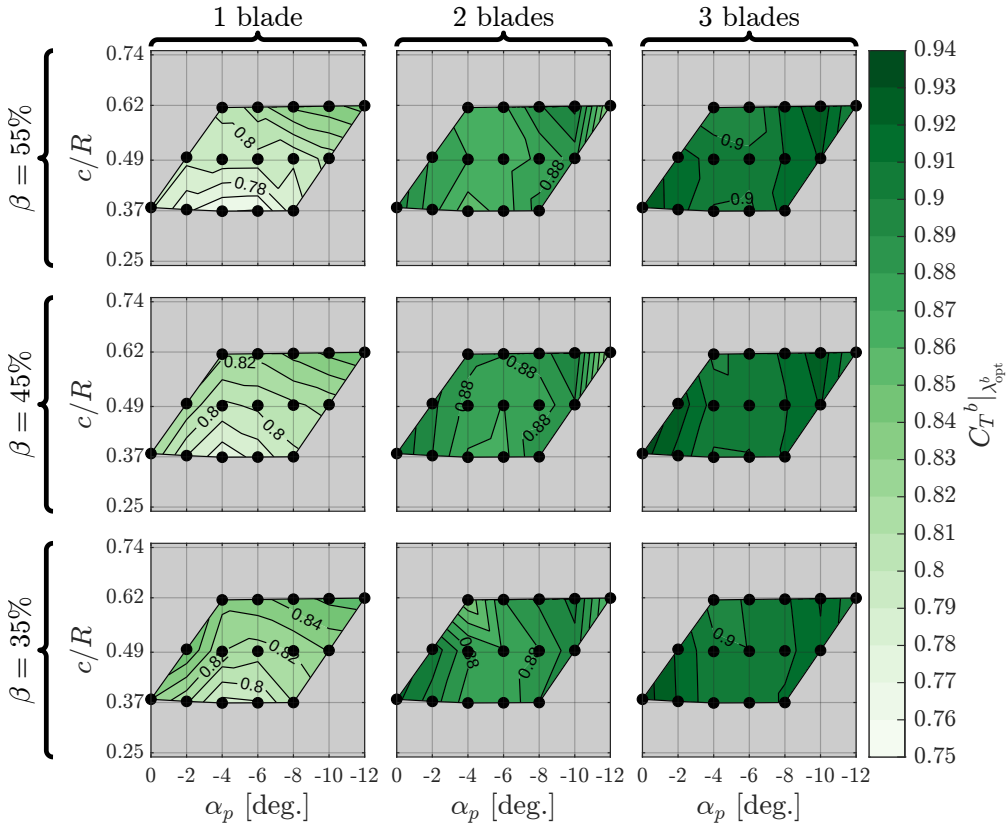

Figure F.1: Contours of the bluff-body scaled $C_T{}^b$ corresponding to maximum $C_P{}^b$ as a function of c/R and α_p for each combination of β and N. Collapse in $C_T{}^b$ at maximum $C_P{}^b$ improves as N increases, which may suggest that Maskell-inspired bluff body performance scaling is more representative of these higher solidity rotors.

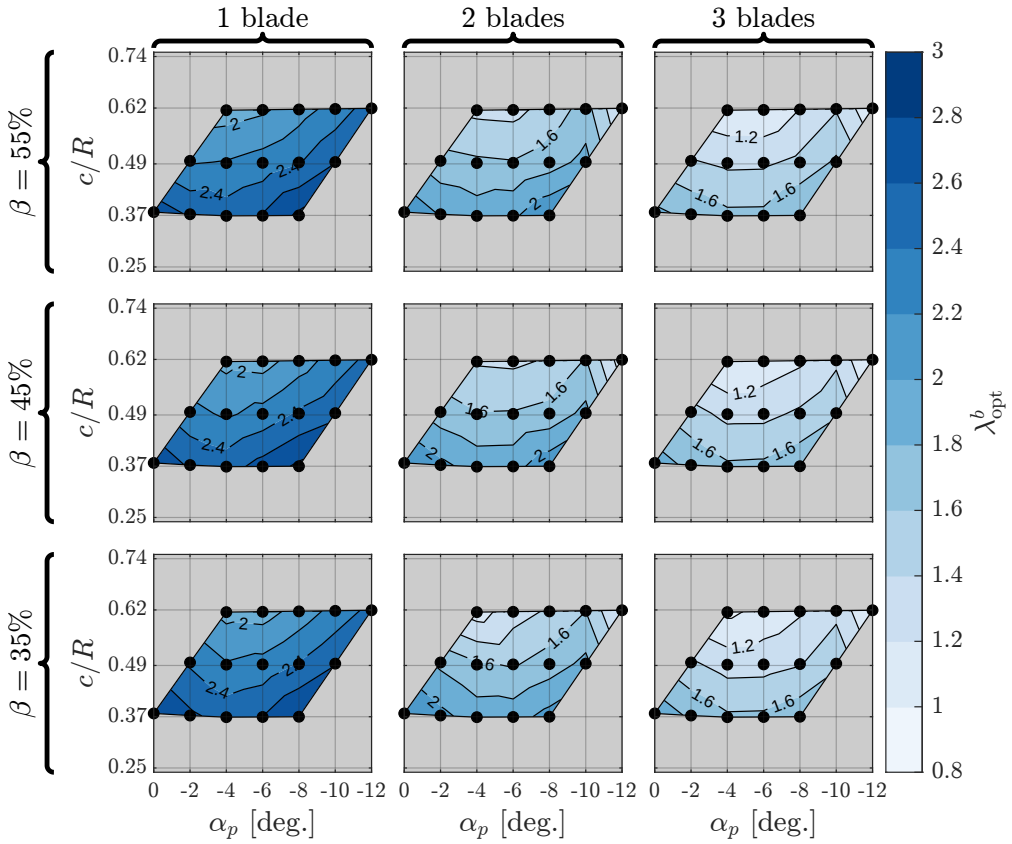

Figure F.2: Contours of the bluff-body scaled λ^b corresponding to maximum ${C_P}^b$ as a function of c/R and α_p for each combination of β and N. Collapse in λ_b at maximum ${C_P}^b$ across the tested blockages is not significantly affected by the rotor geometry.

BIBLIOGRAPHY

[1] E. Maskell, "A Theory of the Blockage Effects on Bluff Bodies and Stalled Wings in a Closed Wind Tunnel," Ministry of Aviation, Reports and Memoranda 3400, 1963. [Online]. Available: https://apps.dtic.mil/sti/citations/ADA955243.

[2] A. Rezaeiha, H. Montazeri, and B. Blocken, "Towards optimal aerodynamic design of vertical axis wind turbines: Impact of solidity and number of blades," *Energy*, vol. 165, pp. 1129–1148, 2018. DOI: 10.1016/j.energy.2018.09.192.

[3] G. Houlsby, S. Draper, and M. Oldfield, "Application of linear momentum actuator disc theory to open channel flow," University of Oxford, Technical Report OUEL 2296/08, 2008. [Online]. Available: https://ora.ox.ac.uk/objects/uuid:5576d575-7bac-44b6-ac79-f698edcda40e.

[4] United Nations General Assembly, *Transforming our world: The 2030 Agenda for Sustainable Development*, 2015.

[5] J. H. Williams *et al.*, "Carbon-Neutral Pathways for the United States," *AGU Advances*, vol. 2, no. 1, e2020AV000284, 2021. DOI: 10.1029/2020AV000284.

[6] International Energy Agency, "World Energy Outlook 2023," International Energy Agency, 2023.

[7] A. LiVecchi *et al.*, "Powering the Blue Economy: Exploring Opportunities for Marine Renewable Energy in Maritime Markets," United States Department of Energy, Washington, D.C., Office of Energy Efficiency and Renewable Energy, 2019.

[8] C. Garrett and P. Cummins, "The efficiency of a turbine in a tidal channel," *Journal of Fluid Mechanics*, vol. 588, pp. 243–251, 2007. DOI: 10.1017/S0022112007007781.

[9] J. I. Whelan, J. M. R. Graham, and J. Peiró, "A free-surface and blockage correction for tidal turbines," *Journal of Fluid Mechanics*, vol. 624, pp. 281–291, 2009. DOI: 10.1017/S0022112009005916.

[10] G. Houlsby and C. Vogel, "The power available to tidal turbines in an open channel flow," *Proceedings of Institution of Civil Engineers: Energy*, vol. 170, no. 1, pp. 12–21, 2017. DOI: 10.1680/jener.15.00035.

[11] T. Kinsey and G. Dumas, "Impact of channel blockage on the performance of axial and cross-flow hydrokinetic turbines," *Renewable Energy*, vol. 103, pp. 239–254, 2017. DOI: 10.1016/j.renene.2016.11.021.

[12] A. Hunt, C. Stringer, and B. Polagye, "Effect of aspect ratio on cross-flow turbine performance," *Journal of Renewable and Sustainable Energy*, vol. 12, no. 054501, 2020. DOI: 10.1063/5.0016753.

[13] S. Brusca, R. Lanzafame, and M. Messina, "Design of a vertical-axis wind turbine: How the aspect ratio affects the turbine's performance," *International Journal of Energy and Environmental Engineering*, vol. 5, no. 4, pp. 333–340, 2014. DOI: 10.1007/s40095-014-0129-x.

[14] Q. Li *et al.*, "Effect of rotor aspect ratio and solidity on a straight-bladed vertical axis wind turbine in three-dimensional analysis by the panel method," *Energy*, vol. 121, pp. 1–9, 2017. DOI: 10.1016/j.energy.2016.12.112.

[15] M. Shiono, K. Suzuki, and S. Kiho, "Output Characteristics of Darrieus Water Turbine with Helical Blades for Tidal Current Generations," in *Proceedings of the International Offshore and Polar Engineering Conference*, vol. 12, Kitakyushu, Japan, 2002, pp. 859–864.

[16] G. Saini and R. P. Saini, "A review on technology, configurations, and performance of cross-flow hydrokinetic turbines," *International Journal of Energy Research*, vol. 43, no. 13, pp. 6639–6679, 2019. DOI: 10.1002/er.4625.

[17] M. R. Castelli, S. De Betta, and E. Benini, "Effect of Blade Number on a Straight-Bladed Vertical-Axis Wind Turbine," *International Journal of Aerospace and Mechanical Engineering*, vol. 6, no. 1, pp. 68–74, 2012. DOI: 10.1299/transjsme.2014fe0223.

[18] Q. Li, T. Maeda, Y. Kamada, J. Murata, K. Furukawa, and M. Yamamoto, "Effect of number of blades on aerodynamic forces on a straight-bladed Vertical Axis Wind Turbine," *Energy*, vol. 90, pp. 784–795, 2015. DOI: 10.1016/j.energy.2015.07.115.

[19] D. B. Araya, T. Colonius, and J. O. Dabiri, "Transition to bluff-body dynamics in the wake of vertical-axis wind turbines," *Journal of Fluid Mechanics*, vol. 813, pp. 346–381, 2017. DOI: 10.1017/jfm.2016.862.

[20] M. A. Miller, S. Duvvuri, and M. Hultmark, "Solidity effects on the performance of vertical-axis wind turbines," *Flow*, vol. 1, 2021. DOI: 10.1017/flo.2021.9.

[21] C. Simão Ferreira and B. Geurts, "Aerofoil optimization for vertical axis wind turbines," *Wind Energy*, vol. 18, no. 8, pp. 1371–1385, 2015. DOI: 10.1002/we.

[22] G. Bedon, S. De Betta, and E. Benini, "Performance-optimized airfoil for Darrieus wind turbines," *Renewable Energy*, vol. 94, pp. 328–340, 2016. DOI: 10.1016/j.renene.2016.03.071.

[23] P. C. Klimas and M. H. Worstell, "Effects of blade preset pitch/offset on curved-blade Darrieus vertical axis wind turbine performance," Sandia National Labs., Albuquerque, NM (USA), SAND-81-1762, 1981. [Online]. Available: https://www.osti.gov/biblio/5243044.

[24] A. J. Fiedler and S. Tullis, "Blade Offset and Pitch Effects on a High Solidity Vertical Axis Wind Turbine," *Wind Engineering*, vol. 33, no. 3, pp. 237–246, 2009. DOI: 10.1260/030952409789140955.

[25] M. Somoano and F. J. Huera-Huarte, "The dead band in the performance of cross-flow turbines: Effects of Reynolds number and blade pitch," *Energy Conversion and Management*, vol. 172, pp. 277–284, 2018. DOI: 10.1016/j.enconman.2018.06.087.

[26] P. G. Migliore, W. P. Wolfe, and J. B. Fanucci, "Flow Curvature Effects on Darrieus Turbine Blade Aerodynamics," *Journal of Energy*, vol. 4, no. 2, pp. 49–55, 1980. DOI: 10.2514/3.62459.

[27] Y. Takamatsu, A. Furukawa, K. Okuma, and K. Takenouchi, "Experimental Studies on a Preferable Blade Profile for High Efficiency and the Blade Characteristics of Darrieus-Type Cross-Flow Water Turbines," *JSME international journal. Ser. 2, Fluids engineering, heat transfer, power, combustion, thermophysical properties*, vol. 34, no. 2, pp. 149–156, 1991. DOI: 10.1299/jsmeb1988.34.2_149.

[28] F. Balduzzi, A. Bianchini, R. Maleci, G. Ferrara, and L. Ferrari, "Blade Design Criteria to Compensate the Flow Curvature Effects in H-Darrieus Wind Turbines," *Journal of Turbomachinery*, vol. 137, no. 1, pp. 011 006–011 006, 2015. DOI: 10.1115/1.4028245.

[29] A. Bianchini, G. Ferrara, and L. Ferrari, "Design guidelines for H-Darrieus wind turbines: Optimization of the annual energy yield," *Energy Conversion and Management*, vol. 89, pp. 690–707, 2015. DOI: 10.1016/j.enconman.2014.10.038.

[30] B. Strom, N. Johnson, and B. Polagye, "Impact of blade mounting structures on cross-flow turbine performance," *Journal of Renewable and Sustainable Energy*, vol. 10, no. 3, p. 034 504, 2018. DOI: 10.1063/1.5025322.

[31] T. Villeneuve, G. Winckelmans, and G. Dumas, "Increasing the efficiency of vertical-axis turbines through improved blade support structures," *Renewable Energy*, vol. 169, pp. 1386–1401, 2021. DOI: 10.1016/j.renene.2021.01.092.

[32] P. Bachant and M. Wosnik, "Effects of Reynolds Number on the Energy Conversion and Near-Wake Dynamics of a High Solidity Vertical-Axis Cross-Flow Turbine," *Energies*, vol. 9, no. 2, pp. 73–73, 2016. DOI: 10.3390/en9020073.

[33] M. A. Miller, S. Duvvuri, I. Brownstein, M. Lee, J. O. Dabiri, and M. Hultmark, "Vertical-Axis Wind Turbine Experiments at Full Dynamic Similarity," *Journal of Fluid Mechanics*, vol. 844, pp. 707–720, 2018. DOI: 10.1017/jfm.2018.197.

[34] H. Ross and B. Polagye, "An experimental assessment of analytical blockage corrections for turbines," *Renewable Energy*, vol. 152, pp. 1328–1341, 2020. DOI: 10.1016/j.renene.2020.01.135.

[35] A. Laneville and P. Vittecoq, "Dynamic Stall: The Case of the Vertical Axis Wind Turbine," *Journal of Solar Energy Engineering*, vol. 108, no. 2, pp. 140–145, 1986. DOI: 10.1115/1.3268081.

[36] C. Simão Ferreira, G. Van Kuik, G. Van Bussel, and F. Scarano, "Visualization by PIV of dynamic stall on a vertical axis wind turbine," *Experiments in Fluids*, vol. 46, no. 1, pp. 97–108, 2009. DOI: 10.1007/s00348-008-0543-z.

[37] A.-J. Buchner, J. Soria, D. Honnery, and A. J. Smits, "Dynamic stall in vertical axis wind turbines: Scaling and topological considerations," *Journal of Fluid Mechanics*, vol. 841, pp. 746–766, 2018. DOI: 10.1017/jfm.2018.112.

[38] A. Snortland, B. Polagye, and O. Williams, "Influence of Near-blade hydrodynamics on Cross-flow Turbine performance," in *Proceedings of the 13th European Wave and Tidal Energy Conference*, Napoli, Italy, 2019.

[39] S. Le Fouest and K. Mulleners, "The dynamic stall dilemma for vertical-axis wind turbines," *Renewable Energy*, vol. 198, pp. 505–520, 2022. DOI: 10.1016/j.renene.2022.07.071.

[40] M. W. Lohry and L. Martinelli, "Unsteady Reynolds-Averaged Navier–Stokes Simulation of Crossflow Rotors, Scaling, and Blockage Effects," *AIAA Journal*, vol. 54, no. 12, pp. 3828–3839, 2016. DOI: 10.2514/1.J055069.

[41] T. Burton, N. Jenkins, D. Sharpe, and E. Bossanyi, *Wind Energy Handbook, Second Edition*. Wiley, 2011. DOI: 10.1002/9781119992714.

[42] I. Paraschivoiu, *Wind Turbine Design with Emphasis on Darrieus Concept*. Polytechnic International Press, 2002.

[43] M. Islam, D. S.-K. Ting, and A. Fartaj, "Aerodynamic models for Darrieus-type straight-bladed vertical axis wind turbines," *Renewable and Sustainable Energy Reviews*, vol. 12, no. 4, pp. 1087–1109, 2008. DOI: 10.1016/j.rser.2006.10.023.

[44] A. A. Mohammed, H. M. Ouakad, A. Z. Sahin, and H. M. Bahaidarah, "Vertical Axis Wind Turbine Aerodynamics: Summary and Review of Momentum Models," *Journal of Energy Resources Technology, Transactions of the ASME*, vol. 141, no. 5, pp. 050 801–050 801, 2019. DOI: 10.1115/1.4042643.

[45] A. Alaimo, A. Esposito, A. Messineo, C. Orlando, and D. Tumino, "3D CFD Analysis of a Vertical Axis Wind Turbine," *Energies*, vol. 8, no. 4, pp. 3013–3033, 2015. DOI: 10.3390/en8043013.

[46] O. Gauvin-Tremblay and G. Dumas, "Two-way interaction between river and deployed cross-flow hydrokinetic turbines," *Journal of Renewable and Sustainable Energy*, vol. 12, no. 3, pp. 034 501–034 501, 2020. DOI: 10.1063/5.0004492.

[47] M. Dave and J. A. Franck, "Analysis of dynamic stall development on a cross-flow turbine blade," *Physical Review Fluids*, vol. 8, no. 7, p. 074 702, 2023. DOI: 10.1103/PhysRevFluids.8.074702.

[48] P. Bachant, M. Wosnik, B. Gunawan, and V. S. Neary, "Experimental Study of a Reference Model Vertical-Axis Cross-Flow Turbine," *PLoS ONE*, vol. 11, no. 9, e.0163799–e.0163799, 2016. DOI: 10.1371/journal.pone.0163799.

[49] B. Strom, S. L. Brunton, and B. Polagye, "Intracycle angular velocity control of cross-flow turbines," *Nature Energy*, vol. 2, no. 8, pp. 1–9, 8 2017. DOI: 10.1038/nenergy.2017.103.

[50] I. Scherl, B. Strom, S. L. Brunton, and B. L. Polagye, "Geometric and control optimization of a two cross-flow turbine array," *Journal of Renewable and Sustainable Energy*, vol. 12, no. 6, p. 064 501, 2020. DOI: 10.1063/5.0022428.

[51] H. C. Tsai and T. Colonius, "Coriolis Effect on Dynamic Stall in a Vertical Axis Wind Turbine," *AIAA Journal*, vol. 54, no. 1, pp. 216–226, 2016. DOI: 10.2514/1.J054199.

[52] A. J. Buchner, M. W. Lohry, L. Martinelli, J. Soria, and A. J. Smits, "Dynamic stall in vertical axis wind turbines: Comparing experiments and computations," *Journal of Wind Engineering and Industrial Aerodynamics*, vol. 146, pp. 163–171, 2015. DOI: 10.1016/j.jweia.2015.09.001.

[53] F. Balduzzi, A. Bianchini, R. Maleci, G. Ferrara, and L. Ferrari, "Critical issues in the CFD simulation of Darrieus wind turbines," *Renewable Energy*, vol. 85, pp. 419–435, 2016. DOI: 10.1016/j.renene.2015.06.048.

[54] C. Simão Ferreira, H. A. Madsen, M. Barone, B. Roscher, P. Deglaire, and I. Arduin, "Comparison of aerodynamic models for Vertical Axis Wind Turbines," in *Journal of Physics: Conference Series*, 2014, pp. 012 125–012 125. DOI: 10.1088/1742-6596/524/1/012125.

[55] P. Bachant and M. Wosnik, "Modeling the near-wake of a vertical-axis cross-flow turbine with 2-D and 3-D RANS," *Journal of Renewable and Sustainable Energy*, vol. 8, no. 5, pp. 053 311–053 311, 2016. DOI: 10.1063/1.4966161.

[56] A. Bianchini, F. Balduzzi, P. Bachant, G. Ferrara, and L. Ferrari, "Effectiveness of two-dimensional CFD simulations for Darrieus VAWTs: A combined numerical and experimental assessment," *Energy Conversion and Management*, vol. 136, pp. 318–328, 2017. DOI: 10.1016/j.enconman.2017.01.026.

[57] A. Hunt and B. Polagye, "Experimental techniques for evaluating the performance of high-blockage cross-flow turbine arrays," in *Proceedings of the 15th European Wave and Tidal Energy Conference*, vol. 15, 2023. DOI: 10.36688/ewtec-2023-203.

[58] J. H. Strickland, "Darrieus turbine: A performance prediction model using multiple streamtubes," Sandia Labs., Albuquerque, N.Mex. (USA), SAND-75-0431, 1975. [Online]. Available: https://www.osti.gov/biblio/5004816.

[59] G. Bedon, E. G. A. Antonini, S. De Betta, M. Raciti Castelli, and E. Benini, "Evaluation of the different aerodynamic databases for vertical axis wind turbine simulations," *Renewable and Sustainable Energy Reviews*, vol. 40, pp. 386–399, 2014. DOI: 10.1016/j.rser.2014.07.126.

[60] A. Snortland, A. Hunt, O. Williams, and B. Polagye. "Influence of the downstream blade sweep on cross-flow turbine performance." arXiv: 2404.19072 [physics]. (2024), [Online]. Available: http://arxiv.org/abs/2404.19072, preprint.

[61] W. J. McCroskey, "The phenomenon of dynamic stall," National Aeronautics and Space Administration, A-8464, 1981.

[62] A. Bianchini, E. A. Carnevale, and L. Ferrari, "A Model to Account for the Virtual Camber Effect in the Performance Prediction of an H-Darrieus VAWT Using the Momentum Models," *Wind Engineering*, vol. 35, no. 4, pp. 465–482, 2011. DOI: 10.1260/0309-524X.35.4.465.

[63] A. Bianchini *et al.*, "Implementation of the "Virtual Camber" Transformation into the Open Source Software QBlade: Validation and Assessment," *Energy Procedia*, vol. 148, pp. 210–217, 2018. DOI: 10.1016/j.egypro.2018.08.070.

[64] J. M. Rainbird *et al.*, "On the influence of virtual camber effect on airfoil polars for use in simulations of Darrieus wind turbines," *Energy Conversion and Management*, vol. 106, pp. 373–384, 2015. DOI: 10.1016/j.enconman.2015.09.053.

[65] S. van der Horst, J. E. van de Wiel, C. S. Ferreira, and N. R. García, "Flow Curvature Effects for VAWT: A Review of Virtual Airfoil Transformations and Implementation in XFOIL," in *34th Wind Energy Symposium*, American Institute of Aeronautics and Astronautics, 2016. DOI: 10.2514/6.2016-1734.

[66] A. Bianchini, F. Balduzzi, G. Ferrara, and L. Ferrari, "Virtual incidence effect on rotating airfoils in Darrieus wind turbines," *Energy Conversion and Management*, vol. 111, pp. 329–338, 2016. DOI: 10.1016/j.enconman.2015.12.056.

[67] P. G. Migliore and W. P. Wolfe, "Effects of flow curvature on the aerodynamics of Darrieus wind turbines," West Virginia University, Morgantown, West Virginia, ORO-5135-77/7, 1980. DOI: 10.2172/5049529.

[68] Y. Takamatsu, A. Furukawa, K. Okuma, and Y. Shimogawa, "Study on Hydrodynamic Performance of Darrieus-type Cross-flow Water Turbine," *Bulletin of JSME*, vol. 28, no. 240, pp. 1119–1127, 1985. DOI: 10.1299/jsme1958.28.1119.

[69] Y. Takamatsu, A. Furukawa, K. Okuma, and K. Takenouchi, "Effects of Geometrical Attitude of Blade on Hydrodynamic Performance of Darrieus-type Cross-flow Water Turbine," *Bulletin of JSME*, vol. 28, no. 240, pp. 1092–1096, 1985. DOI: 10.1299/jsme1958.28.1092.

[70] B. Strom, S. Brunton, and B. Polagye, "Consequences of Preset Pitch Angle on Cross-Flow Turbine Hydrodynamics," in *Proceedings of the 11th European Wave and Tidal Energy Conference*, Nantes, France, 2015.

[71] Q. Li *et al.*, "Effect of solidity on aerodynamic forces around straight-bladed vertical axis wind turbine by wind tunnel experiments (depending on number of blades)," *Renewable Energy*, vol. 96, pp. 928–939, 2016. DOI: 10.1016/j.renene.2016.05.054.

[72] P. Migliore, "Comparison of NACA 6-series and 4-digit airfoils for Darrieus wind turbines," *Journal of Energy*, vol. 7, no. 4, pp. 291–292, 1983. DOI: 10.2514/3.48083.

[73] P. Ouro, T. Stoesser, and L. Ramírez, "Effect of Blade Cambering on Dynamic Stall in View of Designing Vertical Axis Turbines," *Journal of Fluids Engineering*, vol. 140, no. 6, 2018. DOI: 10.1115/1.4039235.

[74] L. Du, G. Ingram, and R. G. Dominy, "Experimental study of the effects of turbine solidity, blade profile, pitch angle, surface roughness, and aspect ratio on the H-Darrieus wind turbine self-starting and overall performance," *Energy Science & Engineering*, vol. 7, no. 6, pp. 2421–2436, 2019. DOI: 10.1002/ese3.430.

[75] R. Howell, N. Qin, J. Edwards, and N. Durrani, "Wind tunnel and numerical study of a small vertical axis wind turbine," *Renewable Energy*, vol. 35, no. 2, pp. 412–422, 2010. DOI: 10.1016/j.renene.2009.07.025.

[76] L. Priegue and T. Stoesser, "The influence of blade roughness on the performance of a vertical axis tidal turbine," *International Journal of Marine Energy*, vol. 17, pp. 136–146, 2017. DOI: 10.1016/j.ijome.2017.01.009.

[77] P. B. S. Lissaman, "Low-Reynolds-Number Airfoils," *Annual Review of Fluid Mechanics*, vol. 15, no. 1, pp. 223–239, 1983. DOI: 10.1146/annurev.fl.15.010183.001255.

[78] T. Nishino and R. H. J. Willden, "The efficiency of an array of tidal turbines partially blocking a wide channel," *Journal of Fluid Mechanics*, vol. 708, pp. 596–606, 2012. DOI: 10.1017/jfm.2012.349.

[79] C. R. Vogel, G. T. Houlsby, and R. H. J. Willden, "Effect of free surface deformation on the extractable power of a finite width turbine array," *Renewable Energy*, vol. 88, pp. 317–324, 2016. DOI: 10.1016/j.renene.2015.11.050.

[80] T. Nishino and R. H. J. Willden, "Two-scale dynamics of flow past a partial cross-stream array of tidal turbines," *Journal of Fluid Mechanics*, vol. 730, pp. 220–244, 2013. DOI: 10.1017/jfm.2013.340.

[81] D. Dehtyriov, A. M. Schnabl, C. R. Vogel, S. Draper, T. a. A. Adcock, and R. H. J. Willden, "Fractal-like actuator disc theory for optimal energy extraction," *Journal of Fluid Mechanics*, vol. 927, A40, 2021. DOI: 10.1017/jfm.2021.766.

[82] R. McAdam, G. Houlsby, M. Oldfield, and M. McCulloch, "Experimental testing of the transverse horizontal axis water turbine," *IET Renewable Power Generation*, vol. 4, no. 6, p. 510, 2010. DOI: 10.1049/iet-rpg.2009.0194.

[83] L. Battisti, L. Zanne, S. Dell'Anna, V. Dossena, G. Persico, and B. Paradiso, "Aerodynamic Measurements on a Vertical Axis Wind Turbine in a Large Scale Wind Tunnel," *Journal of Energy Resources Technology*, vol. 133, no. 3, 2011. DOI: 10.1115/1.4004360.

[84] T. Y. Chen and L. R. Liou, "Blockage corrections in wind tunnel tests of small horizontal-axis wind turbines," *Experimental Thermal and Fluid Science*, vol. 35, no. 3, pp. 565–569, 2011. DOI: 10.1016/j.expthermflusci.2010.12.005.

[85] I. Ross and A. Altman, "Wind tunnel blockage corrections: Review and application to Savonius vertical-axis wind turbines," *Journal of Wind Engineering and Industrial Aerodynamics*, vol. 99, no. 5, pp. 523–538, 2011. DOI: 10.1016/j.jweia.2011.02.002.

[86] S. McTavish, D. Feszty, and F. Nitzsche, "An experimental and computational assessment of blockage effects on wind turbine wake development," *Wind Energy*, vol. 17, no. 10, pp. 1515–1529, 2014. DOI: 10.1002/we.1648.

[87] J. Ryi, W. Rhee, U. Chang Hwang, and J.-S. Choi, "Blockage effect correction for a scaled wind turbine rotor by using wind tunnel test data," *Renewable Energy*, Selected Papers on Renewable Energy: AFORE 2013, vol. 79, pp. 227–235, 2015. DOI: 10.1016/j.renene.2014.11.057.

[88] V. Dossena *et al.*, "An Experimental Study of the Aerodynamics and Performance of a Vertical Axis Wind Turbine in a Confined and Unconfined Environment," *Journal of Energy Resources Technology*, vol. 137, no. 5, 2015. DOI: 10.1115/1.4030448.

[89] H. Jeong, S. Lee, and S.-D. Kwon, "Blockage corrections for wind tunnel tests conducted on a Darrieus wind turbine," *Journal of Wind Engineering and Industrial Aerodynamics*, vol. 179, pp. 229–239, 2018. DOI: 10.1016/j.jweia.2018.06.002.

[90] H. Ross and B. Polagye, "An experimental evaluation of blockage effects on the wake of a cross-flow current turbine," *Journal of Ocean Engineering and Marine Energy*, vol. 6, no. 3, pp. 263–275, 2020. DOI: 10.1007/s40722-020-00172-w.

[91] T. Nishino and R. H. J. Willden, "Effects of 3-D channel blockage and turbulent wake mixing on the limit of power extraction by tidal turbines," *International Journal of Heat and Fluid Flow*, vol. 37, pp. 123–135, 2012. DOI: 10.1016/j.ijheatfluidflow.2012.05.002.

[92] C. A. Consul, R. H. Willden, and S. C. McIntosh, "Blockage effects on the hydrodynamic performance of a marine cross-flow turbine," *Philosophical Transactions of the Royal Society A: Mathematical, Physical and Engineering Sciences*, vol. 371, no. 1985, pp. 20 120 299–20 120 299, 2013. DOI: 10.1098/rsta.2012.0299.

[93] A. Goude and O. Ågren, "Simulations of a vertical axis turbine in a channel," *Renewable Energy*, vol. 63, pp. 477–485, 2014. DOI: 10.1016/j.renene.2013.09.038.

[94] N. Kolekar and A. Banerjee, "Performance characterization and placement of a marine hydrokinetic turbine in a tidal channel under boundary proximity and blockage effects," *Applied Energy*, vol. 148, pp. 121–133, 2015. DOI: 10.1016/j.apenergy.2015.03.052.

[95] J. Schluntz and R. H. J. Willden, "The effect of blockage on tidal turbine rotor design and performance," *Renewable Energy*, vol. 81, pp. 432–441, 2015. DOI: 10.1016/j.renene.2015.02.050.

[96] E. Gauthier, T. Kinsey, and G. Dumas, "Impact of Blockage on the Hydrodynamic Performance of Oscillating-Foils Hydrokinetic Turbines," *Journal of Fluids Engineering*, vol. 138, no. 091103, 2016. DOI: 10.1115/1.4033298.

[97] H. Sarlak, T. Nishino, L. A. Martínez-Tossas, C. Meneveau, and J. N. Sørensen, "Assessment of blockage effects on the wake characteristics and power of wind turbines," *Renewable Energy*, vol. 93, pp. 340–352, 2016. DOI: 10.1016/j.renene.2016.01.101.

[98] M. Badshah, J. VanZwieten, S. Badshah, and S. Jan, "CFD study of blockage ratio and boundary proximity effects on the performance of a tidal turbine," *IET Renewable Power Generation*, vol. 13, no. 5, pp. 744–749, 2019. DOI: 10.1049/iet-rpg.2018.5134.

[99] F. Zilic de Arcos, G. Tampier, and C. R. Vogel, "Numerical analysis of blockage correction methods for tidal turbines," *Journal of Ocean Engineering and Marine Energy*, vol. 6, no. 2, pp. 183–197, 2020. DOI: 10.1007/s40722-020-00168-6.

[100] A. Abutunis and V. G. Menta, "Comprehensive Parametric Study of Blockage Effect on the Performance of Horizontal Axis Hydrokinetic Turbines," *Energies*, vol. 15, no. 7, p. 2585, 7 2022. DOI: 10.3390/en15072585.

[101] D. Zhang, P. Guo, Y. Cheng, Q. Hu, and J. Li, "Analysis of blockage correction methods for high-solidity hydrokinetic turbines: Experimental and numerical investigations," *Ocean Engineering*, vol. 283, p. 115 185, 2023. DOI: 10.1016/j.oceaneng.2023.115185.

[102] H. Ross and B. Polagye, "Effects of dimensionless parameters on the performance of a cross-flow current turbine," *Journal of Fluids and Structures*, vol. 114, p. 103 726, 2022. DOI: 10.1016/j.jfluidstructs.2022.103726.

[103] R. A. McAdam, G. T. Houlsby, and M. L. G. Oldfield, "Experimental measurements of the hydrodynamic performance and structural loading of the Transverse Horizontal Axis Water Turbine: Part 1," *Renewable Energy*, vol. 59, pp. 105–114, 2013. DOI: 10.1016/j.renene.2013.03.016.

[104] R. A. McAdam, G. T. Houlsby, and M. L. G. Oldfield, "Experimental measurements of the hydrodynamic performance and structural loading of the transverse horizontal axis water turbine: Part 2," *Renewable Energy*, vol. 59, pp. 141–149, 2013. DOI: 10.1016/j.renene.2013.03.015.

[105] A. H. Birjandi, E. L. Bibeau, V. Chatoorgoon, and A. Kumar, "Power measurement of hydrokinetic turbines with free-surface and blockage effect," *Ocean Engineering*, vol. 69, pp. 9–17, 2013. DOI: 10.1016/j.oceaneng.2013.05.023.

[106] Y. L. Young, C. M. Harwood, F. M. Montero, J. C. Ward, and S. L. Ceccio, "Ventilation of Lifting Bodies: Review of the Physics and Discussion of Scaling Effects," *Applied Mechanics Reviews*, vol. 69, no. 1, pp. 010 801–010 801, 2017. DOI: 10.1115/1.4035360.

[107] B. Polagye, B. Strom, H. Ross, D. Forbush, and R. J. Cavagnaro, "Comparison of cross-flow turbine performance under torque-regulated and speed-regulated control," *Journal of Renewable and Sustainable Energy*, vol. 11, no. 4, pp. 044 501–044 501, 2019. DOI: 10.1063/1.5087476.

[108] A. Snortland, I. Scherl, B. Polagye, and O. Williams, "Cycle-to-cycle variations in cross-flow turbine performance and flow fields," *Experiments in Fluids*, vol. 64, no. 12, p. 188, 2023. DOI: 10.1007/s00348-023-03725-5.

[109] American Society of Mechanical Engineers, *Test Uncertainty*. 2005. [Online]. Available: https://www.asme.org/codes-standards/find-codes-standards/ptc-19-1-test-uncertainty-(1).

[110] S. Zanforlin and T. Nishino, "Fluid dynamic mechanisms of enhanced power generation by closely spaced vertical axis wind turbines," *Renewable Energy*, vol. 99, pp. 1213–1226, 2016. DOI: 10.1016/j.renene.2016.08.015.

[111] I. Scherl, "Optimization, Modeling, and Control of Cross-Flow Turbine Arrays," Ph.D. dissertation, University of Washington, United States – Washington, 2022. [Online]. Available: http://hdl.handle.net/1773/49403.

[112] O. Gauvin-Tremblay and G. Dumas, "Hydrokinetic turbine array analysis and optimization integrating blockage effects and turbine-wake interactions," *Renewable Energy*, vol. 181, pp. 851–869, 2022. DOI: 10.1016/j.renene.2021.09.003.

[113] D. G. Goring and V. I. Nikora, "Despiking Acoustic Doppler Velocimeter Data," *Journal of Hydraulic Engineering*, vol. 128, no. 1, pp. 117–126, 2002. DOI: 10.1061/(ASCE)0733-9429(2002)128:1(117).

[114] A. Hunt *et al.* "An experimental evaluation of the interplay between geometry and scale on cross-flow turbine performance." arXiv: 2310.20616 [physics]. (2024), preprint.

[115] B. Strom, "Cross-Flow Turbine Fluid Mechanics: Experimental Optimization and Analysis," University of Washington, 2019. [Online]. Available: http://hdl.handle.net/1773/43714.

[116] B. Blackwell and R. Sheldahl, "Selected wind tunnel test results for the Darrieus wind turbine," *Journal of Energy*, vol. 1, no. 6, pp. 382–386, 1977. DOI: 10.2514/3.47948.

[117] R. E. Sheldahl, P. C. Klimas, and L. V. Feltz, "Aerodynamic performance of a 5-metre-diameter Darrieus turbine with extruded aluminum NACA-0015 blades," Sandia National Labs., Albuquerque, NM (USA), SAND-80-0179, 1980. [Online]. Available: https://www.osti.gov/biblio/5303846.

[118] M. H. Worstell, "Aerodynamic Performance of the DOE/Sandia 17-m-Diameter Vertical-Axis Wind Turbine," *Journal of Energy*, vol. 5, no. 1, pp. 39–42, 1981. DOI: 10.2514/3.62496.

[119] T. D. Ashwill, "Measured Data for the Sandia 34-Meter Vertical Axis Wind Turbine," Sandia National Labs., Albuquerque, NM (USA), SAND-91-2228, 1992.

[120] M. Shiono, K. Suzuki, and S. Kiho, "An Experimental Study of the Characteristics of a Darrieus Turbine for Tidal Power Generation," *Electrical Engineering in Japan (English translation of Denki Gakkai Ronbunshi)*, vol. 132, no. 3, pp. 38–47, 2000. DOI: 10.1002/1520-6416(200008)132:3⟨38::AID-EEJ6⟩3.0.CO;2-E.

[121] M. El-Samanoudy, A. A. E. Ghorab, and Sh. Z. Youssef, "Effect of some design parameters on the performance of a Giromill vertical axis wind turbine," *Ain Shams Engineering Journal*, vol. 1, no. 1, pp. 85–95, 2010. DOI: 10.1016/j.asej.2010.09.012.

[122] T. Tanino, S. Nakao, T. Miyaguni, and K. Takahashi, "Influence of Reynolds Number and Scale on Performance Evaluation of Lift-type Vertical Axis Wind Turbine by Scale-model Wind Tunnel Tests," *International Journal of Fluid Machinery and Systems*, vol. 4, no. 2, pp. 229–234, 2011. DOI: 10.5293/IJFMS.2011.4.2.229.

[123] S. Armstrong, A. Fiedler, and S. Tullis, "Flow separation on a high Reynolds number, high solidity vertical axis wind turbine with straight and canted blades and canted blades with fences," *Renewable Energy*, vol. 41, pp. 13–22, 2012. DOI: 10.1016/j.renene.2011.09.002.

[124] G. Zhao, R.-s. Yang, Y. Liu, and P.-f. Zhao, "Hydrodynamic performance of a vertical-axis tidal-current turbine with different preset angles of attack," *Journal of Hydrodynamics, Ser. B*, vol. 25, no. 2, pp. 280–287, 2013. DOI: 10.1016/S1001-6058(13)60364-9.

[125] O. Eboibi, L. A. M. Danao, and R. J. Howell, "Experimental investigation of the influence of solidity on the performance and flow field aerodynamics of vertical axis wind turbines at low Reynolds numbers," *Renewable Energy*, vol. 92, pp. 474–483, 2016. DOI: 10.1016/j.renene.2016.02.028.

[126] H. F. Lam, Y. M. Liu, H. Y. Peng, C. F. Lee, and H. J. Liu, "Assessment of solidity effect on the power performance of H-rotor vertical axis wind turbines in turbulent flows," *Journal of Renewable and Sustainable Energy*, vol. 10, no. 2, p. 023 304, 2018. DOI: 10.1063/1.5023120.

[127] Z. Szczerba, P. Szczerba, K. Szczerba, M. Szumski, and K. Pytel, "Wind Tunnel Experimental Study on the Efficiency of Vertical-Axis Wind Turbines via Analysis of Blade Pitch Angle Influence," *Energies*, vol. 16, no. 13, p. 4903, 13 2023. DOI: 10.3390/en16134903.

[128] A. Rezaeiha, H. Montazeri, and B. Blocken, "Characterization of aerodynamic performance of vertical axis wind turbines: Impact of operational parameters," *Energy Conversion and Management*, vol. 169, pp. 45–77, 2018. DOI: 10.1016/j.enconman.2018.05.042.

[129] B. Hand, G. Kelly, and A. Cashman, "Aerodynamic design and performance parameters of a lift-type vertical axis wind turbine: A comprehensive review," *Renewable*

and Sustainable Energy Reviews, vol. 139, p. 110 699, 2021. DOI: 10.1016/j.rser.2020.110699.

[130] A. Bianchini, F. Balduzzi, G. Ferrara, and L. Ferrari, "Influence of the Blade-Spoke Connection Point on the Aerodynamic Performance of Darrieus Wind Turbines," in *Volume 9: Oil and Gas Applications; Supercritical CO2 Power Cycles; Wind Energy*, Seoul, South Korea: American Society of Mechanical Engineers, 2016, V009T46A012. DOI: 10.1115/GT2016-57667.

[131] P. Bachant, "Physical and numerical modeling of cross-flow turbines," University of New Hampshire, Durham, NH, 2016. [Online]. Available: https://scholars.unh.edu/dissertation/2258.

[132] P. Bachant and M. Wosnik, "Characterising the near-wake of a cross-flow turbine," *Journal of Turbulence*, vol. 16, no. 4, pp. 392–410, 2015. DOI: 10.1080/14685248.2014.1001852.

[133] C. A. Consul, R. H. J. Willden, E. Ferrer, and M. D. McCulloch, "Influence of Solidity on the Performance of a Cross-Flow Turbine," in *8th European Wave and Tidal Energy Conference (EWTEC 2009)*, Uppsala, Sweden, 2009, p. 10.

[134] A. Mandal and J. Burton, "The Effects of Dynamic Stall and Flow Curvature on the Aerodynamics of Darrieus Turbines Applying the Cascade Model," *Wind Engineering*, vol. 18, no. 6, pp. 267–282, 1994. JSTOR: 43749553. [Online]. Available: https://www.jstor.org/stable/43749553.

[135] S. Li and Y. Li, "Numerical Study on the Performance Effect of Solidity on the Straight-Bladed Vertical Axis Wind Turbine," in *2010 Asia-Pacific Power and Energy Engineering Conference*, 2010, pp. 1–4. DOI: 10.1109/APPEEC.2010.5449269.

[136] A. Hunt *et al.*, *[dataset] Experimental data from "A parametric evaluation of the interplay between geometry and scale on cross-flow turbine performance"*, 2023. [Online]. Available: http://hdl.handle.net/1773/50607.

[137] J. O. Dabiri, "Potential order-of-magnitude enhancement of wind farm power density via counter-rotating vertical-axis wind turbine arrays," *Journal of Renewable and Sustainable Energy*, vol. 3, no. 4, pp. 043 104–043 104, 2011. DOI: 10.1063/1.3608170.

[138] B. Gaurier *et al.*, "Tidal energy "Round Robin" tests comparisons between towing tank and circulating tank results," *International Journal of Marine Energy*, Special Issue on Marine Renewables Infrastructure Network, vol. 12, pp. 87–109, 2015. DOI: 10.1016/j.ijome.2015.05.005.

[139] L. Y. Pao and K. E. Johnson, "A tutorial on the dynamics and control of wind turbines and wind farms," in *2009 American Control Conference*, 2009, pp. 2076–2089. DOI: 10.1109/ACC.2009.5160195.

[140] J. Westerweel and F. Scarano, "Universal outlier detection for piv data," *Experiments in Fluids*, vol. 39, 6 2005. DOI: 10.1007/s00348-005-0016-6.

[141] H. Glauert, "Airplane Propellers," in *Aerodynamic Theory: A General Review of Progress Under a Grant of the Guggenheim Fund for the Promotion of Aeronautics*, W. F. Durand, Ed., Berlin, Heidelberg: Springer, 1935, pp. 169–360. DOI: 10.1007/978-3-642-91487-4_3.

[142] A. S. Bahaj, A. F. Molland, J. R. Chaplin, and W. M. J. Batten, "Power and thrust measurements of marine current turbines under various hydrodynamic flow conditions in a cavitation tunnel and a towing tank," *Renewable Energy*, vol. 32, no. 3, pp. 407–426, 2007. DOI: 10.1016/j.renene.2006.01.012.

[143] D. Medici and P. H. Alfredsson, "Measurements on a wind turbine wake: 3D effects and bluff body vortex shedding," *Wind Energy*, vol. 9, no. 3, pp. 219–236, 2006. DOI: 10.1002/we.156.

[144] L. P. Chamorro, R. Arndt, and F. Sotiropoulos, "Reynolds number dependence of turbulence statistics in the wake of wind turbines," *Wind Energy*, vol. 15, no. 5, pp. 733–742, 2012. DOI: 10.1002/we.501.

[145] A. J. Alexander and B. P. Holownia, "Wind tunnel tests on a savonius rotor," *Journal of Wind Engineering and Industrial Aerodynamics*, vol. 3, no. 4, pp. 343–351, 1978. DOI: 10.1016/0167-6105(78)90037-5.

[146] M. J. Barnsley and J. F. Wellicome, "Final report on the 2nd phase of development and testing of a horizontal axis wind turbine test rig for the investigation of stall regulation aerodynamics," ETSU, Technical Report E.5A/CON5103/ 1746, 1990.

[147] K. Steiros, N. Bempedelis, and M. M. Cicolin, "An analytical blockage correction model for high-solidity turbines," *Journal of Fluid Mechanics*, vol. 948, A57, 2022. DOI: 10.1017/jfm.2022.735.

[148] D. Dehtyriov, C. Vogel, and R. Willden, "A Two-scale blockage correction for an array of tidal turbines," *Proceedings of the European Wave and Tidal Energy Conference*, vol. 15, 2023. DOI: 10.36688/ewtec-2023-366.

[149] R. J. Cavagnaro and B. Polagye, "Field performance assessment of a hydrokinetic turbine," *International Journal of Marine Energy*, vol. 14, pp. 125–142, 2016. DOI: 10.1016/j.ijome.2016.01.009.